Radiation damage of highly irradiated silicon sensors

Dissertation

zur Erlangung des Doktorgrades

des Department Physik

der Universität Hamburg

vorgelegt von

Christian Scharf

aus Hamburg

Hamburg

2018

Gutachter der Dissertation:	Prof. Dr. Erika Garutti
	Dr. Michael Moll
Zusammensetzung der Prüfungskommission:	Prof. Dr. Erika Garutti
	Dr. Michael Moll
	Prof. Dr. Peter Schleper
	Prof. Dr. Günter Sigl
	Prof. Dr. Wolfgang Hansen
Vorsitzender der Prüfungskommission:	Prof. Dr. Wolfgang Hansen
Datum der Disputation:	10.07.2018
Vorsitzender Fach-Promotionsausschusses PHYSIK:	Prof. Dr. Wolfgang Hansen
Leiter des Fachbereichs PHYSIK:	Prof. Dr. Michael Potthoff
Dekan der Fakultät MIN:	Prof. Dr. Heinrich Graener

Abstract

Modern particle physics at colliders demands for a continuous increase of the luminosity for colliding particle beams in order to study rare events. The requirements for the performance of the particle detectors are increasing while the detectors are subject to unprecedented fluences of particles. Due to its high radiation-hardness silicon is an integral part of many detector systems in particle physics. This thesis experimentally investigates fundamental, radiation-induced changes of the material properties of silicon sensors for neutron equivalent fluences beyond $10^{15}\,\mathrm{cm}^{-2}$.

An increase of the absorption coefficient of near-infrared light has been measured and parameterized as a function of the fluence. The absorption coefficient is needed to determine the deposited charge for charge collection efficiency measurements using near-infrared light.

An edge-Transient Current Technique *edge-TCT* setup has been built and commissioned. It has been used to determine velocity profiles and charge profiles in strip sensors. These measurements are compared to current and capacitance measurements of pad diodes. An empirical model for the reverse current of diodes has been developed which describes the measurements within a few percent. The parameters of the model have been obtained and parameterized as a function of the fluence and the temperature. A decrease of the low-field carrier mobilities with fluence has been observed and parameterized. Forward current measurements are described by a model for space-charge-limited currents.

For forward-biased strip sensors the product of the trapping times and mobilities has been determined. It was found that this product hardly depends on the electric field. The results mostly agree with the charge collection efficiency of diodes.

For the Phase II upgrade of the Compact Muon Solenoid tracking detector at the Large Hadron Collider, photolithography mask layers for different geometries of pixel sensors with pixel dimensions down to $50 \times 50\,\mu\mathrm{m}^2$ and $100 \times 25\,\mu\mathrm{m}^2$ for different read-out chips, as well as different test structures have been designed. The sensors have been produced and are undergoing beam tests as of the publication date.

Finally, a method for the partial deconvolution of the electronics response from measured current transients is presented which can significantly reduce oscillations and reflections in measurements.

Kurzfassung

Die heutige Elementarteilchenphysik verlangt nach einer beständigen Erhöhung der Luminosität von Teilchenbeschleunigern um seltene Ereignisse zu untersuchen. Die Anforderungen an die Leistungsfähigkeit der Teilchendetektoren steigen beständig, während die Detektoren immer höheren Fluenzen schädigender Strahlung ausgesetzt sind. Aufgrund seiner hohen Strahlenhärte ist Silizium ein integraler Bestandteil vieler Detektorsysteme. Für diese Arbeit wurden viele fundamentale strahlungsbedingte Änderungen der Materialeigenschaften von Siliziumsensoren bei Neutronen-Äquivalenz-Fluenzen größer als $10^{15}\,\mathrm{cm}^{-2}$ experimentell untersucht.

Ein Anstieg des Absorptionskoeffizienten von nahem Infrarotlicht wurde gemessen sowie in Abhängigkeit der Fluenz parametrisiert. Die Ergebnisse werden benötigt, um die erzeugte Ladung bei Messungen der Ladungssammlungseffizienz mit nahem Infrarotlicht zu bestimmen.

Im Laufe dieser Arbeit wurde ein edge-Transient Current Technique *edge-TCT* Messaufbau entwickelt und getestet. Der Messaufbau wurde verwendet, um Geschwindigkeits- sowie Ladungsprofile von Streifensensoren zu erstellen. Diese Messungen wurden mit Strom- und Kapazitätsmessungen von Flächendioden verglichen. Für den Strom unter angelegter Spannung in Rückwärtsrichtung wurde ein empirisches Modell entwickelt, das die Messungen innerhalb weniger Prozent beschreibt. Die Parameter des Modells wurden in Abhängigkeit von der Fluenz bestimmt und parametrisiert. Eine Abnahme der Niedrigfeld-Mobilität der Ladungsträger mit der Fluenz wurde gemessen und parametrisiert. Der Strom in Vorwärtsrichtung wird mit einem Raumladungsgesetz beschrieben.

Außerdem wurde das Produkt aus der Mobilität und der Einfang-Lebensdauer der Ladungsträger für Streifensensoren unter Spannung in Vorwärtsrichtung bestimmt. Die Messungen zeigen, dass sich das Produkt kaum mit dem elektrischen Feld ändert. Die Ergebnisse stimmen größtenteils mit Messungen der Ladungssammlungseffizienz von Flächendioden überein.

Für das Phase II Upgrade des Silizium-Spurdetektors des Compact Muon Solenoid Experimentes wurden die Fotolithografie-Masken für verschiedene Geometrien von strahlungsresistenten Pixelsensoren mit kleinsten Pixelgrößen von $50 \times 50\,\mu\mathrm{m}^2$ und $100 \times 25\,\mu\mathrm{m}^2$ für verschiedene Auslesechips sowie verschiedene Teststrukturen programmiert. Die Sensoren wurden hergestellt und werden zum Zeit-

punkt der Veröffentlichung dieser Arbeit getestet.

Es wurde eine Methode entwickelt, um den Einfluss der Ausleseelektronik auf gemessene Stromtransienten teilweise zu entfalten. Die vorgestellte Methode ist in der Lage Oszillationen sowie Reflektionen von gemessenen Transienten beträchtlich zu verringern.

Contents

Abstract v

Kurzfassung vii

Table of contents xii

1. Introduction 1

1.1. The Large Hadron Collider . . . 1
1.2. Silicon sensors at the Compact Muon Solenoid . . . 2

2. Silicon sensors 6

2.1. Basic concepts . . . 6
2.1.1. The p-n junction . . . 11
2.1.2. Diode current . . . 14
2.1.3. Relaxation . . . 16
2.1.4. Space-charge-limited currents . . . 16
2.2. Radiation damage . . . 18
2.2.1. NIEL hypothesis . . . 20
2.2.2. Point defects . . . 21
2.2.3. Cluster defects . . . 22
2.2.4. Generation current . . . 23
2.3. Radiation detectors . . . 25
2.3.1. Signal generation in pad sensors . . . 25
2.3.2. The weighting potential . . . 26
2.3.3. Radiation-hard sensors . . . 28

3. Experimental methods 31

3.1. Test structures . . . 31
3.1.1. Bare single crystal silicon . . . 31
3.1.2. Pad diodes . . . 32
3.1.3. Strip sensors . . . 33
3.2. Current and capacitance measurements . . . 34
3.3. The Transient Current Technique . . . 35
3.3.1. Pad diode TCT . . . 36

3.3.2. Multi-channel edge-TCT . . . 38
Setup . . . 39
Sample preparation . . . 43
Beam profile . . . 43
Focus finding . . . 44
The charge profile . . . 46
The velocity profile . . . 46
Temperature offset . . . 48
3.4. Transmission spectroscopy . . . 51

4. Light absorption **53**
4.1. Edge-TCT measurements . . . 53
4.1.1. Analysis . . . 53
4.1.2. Results . . . 54
4.2. Transmittance measurements . . . 57
4.2.1. Analysis . . . 57
4.2.2. Results . . . 59
4.3. Conclusion . . . 64

5. Current, capacitance, and electric field **66**
5.1. Introduction . . . 66
5.2. Velocity profiles . . . 71
5.2.1. Reverse bias . . . 72
5.2.2. Forward bias . . . 75
5.3. Reverse current . . . 76
5.3.1. Ohmic region . . . 76
5.3.2. Depletion . . . 78
Parameterization . . . 80
Fluence dependence of the low-field mobility . . . 83
The threshold voltage . . . 86
The exponent . . . 86
The space-charge region . . . 89
5.3.3. Exponential increase of the reverse current . . . 91
The pad current . . . 93
Parameterization . . . 95
5.3.4. Discussion . . . 96
5.4. Forward current . . . 98
5.4.1. Results . . . 98

5.4.2. Parameterization . . . 98
Fit parameters . . . 100
5.4.3. Discussion . . . 103
5.5. Capacitance-voltage characteristics . . . 107
Reverse bias . . . 107
Forward bias . . . 107
5.6. Conclusion . . . 110
Reverse bias . . . 110
Forward bias . . . 111

6. The charge collection length for forward bias 113
6.1. Measurements of pad diodes . . . 113
6.1.1. Analysis . . . 113
Determination of the charge collection length . . . 113
Charge collection for infrared light . . . 115
Fit of the drift velocities and trapping times . . . 116
6.1.2. Results . . . 117
6.2. Measurements with strip sensors . . . 119
6.2.1. Analysis . . . 119
6.2.2. Results . . . 123
6.3. Comparison of diode and strip sensor results . . . 127
6.4. Conclusion . . . 129

7. Measurement of the mobilities 131
7.1. Non-irradiated silicon . . . 131
7.2. Irradiated silicon . . . 134

8. Conclusion 137

A. Design of pixel sensors and test structures 144
A.1. Pixel sensors . . . 147
A.1.1. Biasing schemes . . . 147
A.1.2. PSI46digi . . . 149
A.1.3. ROC4SENS . . . 149
A.1.4. RD53A . . . 149
A.2. Test structures . . . 152
A.2.1. Pad diodes . . . 152
A.2.2. Strip sensors . . . 153
A.2.3. Spaghetti diodes . . . 154
A.2.4. Miscellaneous . . . 154

B. Deconvolution of current transients 157

C. Table of the NIR absorption coefficient with fluence 161

D. Measured and calculated charge collection efficiency of diodes 163

List of Figures 165

List of Tables 170

Bibliography 171

Acknowledgements 187

1. Introduction

Human curiosity has led to the discovery of many different laws of nature and technologies making use of these laws. The knowledge gained by research has fundamentally changed the way we live and the way we perceive the universe over the last few millennia, which is just a blink in the history of life on earth. This knowledge has generated considerable wealth which, in turn, enables us to conduct fundamental research speeding up the technological advance of our civilization.

The aim of this work is to gain further understanding of radiation damage in silicon particle detectors in order to develop efficient and precise detectors with high radiation tolerance. Radiation-tolerant detectors are used in high energy physics, space probes, and x-ray physics, amongst others. High energy physics combines a wide field of research with the aim of identifying and probing the smallest constituents of the universe, the elementary particles, and the interactions between them through the fundamental forces of nature; all of which determines the nature of our universe and all life within.

Our current Standard Model of particle physics is not capable of describing the universe as we see it today. Many open questions remain like the asymmetry between matter and antimatter in the baryogenesis or the origin and nature of the largest part of the universe, dark matter and dark energy. Scientists have invented theories like supersymmetry which could possibly solve certain flaws of the Standard Model and may explain concepts like dark matter. Large particle detectors are being built in order to test predictions made by such theories and to find new physics. Accelerators of many kilometers length are used to accelerate particles almost to the speed of light; just to make them collide within large particle detectors. In a collision, their kinetic energy can be converted into the creation of new particles, according to Einstein's famous $E = mc^2$. Silicon has a wide array of applications in these detectors, some of which will be described here.

1.1. The Large Hadron Collider

The Large Hadron Collider *LHC* [1] is the largest and most powerful particle accelerator so far, located in Central Europe crossing the border between France

and Switzerland near the city of Geneva. It has been built in a global effort by thousands of scientists, engineers, and technicians. At LHC, protons and heavy ions are accelerated almost to the speed of light in a synchrotron in an underground tunnel with a circumference of 27 km at a depth of 100 m. The maximum kinetic energy of the protons is 7 TeV. The proton beams consist of highly focused bunches of 10^{11} protons each. Two beams are collided head-on at certain positions of the synchrotron, where the main experiments are positioned. The maximum center-of-mass energy of the colliding protons is $\sqrt{s} = 14\,\text{TeV}$. At this energy the constituents of the protons can interact, break up the protons, and create new particles. The LHC produces many different, potentially new or poorly studied, particles. In 2012 the detection of a new particle - the Higgs boson - was announced [2, 3] by the experiments ATLAS [4] and CMS [5] at the LHC. The Higgs boson had been postulated [6] in the 1960s and its detection was honored in 2013 as the Nobel prize in physics was awarded to two theoreticians who predicted it, Peter Higgs and François Englert.

The main experiments at LHC are large particle detectors around the interaction points where the collisions happen. Performance-wise, the aim of these detectors is a hermetic coverage of the interaction point in order to detect all particles created or scattered in the collisions.

In order to collect sufficient statistics for rare events the luminosity, which is the particle rate per unit area, is pushed to the limit. LHC operates at a bunch collision frequency of 40 MHz. This means every 25 ns two bunches collide at the interaction points. For each of these bunch-crossings several of the 10^{11} protons per bunch collide and create primary vertices, which is called pile-up. The challenge for the detector system is to disentangle up to hundreds of pile-up events every 25 ns, while the primary vertices are only $\mathcal{O}(100\,\mu\text{m})$ away from each other. At the interaction points the beams have dimensions of about $17 \times 17\,\mu\text{m}^2$ width and 7.6 cm length [7, 8]. A bunch crossing happens within [9] about 150 ps or about 4.5 cm.

1.2. Silicon sensors at the Compact Muon Solenoid

One of the experiments at LHC is the Compact Muon Solenoid *CMS*. Much of the work published here has been performed within the CMS collaboration. The CMS experiment is a 28.7 m long, 15.0 m diameter onion-like detector system with different segmented detector layers around the interaction point. It features a strong

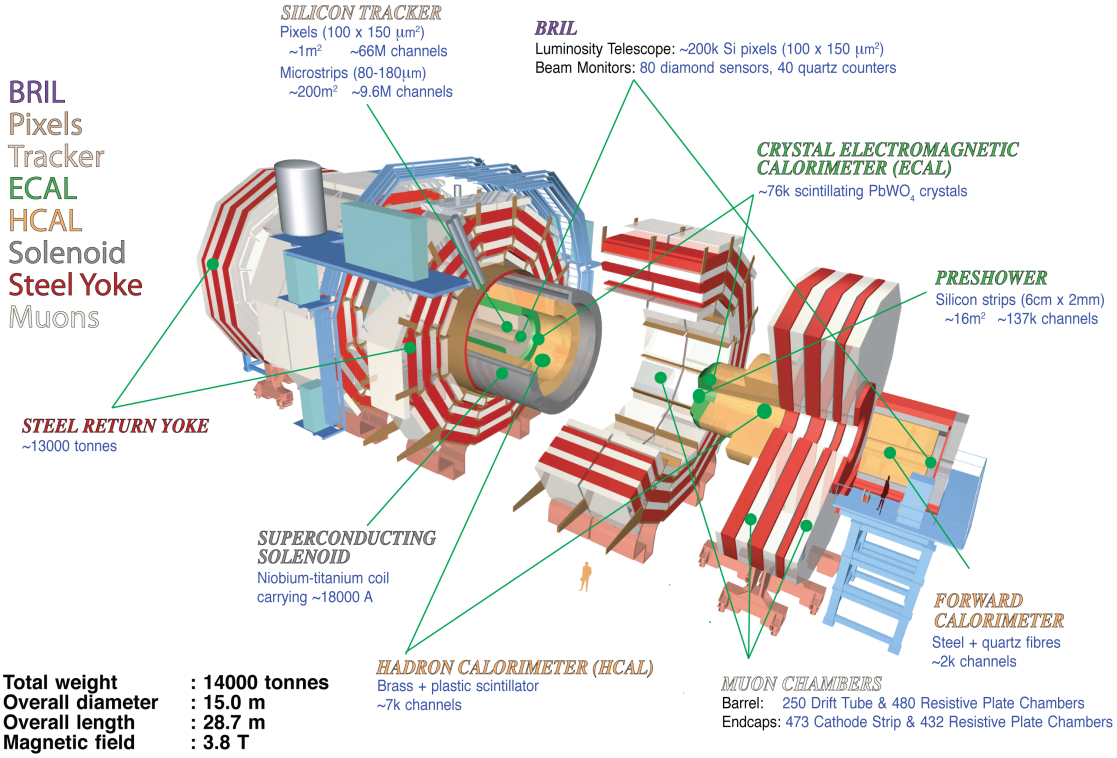

Figure 1.1.: Schematic drawing of the CMS experiment as of 2018 with the different detector systems and the solenoid magnet. From [10].

solenoid magnet with a field strength of 3.8 T and a massive iron return yoke for the magnetic field, which amounts for much of its impressive weight of 14,000 t. Figure 1.1 shows the CMS experiment with the different parts. The different detector layers amount to millions of individual channels. The detector system allows for precise reconstruction of the path and energy of the particles passing through the individual detector layers.

The innermost part of the detector system is the silicon tracking detector which is also a focus of this work. The first tracker layers are just a few centimeters away from the interaction point. The particle flux is the highest for the innermost tracker layers (see fig. 1.2). Since highly energetic radiation damages materials, the inner tracking layers have to be especially radiation tolerant to operate reliably for several years. Additionally, the number of channels per area (the granularity) of the tracker has to be very high in order to decrease the number of busy channels relative to the number of idle channels (the occupancy) since the detector has to distinguish thousands of particle tracks close to each other for each bunch-crossing. A very high position resolution is needed for the precise 3-D reconstruction of particle tracks, primary vertices, secondary vertices from short-lived particles, and for the measurement of the particle momentum. The momentum of charged particles is determined by the bending of the particle track in the magnetic field of the solenoid

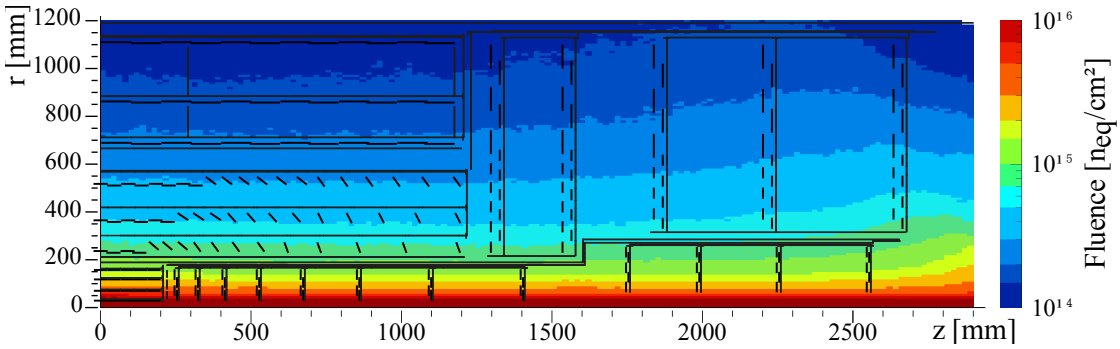

Figure 1.2.: Simulated neutron-equivalent particle fluence Φ_{eq} in the future silicon tracker of CMS after an integrated luminosity of 3000 fb^{-1} at $\sqrt{s}$ = 14 TeV. The figure shows a cross section of a quarter of the tracker. The black lines represent the different detector layers. The interaction point is at zero. From [11].

magnet. 3-D reconstruction of particle tracks is achieved by identifying the position of a particle in several of the consecutive, onion-like tracker layers. Therefore, the innermost tracker layers with the highest track density are instrumented with very fine-pitch pixel sensors. Currently, the pixels (channels) have dimensions of $100 \times 150\,\mu m^2$. The outer layers of the tracker are instrumented with silicon strip sensors which have a larger area per individual channel.

For the so-called Phase II upgrade [11], planned to be installed around 2024, prototypes with different geometries for the innermost pixel layer are being investigated, with pixel dimensions of $50 \times 50\,\mu m^2$ and $100 \times 25\,\mu m^2$. In the scope of this work dynamic code has been developed with many variable parameters for the computer-aided design of the photolithography masks for the production of different pixel sensors for different read-out chips, as well as test structures. The pixel sensors are subject to different beam tests and radiation-hardness studies as of the publication date. The project is described in detail in appendix A.

Surrounding the silicon tracker is the electromagnetic calorimeter which measures the kinetic energy of photons and charged particles. In order to measure highly energetic particle jets and neutral particles a hadronic calorimeter is surrounding the electromagnetic calorimeter. Ideally, all particles should be stopped within the calorimeter to contain and measure the total kinetic energy. For this reason material with a high atomic number, leading to a high stopping power, is used as an absorber.

For the Phase II upgrade silicon will be used in the calorimeter. The High Granularity Calorimeter *HGCAL* [12, 13, 14, 15] will be a sampling calorimeter in the forward direction. In the electromagnetic section it will feature interchanging layers of absorber material and silicon layers as the active sensor material. The

hadronic section will use scintillating material. The silicon sensors have to be especially radiation-hard as collisions of particles with the absorber material lead to hadronic and electromagnetic showers in the calorimeter and significant radiation damage in the sensors. In order to allow for the 3-D reconstruction of showers it will feature pixels with areas of $(0.5 - 1)\,\mathrm{cm}^2$. The sensors are glued directly to printed circuit boards for read-out. The front-end electronics will provide timing information with about 50 ps precision for 4-D reconstruction of the shower development. A high timing resolution of the detector helps to disentangle pile-up events happening at the same reconstructed position of the primary vertex in the interaction region (the luminous region) at different times. The timing The HGCAL will be the largest silicon detector built so far, with a silicon surface area of about $600\,\mathrm{m}^2$.

Ideally, only neutrinos and muons can pass through the calorimeter system and the following solenoid magnet. Muon tracks are identified by the muon chambers surrounding the solenoid magnet (see fig. 1.1).

This work focuses on the effects of radiation damage in silicon after very high hadron fluences of $\Phi_{eq} > 10^{15}$ cm^{-2} 1 MeV neutron equivalent. For the CMS detector, these levels will be reached in the inner layers of the silicon tracker (see fig. 1.2) and in some layers of the silicon based HGCAL.

2. Silicon sensors

This chapter gives a short introduction about the relevant concepts of silicon diodes, radiation damage, and radiation-hard silicon sensors.

Silicon is a semiconductor with an indirect band gap of $E_g \approx 1.12\,\mathrm{eV}$ at room temperature. The mean energy to create an electron-hole pair in silicon by ionizing radiation is about 3.6 eV.

Silicon sensors for radiation detection are usually made of highly pure, high-ohmic silicon. Single crystal silicon is used and the crystal direction commonly used has the Miller indices $\langle 100 \rangle$. Historically, also $\langle 111 \rangle$ silicon has been used which has slightly different physical properties. There are different methods to produce sensor-grade silicon which introduce different impurity concentrations into the silicon (see ref. [16]). Most sensors discussed in this thesis are made of so-called float-zone *FZ* silicon. Here, single polycrystalline silicon rods are pulled through a radio-frequency field which melts the poly-silicon and the melt crystallizes in a single crystal. The lattice direction is determined by a seed crystal. FZ silicon rods are very homogeneous. The impurity concentrations mostly depend on the quality of the polysilicon rod. Additionally, some of the sensors discussed here are made of silicon produced with the so-called magnetic Czochralski *MCZ* method. Silicon is molten in a SiO_2 crucible and a single-crystal rod is pulled from the melt with a seed crystal. The oxygen concentration obtained with this method is usually higher than for the FZ method as the SiO_2 crucible partially dissolves. Also, as some impurities may accumulate in the melt during the pulling of a single crystal rod the impurity concentration may be inhomogeneous throughout the rod with this method. The rods are then cut into so-called wafers and processed further e.g. by introduction of patterned surface structures like implants, oxide layers, and metallic contacts via photolithography.

2.1. Basic concepts

Here, the important relations for semiconductors will be revised, loosely based on Grove [17].

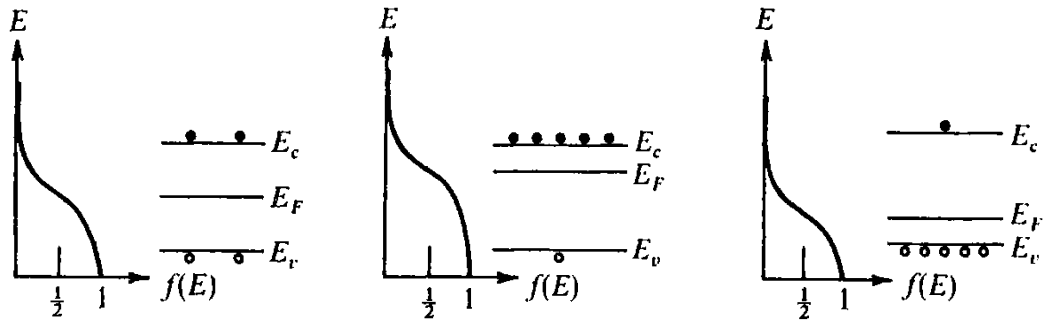

(a) intrinsic (b) n-type (c) p-type

Figure 2.1.: Schematic Fermi-Dirac distribution and the Fermi energy E_F with the free carrier concentration for intrinsic and extrinsic semiconductors. From [17].

The Fermi-Dirac distribution function

$$f(E) = \frac{1}{1 + \exp\left(\frac{E - E_F}{k_B T}\right)} \tag{2.1}$$

shown in fig. 2.1 describes the probability that a state with energy E is occupied by an electron; with the Boltzman constant k_B and the Fermi energy E_F. With equation 2.1 the concentration of free electrons in the conduction band at the energy E_C can be calculated as

$$n = N_C \exp\left(-\frac{E_C - E_F}{k_B T}\right) \tag{2.2}$$

and the concentration of free holes in the valence band at the energy E_V

$$p = N_V \exp\left(-\frac{E_F - E_V}{k_B T}\right) \tag{2.3}$$

with the effective density of states N_C in the conduction band and N_V in the valence band.

Intrinsic silicon[1] has a very low concentration of free carriers and a high resistivity. The product of the free electron concentration n and the free hole concentration p follows the so-called mass-action law

$$np = n_i^2 = N_C N_V \exp\left(-\frac{E_g(T)}{k_B T}\right) \tag{2.4}$$

with the intrinsic concentration of free carriers n_i. The carrier concentrations in

[1] Intrinsic silicon does not contain electrically active impurities which alter the electrical properties.

intrinsic silicon are $n = p = n_i$, ensuring charge neutrality. Here, the the recent parameterization

$$n_i = 1.541 \cdot 10^{15} T^{1.712} \exp\left(\frac{-E_g(T)}{2k_B T}\right) \text{ cm}^{-3} \tag{2.5}$$

from ref. [18] will be used throughout. The band gap energy can be described by

$$E_g(T) = E(0) - \alpha\Theta\left\{\frac{1-3\Delta^2}{\exp(\Theta/T)-1} + a\right\} \tag{2.6}$$

$$a = \frac{3\Delta^2}{2}\left(\sqrt[6]{1 + \frac{\pi^2}{3(1+\Delta^2)}\left(\frac{2T}{\Theta}\right)^2 + \frac{3\Delta^2-1}{4}\left(\frac{2T}{\Theta}\right)^3 + \frac{8}{3}\left(\frac{2T}{\Theta}\right)^4 + \left(\frac{2T}{\Theta}\right)^6} - 1\right) \tag{2.7}$$

with the parameters $E(0) = 1.1701\,\text{eV}$, $\alpha = 3.23 \cdot 10^4\,\text{eV/K}$, $\Theta = 446\,\text{K}$, $\Delta = 0.51$ according to ref. [19]. At room temperature eq. 2.5, 2.6, 2.7 result in $n_i(300\,\text{K}) = 9.68 \cdot 10^9\,\text{cm}^{-3}$ and $E_g(300\,\text{K}) = 1.124\,\text{eV}$.

The concentration of free carriers can be modified by doping silicon. Doped silicon is called extrinsic. Silicon is a group IV element of the table of elements, meaning it has four valence electrons. Introducing group III or group V elements as impurities into the silicon crystal leads to ionization of the impurity atoms in order to share orbital bonds with silicon. The ionization energy is very small ($\sim 40\,\text{meV}$) and the impurities are completely ionized at room temperature. Usually, boron (group III) or phosphorus (group V) are used.

If both group III and V dopants are present in the semiconductor at the same time their charge will partly compensate. The effective doping concentration is now

$$N_{eff} = N_D - N_A \tag{2.8}$$

with the acceptor and donor concentrations $N_{A,D}$. The fixed space charge of ionized impurities is compensated by free carriers. The Fermi energy will adjust according to eq. 2.1 (see fig. 2.1(b), (c)). An acceptor (group III) with concentration N_A will trap electrons and decrease the concentration of free electrons n in the conduction band. If $N_A > N_D$ the semiconductor is called p-type. Electrons are now called minority carriers. The concentration of free holes p in the valence band increases to establish charge neutrality $p - n = N_D - N_A$. Holes are now called majority carriers. If $N_A \gg (n_i,\, N_D)$ the hole concentration is $p \approx N_A$ after the mass-action law $np = n_i^2$. Likewise, a donor (group V) concentration $N_D \gg (n_i,\, N_A)$ leads to an increase of the concentration of free electrons in the conduction band and a

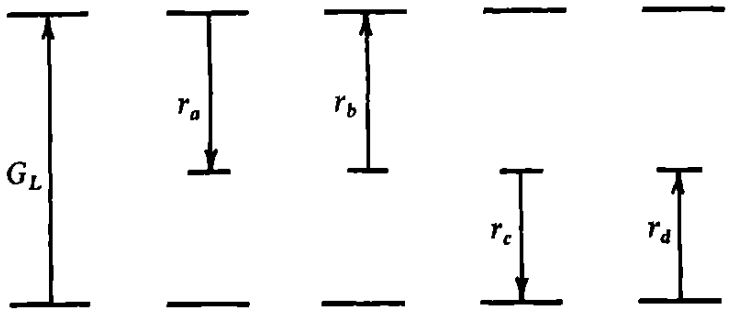

Figure 2.2.: Schematic of Shockley-Read-Hall generation-recombination at deep levels. G_L illustrates an external generation rate i.e. from illumination, r_a electron capture, r_b electron emission, r_c hole capture, and r_d hole release. From [17].

decrease of the concentration of free holes in the valence band. The holes are now minority carriers.

Concluding, p-type silicon has the majority carrier concentration $p \approx N_{eff}$ and the minority carrier concentration $n \approx n_i^2/N_{eff}$; and n-type has $n \approx N_{eff}$ and $p \approx n_i^2/N_{eff}$.

The conductivity of a semiconductor is given by

$$\sigma = e \cdot (n\mu_e + p\mu_h) \tag{2.9}$$

with the elementary charge e. The resistivity is given by $\rho = 1/\sigma$. The carrier mobilities $\mu_{e,h}(\mathscr{E})$ as a function of the electric field[2] $\mathscr{E}$ and the particle fluence have been measured in the course of this work and will be discussed in chapter 7. In an extrinsic n-type semiconductor the conductivity becomes $\sigma \approx e \cdot n\mu_e$ and similar for p-type.

Thermal diffusion of free carriers is described by diffusion constant

$$D_{e,h} = \frac{k_B T}{e} \mu_{e,h} \tag{2.10}$$

and the diffusion length is

$$L_{e,h} = \sqrt{D_{e,h}\tau} \tag{2.11}$$

with the lifetime τ which is determined by the recombination rate (see eq. 2.19).

As mentioned above, dopant atoms with small activation energy will be ionized for $T \gtrsim 50\,\mathrm{K}$. In other words, they introduce energy levels in the band gap very close to the edges of the conduction (acceptor) or valence (donor) band. Such

[2]This chapter uses $\mathscr{E}$ for the electric field to avoid confusion with the energy E. However, the following chapters use E for the electric field.

impurities are called shallow. Other impurities can introduce deep energy levels close to the Fermi energy in intrinsic silicon

$$E_i = \frac{1}{2}\left(E_C + E_V\right) + \frac{1}{2}k_B T \cdot \ln\frac{N_V}{N_C} \tag{2.12}$$

which is close to the mid-gap energy $E_g/2$. In order to charge deep levels (deep defects) with energy E_t a larger energy $\Delta E = E_{C,V} - E_t$ is needed. Some deep defects can be occupied by either holes or electrons if $E_t \sim E_i$. Deep levels are responsible for generation and recombination of free carriers. In general, the occupation of shallow and deep defect levels are described by Shockley-Read-Hall statistics (see fig. 2.2). The probability for a deep level to be occupied by an electron is given by eq. 2.1 with E_t.

The rate of electron capture (see fig. 2.2) is given by

$$r_a = v_{th}^{e}\sigma_n n N_t\left(1-f\right) \tag{2.13}$$

with the concentration of deep levels N_t, the electron capture cross-section σ_n, the thermal velocity $v_{th}^{e,h} = \sqrt{8k_BT/\left(\pi m_{eff}^{e,h}\right)}$, and the effective electron or hole mass $m_{eff}^{e,h}$. The rate of electron emission

$$r_b = e_n N_t f \tag{2.14}$$

depends on the concentration of deep levels occupied by electrons $N_t f$ and the emission probability e_n. The emission probability depends on the distance to the conduction band; e.g. it will be very small for levels close to the valence band introduced by acceptors. Similarly, the rate of hole capture is

$$r_c = v_{th}^{h}\sigma_p p N_t f \tag{2.15}$$

and for hole emission

$$r_d = e_p N_t\left(1-f\right). \tag{2.16}$$

In equilibrium the net generation per unit volume is $G_L = 0$ and the capture and emission rates are $r_a = r_b$ and $r_c = r_d$. From this the electron emission probability can be determined as

$$e_n = v_{th}^{e}\sigma_n N_C \exp\left(-\frac{E_C - E_t}{k_B T}\right) = v_{th}^{e}\sigma_n n_i \exp\left(\frac{E_t - E_i}{k_B T}\right) \tag{2.17}$$

and similar with $(E_i - E_t)$ for e_p. If the emission probability is assumed to be independent of the Fermi energy eq. 2.17 is also valid in non-equilibrium. It is

apparent that the efficiency of generation at deep levels is high if the levels are close to E_i as the emission probabilities of both electrons and holes will be high.

The recombination rate can be estimated assuming a change of the free carrier concentrations via uniform generation G_L i.e. by illumination. In non-equilibrium but steady state $\frac{\mathrm{d}n}{\mathrm{d}t} = G_L - (r_a - r_b) = 0$ and $\frac{\mathrm{d}p}{\mathrm{d}t} = G_L - (r_c - r_d) = 0$ we get $r_a - r_b = r_c - r_d$ and the recombination rate $U_r = r_a - r_b = r_c - r_d$ is

$$U_r = \frac{\sigma_p \sigma_n v_{th} N_t \left(pn - n_i^2\right)}{\sigma_n \left(n + n_i \exp\left(\frac{E_t - E_i}{k_b T}\right)\right) + \sigma_p \left(p + n_i \exp\left(\frac{E_i - E_t}{k_b T}\right)\right)} \tag{2.18}$$

or

$$U_r = \sigma v_{th} N_t \frac{pn - n_i^2}{n + p + 2n_i \cosh\left(\frac{E_t - E_i}{k_B T}\right)} \tag{2.19}$$

for $\sigma_n = \sigma_p = \sigma$, assuming $v_{th}^e = v_{th}^h$ in both cases. Therefore, in non-equilibrium the recombination rate is determined by $np - n_i^2$.

Deep levels also reduce the free carrier concentration in equilibrium (see ref. [20]) in an extrinsic semiconductor as the Fermi energy is shifted towards $E_t \sim E_i$. This is known as carrier removal [21]. Accordingly, for a n-type semiconductor free electrons will be trapped at deep defects and the electron concentration will decrease by $n \approx N_D - N_t$ for $N_t \ll N_D$, assuming $N_A \ll N_D$. Consequently, the conductivity will be decreased. This concept is important for irradiated sensors as we will see later (see chapter 5).

2.1.1. The p-n junction

If the effective doping of silicon abruptly changes from p- to n-type a space-charge region *SCR* (depletion region) develops at the boundary (see fig. 2.3(a)). Due to the difference in hole and electron concentrations in the p and n-regions the carriers will diffuse in order to reach equilibrium. Since the Fermi energy E_F has to be constant over the whole SCR the band structure adjusts accordingly (see fig. 2.3(b)). An electric field (fig. 2.3(c)) builds up until the current by diffusion is the same as the opposite current due to drift in the electric field of the SCR and equilibrium is reached. Only the ionized doping atoms are left creating the fixed space charge and the SCR is almost devoid of free carriers. Outside the SCR the space charge from the ionized dopants is still neutralized by free carriers ($p \approx N_A$ in the p-type and $n \approx N_D$ in the n-type region).

For particle detectors the doping of the p- and n-regions are usually very different; i.e. the p^+-region has a very high doping $|N_{eff}| \approx 10^{19}$ cm^{-3} denoted by

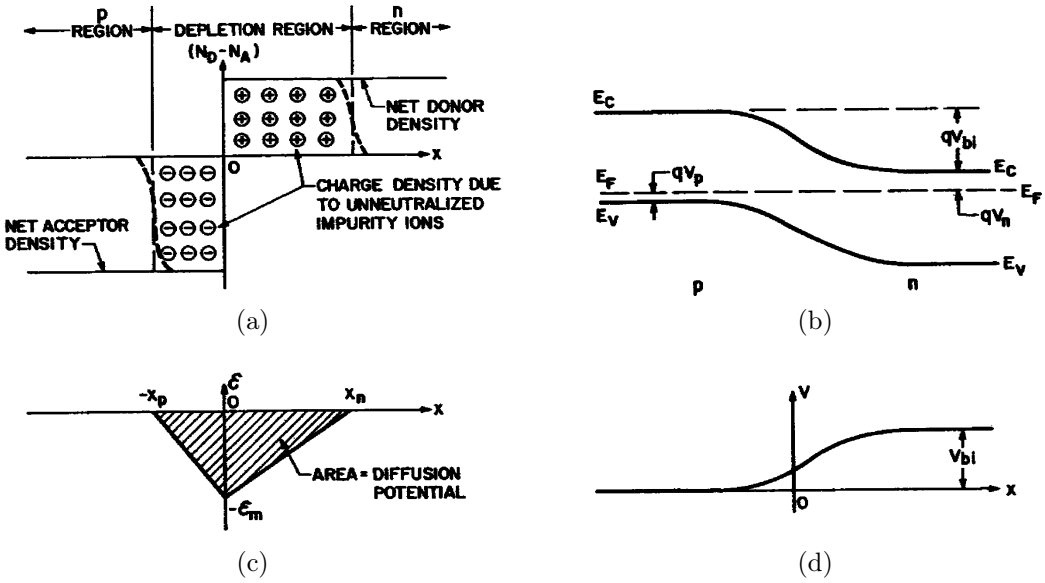

Figure 2.3.: An abrupt asymmetric p-n junction in thermal equilibrium. (a) Fixed space charge distribution, (b) energy band structure, (c) electric field distribution, and (d) the potential. From [22].

the plus sign p^+ while the n-region has a low doping usually $|N_{eff}| \approx 10^{12}\,\mathrm{cm}^{-3}$. This means that the SCR will extend much further into the n-region to achieve charge neutrality. The electric field and the potential U can be determined using the Poisson equation

$$-\frac{\mathrm{d}^2U(x)}{\mathrm{d}x^2} = \frac{\varrho}{\epsilon\epsilon_0} = \frac{eN_{eff}}{\epsilon\epsilon_0} \tag{2.20}$$

with the charge density ϱ, the vacuum permittivity ϵ_0, and the relative permittivity of silicon $\epsilon = 11.9$. Since the width of the SCR in the p^+-region is very small it will be neglected. If the boundary between the p^+ and the n-region is at $x = 0$ and $N_{eff}(x) = const$ the electric field takes the form

$$\mathscr{E}(x) = \frac{eN_{eff}}{\epsilon\epsilon_0}(x - w) \tag{2.21}$$

for $0 \leq x \leq w$ and $w \leq d$ with the width w of the SCR and the total thickness of the n-region d. Accordingly, the potential is

$$U(x) = -\frac{eN_{eff}}{2\epsilon\epsilon_0}(x - w)^2 \tag{2.22}$$

in this region and the so-called built-in potential is often approximated by

$$U_{bi} = -\frac{eN_{eff}}{2\epsilon\epsilon_0}w^2 \tag{2.23}$$

as shown in fig. 2.3(d).

As the concentration of free carriers is very low in the SCR $n, p \ll n_i$ the generation rate can be estimated to

$$U_r = -\frac{\sigma v_{th} N_t n_i}{2\cosh\left(\frac{E_t - E_i}{k_B T}\right)} = -\frac{n_i}{\tau_g} \tag{2.24}$$

using eq. 2.19 with the effective generation lifetime τ_g in the SCR.

If an external bias voltage U is applied to the p-n junction the SCR will decrease in width under forward bias (positive voltage at the p^+ contact) and increase under reverse bias (negative voltage at the p^+ contact). The p^+-n junction works as a diode: Current can flow for forward bias while it is blocked for reverse bias.

Using eq. 2.23, the width of the depletion region for reverse bias is

$$w\left(U\right) = \sqrt{\frac{2\epsilon\epsilon_0}{eN_{eff}}\left(U + |U_{bi}|\right)} \tag{2.25}$$

for $w \leq d$. The built-in voltage is often neglected as it is typically $U_{bi} \approx 0.5\,\mathrm{V}$ much smaller than the applied reverse voltage.

The capacitance $C = \frac{\mathrm{d}Q}{\mathrm{d}U}$ of the SCR assuming parallel electrodes with area A is

$$C\left(U\right) = \epsilon\epsilon_0 \frac{A}{w\left(U\right)} = A\sqrt{\frac{\epsilon\epsilon_0 e\left|N_{eff}\right|}{2\left(U + |U_{bi}|\right)}}. \tag{2.26}$$

At the so-called full-depletion voltage

$$U_d \approx \frac{e\left|N_{eff}\right|}{2\epsilon\epsilon_0} d^2 \tag{2.27}$$

the whole n-region is depleted and the SCR extends for the whole active thickness of the diode d. The electric field for $U > U_d$ is

$$E\left(x\right) = \frac{1}{d}\left(U + U_d\left(1 - \frac{2x}{d}\right)\right) \tag{2.28}$$

and the capacitance reaches a constant value

$$C_d = \frac{\epsilon\epsilon_0 A}{d} \tag{2.29}$$

which is called the geometrical capacitance.

It should be noted that these formulas are a one-dimensional approximation

for infinite planar electrodes. For real diodes edge effects have to be taken into account, as discussed in ref. [23]. Furthermore, for irradiated silicon $N_{eff}(x)$ is not a constant and these formulas are no longer valid.

2.1.2. Diode current

The diode current for an applied external bias voltage has two[3] contributions: The drift current of free carriers generated in the depletion region and the diffusion current of minority carriers diffusing from the neutral n- and p-regions into the depletion region.

The generation current is given by

$$I_g(U) = e\,|U_r|\,w(U)\,A \tag{2.30}$$

with the generation rate $|U_r| = n_i/\tau_0$ in the depletion region, using eq. 2.24 assuming $p, n \ll n_i$. τ_0 is the effective lifetime in the depletion region. It is apparent that the generation current depends on the square root of the voltage due to the $w(U)$ dependence given in eq. 2.25.

The diffusion current is determined by the minority carrier concentrations n_i^2/N_{eff} in the neutral regions adjacent to the depletion region and the diffusion lengths $L_{e,h}$. It is given [17] by

$$I_d^{e,h} = e\frac{D_{e,h}}{L_{e,h}}\frac{n_i^2}{|N_{eff}|}A = e\sqrt{\frac{D_{e,h}}{\tau_{n,p}}}\frac{n_i^2}{|N_{eff}|}A \tag{2.31}$$

with the generation-recombination lifetimes of the minority carriers in the neutral regions τ_n for p-type and τ_p for n-type. Accordingly, for a p^+-n junction the diffusion term of the n-region will dominate due to the much higher concentration of minority carriers n_i^2/N_{eff}: Free holes from the n-region will diffuse into the depletion region and drift towards the p^+-region. For asymmetrical junctions the diffusion term for the highly doped region can be neglected.

The total current is the sum of eq. 2.30 and eq. 2.31

$$I(U) = I_g(U) + I_d^{e,h}. \tag{2.32}$$

[3] At very high electric fields also impact ionization, the Poole-Frenkel effect, band-to-band tunneling, and trap-assisted tunneling may have significant contributions to the current and the relations given here are no longer valid.

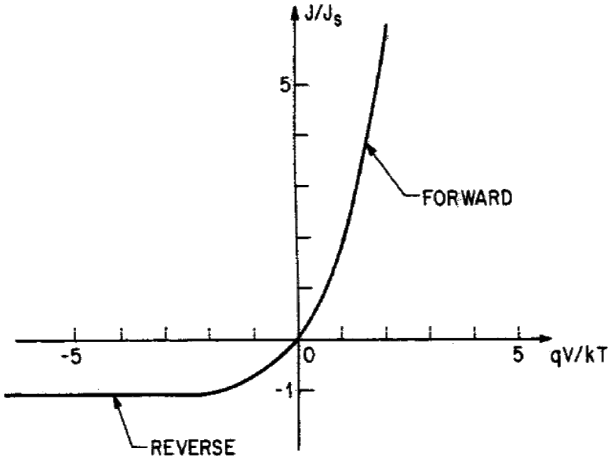

Figure 2.4.: Ideal diode current with eq. 2.34. From [22].

and explicitly for a p^+-n junction

$$I\left(U\right) = \frac{en_i w\left(U\right) A}{\tau_0} + e\sqrt{\frac{D_h}{\tau_p}}\frac{n_i^2}{\left|N_{eff}^n\right|} \tag{2.33}$$

with the hole lifetime τ_p in the n-region with doping $\left|N_{eff}^n\right|$. It should be noted that these relations are only true for $U \gg k_B T/e$ according to ref. [17].

These relations show that the diffusion current will dominate if the width of the depletion region $w\left(U\right)$ is small (forward bias), if the generation lifetime τ_g is long, and if N_{eff} is low. For large $w\left(U\right)$ (reverse bias) and short τ_g the generation term will dominate the current.

For long carrier lifetimes the forward and reverse current of a diode can be approximated by Shockley's ideal diode equation [24]

$$I(U) = I_0\left(\exp\left(\frac{U - R_s \cdot I\left(U\right)}{\eta U_T}\right) - 1\right) \tag{2.34}$$

with the series resistance of the diode R_s, the thermal voltage $U_T = k_B T/e$, the so-called ideality factor[4] $\eta = 1$, and the ideal current after full depletion I_0. In case of small currents (reverse bias and low forward voltages) the voltage drop from the series resistance $R_s \cdot I(U) \approx 0$ can be neglected. Figure 2.4 shows the ideal diode current according to eq. 2.34.

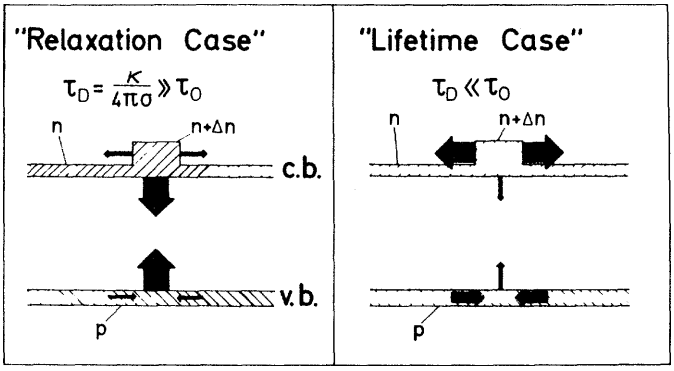

Figure 2.5.: Reaction of a „relaxation" and a „lifetime" semiconductor to a local disturbance. From ref. [25].

2.1.3. Relaxation

Non-irradiated, high-ohmic silicon has a long carrier recombination lifetime $\tau \gg \tau_d$ compared to the dielectric relaxation time $\tau_d = \epsilon\epsilon_0/(4\pi\sigma_i)$ with the intrinsic conductivity σ_i. If a local excess of free charge carriers is introduced into non-irradiated silicon, e.g. by a pulse of light, equilibrium is reached by the movement of free carriers as illustrated in fig. 2.5. This is called dielectric relaxation and it determines the physics of usual semiconductors in the „lifetime regime".

The physics is very different if the recombination lifetime is short $\tau \ll \tau_d$ and the „relaxation regime" is reached [26]. In the relaxation regime, a local excess of free charge carriers is neutralized by recombination as illustrated in fig. 2.5.

An irradiated detector, depending on the irradiation and the temperature, will be somewhere in-between these two regimes as the recombination lifetime is decreased due to the abundance of deep defects; at the same time, excess charge carriers can be temporarily trapped at shallow defects which generates temporarily fixed space charge and promotes dielectric relaxation.[5] Manifacier and Henisch [27] give a discussion of the electric fields in a semiconductor with one injecting contact (forward biased p-n junction) for the competing recombination, trapping, and dielectric relaxation.

2.1.4. Space-charge-limited currents

Space-charge-limited currents *SCLC* describe the current limited by the injection of free carriers. Let us consider the example of a vacuum diode: Thermionic emission of free electrons from a hot cathode leads to a ballistic current of electrons towards a nearby anode. The current is limited by the space charge of the free

[4] For forward bias η is not necessarily constant but $\eta(U) = 1-2$ depending on the recombination mechanisms in the depletion region.

[5] That is, if the detrapping time is longer than the dielectric relaxation time.

electrons themselves. The high concentration of negatively charged free electrons around the cathode leads to a space charge which screens the electric field and prevents further transport. Even if the hot cathode could supply enough electrons to achieve a very high conductivity the conductivity of the diode is finite.[6] Only the free electrons in the field region are accelerated towards the anode. The current follows Child's law [28] $J \propto U^{3/2}$. For a perfect insulator without traps the Mott-Gurney law [29] applies

$$J = \frac{9\epsilon\mu U^2}{8d^3}. \tag{2.35}$$

The situation becomes more complicated if we consider an insulator (semiconductor) with thermally generated free carriers and finite resistivity. In an asymmetrical p-n junction under forward bias, majority carriers can diffuse from the highly doped region into the less doped semiconductor bulk, where they are minority carriers, and increase the conductivity of the bulk. This process is called minority carrier injection. The current will be ohmic at low voltages, determined by the conductivity of the bulk, until at certain voltages the SCLC and the Mott-Gurney law will dominate. As shown by Lampert [30, 31, 32] this transition will happen once the concentration of injected carriers reaches the majority carrier concentration of the bulk n_0 in equilibrium (n_i for intrinsic silicon). This can also be expressed in terms of the transit time. Once the transit time t of the injected carriers is equal to the dielectric relaxation time $t = d/v = d^2/(\mu U) = \tau_D$ the injected carriers can traverse the insulator before dielectric relaxation happens (compare fig. 2.5). The transition between ohmic currents and SCLC will happen at the threshold voltage

$$U_{SCLC} \approx \frac{en_0d^2}{\epsilon\epsilon_0}. \tag{2.36}$$

In the presence of traps the current at low injection levels will be greatly reduced as the injected carriers will be trapped which increases the space charge. Subsequently, the screening of the electric field is increased. The trapped charges cannot contribute to the current. The higher the trap concentration the more the field will be screened. Rose [33] gives a discussion of the transition between ohmic currents and SCLC. According to Rose there will be a competition between the two mechanisms. According to Lampert [30] the transition between the two regimes will happen again when the injected free carrier density is equal to the thermal carrier density n_0. If we assume the total trap concentration $N_t \gg n_0$ the injected free carrier concentration will reach n_0 approximately when all traps are

[6] This is different from, for example, a metal where the carrier concentration is high but the metal is still neutral and the conductivity very high.

filled. For deep traps and electron injection the threshold voltage between the two regimes will be

$$U_{TFL} = \frac{e p_{t,0} d^2}{2\epsilon\epsilon_0} \tag{2.37}$$

analogous to eq. 2.36 with the concentration of traps which are not occupied by electrons in thermal equilibrium $p_{t,0} = N_t - n_{t,0} = N_t (1 - f)$. This is the so-called trap-filled limit *TFL* for SCLC. The current will strongly increase until the trap-free Mott-Gurney law will be reached.

For one-carrier SCLC in an insulator with a constant trap concentration per unit energy in the band gap $N_t(E)$ $\left[\mathrm{cm}^{-3}\mathrm{eV}^{-1}\right]$ Rose [33] (derived in ref. [30]) gives the current as

$$I(U) = e\mu n_0 \cdot A\frac{U}{d} \cdot \exp\left(\Xi\frac{U}{T \cdot d^2}\right) \tag{2.38}$$

with $\Xi = \epsilon\epsilon_0 / (e N_t(E) k_B)$ and the initial thermal equilibrium concentration of free carriers n_0. This formula will be used in sec. 5.4 to describe the forward current of highly irradiated diodes.

2.2. Radiation damage

Particles interacting with crystalline silicon can introduce a number of reversible and irreversible changes in the silicon.[7] Ionizing energy-loss of charged particles due to electromagnetic interactions with the electrons of the material is the basis for the operation of silicon devices as radiation detectors. Ionizing energy-loss is usually reversible since the ionization creates mobile charges. However, ionizing energy loss can generate positive oxide charge in SiO_2 which has a very small mobility. Accordingly, the relaxation time is long and positive charge can accumulate in the oxide layer (see ref. [35]). Free highly mobile electrons will accumulate at the Si-SiO_2 interface to counterbalance the oxide charge. This can lead to conducting layers in the silicon and severely decrease the detection efficiencies of segmented silicon sensors (see e.g. ref. [36, 37, 38]), change the local electric field, and lead to short-circuits or high surface current. Additionally, oxide damage is relevant for high density devices which extensively make use of the oxide like CMOS[8] technology monolithic active pixel sensors and read-out chips *ROC*s.

Signal losses at the surface can be mitigated by minimizing the interfaces of SiO_2

[7] Reference [34] gives a broad overview of available literature.
[8] Complementary metal-oxide-semiconductor *CMOS*.

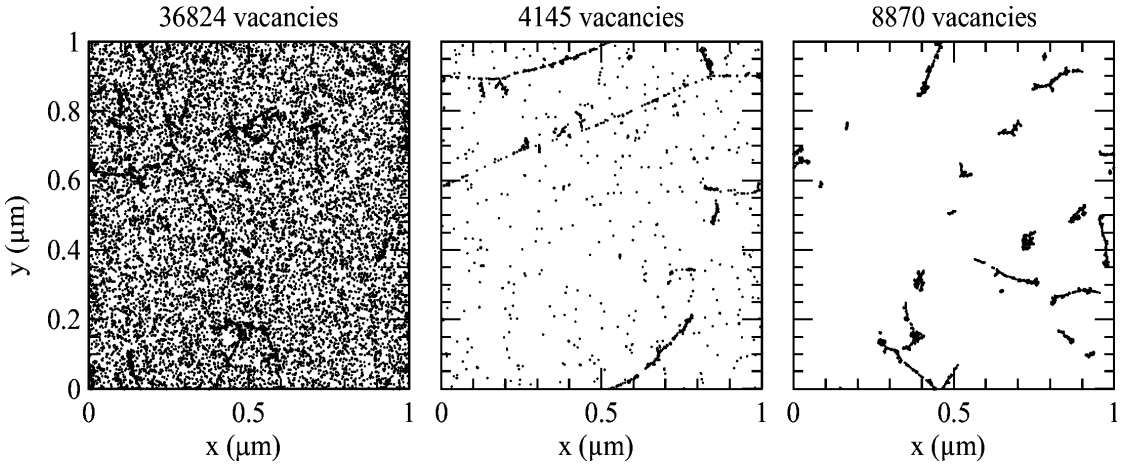

Figure 2.6.: Simulated initial distribution of vacancies produced by 10 MeV/c protons (left), 24 GeV/c protons (middle) and 1 MeV/c neutrons (right). The plots are 2D projections over 1 µm of depth and correspond to an equivalent fluence of $10^{14}\,\mathrm{cm}^{-2}$. From [39].

and the bulk silicon.[9] However, surface damage will not be discussed in this work. Instead, the effects of bulk damage on the physical properties of silicon sensors have been investigated.

If the momentum of an incoming particle is sufficiently high the silicon bulk can be damaged. This is called non-ionizing energy loss *NIEL* (see sec. 2.2.1). Atoms can be displaced from their original position in the crystal lattice. The displaced atom is now called an interstitial and it leaves a vacancy. The interstitial-vacancy pair is called Frenkel pair. Vacancies and interstitials are mobile at room temperature and can recombine or form defect complexes, some of which are stable. The mean energy needed to displace a silicon atom from its lattice position is about 25 eV. The displaced atom is called primary knock on atom *PKA* [40, 41]. If the recoil energy of the PKA is above 25 eV the silicon atom can create new Frenkel pairs in a cascade of collisions. The concentration of defects generated in such a cascade is very high and defect clusters can be formed. The mobilities and the recombination rates of defects can be increased by increasing the temperature which is used to anneal certain defects (see e.g. ref. [42, 43]).

Bulk defects are grouped into point defects and clusters. Figure 2.6 shows the simulated initial (no annealing) distribution of vacancies after irradiation with different particles of different momentum. Low energy protons produce a huge amount of localized point defects while low energy neutrons rather produce clusters of defects along atomic recoil cascades. For example, vacancies or interstitials or composites of the latter ones and with impurity atoms are point defects. Point

[9] Highly doped ($N_{eff} \sim 10^{19}\,\mathrm{cm}^{-3}$) contacts are not affected by fixed oxide charge.

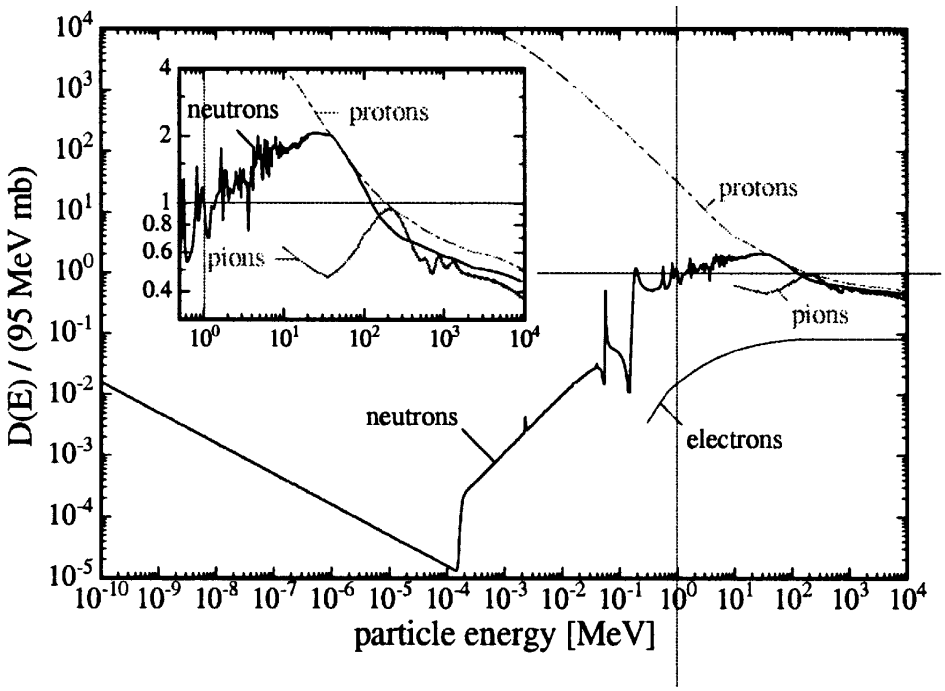

Figure 2.7.: Non-ionizing energy loss $D(E)$ of various particles as a function of the energy normalized to the $D(E)$ of 1 MeV neutrons (crosshair). From [43].

defects introduce discrete energy levels in the silicon band gap. In clusters, the concentration of point defects is very high. The point defects can communicate with each other via Coulomb interaction [44] so they do have a broad energy spectrum rather than a discrete one (see e.g. [45, 46, 47]).

2.2.1. NIEL hypothesis

The non-ionizing energy loss *NIEL* hypothesis (see e.g. ref. [48, 49, 16]) describes the introduction of defects into the silicon lattice by the nuclear displacement from irradiation with particles. The introduction of defects is assumed to be proportional to the fluence Φ with the so-called hardness factor κ, where κ accounts for the energy loss $D(E)$ due to nuclear displacement (recoil) as a function of the particle type and energy relative to 1 MeV neutrons. Figure 2.7 shows $\kappa = D(E)/D(95\,\text{MeV mb})$ vs. E calculated theoretically for different particles (see e.g. ref [50]). This concept is used to normalize the fluences of irradiations with different particles of different energies to the equivalent fluence

$$\Phi_{eq} = \kappa \cdot \Phi \tag{2.39}$$

after irradiation with 1 MeV neutrons. It is used mostly for hadrons and less justified for leptons and photons which produce different defects than hadrons [51].

Defect	Type	E_t [eV]	g [cm^{-1}]
$(V-\mathrm{O})$	A	E_C−0.176	1.1
$(V-V)^{-2}$	A	E_C−0.224	1.5
$(V-V)^{-}$	A	E_C−0.424	1.5
-	A	E_C−0.4	1.5
-	e-trap	E_C−0.52	0.03
$(\mathrm{C}_i-\mathrm{O}_i)$	D	E_V+0.36	1.1
-	h-trap	E_V+0.36	2.3
-	h-trap	E_V+0.48	0.08
-	h-trap	E_V+0.53	0.08
-	h-trap	E_V+0.51	0.03

Table 2.1.: Energy levels E_t and estimated introduction rates g of various known radiation-induced defects. „A" denotes acceptors, „D" donors, V vacancies, and C and O are carbon and oxygen. From various sources collected in ref. [54].

However, also for hadrons the introduction rates of the defects do not necessarily scale with κ (see ref. [52]).

2.2.2. Point defects

The concentrations N_t and energy levels E_t of electrically active point defects can be determined with various methods like deep-level transient spectroscopy [53]. The fluence dependence of N_t is described by the introduction rate g so $N_t = g \cdot \Phi_{eq}$. Table 2.1 gives the distances from the conduction band E_C and the valence band E_V as well as g for several known radiation-induced defects. The defects have different effects on the sensor performance depending on the distance from the band edges and the capture cross sections for free carriers. Shallow defects generally act as acceptors or donors and change the effective doping of the bulk. Deep defects (near $E_i \approx 0.56\,\mathrm{eV}$) act as generation-recombination centers which increase the free carrier concentrations in depleted silicon (increase of the volume current) and reduce the free carrier concentrations in neutral silicon (decrease of the conductivity by carrier removal). They can also act as so-called traps which temporarily trap free charge carriers reducing the measured charge for fast current transients and changing the effective doping depending on the occupation of the defects.

The aforementioned mechanisms lead to the main effects of radiation damage on the sensor performance: Increased volume generation current, reduction of the carrier lifetimes and the sensor signal, and a change of the effective doping leading to position dependent effective doping as well as carrier removal and neutral regions with sizeable electric field in the sensors. This is especially severe as the noise

increases with the fluence due to high current while the signal decreases. Also, the voltage needed for full depletion changes with the fluence due to the introduction of both acceptors and donors, and by deactivation of the dopants phosphorus and boron [55]. The net change of the effective doping with the fluence introduces more acceptors than donors. This means initially n-type silicon will turn into p-type silicon after a certain fluence which is known already since the 1940s as type-inversion or space-charge sign inversion [56]. The voltage needed for full depletion of p^+n sensors first decreases with the fluence until it increases again after type inversion. For p-type sensors the full depletion voltage always increases with the fluence.

The effective doping under full depletion and for moderate fluences $\Phi_{eq} < 10^{15}\,\mathrm{cm}^{-2}$ is usually described by

$$N_{eff}\left(\Phi_{eq}\right) = N_D^0 \exp\left(-c_D \cdot \Phi_{eq}\right) - g_A \Phi_{eq} - N_A^0 \cdot \exp\left(-c_A \cdot \Phi_{eq}\right) \tag{2.40}$$

with the initial acceptor and donor concentrations $N_{A,D}^0$, the donor removal rate $c_D \approx 2.4 \cdot 10^{-13}\,\mathrm{cm}^2$ and the acceptor removal rate $c_A \approx 2 \cdot 10^{-13}\,\mathrm{cm}^2$ (ref. [55]), and the introduction rate of acceptor-like shallow defects $g_A \approx 0.03\,\mathrm{cm}^{-1}$ (ref. [57, 55] for phosphorus and boron). Strictly speaking, also a term $g_D \Phi_{eq}$ should be taken into account for the introduction donor-like defects. But, it is often neglected since $g_D < g_A$. These values are for very pure silicon and can be engineered by introducing impurities like oxygen which can partly deactivate certain defects (see ref. [21, 58]). There are also efforts to replace boron with the heavier gallium to improve the radiation-hardness because of the higher displacement energy of gallium atoms (see ref. [59, 60]).

For higher fluences $\Phi_{eq} > 10^{14}\,\mathrm{cm}^{-2}$ the concept of $N_{eff}\left(x\right) = const$ is not justified as the influence of deep defects becomes significant. Effects such as carrier removal and trapping of carriers lead to non-constant N_{eff} in the sensor. $N_{eff}\left(x, \Phi_{eq}\right)$ can assume values between zero and $\gg N_{eff}\left(\Phi_{eq} = 0\right)$ in the same sensor.

2.2.3. Cluster defects

Cluster defects are extended regions $\mathcal{O}\left(100\,\text{Å}\right)$ with a very high concentration of point defects caused by atomic recoils with energy above about 10 keV (see ref. [61]). The concentration of point defects is so high that the individual defects can communicate with each other. If one point defect in a cluster is occupied by a charge carrier the activation energy to ionize neighboring point defects in the cluster will change due to Coulomb interaction (see fig. 2.8). Due to the Coulomb interaction cluster defects do not occupy a static, discrete energy level in the band

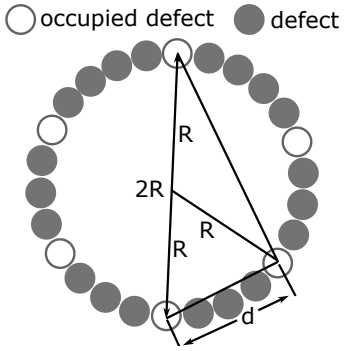

Figure 2.8.: Cluster defect representation used to derive the Coulomb interaction in a loop geometry of partially charged point defects. Modified from [44].

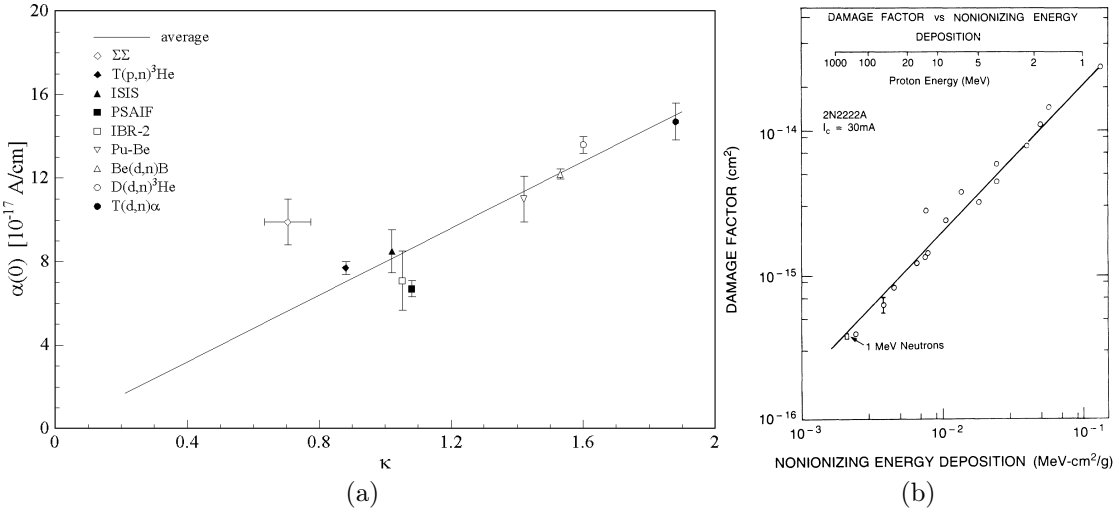

(a) (b)

Figure 2.9.: Measured slope $\alpha(0)$ and calculated hardness parameters κ for different particle sources (a) from [64]; and the „damage factor" for transistors vs. NIEL for different proton energy (b) from [65].

gap but rather a broad spectrum in energy depending on the occupation of the point defects.

Especially for very high fluences $> 10^{14}\,\mathrm{cm}^{-2}$ cluster defects are crucial for the operation of radiation detectors as they influence the aforementioned electrical properties of the detectors. Cluster defects created by radiation damage are not well studied up to to now [45, 62, 46, 44, 51]. A model to extract information on cluster defects from thermally stimulated current *TSC* spectroscopy is presented in ref. [63].

2.2.4. Generation current

The change of the generation current

$$\frac{\Delta I}{V} = \alpha\,(0) \cdot \Phi \tag{2.41}$$

in depleted bulk silicon with the volume $V = Aw$ after irradiation has been found to be proportional to the fluence [42, 66] of the particles used for irradiation with the proportionality factor $\alpha\,(0)$ and independent of the initial doping and process. Figure 2.9 shows experimental data for $\alpha\,(0)$ versus simulation results of κ (see sec. 2.2.1) for different particles at different energy. We observe ${}^{\alpha(0)}/_{\kappa} = const = \alpha$. The „current related damage constant" α is inversely proportional to the generation lifetime $I/V = en_i/\tau_0$ (see eq. 2.30) and it is independent of the particle type and energy. Thus, the defects responsible for the generation of volume generation current scale with NIEL at the fluences investigated.

Irradiations for this work were performed at CERN PS [67] with 24 GeV/c protons with the most recent[10] hardness factor of $\kappa = 0.62$ determined from measurements of ΔI so

$$\frac{\Delta I}{\kappa\Phi \cdot V} = \alpha_0 = 3.99 \cdot 10^{-17}\,\mathrm{A/cm} \tag{2.42}$$

for silicon after 80 min annealing at 60 °C for all Φ at the reference temperature $T_R = 293.15\,\mathrm{K}$ according to ref. [70]. The temperature dependence of α after 1 MeV neutron equivalent fluence irradiation is given as

$$\alpha\,(T) = \alpha_0 \cdot \left(\frac{T}{T_R}\right)^2 \exp\left(\frac{E_g}{2k_B} \cdot \left(\frac{1}{T_R} - \frac{1}{T}\right)\right). \tag{2.43}$$

A more correct treatment is demonstrated in ref. [71] and utilizes the effective energy $E_{eff} = 1.21\,\mathrm{eV}$ instead of E_g for current generation in radiation damaged silicon at a defect near mid-gap (compare eq. 2.19). This value may be closer to $E_g\,(T_R)$ for fluences $> 10^{15}\,\mathrm{cm}^{-2}$ according to ref. [71]. A discussion is given in sec. 5.3.2.

However, it is not well-established whether the proportionality holds at fluences beyond $10^{15}\,\mathrm{cm}^{-2}$ as α is determined from the current per unit of depleted volume, usually at the full depletion voltage U_d for fluences $\Phi_{eq} < 10^{15}\,\mathrm{cm}^{-2}$. For higher fluences there is no well defined U_d as the concentration of defects is very high and the capacitance-voltage (C/V) characteristic - which is usually used for the determination of U_d - is a strong function of the frequency. There have been efforts (see ref. [72, 43]) to use the saturation of charge collection efficiency CCE measurements to determine U_d and the frequency for C/V measurements where the results of U_d agree. But, as U_d increases with Φ_{eq} this method is not easily applicable. Additionally, for $\Phi_{eq} \sim 10^{14}\,\mathrm{cm}^{-2}$ there is no clearly defined depleted region. Instead, the so-called double junction (see ref. [73, 54], sec. 5.2) is observed

[10] Values used earlier can be found in ref. [68, 69].

with high fields near the contacts and a low-field region in-between. Other possible contributions to the reverse current which can increase the current even after full depletion will be discussed in sec. 5.3.3.

To make things worse, the introduction rates of certain defects do not scale with *NIEL* which might change the linear increase of $1/\tau_g\,(\Phi_{eq})$ (see ref. [39]). Still, this model is used to compare samples irradiated with different particles and has often been verified up to $10^{15}\,\mathrm{cm}^{-2}$ and with certain assumptions about the depleted volume also at higher fluences.

2.3. Radiation detectors

Silicon has many different applications in radiation detection. The technology is very advanced to produce pure silicon and to engineer doping concentrations as well as processing different layers e.g. of oxide, conducting, and passivation layers with photolithography - all with very high precision. This is one of the main advantages towards other materials such as diamond or GaAs. Here, the focus is on silicon sensors used in high energy physics.

Since silicon has a relatively small atomic number of $Z = 14$ the energy loss of highly energetic particles in silicon is relatively low according to the Bethe-Bloch formula $\frac{\mathrm{d}E}{\mathrm{d}x} \propto Z^2$. This makes silicon an ideal material for tracking applications. Trackers require low radiation lengths in order to minimize multiple scattering. Another important reason to use silicon is the high position resolution which can be achieved with silicon sensors due to the possibility to build highly granular detectors. Apart from tracking, silicon sensors are also used in sampling calorimeters. A timing resolution in the order of tens of picoseconds can be achieved with silicon sensors. This opens the possibility to operate 4-D timing detectors [74, 13]. Another important point for silicon is its radiation-hardness which enables the use in high luminosity detectors, such as CMS, in the first place. The radiation-hardness is constantly improved by new sensor designs (see sec. 2.3.3 and appendix A), defect engineering (see e.g. ref. [59]), and mitigation of surface damage effects.

2.3.1. Signal generation in pad sensors

Ionizing radiation passing the active volume of the sensor generates free charge carriers by Coulomb interactions which drift in an applied electric field and generate a signal in the electrodes. Figure 2.10 illustrates the drift of charge carriers produced by a particle in the electric field of a pad diode under reverse bias.

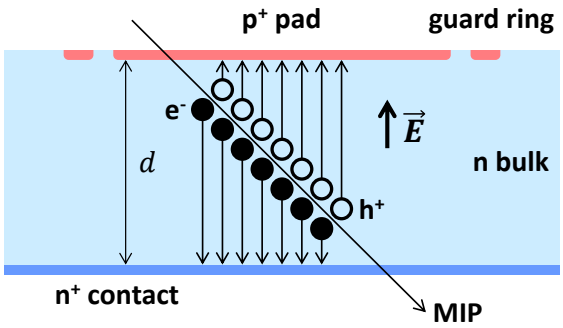

Figure 2.10.: Schematic of a silicon pad diode operated at full depletion as an radiation detector. A minimum-ionizing particle creates electron-hole pairs along its track which drift towards the electrodes in an applied field. The drifting charge carriers induce a signal at the electrodes.

A minimum-ionizing particle *MIP*[11] produces about 73 free electron-hole pairs per µm in silicon on average. If a reverse bias voltage which ensures full depletion is applied to a silicon diode all generated free charge carriers will drift towards the electrodes. The signal induced in a pad sensor is

$$I(t) = -\frac{e}{d} \cdot \left(N_e(t)\, v_e(t) + N_e(t)\, v_h(t)\right). \tag{2.44}$$

Assuming the trapping times $\tau_{e,h}$ are constant in the sensor the number of drifting charge carriers is

$$N_{e,h}(t) = N_0 \cdot \exp\left(-\frac{t}{\tau_{e,h}}\right) \tag{2.45}$$

with the number of free charge carriers created by the MIP N_0 and the drift velocities $v_{e,h}$. If there is no trapping the full charge $Q_0 = N_0 \cdot e$ is measured. If the trapping times $\tau_{e,h}$ are finite the collected charge will be reduced. In order to qualify radiation damaged silicon sensors the charge collection efficiency is often used

$$CCE = \frac{Q}{Q_0} \tag{2.46}$$

with $Q = \int I \mathrm{d}t$. The trapping times are usually shorter than the recombination lifetimes. They describe the charge lost within the integration time of $\mathcal{O}$ (ns) of the detector which may be shorter than the detrapping times of shallow defects of $\mathcal{O}$ (µs).

2.3.2. The weighting potential

The weighting potential Φ_w describes the coupling of a charge to the electrode which is being read out (r/o). According to Ramo's theorem [76], it can be de-

[11] A MIP is a hypothetical particle with the momentum which corresponds to the minimum ionizing energy loss according to the Bethe-Bloch formula.

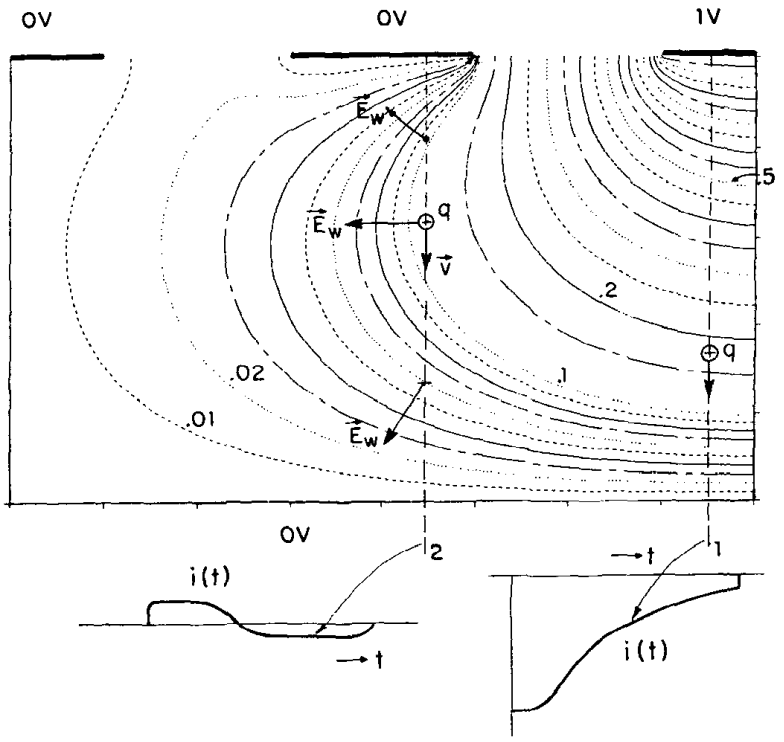

Figure 2.11.: Schematic cross section of a strip sensor showing the equipotential lines of the weighting field $\overrightarrow{E_w}$. To calculate the weighting field, the top left strip has a voltage of 1 V applied and all other electrodes are on ground potential. The two vertical lines show hypothetical passing charge not influenced by the electric field. The corresponding signal as a function of time induced in the top right strip is shown below. Modified from [75].

termined by solving the Poisson equation for the electrical potential applying 1 V bias to the r/o electrode while applying 0 V to all other electrodes in vacuum.

For a pad diode with a small thickness compared to the pad area the weighting potential is simply $1/d$ and already considered in eq. 2.44. For segmented sensors it can be increasingly complex depending on the configuration of the electrodes. Figure 2.11 shows the weighting potential for a strip sensor and the current transients induced in the r/o strip for a charge q passing through the sensor at different positions. The integrated charge is $Q = \int I(t)\,\mathrm{d}t \approx q$ at the r/o strip if the charge passes at the r/o strip. On the other hand, if it passes at the next neighbor the integrated charge is $Q \approx 0$ and the induced signal on the r/o strip is bipolar. However, this is only true if the integration time is longer than the signal duration of usually $1\,\mathrm{ns} - 50\,\mathrm{ns}$ depending on the thickness, the drift velocities, and the trapping times.

For edge-TCT (see sec. 3.3.2) charge carriers are generated approximately uniformly parallel to the surface of the sensor and perpendicular to the strip direction (from left to right in fig. 2.11). This means that charge carriers are drifting towards

all strips along the axis of charge deposition. All bipolar contributions to signal in the r/o strip from the charge drifting towards neighboring strips cancel resulting in a constant weighting field as for a pad sensor.

The weighting field described above is only valid for static electrodes and fixed space charge. If there are accumulation layers of mobile electrons at the Si-SiO_2 interface between the strips this concept is not valid anymore.

2.3.3. Radiation-hard sensors

As mention above, radiation damage increases the volume generation current, which is also called the leakage current, and decreases the carrier lifetime. High leakage current poses a problem for radiation detectors as the power dissipation and the noise increase. The power dissipation can be decreased by reducing the operating voltage as $P = I(U) \cdot U$. However, applying high voltages leads to a high mean electric field $\mathscr{E} = U/d$ with the distance of the electrodes d. A high electric field means high drift velocities $v = \mu\mathscr{E}$ and less trapping $Q(t) = Q_0 \cdot \exp(-t/\tau)$ as the charge collection time $t_c \approx d^2/(\mu U)$ is reduced. Another issue is the increasing voltage needed for full depletion $U_d \propto N_{eff} \cdot d^2$ as the effective doping increases with fluence. If the sensor is operated at voltages below U_d the active volume is decreased. The charge deposited outside the active volume in the neutral region will be mostly lost[12] due to the short diffusion lengths in irradiated silicon.

Most of these issues can be addressed by reducing the thickness d of the sensor. However, the initial charge Q_0 for the non-irradiated sensors will decrease if the path length of the ionizing particle in the sensor decreases, influencing the signal-to-noise ratio. Another important issue for highly segmented sensors is the weighting field. The weighting field is high close to the read-out electrodes. Radiation-hard sensors use n^+ implants for the segmented read-out electrodes to make sure the p-n junction is at the segmented side even after type-inversion for n^+n read-out and the SCR with high electric field develops in the region of high weighting field. In this way the drift distances in the region of high weighting potential are maximized.

Figure 2.12 shows the signal measured in irradiated pad diodes in units of electrons per µm compared to the charge deposited along the track of a MIP in non-irradiated silicon of $73\,e^-/\mu m$. For the lowest fluences sensors of about 320 µm active thickness[13] have been used, for higher fluences sensors of 200 µm active

[12] This is only true if there is no field in the neutral region (see chapter 5).
[13] The active thickness describes the thickness of the bulk silicon with low doping concentration.

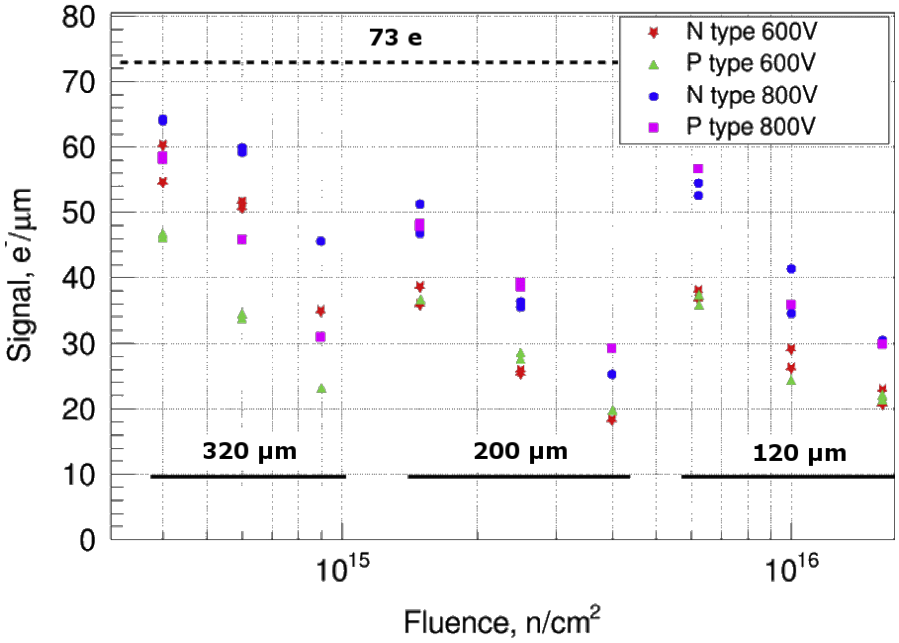

Figure 2.12.: Measured charge in $e^-/\mu m$ in irradiated pad diodes of different thickness irradiated to different fluences compared to the average charge deposited by a MIP in non-irradiated silicon of $73\,e^-/\mu m$. The results were obtained by injecting charge with infrared light at bias voltages of 600 V and 800 V at 253 K. The collection efficiency is not corrected for the increase of the deposited charge with fluence. Previously published in ref. [12].

thickness, and for the highest fluences up to $\Phi_{eq} = 1.3 \cdot 10^{16}\,\mathrm{cm}^{-2}$ an active thickness of 120 µm has been used. All diodes were reverse biased at 600 V and 800 V. We can nicely observe how the measured charge for each thickness decreases with fluence - and how the collection efficiency can be recovered by decreasing the sensor thickness at higher fluences. The measurements were performed with the setup described in sec. 3.3.1 and are described in ref. [12, 77]. The total charge deposited by light was assumed constant and not corrected for the increase of the absorption coefficient reported in chapter 4, which increases the deposited charge by up to 20 % for the highest fluence. This means that the charge collection efficiency is overestimated by up to 20 % when using light if the change of the light absorption is not considered.

Current developments towards radiation-hard sensors are to make „traditional" planar sensors thinner $\sim 100\,\mu m$, which is described in this work, and to use 3-D sensors (see e.g. ref. [78, 79]). Planar sensors have the advantage of lower price and proven technology while 3-D sensors are still expensive and not feasible to cover large areas with sensors.

The electrodes of 3-D sensors are vertical columns through the bulk of the sen-

sor rather than on the surface. This means the electrode spacing[14] can be chosen almost independent of the thickness of the bulk and it is not coupled to the granularity. This allows for low operational voltages while maintaining high detection efficiency even after high fluences. However, there are drawbacks such as charge losses for normal incidence through columns.

Efforts to develop new radiation-hard planar pixel sensors for the innermost pixel barrel layers of the future CMS tracker after the Phase-II upgrade will be discussed in appendix A. Several different designs are presented with pixel sizes down to $50 \times 50\,\mu m^2$ and $25 \times 100\,\mu m^2$.

[14] One read-out channel with a certain surface area can have multiple columns and a column spacing down to 27 µm has been achieved [80].

3. Experimental methods

This chapter gives an overview of the investigated samples and the measurement setups. First, the different samples are explained and the relevant parameters are given in sec. 3.1. Then, the current-voltage and capacitance-voltage measurement setup is introduced in sec. 3.2. The Transient Current Technique *TCT* is explained in sec. 3.3 with a detailed discussion of the edge-TCT setup which has been developed in the course of this thesis. The last section 3.4 explains the spectrophotometer used for transmittance measurements.

3.1. Test structures

The irradiations for this thesis have been performed at the irradiation facility [67] at the Proton Synchrotron *PS* at CERN with protons of 24 GeV/c momentum. The scaling factor used throughout this work is $\kappa = 0.62$ from ref. [70] for $\Phi_{eq} = \kappa \cdot \Phi$ with the fluence of 24 GeV/c protons Φ and the 1 MeV neutron equivalent fluence Φ_{eq}.

No annealing studies have been performed. Some samples have been measured as-irradiated without intentional annealing; however, those samples still have a certain annealing since the irradiations were performed at room temperature for several weeks. Some samples have been measured after 10 min annealing at 60 °C.

3.1.1. Bare single crystal silicon

Several not processed high-purity silicon crystals cut from wafers were investigated. The bare silicon crystals are cut out of $d \approx 285\,\mu\text{m}$ thick wafers produced for oxide growth studies. There is no thermal oxide on the silicon surface which would change the reflectivity. Several silicon crystals were irradiated. The measured

d [µm]	278	283	281	282	303
Φ_{eq} [10^{15} cm^{-2}]	0	2.39±0.19	4.90±0.35	6.39±0.46	8.62±0.61

Table 3.1.: Thickness d and fluence Φ_{eq} of the silicon samples used for transmission measurements with infrared light. The uncertainty of d is about 1 µm.

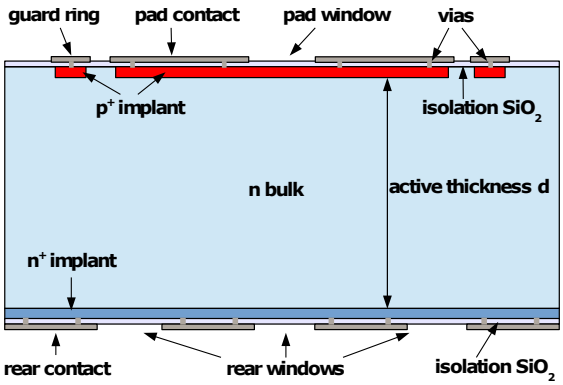

Figure 3.1.: Schematic cross-section of a pad diode with n-type bulk. Previously published in ref. [81].

Name	FTHN	FTHP	MCZN	MCZP	CIS100	CIS111	RD48
Bulk doping	n	p	n	p	n	n	n
$d\,[\mu m]$	200	200	200	200	285	287	300
$U_d\,[V]$	90	120	150	100	50	67.5	19.5
$N_{eff}\,[cm^{-3}]$	$3 \cdot 10^{12}$	$4 \cdot 10^{12}$	$5 \cdot 10^{12}$	$3.3 \cdot 10^{12}$	$8 \cdot 10^{11}$	10^{12}	$3 \cdot 10^{11}$
$A\,[mm^2]$	4.4 (24.4)				24.4	24.4	?
$C(U_d)\,[pF]$	2.7 (12.3)				9.3	9.3	10.3
$N_O\,[cm^{-3}]$	10^{17}	10^{17}	10^{17}	$4 \cdot 10^{17}$	$< 10^{17}$	$< 10^{17}$	?

Table 3.2.: Physical properties of the investigated diodes. A refers to the pad area of the diodes, $C(U_d)$ is the capacitance at full depletion, and N_O is the oxygen concentration.

thickness and Φ_{eq} of the crystals are given in table 3.1. The crystals were measured as-irradiated.

3.1.2. Pad diodes

Several different diodes produced by different companies were investigated for this thesis. The structure of the diodes is shown in fig. 3.1. The diodes have shallow implants $\approx (1-2)$ µm with a very high doping concentration and a low-doped bulk in-between. The active thickness d is the thickness of the bulk. The pad of the diode is surrounded by a guard ring in order to define the active volume and to reduce the influence of surface and edge effects on the pad. The diodes have windows in the pad aluminum contact and the back side contact is an aluminum grid with windows. The windows are needed to generate free charges in the active volume by illumination with light.

The diodes produced by Hamamatsu *HPK* [82] are labelled *FTH* for float-zone silicon and *MCZ* for magnetic Czochralski silicon. All of the HPK diodes have a crystal orientation of $\langle 100 \rangle$. Additionally, n-type diodes of $\langle 100 \rangle$ and $\langle 111 \rangle$ crystal orientation float-zone silicon produced by CiS [83] were investigated. They

Φ_{eq} [cm^{-3}]	FTHN	FTHP	MCZN	MCZP	CIS100
$8.87 \cdot 10^{14}$	×	×	×	×	✓
$1.14 \cdot 10^{15}$	×	×	×	×	✓
$2.94 \cdot 10^{15}$	✓	✓	×	×	×
$4.35 \cdot 10^{15}$	×	×	×	×	✓
$4.90 \cdot 10^{15}$	✓	✓	×	×	×
$6.07 \cdot 10^{15}$	✓	×	×	×	×
$7.25 \cdot 10^{15}$	×	×	×	×	✓
$7.75 \cdot 10^{15}$	✓	✓	×	×	×
$9.36 \cdot 10^{15}$	×	×	×	×	✓
$1.30 \cdot 10^{16}$	✓	✓	✓	✓	✓
Annealing [min@°C]	10@60	10@60	10@60	10@60	0@0

Table 3.3.: Available fluences Φ_{eq} for the diodes and the annealing stage.

are labeled *CIS100* and *CIS111*. One very high-ohmic ⟨111⟩ diffusion-oxygenated float-zone *DOFZ* n-type diode produced by STMicroelectronics [84] was investigated, labeled *RD48*. The doping concentration, bulk thickness, depletion voltage, geometrical capacitance, and other parameters are given in tab. 3.2.

Some of the diodes were irradiated with 24 GeV/c protons to the fluences given in table 3.3. The fluence was determined from the dosimetry of aluminum plates which are irradiated with the samples and are activated from the irradiation. The uncertainty of Φ_{eq} is about 7 %. The FTH and MCZ diodes were measured after annealing for 10 min at 60 °C while the CIS100 diodes were measured as-irradiated.

3.1.3. Strip sensors

For the edge-TCT measurements strip sensors were investigated, from the same ⟨100⟩ wafers with the same N_{eff} as the CiS diodes labeled CIS100. The sensors have an active thickness of 285 µm, a pitch of 80 µm, an implant width of 18 µm, and a metal width of 16 µm. The die size is $1 \times 1\,\mathrm{cm}^2$.

A strip sensor fixed and wire-bonded to the printed-circuit board *PCB* is shown in fig. 3.8(a). The AC-pads (capacitive coupling) are connected to the read-out electronics. The strip implant is connected to a current collection ring, which surrounds the strips, via a poly-silicon resistor similar to fig. A.7. The AC-pads and the periphery with the current collection ring and the guard rings are shown in fig. 3.2. The 4th and the 9th strip are read out. The distance from the edge[1] to the first read-out strip is 1350 µm and the distance between the read-out strips is 400 µm. The neighboring strips, the current collection ring, and the innermost guard ring are connected to ground via 50 Ω.

[1]The left edge in fig. 3.2, which is illuminated for edge-TCT (see sec. 3.3.2).

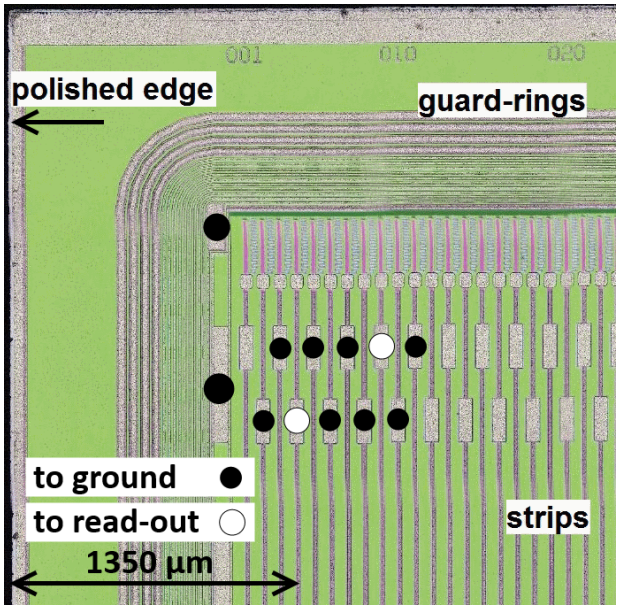

Figure 3.2.: Microscope picture of a strip sensor. The AC-pads of the read-out strips are highlighted with white circles. The black circles highlight the positions of the wire-bonds to ground via 50 Ω. Modified from [85].

Some sensors were irradiated to the fluences given tab. 3.3 for CIS100. The irradiated sensors were measured as-irradiated.

3.2. Current and capacitance measurements

The current-voltage I/V and capacitance-voltage C/V measurements were performed at a setup which allows for connection and measurement of the pad and the guard ring. The device under test *DUT* is placed on a temperature-controlled chuck ($\Delta T \approx \pm 0.1\,\mathrm{K}$) and can be fixed by vacuum. The chuck provides the high voltage[2] connection to the back side of the DUT. The setup is located in a shielding, light-tight metal box and flushed with dry air to avoid condensation of ambient humidity at low temperatures. The dew point was always below 243 K. The pad current is measured with a Keithley [86] 6517 ampere meter with an accurancy of about 0.1 % and the guard ring current is measured with a Keithley 6485.

The capacitance of the pad is measured with a LCR meter with an AC voltage of ±50 mV amplitude on top of the DC voltage. The frequency of the AC voltage was between 200 Hz and 1 MHz.

For all I/V and C/V measurements a constant voltage offset of +19.5 mV compared to the value set at the voltage source was taken into account. Figure 3.3

[2]Here: Up to 1000 V.

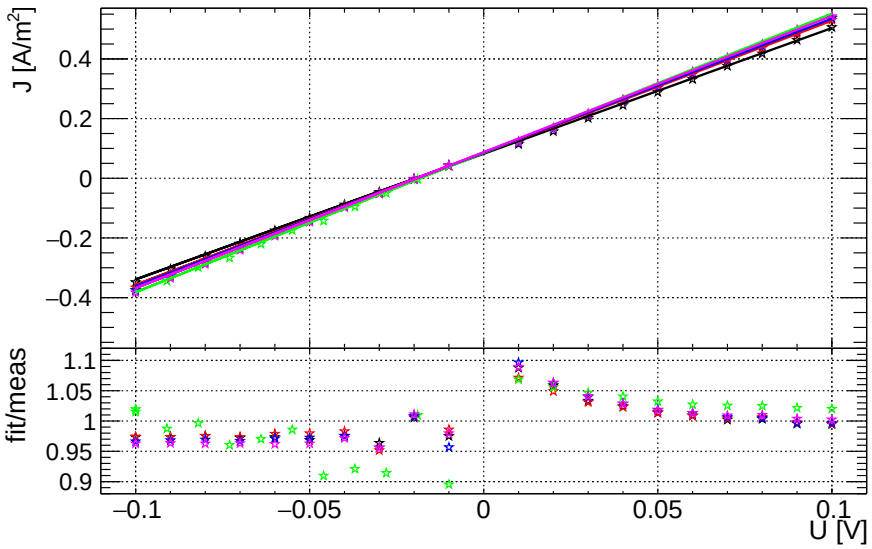

Figure 3.3.: Determination of the voltage offset for the I/V and C/V measurements with devices which behave like resistors (crosses). The fits (lines) yield an offset of 19.5 mV.

shows measurements of irradiated sensors which behave like resistors. The offset was determined from the fit of Ohm's law of the measurements.[3]

Heating of the samples can be neglected. If the current of the DUT is very high one has to ensure that the temperature can adjust to the change of the current which is heating the sample. The measurements were tested for possible hysteresis with $\pm\Delta U$ due to increasing or decreasing heating power $\Delta P = \Delta I \cdot \Delta U$. A waiting time between the voltage steps ΔU was adjusted to ensure the temperature has stabilized when measurements are taken.

3.3. The Transient Current Technique

The Transient Current Technique *TCT* is an important tool for the understanding of radiation detectors. Sub-nanosecond laser light pulses generate free charge carriers in the device under test *DUT* and the resulting transient current is recorded. The position of the initially generated carriers can be chosen using light of different wavelengths λ to illuminate the front side, back side, or the edge of the DUT.

Two different setups were used: A rather simple setup for pad diodes and a multi-channel setup which can record up to four channels for segmented sensors.

[3]The residuals shown in fig. 3.3 suggest the offset is different for positive and negative voltage.

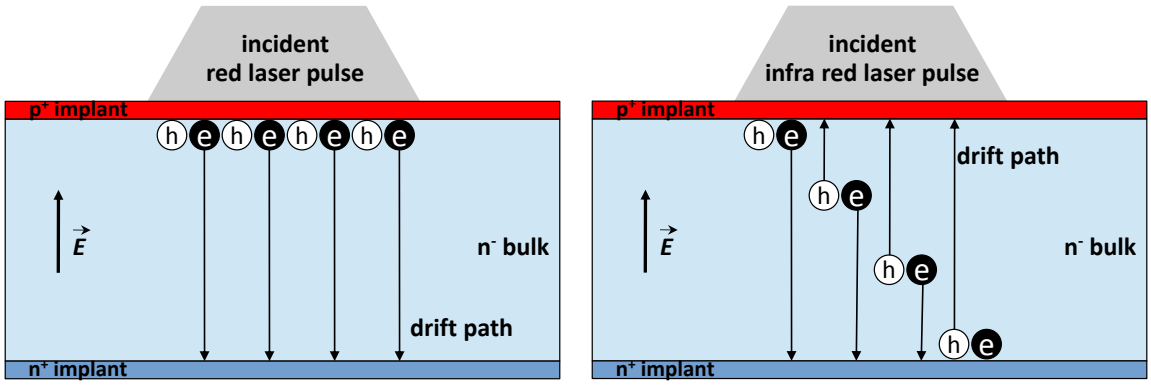

Figure 3.4.: Schematic of the initial charge distribution and the subsequent drift direction of charge carriers generated by short light pulses for $\lambda = 675\,\text{nm}$ in (a) and 1064 nm in (b). The sensor is reverse biased above full depletion. Previously published in ref. [81].

3.3.1. Pad diode TCT

The pad diode TCT setup allows for front and back injection of laser light pulses into pad diodes. It is described in detail in ref. [81]. The setup is used to measure the current transients of electrons and holes drifting through the pad sensor and to determine the charge collection efficiency of irradiated silicon sensors.

Pad diodes are placed on a temperature-controlled chuck ($\Delta T \approx \pm 0.2\,\text{K}$) with a small hole for back side illumination. The setup can be sealed and flushed with dry air. The DUT can be cooled down to 223 K. Heating of the sample is not an issue as the sample is placed directly on the cold-chuck and the temperature sensor is close to the sample.

High voltage is applied to the pad using a needle. The pad is read out via 50 Ω cables and a bias-T. The signal is amplified and fed into a Tektronix [86] DPO 4104 oscilloscope with a bandwidth of 1 GHz and a sampling rate of 5 GHz. In order to decrease the fluctuations due to electronics noise 512 current transients are averaged for each recorded waveform. The guard ring is floating for this setup.

Two different lasers are available: One with light of $\lambda = 675\,\text{nm}$, which corresponds to an absorption length in silicon of about 3 µm at room temperature, and one with $\lambda = 1064\,\text{nm}$, which corresponds to an absorption length of about 1000 µm at room temperature. Thus, charge carriers are generated only at the surface of the sensor for the 675 nm light while the generated charge is almost constant along the path of the light for 1064 nm.

Figure 3.4(a) shows the initially generated charge and the drift direction for a

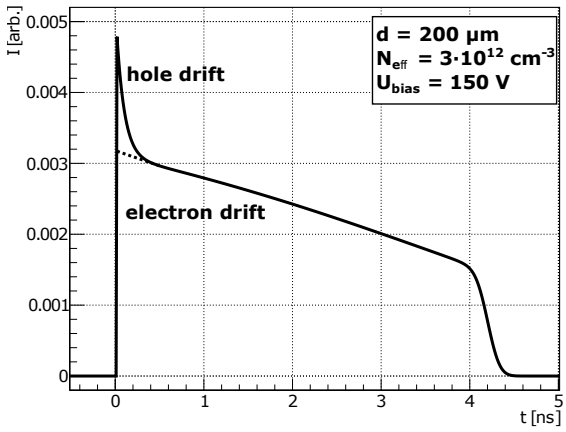

Figure 3.5.: Simulation of a transient current pulse for the situation depicted in fig. 3.4(a), not taking effects of read-out electronics into account. The holes are collected within 0.2 ns while the electrons drift through the sensor to the opposite electrode. Previously published in ref. [81].

675 nm light pulse injected at the front side of a n-type bulk diode. The generated free holes are immediately collected at the illuminated electrode while the electrons are drifting towards the opposite electrode (see fig. 3.5). The current transient is caused mostly by electrons drifting through the whole sensor. Similarly, the current transient is caused by drifting holes if the back side of the sensor is illuminated.

Figure 3.4(b) shows the initially generated charge for 1064 nm illumination. The initial charge distribution is almost constant and the transient current is caused by simultaneous electron and hole drift, similar to the current transient induced by a MIP.

Figure 3.5 shows the simulated transient current for illumination of the junction of a reverse biased n-type bulk diode with an infinitely short pulse of 675 nm light. The holes are collected immediately and have a very small contribution to the total current transient. The transient current pulse is dominated by the electrons drifting to the opposite electrode. The signal is decreasing since the electric field is linear with the maximum field at the front side.

The laser light is not focused and has a spot size of about 300 µm at the sensor surface. The lasers are tuned to generate $\sim 10^6$ electron-hole pairs for each light pulse. The full-width at half maximum $FWHM$ of the laser light pulses is < 50 ps. The pulse frequency is 200 Hz. The laser driver provides a trigger signal to the oscilloscope.

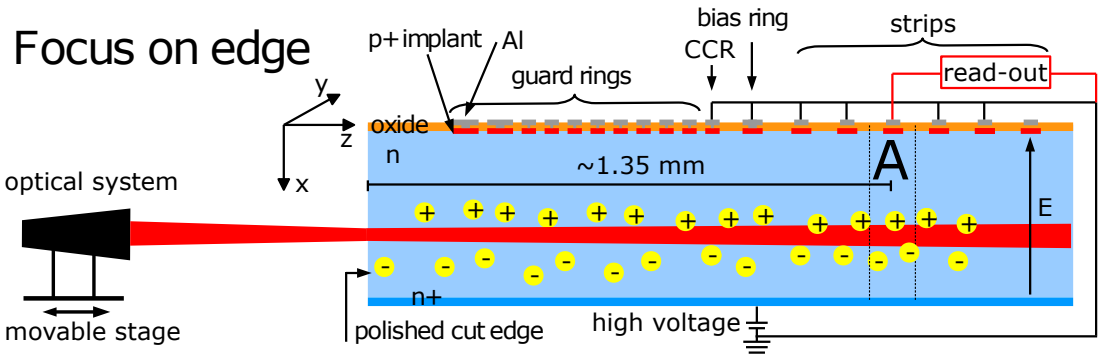

Figure 3.6.: Schematic principle of edge-TCT. A beam of focused infrared laser light illuminates the edge of a strip sensor, penetrates deep into the sensor, and generates free charge carriers along its path. The position x of the initially generated charge can be adjusted by shifting the beam. Current transients are recorded as a function of x for the strips connected to read-out electronics. The surrounding strips are connected to ground potential via 50 Ω. Modified from [85].

3.3.2. Multi-channel edge-TCT

TCT with pad diodes has certain limitations. If the carrier lifetimes are very short, carriers injected at the surface will not traverse the whole sensor. Accordingly, the information on the bulk obtainable from the current transients is limited. However, edge-TCT offers the possibility to create charge carriers at any desired depth in the sensor, as shown in fig. 3.6. Information about the electric field and the charge collection as a function of the distance from the surface can be obtained.

Infrared light with a long absorption length in silicon is used for edge-TCT. The edge of strip sensors is illuminated with focused laser light pulses and the focus of the beam can be shifted in three dimensions. The strips are connected to read-out electronics and the transient current can be measured as a function of the position of the initially generated charge carriers.

In order to measure strip sensors the individual channels are wire-bonded to PCBs or ceramics which connect them to read-out electronics. For edge-TCT, the edge of the sensors has to be polished in order to enable the light to enter the sensor with minimum scattering at the surface of the edge.

An existing multi-channel TCT setup, which is described in detail in ref. [87], was modified in the course of this thesis in order to perform edge-TCT measurements. A shielding box and a PCB were developed in collaboration with DESY [88] and are by now also used by other institutes. Additionally, a base plate housing external water cooling and a second cooling stage with a Peltier element was developed which can be turned easily for edge and front or back illumination of the DUT.

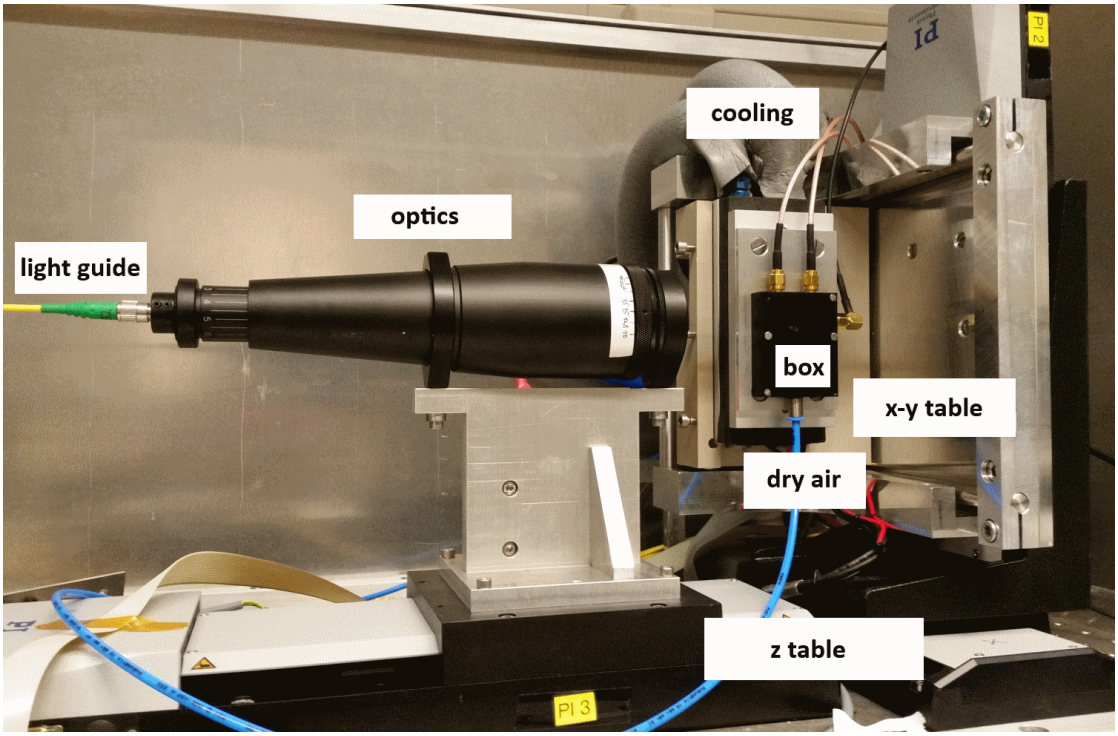

Figure 3.7.: Picture of the multi-channel edge-TCT setup. The DUT is inside the small black box right-center. The whole system is enclosed in a light-tight metal box and flushed with dry air for measurements. Modified from [85].

The commissioning of the setup as well as the methods for the sample preparation and positioning of the laser beam are described in detail in ref. [85].

The requirements for the setup were:

- The possibility for edge, front, and back side illumination in the same setup.
- Connections for two read-out channels and several ground connections for the neighboring strips and the periphery.
- High voltage tolerance up to 1000 V.
- Focusing of the laser light beam to a few µm spot size.
- Small air volume in the box for fast flushing with dry air.
- Small temperature-controlled volume for fast cooling to $T < 243\,\mathrm{K}$.

Setup The multi-channel edge-TCT setup is shown in fig. 3.7. The DUT is fixed inside a small box which is flushed with dry air. The box is fixed to a temperature-controlled ground plate which can be turned for edge and front/back illumination. The whole system is located inside a bigger shielded box which is flushed with dry

air as well. All electronics are outside the box except for the moving stages and the Peltier element.

The laser light is fed into an optical system via light fibers. The optical system is positioned on a movable stage (the z-direction) and focuses the light pulses towards the DUT. The x-direction (normal to the sensor surface for edge illumination) and the y-direction (parallel to the long side of the strips) are controlled with an x-y table. The precision of the moving stages is $(20 - 30)$ nm. All measurements discussed here were performed with a step size $\Delta x = 1\,\mu$m along x.

The strip sensors are fixed to the PCB as shown in fig. 3.8(a). The 4th and the 9th strip are read out and the surrounding ± 2 strips are connected to ground potential via $50\,\Omega$. The current collection ring surrounding the strip area and the innermost guard ring are also connected to ground potential via $50\,\Omega$. The wire-bonding pattern is shown in detail in fig. 3.2. High voltage is supplied by a gold-plated pad to the back side of the sensors.

The signal is attenuated with 10 dB electrical attenuators which significantly reduces reflections of the signal. Short cables (1 m) connect the read-out channels to the attenuators. The attenuated signal is amplified with 10 kHz to 2 GHz bandwidth amplifiers. The amplified signal is fed into a Tektronix DPO 7254 oscilloscope with 2.5 GHz bandwidth and 20 GS/s sampling rate for two channels. 1024 current transients are averaged for each recorded waveform.

Figure 3.8(b) shows a close-up of the sensor with the sketched light beam. At first, some samples were positioned more to the right and the laser beam was very close or even under the bond pad for the first read-out strip. This can lead to charge losses near the sensor surface for this strip, especially for irradiated sensors. The collected charge near the surface was very different for the two strips, as discussed in sec. 4.2.2. All sensors were shifted to the left after this was noticed. The collected charge near the surface increased for the first strip, while the collected charge for the second strip did not change. For those measurements where significant differences between the two strips are observed only the results for the second strip were analyzed.

Several different lasers emitting light of different wavelengths are available. However, only a laser emitting $\lambda = 1052$ nm light pulses with $FWHM \approx 50$ ps was used for this work. The absorption length in silicon at this wavelength is 620 µm at room temperature and 1400 µm at 243 K, where most measurements were performed. The laser driver provides a trigger signal to the oscilloscope. A pulse frequency of 1 kHz was used throughout. The optical system is described in ref. [87, 85]. The

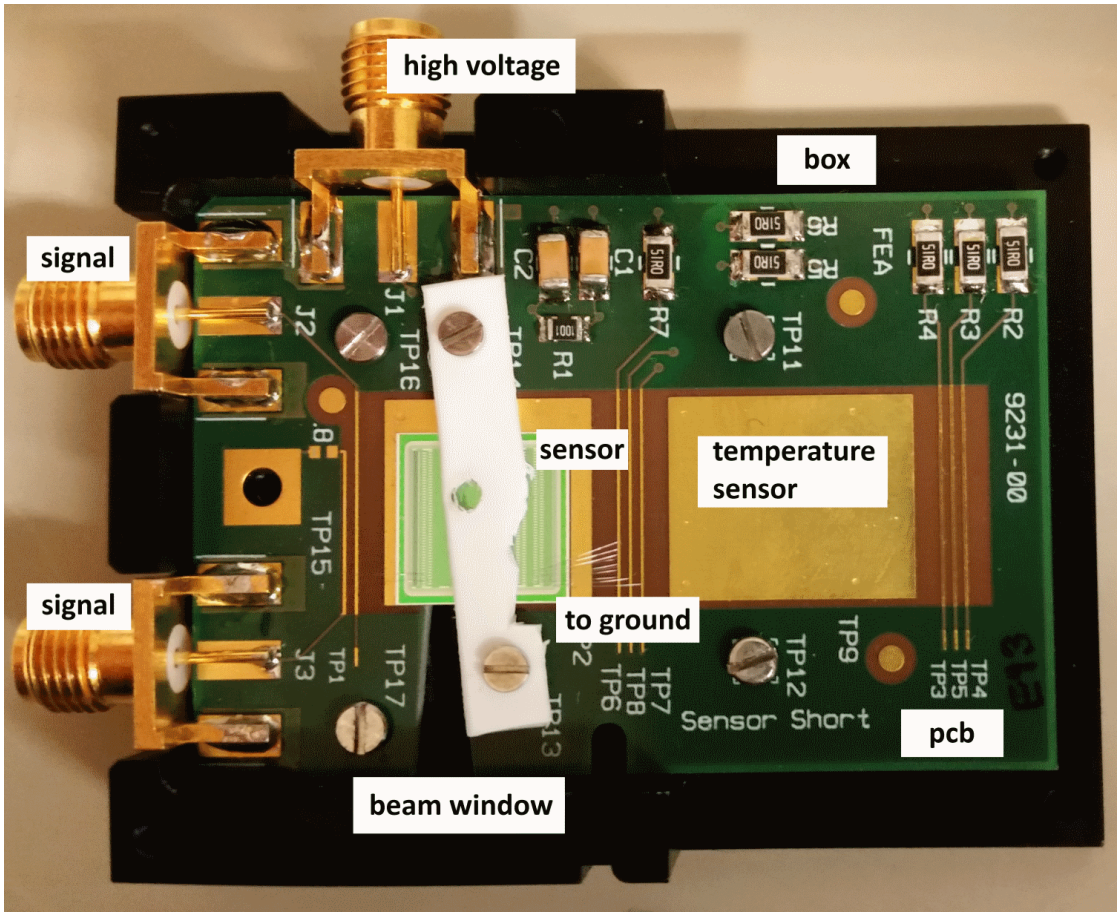

(a)

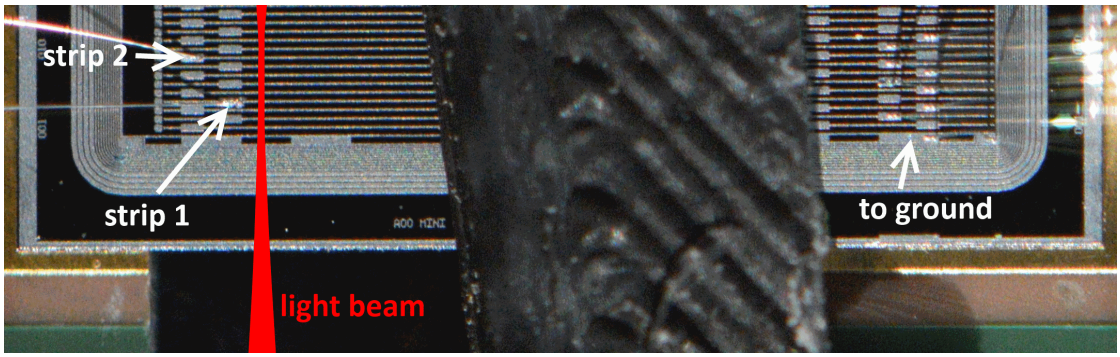

(b)

Figure 3.8.: (a) Picture of the PCB with a wire-bonded strip sensor. During a measurement, the temperature sensor (not shown) is fixed to the pad on the right. Modified from [85]. (b) Shows a close-up of a sensor with the two strips connected to the read-out on the left. The wire-bonds connecting the periphery and neighboring strips to ground are indicated on the right. The y-position of the pulsed laser light beam is sketched.

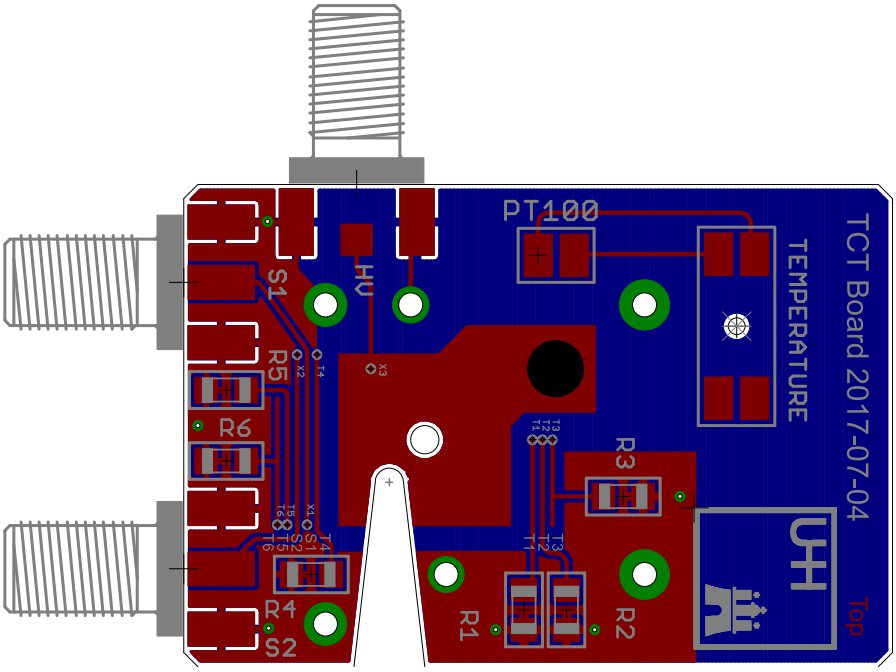

Figure 3.9.: Drawing of the second-generation PCB. The position of the temperature sensor, indicated by the black circle, is at the extension of the gold-plated pad on which the DUT is located.

light intensity was minimized to ensure there is no plasma effect (see sec. 2.1.4 and ref. [89, 90, 85]) due to high carrier densities which would change the transient current.

The temperature sensor, with thermal grease applied, is fixed on a second pad of the PCB adjacent to the pad where the DUT is placed, as shown in fig. 3.8(a). The temperature sensor is not on the same pad as the DUT since it was planned to perform measurements on larger sensors and it was not planned to measure with high heating power $P = I \cdot U$ of the DUT. However, many measurements were performed with forward biased sensors and rather high currents corresponding to a heating power of up to almost 0.5 W. The heat conductivity of the PCB is not sufficient to ensure that the temperature of the DUT is equal to the temperature at the second pad under these conditions, as discussed below. Therefore, a revised version of the PCB with higher power rating has been developed and produced, where the temperature sensor is fixed directly on the same pad where the DUT is located. This ensures that the DUT is at the desired temperature and there is no thermal runaway. The revised version of the PCB is shown in fig. 3.9. All measurements presented here were performed with the original PCB shown in fig. 3.8.

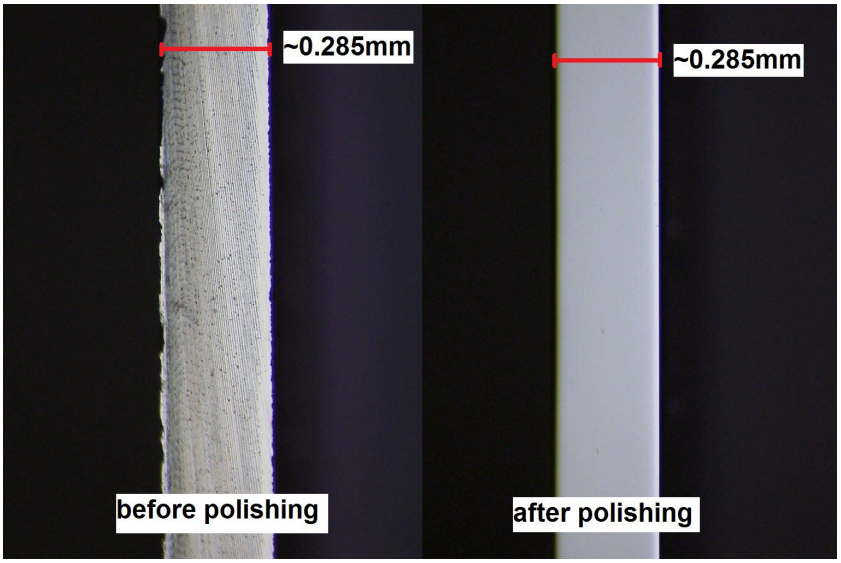

Figure 3.10.: The edge of a sensor before and after polishing. From [85].

Sample preparation The edge of the strip sensors used for edge-TCT has to be polished to assure a homogeneous beam profile in the sensor. The sensors were first tested with the I/V and C/V setup. Then, the edges were polished first with 3 µm grade diamond lapping film if deep scratches were visible. If no deep scratches were visible anymore, the sensors were fixed in a 3-D printed plastic handler which is attached to a polishing machine. The machine rotates the handler with the sensor on a textile soaked in de-ionized water and diamond polishing pastes of $(1 - 0.1)$ µm grades. This procedure was continued until no scratches were visible on the edge.

Figure 3.10 shows the edge of a strip sensor before and after polishing. No scratches are visible after polishing and the surface of the edge is very uniform. However, the reflections at the left and right corner of the polished edge differ from each other, indicating a rounding of the edges due to the polishing procedure. This has proven to be a problem since the beam is refracted when the rounded corners are illuminated. The beam is widened and the whole volume is illuminated if the rounded corners are illuminated, limiting the information near the corners; especially, since the first read-out strip is 1350 µm away from the edge.

Beam profile Assuming a Gaussian beam, the spot size, or „beam waist", of the intensity of the beam is

$$\omega(z) = \omega_0 \sqrt{1 + \left(\frac{z - z_0}{z_R}\right)} \tag{3.1}$$

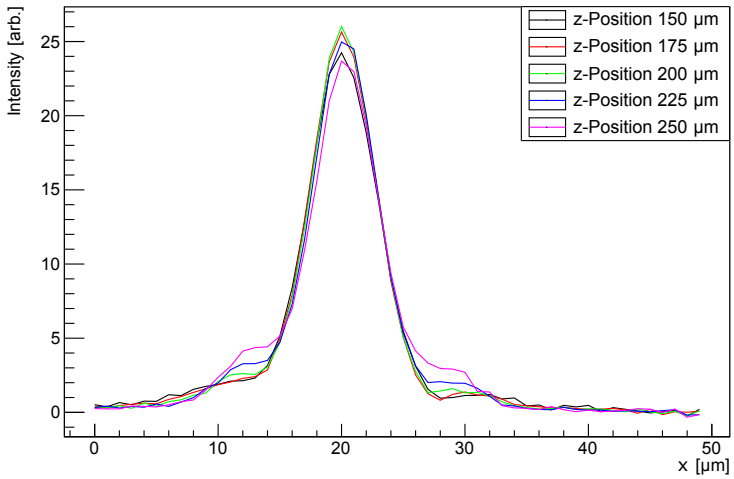

Figure 3.11.: Intensity of the edge-TCT laser light beam for different z positions of the focus. From [85].

with the axis of the light beam z. The root mean square minimum spot size

$$\omega_0 = \frac{FWHM_0}{\sqrt{2\ln(2)}} \tag{3.2}$$

is reached in the focus of the beam at $z = z_0$. The widening of the beam with z depends on the Rayleigh length z_R which, in turn, depends on the optical system and the wavelength of the light. At $z = z_0 \pm z_R$ the width of the beam is $\omega(z_0 \pm z_R) = \omega_0\sqrt{2}$. The theoretical limit for the minimum spot size in air is $\omega_0^{theo} = 3.5\,\mu\text{m}$ for the optical system used and 1052 nm light. The real spot size has been measured by scanning the beam over the corners of the window in the pad aluminum contact of a non-irradiated diode, as reported detail in ref. [85]. The measured minimum spot size is $\omega_0^{meas} = 7.1\,\mu\text{m}$ and the Rayleight length is $z_R^{meas} = 83\,\mu\text{m}$ in air. Figure 3.11 shows the measured beam profile for different focus positions z. In silicon, the opening angle of the beam decreases. The Rayleigh length increases by the refractive index of silicon n_{Si} and becomes $z_R^{Si,meas} \approx 300\,\mu\text{m}$. This is beneficial for measurements as the opening angle of the beam decreases. Consequently, the beam width changes less rapidly with z in silicon than in air.

Focus finding Before each measurement, the position of the focus of the beam relative to the edge (or surface for front/back illumination) of the sensor has to be determined. For this purpose, the focus is first adjusted by eye using a different laser emitting visible light. Then, the setup is closed and the desired temperature is set. The beam is scanned over one of the corners of the edge along the x-axis (defined in fig. 3.6) for different positions of the focus along the z-axis. The induced charge is integrated for each position x of the initially generated charge and the

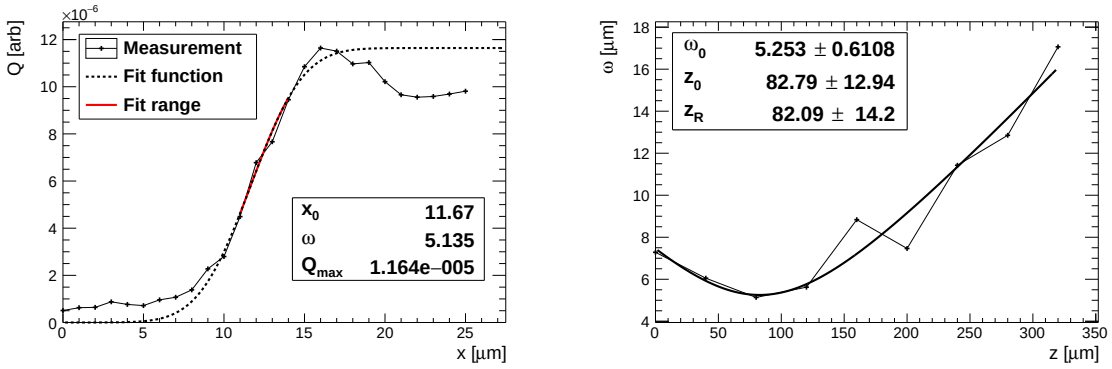

(a) (b)

Figure 3.12.: Determination of the position of the focus for edge-TCT. The width of the beam $\omega(z)$ is measured for different positions of the focus z by scanning the beam over the corner of the edge of a sensor and recording the measured charge as a function of x. Eq. 3.3 is fitted to the resulting charge profiles. (a) Shows the charge profile $Q(x)$ and the fit at $z = 80\,\mu\text{m}$. (b) Shows the beam profile $\omega(z)$ (crosses) from the charge profiles with a fit (line) of eq. 3.1. The focus is at the edge of the sensor for $z_0 = 83\,\mu\text{m}$. The sensor shown here is highly irradiated and reverse bias is applied.

resulting charge profile[4] $Q(x)$, shown in fig. 3.12(a), is fitted with an error function

$$Q(x) = \frac{Q_{max}}{2}\left(1 - \text{erf}\left(\frac{\sqrt{2}\,(x - x_0)}{\omega(z)}\right)\right) \tag{3.3}$$

for each z-position. The maximum $Q_{max} = \max(Q(x))$ of the charge profile is a fixed parameter in the fit. The position of the corner of the edge x_0 and the width of the beam $\omega(z)$ are free parameters. The fit is performed usually between $0.2 \cdot Q_{max}$ and $0.8 \cdot Q_{max}$. The resulting spot size $\omega(z)$ is fitted with eq. 3.1 in order to determine z_0 as shown in fig. 3.12(b).

This procedure is non-trivial if irradiated sensors are investigated and the measured charge is very small and not constant in the sensor bulk. Figure 3.12 shows a highly irradiated sensor with non-constant charge in the bulk as a worst-case scenario.

Once the position of the focus is known, the measurements are performed either with the focus at the edge (at the determined z_0) or the focus is shifted by $\Delta z = \frac{1550\,\mu\text{m}}{n_{Si}} = 435\,\mu\text{m}$ so it is in-between the two read-out strips. It has been found [85] that the current transients hardly change if the focus is between the strips or moved by $\pm z_R$.

[4]Explained below.

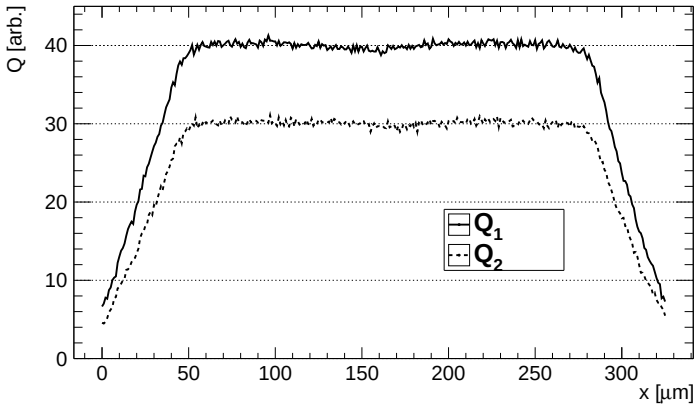

Figure 3.13.: Charge profiles $Q_{1,2}(x)$ for the two read-out strips as a function of the position of the beam obtained for a non-irradiated sensor at a reverse bias voltage above full depletion. The strips are at $x \approx 20\,\mu\text{m}$ and the back side is at $x \approx 305\,\mu\text{m}$. The charge of the second strip is $Q_2 < Q_1$ due to absorption of light in-between the strips which reduces the initially generated charge for the second strip. The sensor is non-irradiated with $d = 285\,\mu\text{m}$.

The charge profile The charge profile is the measured charge as a function of the position of the initially generated charge along the x-direction perpendicular to the surface of the sensor. In order to obtain the charge profile, the sum of the current transients[5] $Q(x) = \sum_t I(t)$ is determined for the duration of the current pulse at each injection position x. Figure 3.13 shows the charge profiles for the two read-out strips of a non-irradiated strip sensor.

The charge profile can be used to determine the charge collection efficiency of irradiated sensors as a function of the position of the initially generated charge. A detailed discussion of the charge profiles of irradiated sensors is given in chapter 6.

It was found that the profile of the charge collection efficiency $Q(x,T)/Q_0(x,T)$ for irradiated sensors hardly depends on the temperature and sensor annealing[6] as shown in ref. [91, 92].

The velocity profile The „velocity profile" actually shows a charge $Q(x)$ similar to the charge profile; but, only the rising edge of the transient current pulse is summed up. The sum is called the „prompt current". The prompt current method [93] is used to obtain information about the electric field $E(x)$ as a function of the position in the sensor x.

The transient current induced at the read-out electrode is

$$I(x,t) = Q_0\left(v_e(t) \cdot \exp\left(-t/\tau_e\right) + v_h(t) \cdot \exp\left(-t/\tau_h\right)\right) E_w(x) \tag{3.4}$$

[5] Examples of current transients are shown in fig. 3.15(a).
[6] If the annealing is below 100 min at 60 °C.

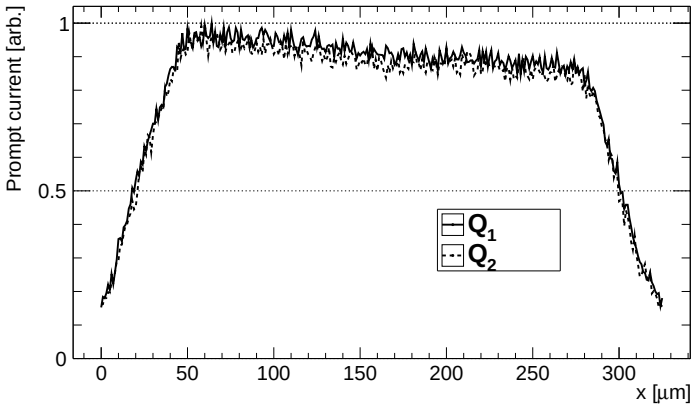

Figure 3.14.: Normalized velocity profiles for the two read-out strips determined from the same measurement as the charge profiles shown in fig. 3.13. The prompt current decreases from the front side towards the back side since the electric field in the sensor is linearly decreasing according to eq. 2.28.

with the initially generated charge $Q_0 = eN^0_{e,h}$, the effective electron and hole trapping times[7] $\tau_{e,h}$, the weighting field $E_w(x)$, and the drift velocity $v = \mu E$. The weighting field is approximately constant $E_w(x) = 1/d$ for edge-TCT (see sec. 2.3.2). The charge generation by a very short laser pulse is assumed instantaneous at $t = 0$.

Now, the drifting charge after a short time interval $\Delta t \ll \tau_{e,h}$ is $Q(\Delta t) \approx Q_0$ if no charge is collected at the electrodes. Accordingly, the transient current becomes

$$\lim_{\Delta t \to 0} (I(x, \Delta t)) = \frac{Q_0}{d} \cdot (\mu_e(E) + \mu_h(E)) E(x). \tag{3.5}$$

This relation is used to measure the velocity profile with edge-TCT.

Since the rise-time of the transient current pulse is finite, the rising edge of the transient current pulse (shown in fig. 3.15(a)) is summed up for a short time interval Δt. The resulting *prompt current* $= \sum_{\Delta t} I(t)$ is proportional to the sum of the drift velocities $v_e(x) + v_h(x)$, at least as long as $\Delta t \ll \tau_{e,h}$ and as long as the carriers are not collected within Δt and do not drift too far from the position of the initially generated charge x. Therefore, the prompt current can provide information about the electric field with $v(x) = \mu(E) \cdot E(x)$ if $\mu(E)$ is precisely known. Only limited information about $E(x)$ can be obtained for very high fields where the velocity saturates and $\frac{\mathrm{d}v}{\mathrm{d}E} \to 0$.

For the measurements presented here $\Delta t = 200\,\mathrm{ps}$ is used, corresponding to a drift length of $\sim 20\,\mu\mathrm{m}$ at the saturation velocity $\sim 10^7$ cm/s. Since the signal is

[7] Here, $\tau_{e,h}(x)$ assumed constant. Usually, $\tau_{e,h}(x) \neq const$ for non-constant defect occupation.

triggered and 1024 current transients are averaged the signal always starts at the same time and the jitter is negligible. Therefore, the prompt current was always determined as the sum of the transient current over the same time window.[8] The influence of the integration time Δt on the velocity profile is discussed in ref. [85].

Altogether, the prompt current as a function of the position of the initially generated charge x provides information about the electric field $E(x)$ in the sensor. Figure 3.14 shows the velocity profile for a non-irradiated sensor. It was obtained from the same current transients which were used to determine the charge profile shown in fig. 3.13, simply by choosing a different integration time Δt. The slope of the electric field is reproduced in the velocity profile while the charge profile is constant, as expected.

It should be noted that for the high fluences investigated here the trapping times become very short $\tau_{e,h} < 1\,\text{ns}$. Trapping may influence the measured velocity profiles as the assumption $\Delta t \ll \tau_{e,h}$ may not be justified anymore.

Temperature offset As mentioned above, the difference between the measured temperature and the temperature of the DUT may be a problem with the first generation PCB as the heating power was up to $0.5\,\text{mA} \cdot 1000\,\text{V} = 0.5\,\text{W}$. The temperature sensor is not on the same pad where the DUT is located as shown in fig. 3.8(a). This means that strong heating of the DUT leads to a temperature difference between the two pads due to the limited thermal conductivity of the PCB. The temperature stability with time is not affected and the variations are less than $\pm 0.3\,\text{K}$.

Figure 3.15(a) shows the transient current pulses of a forward biased, irradiated sensor with high current at different voltages. It can clearly be seen that the rising edge of the current transient hardly changes when the voltage is increased while the sum over the whole transient increases.

Figure 3.15(b) shows the sum of the charge profiles $Q(U) = \sum_x Q(x, U)$ over all beam positions x and the sum of the velocity profiles over all x at each voltage U. The sum of the charge profiles increases as expected from diode TCT measurements discussed in sec. 6.1. While the charge collection efficiency hardly depends on the temperature, as shown in ref. [92], the initially generated charge[9] $Q_0(T)$ at the read-out strip decreases with the temperature for the case shown here. I.e. Q_0 would decrease by about 12 % if the sensor is heated from 243 K to 253 K due to the change of the absorption coefficient. The absorption coefficient can be determined

[8] From 36.7 ns to 36.9 ns, see the insert of fig. 3.15(a).
[9] Given in eq. 4.1 in the following chapter.

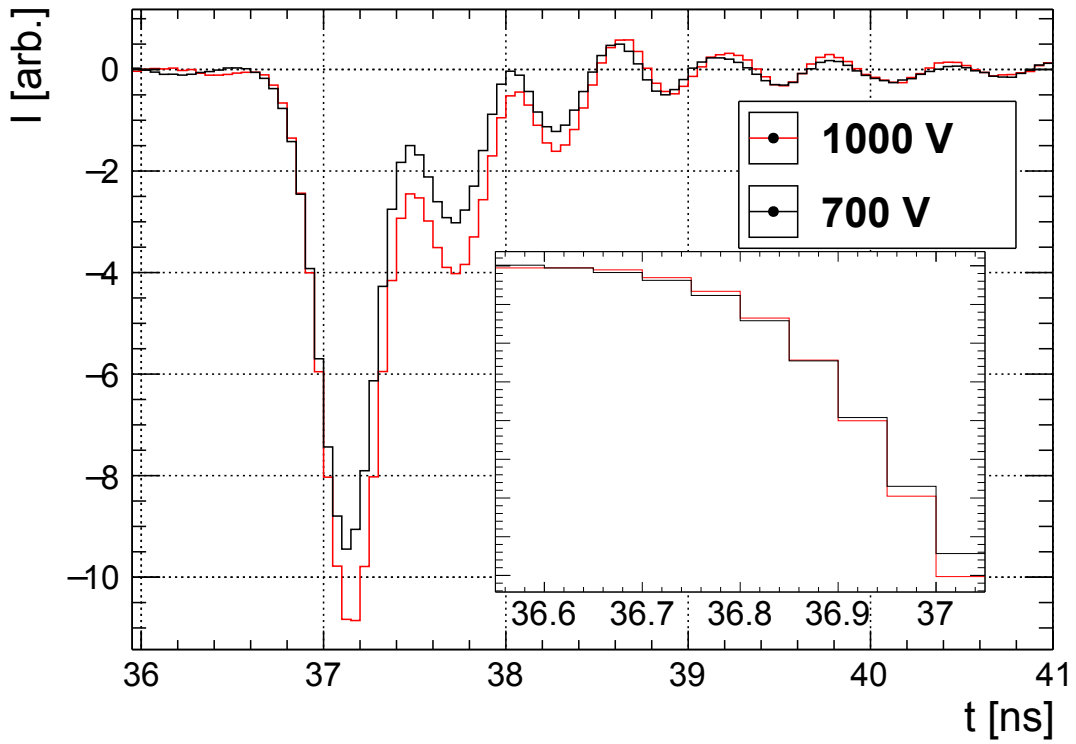

(a)

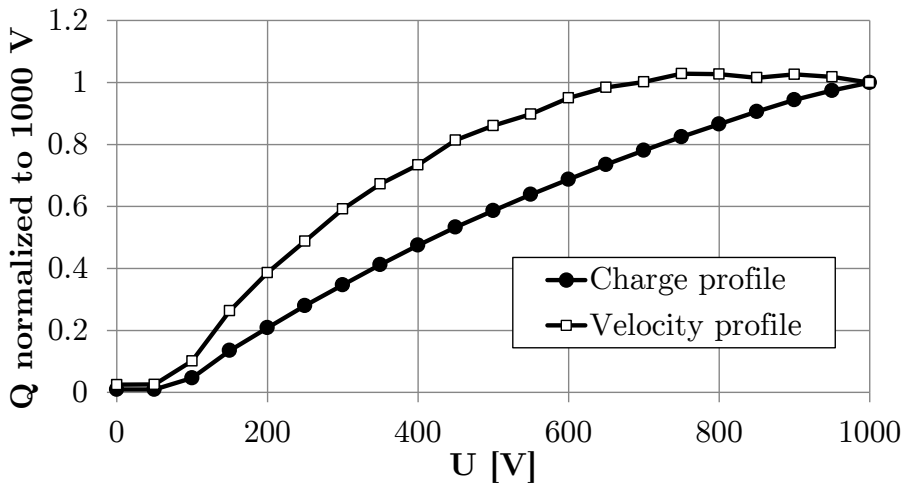

(b)

Figure 3.15.: (a) Current transients of a forward biased sensor at 1000 V (red) and 700 V (black). The initial charge was generated at $x = 150\,\mu\text{m}$ corresponding to $\sim d/2$ in the sensor. The transient current is summed from 36 ns to 41 ns for the charge profile $Q(x) = \sum_t I(t)$ and from 36.7 ns to 36.9 ns for the velocity profile. The insert shows the rising edge of the signal where the prompt current is determined. (b) Sum of the charge profiles $\sum_x Q(x)$ and velocity profiles over all x at each bias voltage normalized to the value at 1000 V. The sum of the velocity profiles $\sum_x \sum_{36.7\,\text{ns}}^{36.9\,\text{ns}} I(x,t,U)$ saturates around 700 V while the sum of the charge profiles $\sum_x \sum_{36\,\text{ns}}^{41\,\text{ns}} I(x,t,U)$ increases. The sensor was irradiated to $\Phi_{eq} = 1.3 \cdot 10^{16}\,\text{cm}^{-2}$ and the second readout strip at $T = 243\,\text{K}$ is shown.

from the same measurement as shown in sec. 4.1. Indeed, the measured absorption coefficient slightly depends on the bias voltage which may be caused by heating of the sample. However, the measured change of the absorption coefficient always corresponds to an increase of T of the DUT of less than 10 K. Accordingly, it seems like the temperature of the DUT is not very different from the measured temperature.

However, the sum of the velocity profiles does not increase for forward voltages exceeding 700 V for the sensor shown in fig. 3.15(b). This could be caused by heating of the samples with increasing voltage as the drift velocities[10] also decrease with the temperature and the prompt current is $\propto Q_0(T)(v_e(T) + v_h(T))$. The absolute value of the exponent of T is < 3 for the velocity[11] while it is ≈ 4 for the absorption coefficient (see sec. 4.2.2). Accordingly, the effect of decreasing drift velocities should be much less than the effect of decreasing Q_0 with increasing temperature offset. If heating of the sample would cause the constant velocity profiles this effect should be visible in the charge profiles as well. This effect was only observed for highly irradiated sensors at high forward bias voltages where the current increases sharply with increasing voltage (see sec. 5.2). The heating power for the sensor shown in fig. 3.15 starts to increase exponentially from 13 mW at around 300 V, to 90 mW at 700 V, and finally 300 mW at 1000 V. It should be checked with the new version of the PCB whether this effect persists when the temperature of the DUT is precisely known.

It should be noted, that the measurement shown in fig. 3.15 is the worst case for the highest fluence investigated. For lower fluences the current I increases much more steeply with the voltage U and it starts to increase at lower voltages (compare fig. 5.3) so there are less steps with heating power $U \cdot I > (50 - 100)$ mW. Additionally, the initial charge $Q_0(T)$ is less sensitive to an increase of T for lower fluences. E.g. it changes only by 1.3 % for the second read-out strip if a non-irradiated sensor is heated from 243 K to 253 K.

Altogether, large differences between the measured T and the real temperature of the DUT can not be ruled out for heating power $> (50 - 100)$ mW. The velocity profiles hint to higher differences, while the charge profiles do not deviate significantly from the expectation. The maximum difference between the measured temperature and the temperature of the DUT is estimated to be below 10 K from measurements of the absorption coefficient as a function of the bias voltage.

[10] The drift velocity also saturates at high fields; but, at higher fields than the maximum value 35 kV/cm shown in fig. 3.15(b).

[11] The exponent is ~ 0.3 at high electric fields where the velocity saturates, as given in chapter 7.

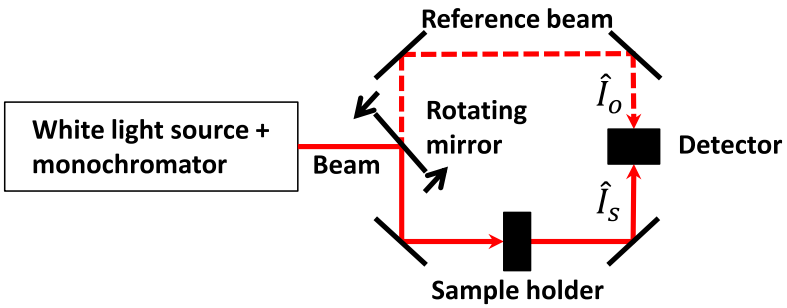

Figure 3.16.: Schematic of the spectrophotometer used for light absorption measurements.

For most measurements the heating power was < 50 mW and the temperature difference between the DUT and the temperature sensor is negligible.

3.4. Transmission spectroscopy

Near-infrared *NIR* light transmission measurements on bare silicon crystals have been performed with an Agilent [94] Cary 5000 UV-VIS-NIR spectrophotometer. Wavelengths ranging from 950 nm to 1300 nm have been investigated.

The spectrophotometer uses a white light source. Individual wavelengths are selected with a grating and an aperture creating a monochromatic light beam. A rotating mirror sends the beam alternating through a sample compartment and an empty reference compartment as shown schematically in fig. 3.16. A light detector measures the intensity of the beam passing the sample $\hat{I}_s$ and the reference intensity of the beam $\hat{I}_0$ passing the empty compartment. In this way the transmittance $\hat{T}_{tot} = \hat{I}_s/\hat{I}_0$ of the sample is measured.

The samples are taped to a sample holder with a 0.5 mm square aperture in the focal point of the beam. The minimum $FWHM$ of the light beam is around 1 cm at the focal point. All measurements have been performed at (293 ± 2) K and with air inside the spectrometer.

Before each measurement, the aperture of the sample holder is first fully blocked and then opened to perform 0 % and 100 % baseline calibrations. Afterwards, samples can be inserted into the beam.

The sample holder is fixed by a screw. However, the fixation is not very stable so one has to be very careful not to change the sample holder position when the sample is changed. If the position of the sample holder is changed also the position aperture changes (see fig. 4.6) with respect to the focus of the beam and the baseline calibration has to be repeated. The measured $\hat{T}_{tot}$ was found to be reproducible within 0.1 % for $\lambda \geq 1025$ nm and within 0.7 % for $\lambda < 1025$ nm if

the sample holder was not moved accidentally.

Transmission measurements were also attempted with diodes. However, the reflectivity is changed by reflection and interference in the thin thermal oxide layer on the diodes which makes it difficult to interpret the measurements and to compare samples with different oxide thickness.

Additionally, measurements with a different spectrometer employing a Michelson interferometer have been attempted at the Ruhr Universität Bochum. A Michelson interferometer allows scanning all wavelengths at once, minimizing the time needed for a complete scan of the relevant wavelengths. The spectrometer can be evacuated for a higher precision in the region of ambient gas absorption lines (especially water vapor). An aperture mounted on a water-cooled Peltier element was developed to control the temperature of the sample and to measure the absorption length as a function of the temperature.

Furthermore, it was planned to measure the light absorption in highly irradiated sensors with applied bias voltages in the Bochum setup. In principle, the setup should have also been capable of performing defect spectroscopy at high wavelengths up to $\lambda = 20\,\mu\text{m}$ ($\approx 50\,\text{meV}$). Unfortunately, the measurements were not found to be reproducible to the level of precision needed here. Possible reasons are a misalignment of the interferometer and saturation of the InGaAs detector used for near-infrared light.

4. Light absorption

When the charge collection in highly irradiated silicon diodes was investigated in the course of this work, the charge collection efficiency was found to be higher than expected for the illumination with infrared light. A possible explanation of the unexpectedly high collection efficiency is an increase of the generated free charge carriers due to the absorption of infrared light at defects introduced by irradiation. Indeed, an increase of the absorption of infrared light in irradiated silicon is well known since the 1950s and exploited for infrared *IR* spectroscopy of defect levels in irradiated silicon (see e.g. [95]). The increase of the absorption for a wide range of wavelengths and with annealing has been measured by Fan and Ramdas [96]. They report a certain photo-conductivity in irradiated silicon up to wavelengths of $\lambda = 3\,\mu\text{m}$, where non-irradiated silicon is transparent and no free carriers are produced. However, the near-infrared *NIR* spectrum which is used for TCT measurements was not studied in detail. Fan and Ramdas mention a shift of the absorption edge of silicon ($\sim E_g$) by up to $-0.1\,\text{eV}$. Here, the absorption coefficient α of infrared light in silicon has been measured as a function of the equivalent fluence. Additionally, the change of the number of free carriers generated by infrared light has been determined as a function of the fluence with an electric field applied.

In this chapter $\alpha = 1/\lambda_{abs}$ denotes the attenuation coefficient.

4.1. Edge-TCT measurements

4.1.1. Analysis

Edge-TCT can be used to measure the light attenuation coefficient α for the wavelength (here $\lambda = 1052\,\text{nm}$) of the laser light used by comparing the charge $Q_{1,2}$ deposited under two separate read-out strips of a strip sensor as shown in fig. 4.1. The charge measured at the first read-out strip is

$$Q_1 = eN_0\alpha \int_{z_1-\frac{p}{2}}^{z_1+\frac{p}{2}} \exp\left(-\alpha \cdot z\right) \mathrm{d}z = eN_0 \cdot \exp\left(-\alpha z_1\right) \cdot 2\sinh\left(\alpha\frac{p}{2}\right) \tag{4.1}$$

with the initial number of electron-hole pair generating photons N_0, the elementary charge e, the strip pitch p, and the position of the center of the first strip z_1 with

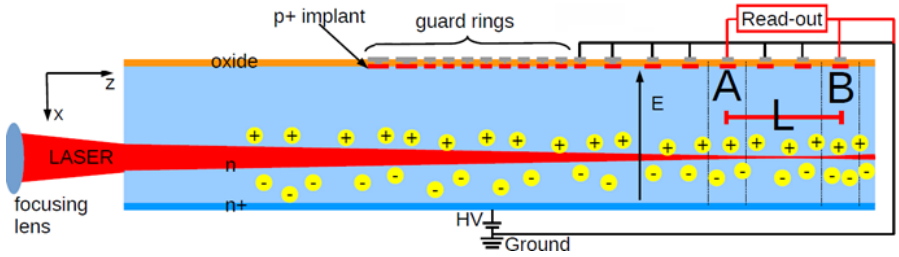

Figure 4.1.: Schematic of attenuation measurements with the edge-TCT setup. The ratio of the charge induced in two read-out strips is used to determine α. The focus is placed in-between the read-out strips. All strips are on ground potential via 50 Ω. From [85].

respect to the edge of the sensor. For a distance L between the two read-out strips the charge measured at the second read-out strip is $Q_2 = e^{-\alpha \cdot L} Q_1$. Consequently, the attenuation coefficient can be determined using

$$\alpha = -\frac{ln\left(\frac{Q_2}{Q_1}\right)}{L}. \tag{4.2}$$

It should be noted that these formulas assume the same weighting field at both strips and perfect alignment of the beam with respect to the sample. Trapping does not influence Q_2/Q_1 since the relative fraction of lost charge is independent of the initial number of free carriers N_0 (see eq. 2.45).

4.1.2. Results

The distance between the read-out strips was chosen five times the pitch $L = 5p = 400\,\mu m$. The light attenuation over the distance L is sufficient to determine $\alpha(1052\,nm)$ for the laser light of the edge-TCT setup. However, the results have proven to be very sensitive to misalignment of the laser beam and inhomogeneity of the fields near the read-out strips for irradiated sensors.

Figure 4.2(a) shows the measured charge profiles of both read-out strips $Q_{1,2}(x)$ under forward bias for an irradiated sensor and fig. 4.2(b) shows $\frac{Q_2}{Q_1}(x)$. At low bias voltages $\frac{Q_2}{Q_1}(x)$ is very non-homogeneous near the strip-side and more homogeneous at high bias voltages and near the back side of the sensor. Losses of $Q_1(x)$ are experienced near the strip-side but not or less for the second read-out strip $Q_2(x)$ as seen in figure 4.2 at $U = -200\,V$. The laser beam is closer to the bond pad of the first read-out strip than that of the second read-out strip (see sec. 3.3.2, fig. 3.8(b)) which can cause the field lines to end in the oxide. Charge carriers drifting towards

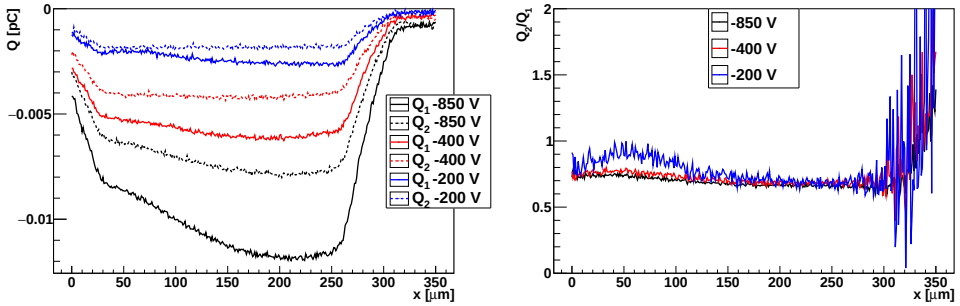

(a) (b)

Figure 4.2.: Charge profiles (a) of the two read-out strips $Q_1(x)$ and $Q_2(x)$ and the ratio (b) of the charge profiles $\frac{Q_2}{Q_1}(x)$. The strip sensor is irradiated to $\Phi_{eq} = 9.4 \cdot 10^{15}\,\mathrm{cm}^{-2}$ and under forward bias at 243 K. The strips are at $x \approx 20\,\mu\mathrm{m}$.

the oxide will induce less charge in the read-out electrode. It should be noted that large differences of $Q_1(x)$ were observed near the strip-side of an irradiated sensor after a small droplet of soldering flux was accidentally deposited near the first strip.[1] This shows the sensitivity of this method to surface effects.

Misalignment of the laser beam can be problematic since the integrated charge depends on the position of the laser beam if the electric field is not constant. If the laser beam is tilted with respect to the sample it will be at different positions for each of the strips: $Q_1(x_1)$ and $Q_2(x_2)$ with $x_1 \neq x_2$. However, the misalignment is hard to disentangle from differences in the fields below the two strips, as discussed above, and possible inhomogeneities for the first read-out strip because of the proximity to the periphery of the sensor. Comparison of simulations with measurements of non-irradiated sensors and comparison of the collection times of electrons and holes for both read-out strips suggest that there is some misalignment. However, the difference between x_1 and x_2 was found to be below 5 µm which corresponds to an angle of the beam of $< 10\,\mathrm{mrad}$.

In order to minimize the effects of possible misalignment, only the charge profiles for forward bias have been used for the determination of $\alpha\,(\Phi_{eq})$ since the electric field is more homogeneous compared to reverse bias (see sec. 5.2). Only for the non-irradiated sensors reverse bias has been used for the determination of $\alpha\,(\Phi_{eq})$ since they can not be operated under high forward bias and there is no trapping so the electric field does not need to be constant.

The ratio $\frac{Q_2}{Q_1}(x)$ is almost constant near the back side[2] of the sensors because the electric field is more homogeneous and $\frac{Q_2}{Q_1}\,(x)$ is hardly affected by surface ef-

[1] This data is not included in the results.
[2] Between 180 µm $< x <$ 280 µm in fig. 4.2.

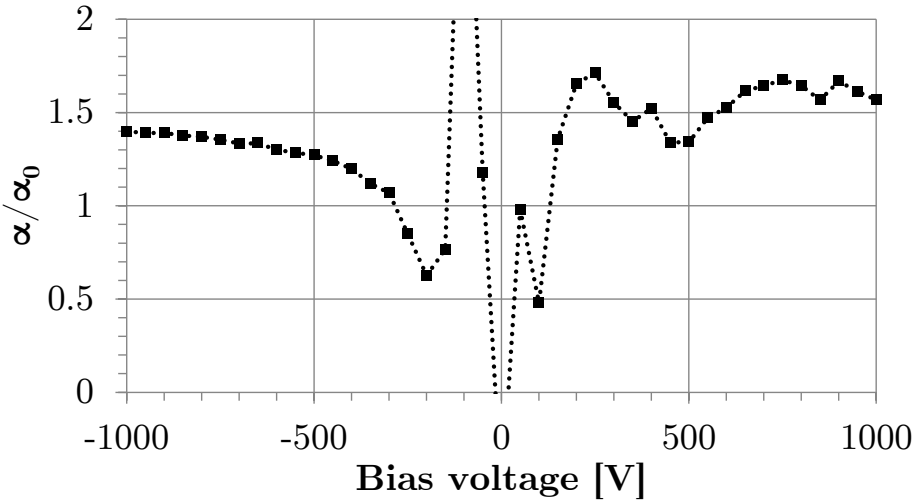

Figure 4.3.: Ratio of $\alpha\left(\Phi_{eq} = 9.4 \cdot 10^{15}\,\mathrm{cm}^{-2}\right)$ and the literature value α_0 for non-irradiated silicon versus the bias voltage of the sensor with $\Phi_{eq} = 9.4 \cdot 10^{15}\,\mathrm{cm}^{-2}$ at 243 K and for $\lambda = 1052\,\mathrm{nm}$. Negative voltages correspond to forward bias and positive to reverse bias.

fects. Therefore, the mean values of $\frac{Q_2}{Q_1}(x, U)$ near the back side and only at high forward bias voltages where $-\ln\left(\frac{Q_2}{Q_1}(x, U)\right)/L \approx const = \alpha$ have been used for the determination of $\alpha\left(\Phi_{eq}\right)$. The statistical error of $\alpha\left(\Phi_{eq}\right)$ obtained in this way is very small ($< 0.1\,\%$) because several bias voltages with usually 100 positions each are averaged. However, the systematic error may be large due to the effects discussed above.

Figure 4.3 shows the ratio of the averaged $\alpha\left(\Phi_{eq} = 9.4 \cdot 10^{15}\,\mathrm{cm}^{-2}\right)$ and the literature value α_0 for non-irradiated silicon versus the bias voltage for the same sensor as in fig. 4.2. The average values were obtained by averaging between $x = 180\,\mu\mathrm{m}$ and $x = 280\,\mu\mathrm{m}$ with a step size of $\Delta x = 1\,\mu\mathrm{m}$. For the determination of $\alpha\left(\Phi_{eq}\right)$ the mean value for $-1000\,\mathrm{V} < U < -500\,\mathrm{V}$ has been used, where $\alpha\left(\Phi_{eq}, U\right)$ changes by about $10\,\%$.[3] This procedure was taken for all measured samples.

The ratio slightly increases with the negative forward bias voltage. This can be explained by the larger losses of $Q_1(x)$ near the oxide and bond pad at lower bias voltages (see fig. 4.2(b)). At high voltages the increase of α is probably dominated by heating of the sensor as discussed in sec. 3.3.2. Accordingly, the change of the light absorption might be slightly overestimated with this method. Assuming the change is caused only by heating of the sample this would correspond to an increase of T of the DUT by 6 K. However, as the current increases with the voltage the trap occupation changes which might influence the measured absorption coefficient.

[3] The mean value is $\alpha\left(\Phi_{eq}\right)/\alpha_0 = 1.34$ for fig. 4.3.

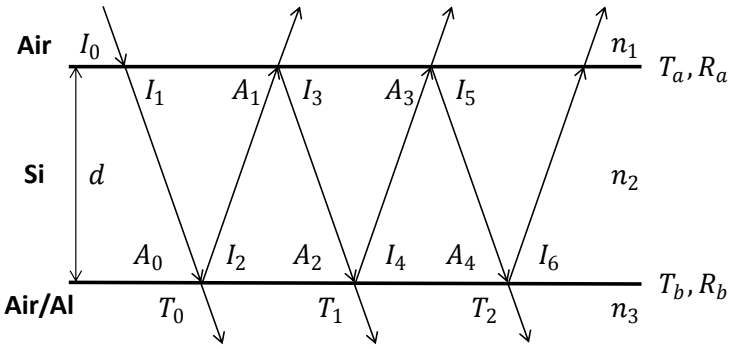

Figure 4.4.: Transmission and absorption of incident light with intensity I_0 in a plate of silicon with thickness d. The $n_{1,2,3}$ denote the refractive indices of the different media and $\hat{T}_{a,b}$ and $\hat{R}_{a,b}$ the transmittance and reflectance at each interface. The nomenclature for the individual intensities in the silicon is I_l with $l \geq 1$, and $\hat{T}_i$ and A_i for the transmitted and the absorbed intensities with $i \geq 0$. The angle of incidence is just for visualization, in the experiment this angle is 90 degrees.

The results for all fluences will be discussed in the following section together with the spectrophotometer results (see fig. 4.8).

4.2. Transmittance measurements

4.2.1. Analysis

In order to measure the absorption length λ_{abs} of a thin plate of silicon with transmission spectroscopy the refractive index of silicon $n(\lambda)$ has to be known as a function of the wavelength and reflections at the surfaces have to be taken into account. Following the Fresnel equations, for normal incidence on a flat interface between two media the reflectance is

$$\hat{R} = \left| \frac{n_1 - n_2}{n_1 + n_2} \right|^2 \tag{4.3}$$

with the refractive indices of the individual media $n_{1,2}$. The transmittance is

$$\hat{T} = 1 - \hat{R}. \tag{4.4}$$

Figure 4.4 shows a schematic of light being reflected, absorbed, and transmitted in a silicon plate of thickness d. For air-silicon-air[4] the reflectance at both interfaces

[4]The samples used here have no thermally grown oxide layers.

becomes $\hat{R} = \left(\frac{n_{Si}-1}{n_{Si}+1}\right)^2$ since $n_1 = n_3 = n_{air} = 1$. The intensity after entering the silicon plate is $I_1 = I_0\hat{T}$. After traversing the plate the first time the absorbed intensity is

$$A_0 = I_1\left(1 - \exp\left(-\frac{d}{\lambda_{abs}}\right)\right) \tag{4.5}$$

with the absorption length $\lambda_{abs} = \alpha^{-1}$. The transmitted intensity is

$$\hat{T}_0 = I_1\hat{T} \cdot \exp\left(-\frac{d}{\lambda_{abs}}\right). \tag{4.6}$$

The internally reflected intensity is $I_2 = I_1\hat{R} \cdot \exp\left(-\frac{d}{\lambda_{abs}}\right)$ and the absorbed intensity for the internally reflected beam is

$$A_1 = I_2\left(1 - \exp\left(-\frac{d}{\lambda_{abs}}\right)\right). \tag{4.7}$$

The transmitted intensity after the second internal reflection is

$$\hat{T}_1 = I_3\hat{T} \cdot \exp\left(-\frac{d}{\lambda_{abs}}\right). \tag{4.8}$$

Concluding, the intensity is $I_i = I_0\hat{T}\left(\hat{R}\exp\left(-\frac{d}{\lambda_{abs}}\right)\right)^{i-1}$ for $i \geq 1$. The total absorbed intensity becomes

$$A_{tot} = \left(1 - \exp\left(-\frac{d}{\lambda_{abs}}\right)\right)\sum_{i=0}^{\infty} I_{i+1} = I_0\hat{T} \cdot \frac{1 - \exp\left(-\frac{d}{\lambda_{abs}}\right)}{1 - \hat{R} \cdot \exp\left(-\frac{d}{\lambda_{abs}}\right)} \tag{4.9}$$

and the total transmittance becomes

$$\hat{T}_{tot} = \hat{T} \cdot \exp\left(-\frac{d}{\lambda_{abs}}\right)\sum_{i=0}^{\infty} I_{2i+1} = \frac{I_0\hat{T}^2}{\exp\left(+\frac{d}{\lambda_{abs}}\right) - \hat{R}^2 \cdot \exp\left(-\frac{d}{\lambda_{abs}}\right)}. \tag{4.10}$$

Following eq. 4.10 and with $0 < \hat{T}$, $\hat{R}$, $\hat{T}_{tot} < 1$, and $\frac{d}{\lambda_{abs}} > 0$ the absorption length can be calculated from the measured $\hat{T}_{tot}$:

$$\lambda_{abs} = \frac{d}{ln\left(\frac{\hat{T}^2 + \sqrt{\hat{T}^4 + 4\hat{R}^2\hat{T}_{tot}^2}}{2\hat{T}_{tot}}\right)} \tag{4.11}$$

with $\hat{T}(n)$ and $\hat{R}(n)$ calculated with $n_{Si}(\lambda)$ of ref. [97].

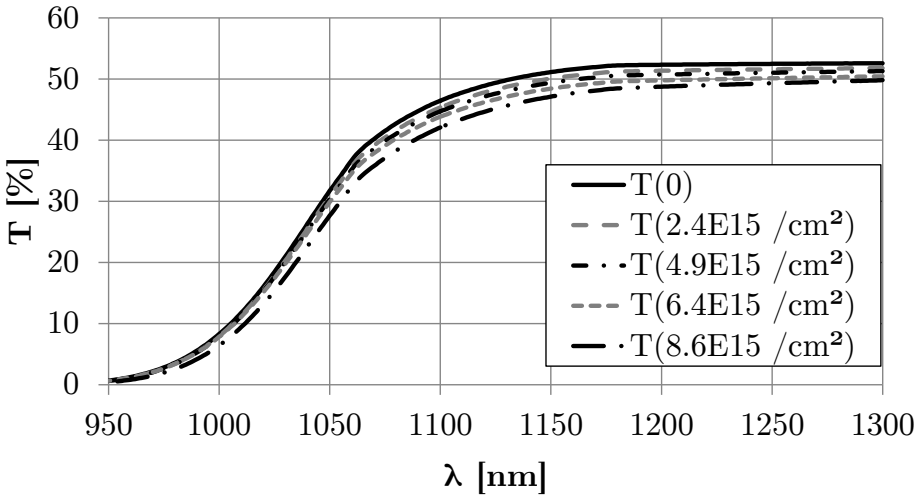

Figure 4.5.: Transmittance $\hat{T}(\Phi_{eq})$ at 293 K measured with silicon plates irradiated to different equivalent fluences Φ_{eq}. The values are given in tab. C.1. $\hat{T}$ at $\lambda = 1300\,\text{nm}$ calculated with the literature absorption length $> 1\,\text{m}$ is 52.8 %.

4.2.2. Results

Here, the spectrophotometer (see sec. 3.4) measurements for the bare silicon pieces listed in table 3.1 will be discussed together with the edge-TCT results. All transmission measurements were performed at $(293 \pm 1)\,\text{K}$. The data presented here was obtained with $\Phi_{eq} = 0.62 \cdot \Phi$ for 24 GeV/c proton irradiation.

Figure 4.5 shows the measured total transmittance[5] $\hat{T}$ as a function of the wavelength λ for different Φ_{eq}. At $\lambda = 950\,\text{nm}$ $\hat{T}$ is close to zero as α is very large. For $\lambda > 1200\,\text{nm}$ $\hat{T}$ does barely change and approaches the theoretical value of eq. 4.10 using the literature values of α for the non-irradiated silicon plate.

A decrease of $\hat{T}$ with increasing Φ_{eq} can clearly be seen. The transmittance even decreases with Φ_{eq} for $\lambda > 1200\,\text{nm}$, where $\alpha \to 0$ for non-irradiated silicon. Other groups using a two-photon absorption TCT setup [98] with laser light of 1300 nm and 1500 nm wavelength confirm a significant charge generation by single-photon absorption in silicon after high fluences, while no charge is generated in non-irradiated silicon with the same method.

The transmittance measurements have been performed repeatedly to test the reproducibility of the results. Figure 4.6 shows the transmittance $\hat{T}(\Phi_{eq})$ at $\lambda = 1052\,\text{nm}$ for two consecutive measurements with new sample fixation at the sample holder and 0 % and 100 % baseline calibration scans in-between the measurements. For both scans, first the non-irradiated sample was measured, then the irradiated

[5] $\hat{T}$ now denotes $\hat{T}_{tot}$ of eq. 4.10.

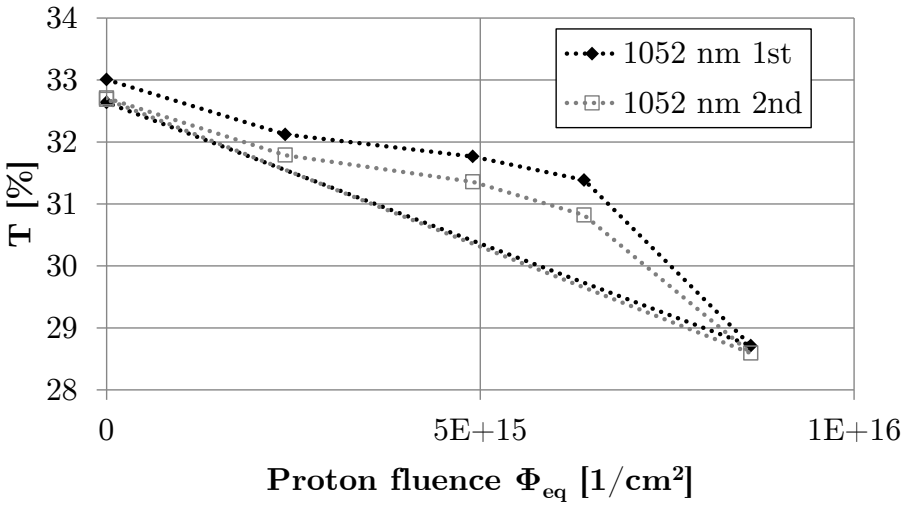

Figure 4.6.: Comparison of the transmittance $\hat{T}$ at 1052 nm for two measurements (diamonds, squares) performed with separate sample fixation and new calibration of the setup in-between.

samples starting with the highest fluence $\Phi_{eq} = 8.6 \cdot 10^{15}\,\mathrm{cm}^{-2}$, and in the end again the non-irradiated sample. The first spectral scan shows a constant offset of about 1 % relative to the second scan for all measurements except for the first measurement of the non-irradiated sample and the the consecutive measurement of the highest fluence. The offset is due to an accidental shift of the sample holder position with respect to the focus of the light beam which happened when switching from the sample with $8.6 \cdot 10^{15}\,\mathrm{cm}^{-2}$ to the sample with $6.4 \cdot 10^{15}\,\mathrm{cm}^{-2}$. Therefore, the second measurement was used for the determination of α.

The absorption length $\lambda_{abs} = \alpha^{-1}$ was determined using eq. 4.11 and $n(\lambda)$ of ref. [97].[6] Figure 4.7 shows a comparison of the measured λ_{abs} to the literature values of ref. [97] for measurements of a non-irradiated silicon plate. The maximum deviation of the measured absorption length of non-irradiated silicon from the literature values is 4 % in the region between $\lambda = 950\,\mathrm{nm}$ and 1130 nm. For $\lambda > 1150\,\mathrm{nm}$ the deviation to the literature values is large as λ_{abs} becomes much larger than the thickness of the silicon plate and the absorbed intensity in the sample becomes negligible.

The attenuation coefficient is parameterized as

$$\alpha(\Phi_{eq}) = \alpha_0 + \alpha_N(\Phi_{eq}) \tag{4.12}$$

with the contribution $\alpha_N(\Phi_{eq}) \propto \sum_j N_j(\Phi_{eq})\,\sigma_j$ by absorption of radiation-induced

[6] It should be noted that the results are very sensitive to small changes of $n(\lambda)$.

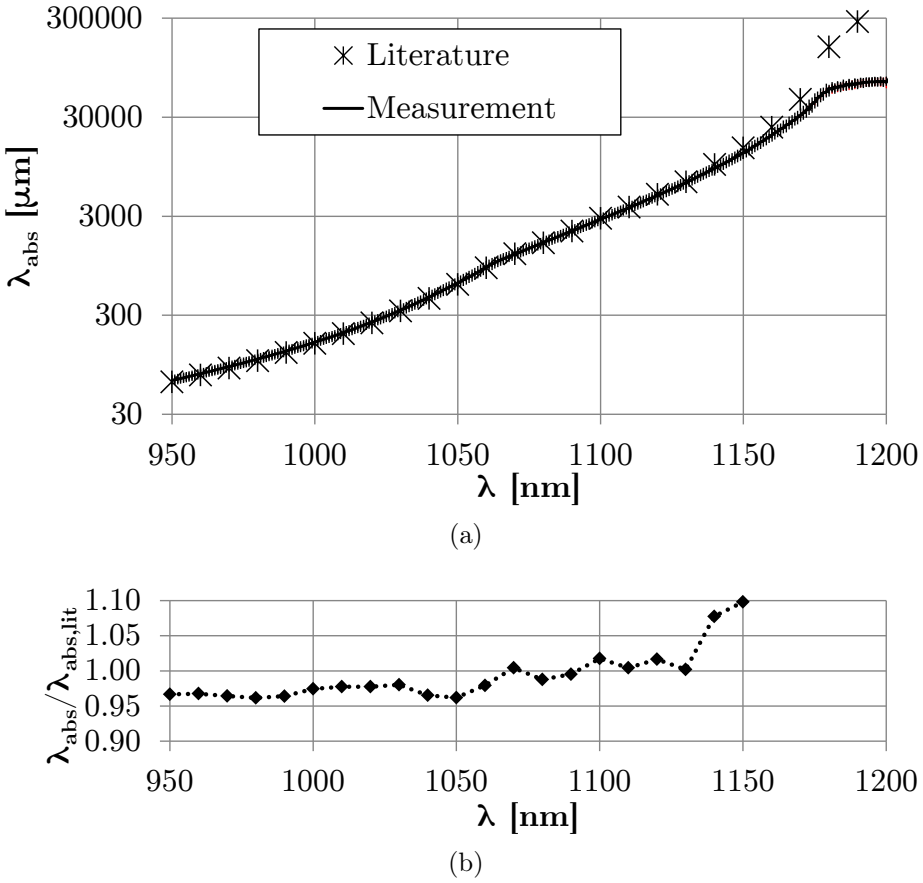

Figure 4.7.: (a) Comparison of the literature absorption length at 293 K from ref. [97] and the measurements performed with a non-irradiated silicon plate. (b) Shows the ratio.

defects, the defect concentration $N_j(\Phi_{eq})$, and the light absorption cross section σ_j. If the introduction of light absorbing defects is assumed $N_j(\Phi_{eq}) \propto \Phi_{eq}$ one obtains $\alpha_N(\Phi_{eq}) \propto \Phi_{eq}$. Now, if the temperature dependence of the absorption of infrared light on radiation-induced defects is assumed to be the same as the temperature dependence of phonon-aided inter-band absorption in non-irradiated silicon, the ratio of the attenuation coefficient before irradiation $\alpha_0(T)$ and after irradiation $\alpha(\Phi_{eq}, T)$ should be independent of the temperature T. Thus, a parameterization of the attenuation coefficient is introduced:

$$\alpha(\Phi_{eq}, T, \lambda) = \alpha_0(T, \lambda) \cdot \left(1 + \frac{\Phi_{eq}}{\Phi_{abs}(\lambda)}\right) \tag{4.13}$$

with the damage parameter $\Phi_{abs}(\lambda)$.

Figure 4.8 shows $\frac{\alpha(\Phi_{eq},T)}{\alpha_0(T)} - 1$ vs. Φ_{eq} for $\lambda = 1052\,\text{nm}$ extracted from the spectrophotometer measurements at 293 K shown in figure 4.5. Additionally, the results from the edge-TCT measurements with high electric field in the samples at 253 K

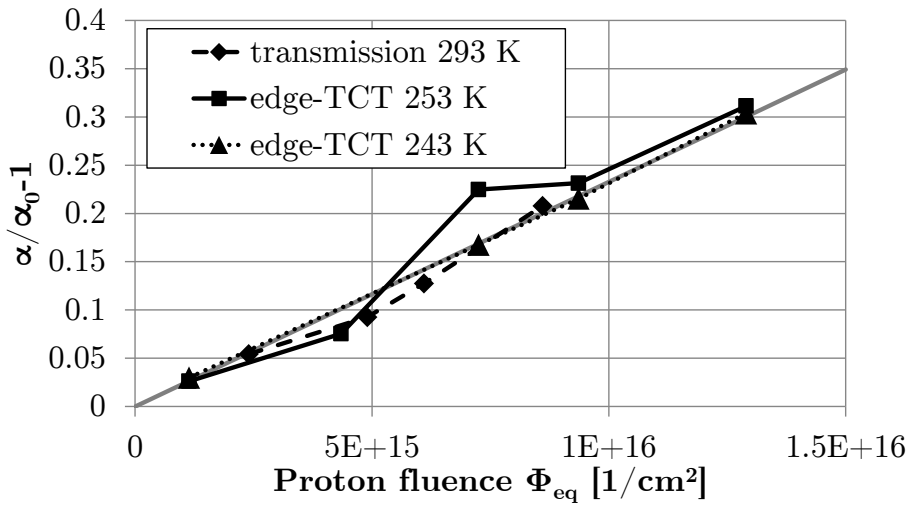

Figure 4.8.: Relative change of the attenuation coefficient at 1052 nm with irradiation $\frac{\alpha(\Phi_{eq},T)}{\alpha_0(T)} - 1$ at different temperatures. The data at 293 K was obtained with transmission measurements of bare silicon pieces. The data at lower temperature was obtained with edge-TCT measurements of strip sensors. The gray line shows the fit.

and 243 K are shown. It turns out that $\frac{\alpha(\Phi_{eq},T)}{\alpha_0(T)} - 1$ is proportional to Φ_{eq} and independent of T at $\lambda = 1052\,\text{nm}$. Therefore, the temperature dependence seems to be the same for absorption at defects and inter-band absorption in non-irradiated silicon. Furthermore, this result implies that the additional absorption at defects in irradiated silicon directly translates into the creation of additional free carriers since the transmission and edge-TCT measurements agree. Using eq. 4.13, $\Phi_{abs}\,(1052\,\text{nm}) = (4.30 \pm 0.59) \cdot 10^{16}\,\text{cm}^{-2}$ is obtained from linear regression of the results at all investigated temperatures.

Figure 4.9(a) shows the mean $\Phi_{abs}\,(\lambda)$ determined from the spectrophotometer measurements at $T = 293\,\text{K}$ with α_0 for the non-irradiated sample and $\alpha\,(\Phi_{eq})$ at $\Phi_{eq} = (2.4,\ 4.9,\ 6.4,\ 8.6) \cdot 10^{15}\,\text{cm}^{-2}$. For the following analysis it is assumed that $\Phi_{abs}\,(\lambda, \not{T})$ is independent of the temperature at all λ investigated due to the results at $\lambda = 1052\,\text{nm}$ discussed above. Figure 4.9(b) shows an exponential fit $\Phi_{abs}\,(\lambda) = 2.84 \cdot 10^{15} \cdot \exp\left(-3.23 \cdot 10^{-2}\,\text{nm}^{-1} \cdot \lambda\,[\text{nm}]\right)\text{cm}^{-2}$ of the data in the range $1040\,\text{nm} < \lambda < 1080\,\text{nm}$ which can be used for estimation of the change of the absorption coefficient at wavelengths different from the ones used in this work.

The results for $\alpha\,(\lambda, T = 293\,\text{K}, \Phi_{eq})$ and $\Phi_{abs}(\lambda)$ are given in appendix C for a wide range of λ. For $\lambda = 1064\,\text{nm}$ the parameterization

$$\alpha_0\,(1064\,\text{nm}, T) = \left(\frac{T\,[\text{K}]}{172.3}\right)^{4.25}\,\text{cm}^{-1} \tag{4.14}$$

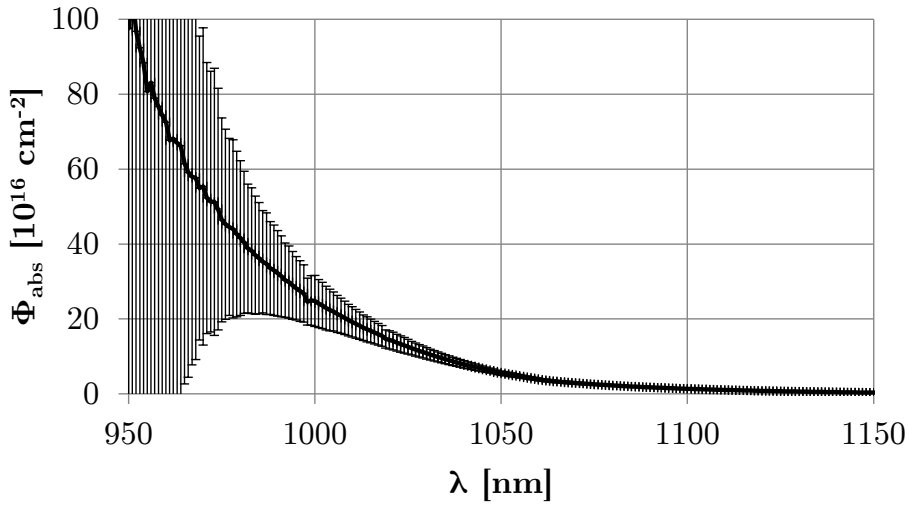

(a)

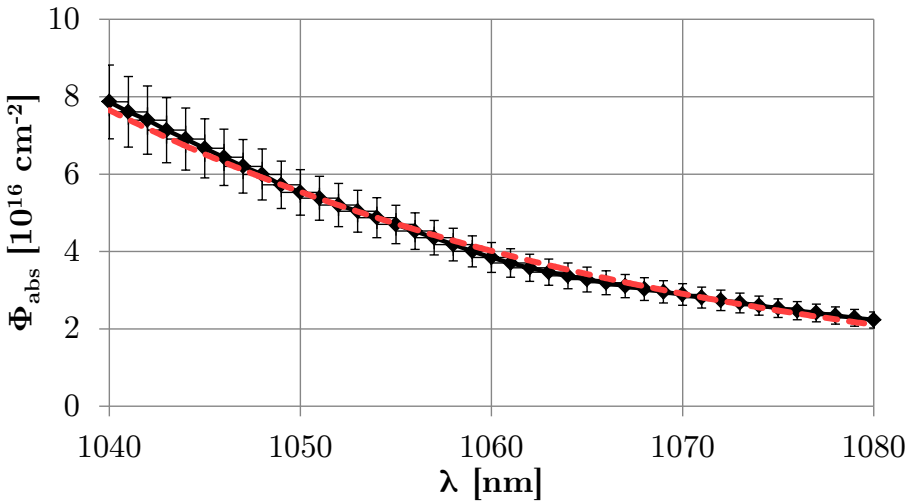

(b)

Figure 4.9.: $\Phi_{abs}(\lambda)$ at 293 K for the range of λ where the spectrophotometer measurements are sensitive (a); and the relevant range 1040 nm $< \lambda <$ 1080 nm used for TCT setups (b) with fit (dashed line).

of ref. [99] has been used, which agrees to 0.8 % with the measurements at 293 K. The damage parameter is $\Phi_{abs}\,(1064\,\mathrm{nm}) = (3.37 \pm 0.36) \cdot 10^{16}\,\mathrm{cm}^{-2}$.

For $\lambda = 1052$ nm the parameterization

$$\alpha_0\,(1052\,\mathrm{nm}, T) = \left(\frac{T\,[\mathrm{K}]}{146.2}\right)^{3.86}\,\mathrm{cm}^{-1} \tag{4.15}$$

gives the best fit to the data obtained with edge-TCT and the spectrophotometer measurements. The damage parameter is $\Phi_{abs}\,(1052\,\mathrm{nm}) = (4.30 \pm 0.59) \cdot 10^{16}\,\mathrm{cm}^{-2}$ as given above.

4.3. Conclusion

The measurements show that the absorption of near-infrared light increases proportional to the fluence and that this increase can be directly translated into an increase of the number of generated eh pairs. Therefore, the change of $\alpha(\Phi_{eq})$ has to be taken into account for charge collection efficiency measurements of irradiated sensors utilizing light. Otherwise, the charge collection efficiency will be overestimated. Also, extracted parameters such as the trapping time will be overestimated. Whether or not taking the change of $\alpha(\Phi_{eq})$ into account is important depends mostly on two[7] parameters: The fluence and the thickness of the device under test. The higher the fluence, the bigger the change will be. If the fluence is well below $\Phi_{abs}(\lambda)$ the change of the attenuation coefficient can be neglected. If the thickness of the sample is large the change in the absorbed intensity will be less compared to a thin sensor. Figure 4.10 shows the increase of the absorbed light intensity calculated with eq. 4.9, 4.13, 4.14, 4.15 with the fluence for different thickness of the sensors d. This increase corresponds to the increase of the initially deposited charge $Q_0(\Phi_{eq})$ which shows the necessity to consider the effect described here.

It should be noted that a simple piece of silicon was considered here. Usually, sensors have an aluminum contact at the back side which reflects about 90 % of the light compared to about 30 % for silicon, decreasing this effect by effectively increasing the sensor thickness in the calculation. Additionally, silicon sensors have oxide layers and possibly other layers on the surface which change $\hat{R}$ and $\hat{T}$ depending on the thickness of the layers and the wavelength.

According to Fan and Ramdas [96], the increase of the absorption coefficient in the NIR region can be described by a shift of the absorption edge of silicon towards lower energy. They note that the shift will saturate at around 0.1 eV for very high fluences $\Phi \approx 10^{19}\,\mathrm{cm}^{-2}$. Accordingly, the saturation can be neglected for the fluences investigated here. Additionally, they did investigate the annealing behavior of the increase of the absorption coefficient. They found no change of $\alpha(\lambda = 1.8\,\mu\mathrm{m})$ for annealing temperatures below 413 K which is much higher than the annealing temperatures used for silicon sensors. Therefore, the absorption coefficient is assumed to be independent of the annealing at moderate temperatures.

It should be noted that the refractive index of silicon is influenced by electric fields as shown in ref. [100]. However, it can be neglected as the change at $E =$

[7] Also the temperature has minor impact on the change of the absorbed light. If temperature is high so is $\alpha(T)$. A large fraction of the light will be absorbed in the sample anyway. But, for infrared light and the typical sensor thickness of several 100 µm this is only the case at temperatures well beyond usual applications (compare eq. 4.14, 4.15).

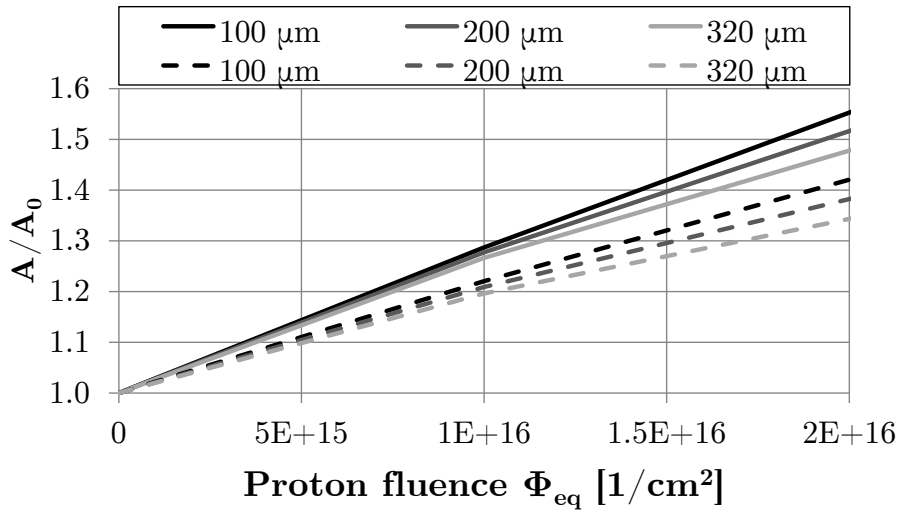

Figure 4.10.: Increase of the total absorbed light intensity $A(\Phi_{eq})$ relative to A_0 in non-irradiated silicon sensors for different thicknesses at 243 K. The dashed lines show $\lambda = 1052\,\text{nm}$ and the solid lines 1064 nm.

50 kV/cm for $\lambda = 1070\,\text{nm}$ is small with $\Delta n \approx 10^{-6}$. Also, free-carrier absorption is assumed to be small as the carrier concentration and the current for the edge-TCT measurements is usually $< 100\,\mu\text{m}$ (see sec. 5.4) and the results with and without a current agree. However, this might contribute to the voltage dependence shown in fig. 4.3.

Comparison of charge collection efficiency measurements with the diode TCT setup ($\lambda = 1064\,\text{nm}$) and measurements with a radioactive source emitting MIP-like electrons show no significant differences up to the maximum fluence $\Phi_{eq} = 9 \cdot 10^{14}\,\text{cm}^{-2}$ investigated in ref. [12] which agrees with the values of Φ_{abs} obtained here. However, charge collection measurements with 1060 nm light and MIPs of 75 µm thick sensors irradiated to $10^{16}\,\text{cm}^{-2}$ published in ref. [101] suggest a very similar charge collection efficiency for infrared light and MIPs while a difference of about 30 % would be expected if the mean number of free charge carriers created per MIP does not change.

5. Current, capacitance, and electric field

This chapter is devoted to the description and systematic comparison of current-voltage I/V and capacitance-voltage C/V characteristics of irradiated pad diodes with the information about the electric field obtained from edge-TCT measurements of strip sensors.

Strip sensors and diodes with initial n-type bulk with 285 µm thickness from the same production run have been investigated. The strip sensors and the diodes have been irradiated to the same fluences. Additionally, p-type and n-type diodes of 200 µm thickness have been investigated in order to determine the dependence on the thickness and to study possible differences between initially p-type and n-type bulk. It is found that all diodes have an effectively p-type bulk and the junction is at the n^+ implant after irradiation. The I/V and C/V behavior for initially n- and p-type is approximately the same; but, with opposite voltage sign. For the initially n-type bulk diodes the junction is on the back side with a doping structure p^+-p-n^+ after irradiation with high hadron fluences. For the p-type diodes the junction is on the front side with a structure n^+-p-p^+.

First, available literature on highly irradiated silicon will be discussed in sec. 5.1. Then, velocity profiles obtained from edge-TCT measurements will be presented in sec. 5.2, followed by a discussion of the current measurements under reverse bias in sec. 5.3 and forward bias in sec. 5.4. Empirical models are introduced to describe the I/V measurements. Additionally, C/V measurements are discussed shortly in sec. 5.5. The results are summarized in sec. 5.6. All results have been obtained at $T = 243\,\mathrm{K}$ unless otherwise stated. In this chapter α describes the current-related damage parameter as defined in eq. 2.43.

5.1. Introduction

In the literature, the I/V behavior of diodes with high defect concentrations has often been approached as treating the material as a „relaxation semiconductor" [102] (see sec. 2.1.3). For forward bias with one carrier injecting contact, also space-

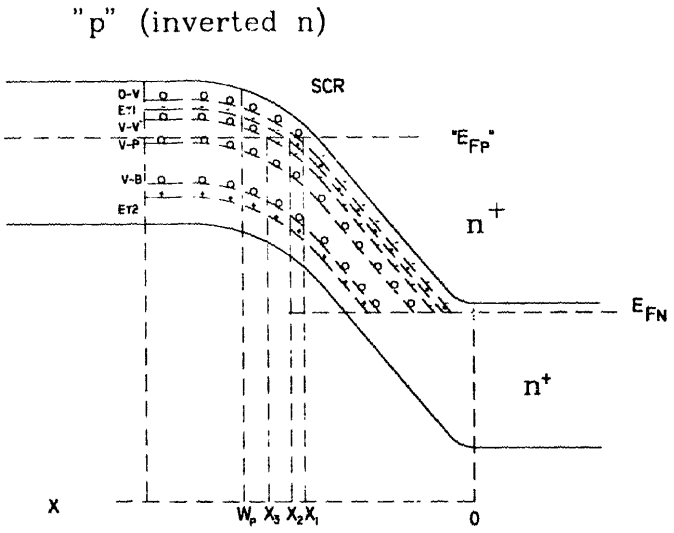

Figure 5.1.: Energy band diagram of a highly irradiated silicon diode with an applied voltage. The bulk (left) is type-inverted former n-type. Charge neutrality in the bulk is established by charged deep defects rather than free carriers. The Fermi energy E_{Fp} is near mid-gap and the carrier concentrations in the valence and conduction band are low and near the value of intrinsic silicon. From [110].

charge-limited currents *SCLC* (see sec. 2.1.4) have been used to describe I/V measurements, with similar outcome. Publications often consider semiconductors with intrinsically high defect concentrations, such as GaAs [26, 102, 103], CdS [30], and organic semiconductors [104]. But, also irradiated silicon has been studied [105, 106, 107, 108, 109].

In non-irradiated, non-depleted bulk silicon free majority carriers are abundant $n \vee p = N_{eff,0}$. Highly irradiated silicon has a high concentration of deep defects $N_t \gg N_{eff,0}$. The usually abundant free majority carriers in non-depleted bulk silicon will get trapped at these defects. Charge neutrality in highly irradiated, non-depleted silicon is the result of charged deep defects rather than free majority carriers as schematically shown in fig. 5.1 in the region „p" (inverted n). The Fermi energy is pinned at, or close to, the mid-gap position as shown in ref. [111]. The material has carrier concentrations close to the values of intrinsic silicon $n \approx p \approx n_i$ according to the Fermi-Dirac distribution function eq. 2.1 and the same concentration of positively and negatively charged defects; in other words, the net fixed space charge density is $N_{eff} \approx 0$. Consequently, the resistivity is very high and independent of the initial $N_{eff,0}$ before irradiation. This mechanism of majority carrier trapping and increasing resistivity is well-known as carrier removal [21, 112, 34] and was found to be largely independent of the material and initial impurity concentrations [62].

Shallow traps still play an important role as the same highly irradiated bulk silicon behaves like p-type material if a reverse bias voltage is applied. Reverse bias partially depletes the material of free carriers so the occupation of deep defects changes and shallow defects are no longer compensated by charged deep defects („SCR" in fig. 5.1). Consequently, there is a net space charge density $N_{eff} \neq 0$ in the depleted region. The free carrier concentrations n and p now depend on the generation rates, trapping, and the electric field. Therefore, in highly irradiated detectors the depletion region, or space-charge region *SCR,* denote the region where shallow defects are not compensated by charged deep defects and where the carrier concentrations are $n, p \leq n_i$.[1] Unfortunately, the picture becomes much more complex than in non-irradiated diodes since the occupation of defects is position-dependent and even overcompensation of shallow defects is possible (double junction, see ref. [54]).

The net space charge density N_{eff} in the SCR is related to the carrier density. Assuming a constant carrier generation rate throughout the SCR the generated electrons and holes will drift in opposite directions. At the electron collecting contact n will be high and p will be close to zero and vice versa at the hole collecting contact, assuming only generation current in the SCR. This means $n(x) \neq p(x)$, even if the mobilities of electrons and holes would be equal. Some of the free carriers will be trapped, introducing additional space charge so $N_{eff}(x) \neq const.$ Additionally, if carriers generated in the SCR drift into the usually neutral bulk, and carriers from the neutral bulk into the SCR, the transition region will have highly non-uniform space charge from the high N_{eff} of charged shallow defects to $N_{eff} \approx 0$ in the neutral bulk. Furthermore, there may be a second junction at the p^+-p transition. Both acceptor-like and donor-like shallow and deep defects are introduced by radiation damage. Holes diffusing from the p^+-implant, where $p \approx N_{eff}$, into the p-type bulk, where $p \approx n_i$, can get trapped at donor-like defects and may introduce positive space charge (overcompensation). This may lead to the so-called double junction. Concluding, the concept of depletion is not well-defined in highly irradiated sensors as $N_{eff}(x) \neq const.$

Borchi et al. [113] have shown in Hall measurements of the resistivity of silicon materials with different initial $N_{eff,0}$ that all materials become near intrinsic and p-type after sufficiently high fluence $\Phi_{eq} > 10^{13}\,\mathrm{cm}^{-2}$ and $g_{eff}\Phi_{eq} \gtrsim N_{eff,0}$ for high initial doping, with an effective introduction rate of deep defects $g_{eff} \sim \mathcal{O}(1\,\mathrm{cm}^{-1})$. Figure 5.2 shows the measured Hall resistivity of different structures with initial doping concentrations between $|N_{eff,0}| = (5 \cdot 10^{11} - 1.4 \cdot 10^{15})\,\mathrm{cm}^{-3}$ before and

[1] This is probably only true if no bias voltage is applied (see sec. 5.3.1).

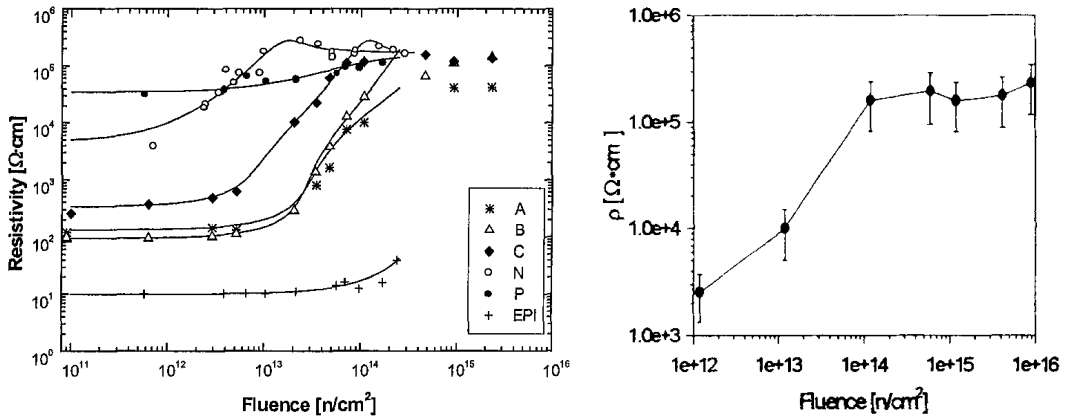

(a) (b)

Figure 5.2.: (a) Hall resistivity vs. neutron fluence of silicon samples with initial doping concentrations between $N_{eff} = 5 \cdot 10^{11}\,\mathrm{cm}^{-3} - 1.4 \cdot 10^{15}\,\mathrm{cm}^{-3}$ at 300 K from [113]. All samples were initially n-type bulk except for „P" and „EPI". (b) Shows results for initially n-type silicon up to a fluence of $10^{16}\,\mathrm{cm}^2$. From [114].

after irradiation with different fluences. For high fluences the resistivity approaches the expected value for intrinsic silicon $\rho_i \approx 3 \cdot 10^5\,\Omega\mathrm{cm}$ at 300 K. For the initially n-type samples the resistivity shows a maximum and then decreases slightly while the p-type does not show a maximum. This is an indication that the n-type reaches the intrinsic state at type inversion (see sec. 2.2) and then turns p-type. Also, it implies that $p > n$. However, the difference between p- and n-type seems to be rather small. Very similar results were obtained by introducing gold into doped silicon as discussed in ref. [20].

Additionally, the same results have been obtained in measurements and simulations of irradiated silicon with up to 6 defect levels in the simulation by Li [110] and in simulations by Lutz [115] assuming two energy levels $\pm 0.05\,\mathrm{eV}$ from mid-gap which pin the Fermi energy at mid-gap for high defect concentrations.

Figure 5.3(a) shows the absolute value of the current versus the absolute value of the voltage for a set of highly irradiated diodes and for forward and reverse bias voltage. It is apparent that this behavior is completely different from the ideal Shockley diode equation 2.34 shown in fig. 2.4. The results of the measurements for reverse and for forward bias will be discussed separately using the insight gained with the edge-TCT measurements.

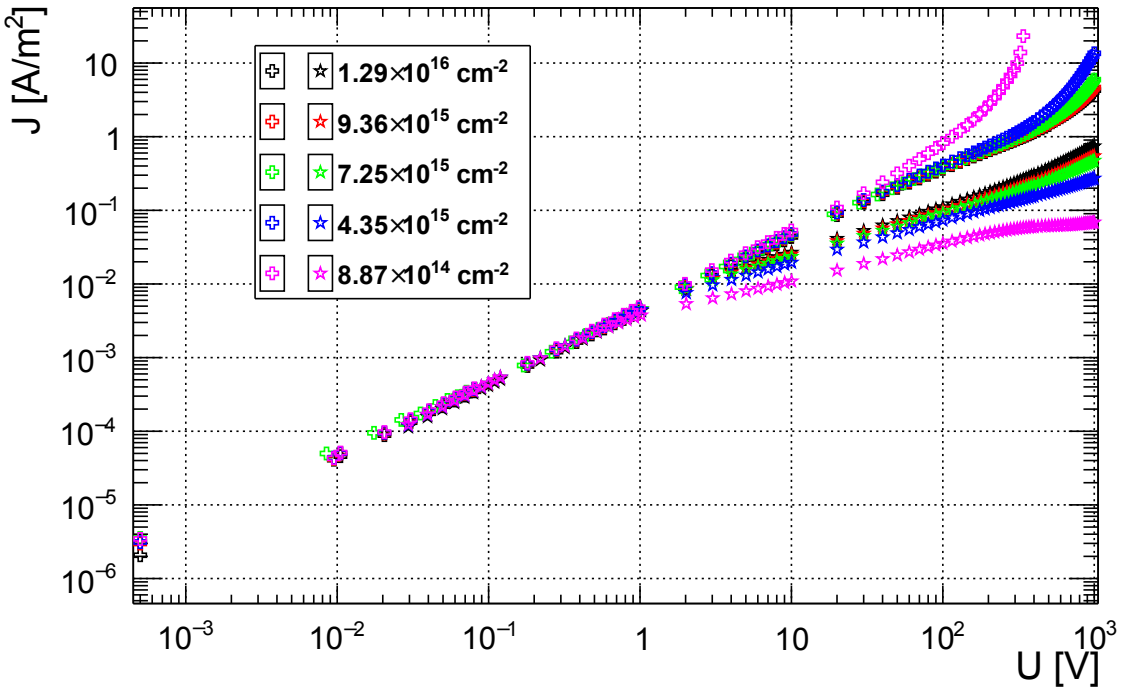

(a)

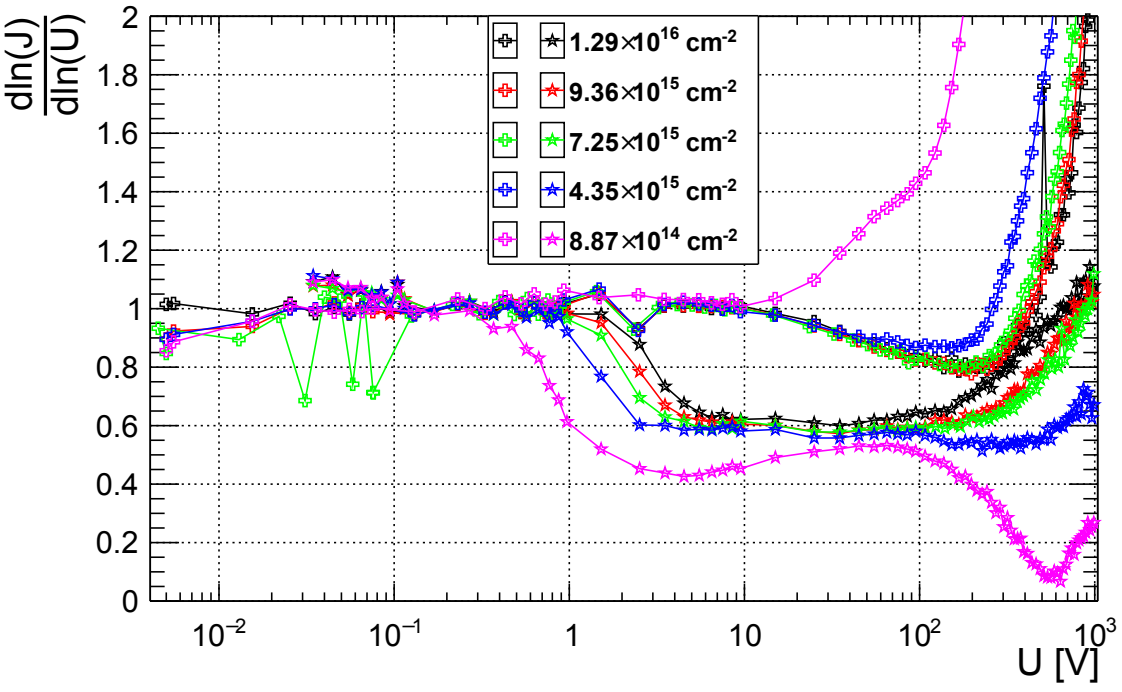

(b)

Figure 5.3.: Current density $|J|$ vs. $|U|$ (a) and $\frac{dln(|J|)}{dln(|U|)}$ vs. $|U|$ (b) of 285 µm thickness initially n-type diodes irradiated to different equivalent fluences at 243 K. The stars show reverse bias and the crosses forward bias.

5.2. Velocity profiles

Here, the velocity profiles of the irradiated strip sensors described in sec. 3.1.3 are discussed for forward and reverse bias in order to estimate the electric field distribution in the sensors. The velocity profiles are obtained with the prompt current method described in sec. 3.3.2. The electric field is not extracted as $v_{e,h}(E)$ is not well known for irradiated silicon (see sec. 7). At high fields the velocities saturate so $v_e(E)+v_h(E) \approx const$ and small uncertainties of the parameterizations lead to large uncertainties of the calculated E. Additionally, the trapping times are very short and may be in the order of the integration time of 200 ps.

Still, the velocity profiles are a valuable tool to get a rough idea about the electric field distribution in irradiated sensors. The ones shown here have been obtained for the second read-out strip (see sec. 3.3.2). The measurements were performed in steps of $\Delta x = 1\,\mu\text{m}$. Each point of the plots shown here is the average over $\pm 6\,\mu\text{m}$ in order to improve the readability.[2]

Figure 5.4 shows velocity profiles for the sensor irradiated to a fluence of $8.9 \cdot 10^{14}\,\text{cm}^{-2}$. The shape hardly depends on the temperature in the range 243 K and 253 K. The amplitude for 243 K is higher as the drift velocities are higher and the deposited charge Q_0 increases by about 45 % because of the larger absorption length (see eq. 4.1). If available, the measurements at 243 K will be discussed because of the higher amplitude of the velocity profiles and a lower heating power at lower sensor currents.

Under forward bias (−200 V) there is a low field at the p-n$^+$ junction of the sensor and the electric field is increasing towards the strips. The junction is at the back side of the sensor and not at the strips as the bulk material is type-inverted former n-type. It is very likely that the field at the junction is zero and the small peak near the junction is due to refraction of the light beam at the edge (see sec. 6.2.1).

Under reverse bias the sensor starts to deplete from the back side (200 V). But, there is a sizeable electric field in the bulk increasing towards a second peak near the strips. At high reverse bias (900 V) full depletion is observed like in a non-irradiated diode with a nearly linear velocity profile in the bulk.

Figure 5.5 and 5.6 show the absolute values of the velocity profiles for reverse and forward bias at all investigated fluences with the focus between the strips. Additionally, figure 5.7 shows the velocity profiles with the focus at the edge of one of the sensors for a better resolution near the contacts.

[2] Figure 3.14 shows velocity profiles without averaging.

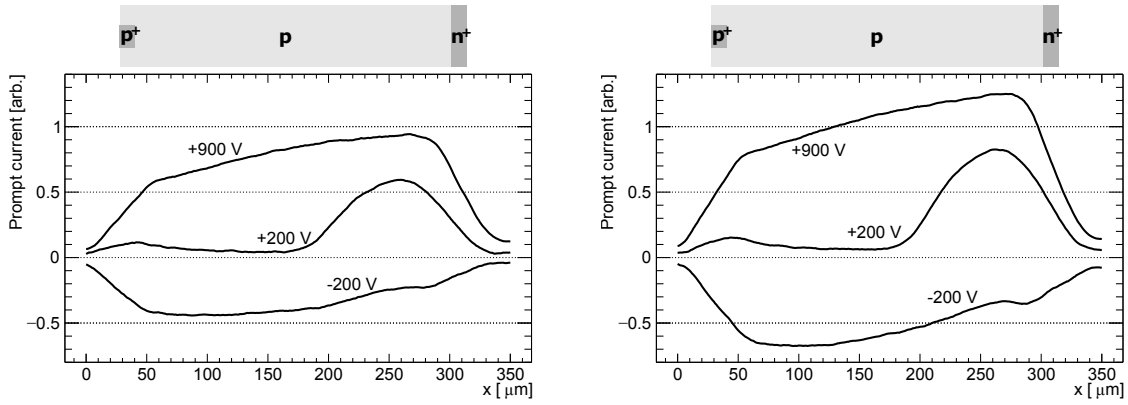

(a) 253 K (b) 243 K

Figure 5.4.: Velocity profiles of the strip sensor irradiated to $\Phi_{eq} = 8.9 \cdot 10^{14}\,\mathrm{cm}^{-2}$. The focus was between the strips. On top a schematic cross section of the sensor perpendicular to the strips is shown for illustration: The front side of the sensor with the p^+-doped strips is at $\sim 30\,\mu\mathrm{m}$ followed by the type-inverted former n-type, now p-type, bulk. The back side with the p-n^+ junction is at $\sim 320\,\mu\mathrm{m}$. Negative bias voltage corresponds to forward bias.

5.2.1. Reverse bias

For reverse bias a double peak structure can be observed at $\Phi_{eq} = 8.9 \cdot 10^{14}\,\mathrm{cm}^{-2}$ and $4.4 \cdot 10^{15}\,\mathrm{cm}^{-2}$ at low voltages (fig. 5.5(a), (c)). The peak at the front side ($x \approx 50\,\mu\mathrm{m}$) is much smaller than the peak at the junction. This is the so-called „double junction" (see ref. [54]). The double junction is not very pronounced compared to previous results for p-type bulk strip sensors (e.g. ref. [116]), probably because the sensors investigated here are not annealed (see ref. [92]).

The width of the high field depletion region at the junction (back side) is decreasing with increasing fluence since the effective doping concentration is increasing with the fluence (see eq. 2.25, 2.40). At the highest fluence (fig. 5.6(a)) the velocity profile is almost constant below 250 V. For higher voltages the depletion region with high field is observed growing from the junction. Since the diffusion length within the integration time of 200 ps is very low these measurements can be used to estimate the width of the depletion region w growing from the back side. As a simple approximation the velocity profiles are normalized to the maximum value and then the full width at half maximum $FWHM \approx w$ is determined. The results will be discussed in sec. 5.3.2, fig. 5.17.

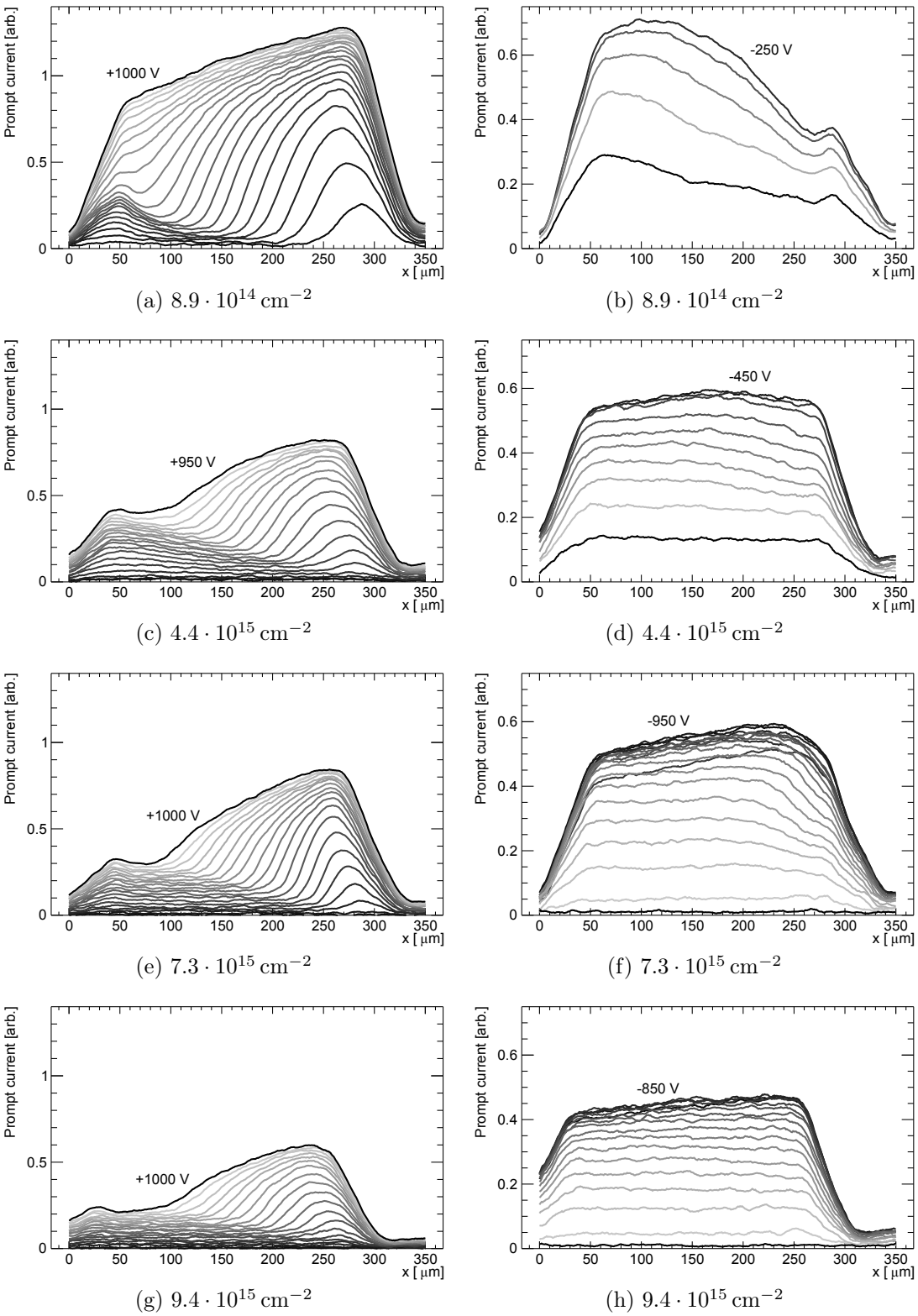

(a) $8.9 \cdot 10^{14}\,\mathrm{cm}^{-2}$ (b) $8.9 \cdot 10^{14}\,\mathrm{cm}^{-2}$

(c) $4.4 \cdot 10^{15}\,\mathrm{cm}^{-2}$ (d) $4.4 \cdot 10^{15}\,\mathrm{cm}^{-2}$

(e) $7.3 \cdot 10^{15}\,\mathrm{cm}^{-2}$ (f) $7.3 \cdot 10^{15}\,\mathrm{cm}^{-2}$

(g) $9.4 \cdot 10^{15}\,\mathrm{cm}^{-2}$ (h) $9.4 \cdot 10^{15}\,\mathrm{cm}^{-2}$

Figure 5.5.: Velocity profiles for reverse (left) and forward (right) bias of the sensors irradiated to Φ_{eq} given in the legend. The bias voltage was ramped from $\pm 50\,\mathrm{V}$ to the maximum voltage given in the figures in steps of $\Delta U = 50\,\mathrm{V}$. The focus was between the read-out strips. The data was obtained at 243 K except for (c) and (d) where $T = 253\,\mathrm{K}$.

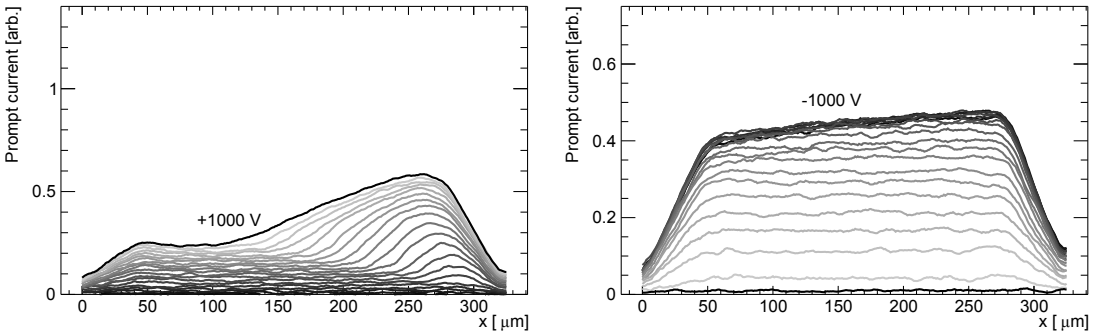

(a) $1.3 \cdot 10^{16}\,\mathrm{cm}^{-2}$ (b) $1.3 \cdot 10^{16}\,\mathrm{cm}^{-2}$

Figure 5.6.: Velocity profiles for reverse (a) and forward (b) bias with $\Delta U = 50\,\mathrm{V}$ at 243 K. The focus was between the strips.

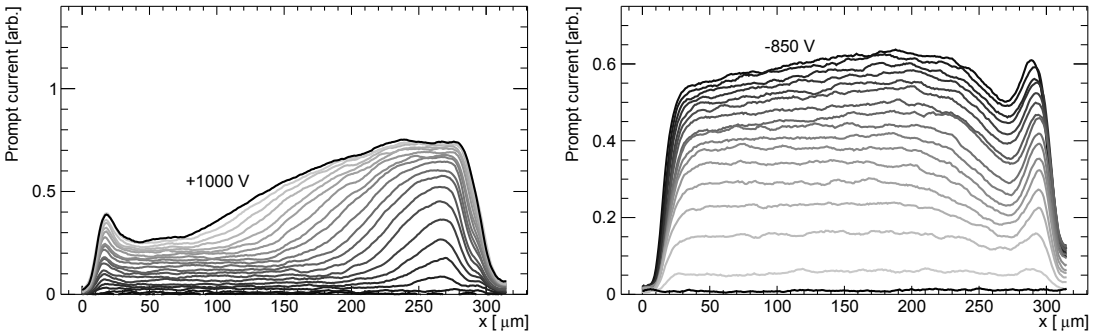

(a) $7.3 \cdot 10^{15}\,\mathrm{cm}^{-2}$ (b) $7.3 \cdot 10^{15}\,\mathrm{cm}^{-2}$

Figure 5.7.: Velocity profiles with the focus at the edge of the sensor for reverse (a) and forward (b) bias with $\Delta U = 50\,\mathrm{V}$ at 243 K (compare fig. 5.5(e), (f)).

5.2.2. Forward bias

As described above, the velocity profile for forward bias increases from a minimum at the back side junction towards the front side for the lowest fluence $8.9 \cdot 10^{14}\,\mathrm{cm}^{-2}$ (see fig. 5.5(b)). At $4.4 \cdot 10^{15}\,\mathrm{cm}^{-2}$ and $7.3 \cdot 10^{15}\,\mathrm{cm}^{-2}$ the minimum at the junction can hardly be observed in fig. 5.5(d) and fig. 5.5(f), respectively; but, the velocity profile is slightly decreasing towards the junction. However, the minimum can clearly be seen in the velocity profile of the sensor irradiated to $7.3 \cdot 10^{15}\,\mathrm{cm}^{-2}$ shown in fig. 5.7(b). For this measurement the focus of the light was at the edge of the sensor, improving the resolution near the edges.[3]

The velocity profile is almost constant with x in the bulk at low voltages. However, at high bias voltages and for $\Phi_{eq} > 4.4 \cdot 10^{15}\,\mathrm{cm}^{-2}$ the velocity profile shows a maximum near the junction followed by an approximately linear decrease towards the front side (fig. 5.5(f), (h), and fig. 5.6(b)). The slope seems to increase with the voltage; but, not very pronounced. The almost constant slope implies there is constant positive space charge in the bulk. If the absolute electric field could be determined the space charge density could be calculated.

Estimating from the slope of $v_e + v_h$ the space charge density is rather low. If a linear relation $v(E) \propto E$ is assumed the space charge concentration can be roughly estimated with eq. 2.27 and eq. 2.28 using the maximum of the velocity profile v_{max} (at $x \approx 275\,\mu\mathrm{m}$ in fig. 5.6(b)), the value near the front side v_{min} (at $x \approx 50\,\mu\mathrm{m}$), and U. For the sensor shown in fig. 5.6(b) one can estimate $v_{max} \approx 0.45\,\mathrm{arb.}$ and $v_{min} \approx 0.4\,\mathrm{arb.}$ at $U = 1000\,\mathrm{V}$. This leads to a space charge density of $N \sim U \cdot \frac{v_{max} - v_{min}}{v_{max} + v_{min}} \cdot \frac{\epsilon\epsilon_0}{ed^2} \approx 10^{12}\,\mathrm{cm}^{-3}$. Again, this is only a very rough estimate. The actual value of N should be larger since the change of E is underestimated by the assumption $v(E) \propto E$ which neglects velocity saturation. The reason for the slope is probably uniform filling of traps by space-charge-limited currents as discussed in chapter 5.4.

Additionally, constant or even decreasing absolute values of the velocity profiles can be observed at high voltages. This can also be observed at the lowest fluence between $-200\,\mathrm{V}$ and $-250\,\mathrm{V}$ (fig. 5.5(b)). Heating of the sensors may be the cause as discussed in sec. 3.3.2.

[3] The peak at the junction ($x \approx 50\,\mu\mathrm{m}$) is due to refraction of light into the bulk.

5.3. Reverse current

The slope $S = \frac{dln(I)}{dln(U)}$ for irradiated diodes gives an idea about different current regimes (see fig. 5.3(b)).[4] The reverse current $I(U)$ can be divided in three distinct regions. At low voltage $U < (1-3)$ V the current is ohmic $I(U) = U/R_{ohm}$ with $S = 1$. After a certain threshold voltage $U_{th}(\Phi_{eq})$, which increases with the fluence, the current increases with $S \sim 0.6$. At still higher voltage S decreases for the lowest fluence and then increases again. The voltage where S increases is lower for the higher fluences. The different regions will be discussed separately below.

5.3.1. Ohmic region

At low voltage $U \lesssim 1$ V the diode current behaves like the current for a piece of intrinsic silicon. The current can be described by Ohm's law. The resistance $R_{ohm} = \frac{dU}{dI}$ has been determined for low forward and reverse bias voltages between -0.1 V and $+0.1$ V for the 285 µm thick n-type diodes. For the 200 µm n- and p-type diodes it has been determined between -2 V and $+2$ V. The results of the resistivity $\rho_{ohm} = R_{ohm}A/d$ for all diodes are shown in fig. 5.8 (compare fig. 5.9(a)), with the diode thickness d and the pad area A. The large error bars observed for three measurements are due to the limited number of voltage steps for these measurements leading to fluctuations of $\frac{dU}{dI}$. Here, only estimates with simple assumptions are given. A more detailed discussion with a fit for a larger range of voltages will be given in section 5.3.2.

The ohmic resistivity $\rho_{ohm}(\Phi_{eq})$ is very close to the intrinsic value

$$\rho_i = \frac{1}{en_i\left(\mu_0^e + \mu_0^h\right)} \tag{5.1}$$

independent of the initial doping and thickness of the diodes, with $\mu_0^{e,h}$ the low-field mobilities. $\rho_{ohm}(\Phi_{eq})$ increases weakly with the fluence. The increase from the minimum fluence $8.9 \cdot 10^{14}\,\mathrm{cm}^{-2}$ to the maximum fluence $1.3 \cdot 10^{16}\,\mathrm{cm}^{-2}$ is about 9 %. The authors of ref. [114] found a similar increase of the resistivity with the fluence measured with Hall measurements at a different temperature.

The increase of the resistivity with fluence can be explained by a decrease of the low field mobility μ_0 with increasing defect concentration, similar to the one reported in ref. [117] for GaAs. The line in fig. 5.8 shows a fit of the data with the

[4] S is the exponent of the applied voltage $I(U) \propto U^S$ if $S(U) = const$ (compare fig. 5.3(a), (b)).

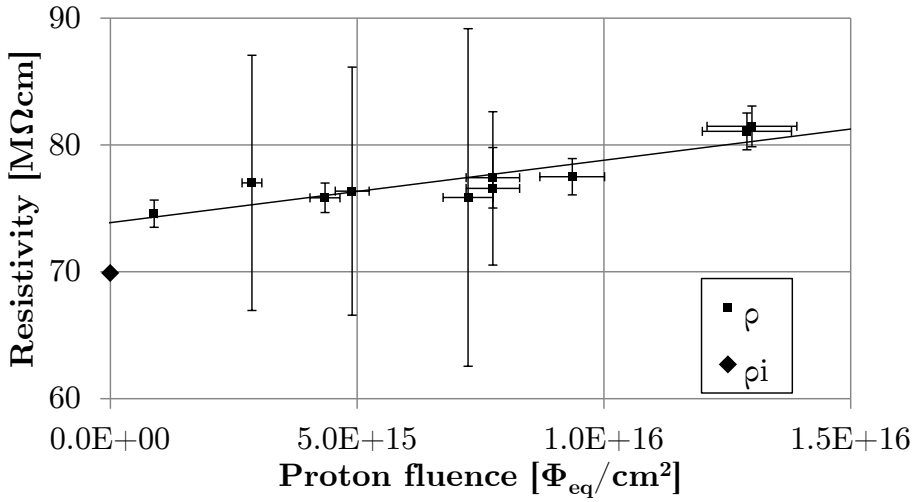

Figure 5.8.: Resistivity at low bias voltages $\rho_{ohm}(\Phi_{eq})$ determined for n- and p-diodes of different thicknesses as a function of the fluence at 243 K and the literature value $\rho_i(243\,\mathrm{K})$ for intrinsic silicon (diamond). The solid line shows a fit of the data.

empirical parameterization

$$\rho_{ohm}(\Phi_{eq}) = \rho_0 + \frac{\Phi_{eq}}{\beta_{ohm}}. \tag{5.2}$$

The fit yields $\rho_0 = 73.9\,\mathrm{M\Omega cm}$ and $\beta_{ohm} = 2.0 \cdot 10^{15}\,\mathrm{M\Omega^{-1}cm^{-3}}$. The fluence-dependence of the low field mobilities is roughly

$$\mu_0^e(\Phi_{eq}) + \mu_0^h(\Phi_{eq}) = \left(e n_i \rho_0 \left(1 + \frac{\Phi_{eq}}{\beta_{mob}} \right) \right)^{-1} \tag{5.3}$$

with the parameters $\beta_{mob} = \beta_{ohm} \cdot \rho_0 = 1.5 \cdot 10^{17}\,\mathrm{cm^{-2}}$ and ρ_0.

Now, $\rho_0 = 73.9\,\mathrm{M\Omega cm}$ from the fit is about 6 % higher than the intrinsic resistivity $\rho_i(243.15\,\mathrm{K}) = 69.9\,\mathrm{M\Omega cm}$ calculated with eq. 2.5, 5.1 and the low field mobility of sec. 7 or 63.8 MΩcm when the Jacoboni [118] low field mobility is used.

Strictly speaking, the mean current densities of electrons and holes leaving the diode should be equal $J_n = env_e = epv_p = J_p$ for generation current in order to conserve charge neutrality. Accordingly, the mean carrier concentrations for generation current should be $n = n_i\sqrt{\mu_h/\mu_e}$ and $p = n_i\sqrt{\mu_e/\mu_h}$ with $n\mu_e = p\mu_h$ and $np = n_i^2$. The assumption of $n \approx p \approx n_i$ is probably only valid if there is no electric field applied. However, this does not change the parameterizations presented here. Others [106, 119, 120] have used $n\mu_e = p\mu_h$ for the bulk so a

„maximum resistivity" is reached

$$\rho_{max}^{-1} = 2en_i\sqrt{\mu_e\mu_h} \tag{5.4}$$

for relaxation material. This yields $\rho_i = 78.3\,\mathrm{M\Omega cm}$ for the mobility of this work and $\rho_i = 76.5\,\mathrm{M\Omega cm}$ for the Jacoboni mobility, which is slightly closer to the extrapolated value ρ_0. However, the fluence dependence is not affected assuming the same decrease of the electron and hole mobilities $\sqrt{\mu_0^e\left(\Phi_{eq}\right)\mu_0^h\left(\Phi_{eq}\right)} = \sqrt{\mu_0^e\left(0\right)\mu_0^h\left(0\right)}\cdot\left(1+\frac{\Phi_{eq}}{\beta_{mob}}\right)^{-1}$.

The relation $n\mu_e = p\mu_h$ was previously used for the description of the space-charge region *SCR* instead of the bulk: Queisser, Casey, and van Roosbroeck [26] describe a dependence of R_{ohm} on an initial width w_0 of the SCR from the built-in voltage, the SCR having the maximum resistivity ρ_{max}. They argue w_0 does not change at low bias voltages until a threshold voltage is reached.[5] Accordingly, $R_{ohm} = \frac{w_0}{A}\rho_{max}$ would be independent of the thickness for relaxation material, neglecting the bulk resistance. However, the results of this work show that the diode resistance R_{ohm} at low bias voltages depends on the diode thickness (see fig. 5.9(a)). For highly irradiated silicon the ohmic resistance is clearly dominated by the non-depleted, near-intrinsic bulk and not influenced by a depletion region.

As a concluding remark it should be pointed out that the highly irradiated silicon shows some interesting behavior. An increase of the resistivity with fluence is observed even beyond that of intrinsic silicon, which is assumed to be caused by decreasing carrier mobilities with the fluence. Furthermore, the low voltage resistivity of highly irradiated silicon is independent of the initial bulk doping concentration and whether it was n- or p-type for initial $N_{eff} \lesssim 5\cdot10^{12}\,\mathrm{cm^{-3}}$ and $\Phi_{eq} \gtrsim 10^{15}\,\mathrm{cm^{-2}}$.

5.3.2. Depletion

For reverse voltages $1\,\mathrm{V} \lesssim U \lesssim 100\,\mathrm{V}$ the exponent is $S \sim 0.6$, similar to a growing depletion region for non-irradiated sensors. Naively, one would expect a finite depletion depth at zero bias from the built-in voltage and an immediate growth of the depletion region $w \propto \sqrt{U_{bi}+U}$ for an applied reverse voltage as in eq. 2.25. Assuming a certain high resistivity of the depletion region ρ_{SCR} and

[5] Modified from ref. [26]: At low reverse bias voltage the width of the SCR does not change because depletion is moderated by diffusion. The SCR starts to grow by Δw when U becomes comparable to the equilibrium contact potential $U_c = \ln\left(n_0/n_m\right)\cdot k_BT/q$ plus the voltage drop in the bulk, with $U_c = 0.1\,\mathrm{V}$ for GaAs, $n_m = n_i\sqrt{\mu_e/\mu_h}$ in the SCR, and n_0 in the n-type bulk. The increase of the resistance is now $\Delta R \propto \Delta w$ so $\Delta R \propto \sqrt{\Delta U}$ for an asymmetrical junction [121].

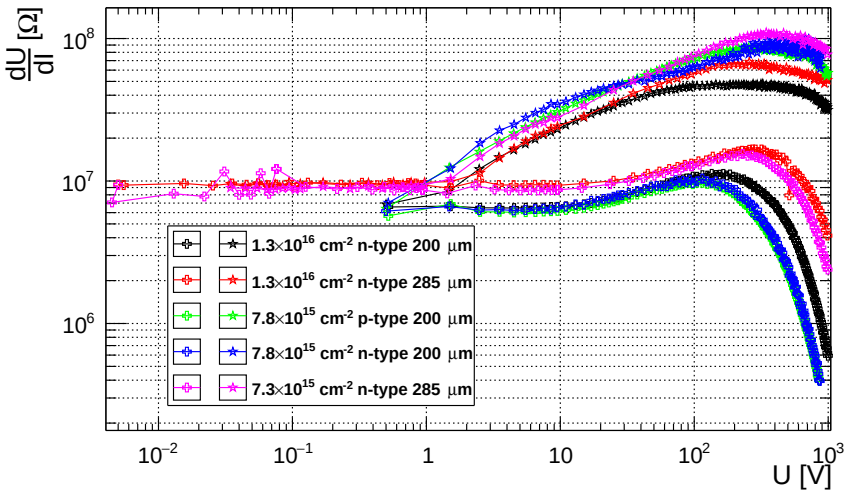

(a) $R = \frac{\mathrm{d}U}{\mathrm{d}I}$ vs. U

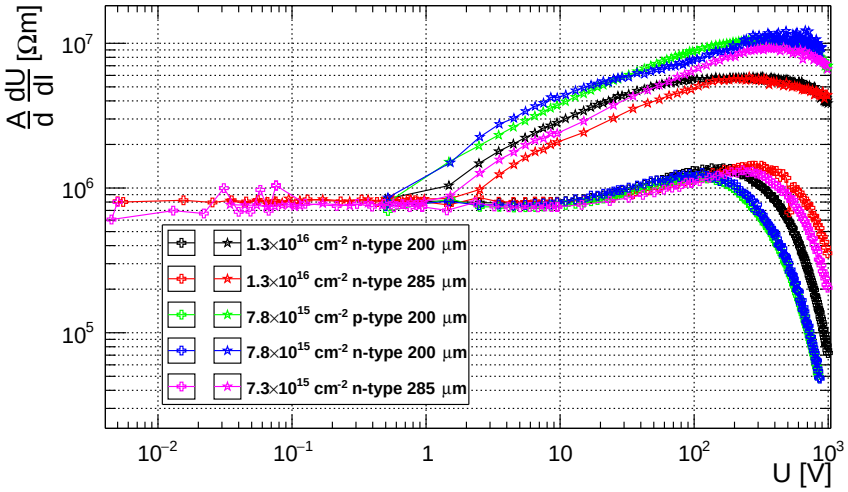

(b) $\rho = \frac{A}{d}\frac{\mathrm{d}U}{\mathrm{d}I}$ vs. U

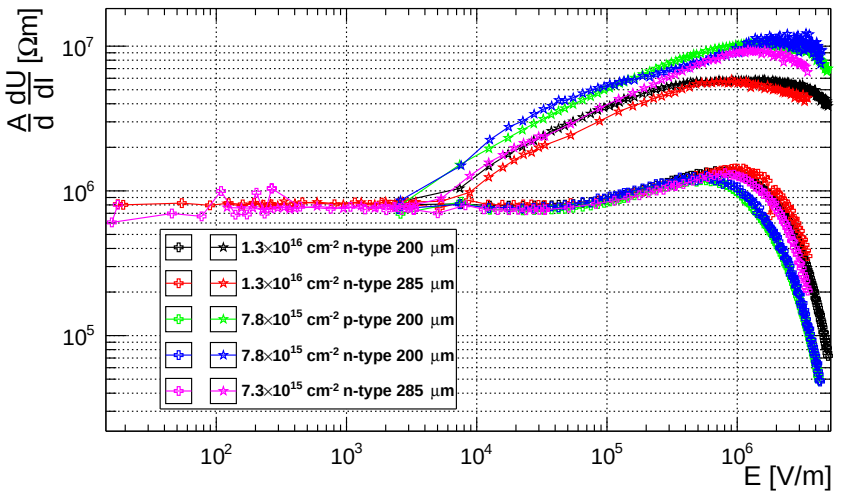

(c) $\rho = \frac{A}{d}\frac{\mathrm{d}U}{\mathrm{d}I}$ vs. E

Figure 5.9.: Differential values of the current measurements for forward (stars) and reverse bias (crosses) at 243 K. Diodes of $d = 200\,\mu\mathrm{m}$ and $285\,\mu\mathrm{m}$ irradiated to $\Phi_{eq} = 1.3 \cdot 10^{16}\,\mathrm{cm}^{-2}$ and $\sim 7.6 \cdot 10^{15}\,\mathrm{cm}^{-2}$ are compared.

very low resistivity in non-depleted bulk $\rho_{ohm} \approx 0$ one would expect the resistance $R(w) = \rho_{SCR} \cdot \frac{w}{A} \propto \sqrt{U_{bi} + U}$ and the current $I = \frac{U}{R(w)} \propto \sqrt{U}$, neglecting the built-in voltage. However, the ohmic current discussed above is observed at low reverse voltage. After a threshold voltage U_{th} the exponent S of the voltage $I \propto U^S$ is usually $S \geq 0.5$ as seen in fig. 5.3(b). S also increases with fluence. This implies that the resistance $R \propto U^{1-S}$ increases slower than the expectation $R \propto \sqrt{U}$.

The threshold voltage depends on the thickness of the diode and increases with fluence as can be seen in fig. 5.9(a). The resistance R for $U > U_{th}$ reaches approximately the same values for the diodes of different thickness irradiated to the same fluence.

Parameterization Here an empirical model to describe the reverse current will be discussed. One approach to describe the current is to approximate the contributions of the bulk and of the depletion region by $R = \rho_{ohm} \cdot \frac{d-w}{A} + \rho_{SCR} \cdot \frac{w}{A} = R_{ohm} + \frac{w}{A} \cdot (\rho_{SCR} - \rho_{ohm})$ with $\rho_{SCR} \gg \rho_{ohm}$. The width of the depletion region $w(U)$ starts to increase once the voltage drop over the bulk is $IR_{ohm} = I\rho_{SCR}\frac{w(U)}{A} \equiv I\widetilde{R}_{SCR} \cdot U^{1-S}$ with an effective resistance of the depletion region $\widetilde{R}_{SCR}(\Phi_{eq}, A)$ and an effective, unitless „width" of the depletion region U^{1-S}. The threshold voltage is now

$$U_{th}(d, \Phi_{eq})\,[\mathrm{V}] = \left(\frac{R_{ohm}}{\widetilde{R}_{SCR}}\right)^{\frac{1}{1-S}} = \left(\frac{\rho_{ohm}(\Phi_{eq}) \cdot \frac{d}{A}}{\widetilde{R}_{SCR}(\Phi_{eq}, A)}\right)^{\frac{1}{1-S(\Phi_{eq})}}. \tag{5.5}$$

It depends on the thickness of the diode and increases with fluence as can be seen e.g. in fig. 5.9(a).

The resistance can now be parameterized as

$$R(U) = \begin{cases} \rho_{ohm}(\Phi_{eq}) \cdot \frac{d}{A} & U \leq U_{th} \\ \widetilde{R}_{SCR}(\Phi_{eq}, A) \cdot U^{1-S(\Phi_{eq})} & U \geq U_{th} \end{cases}. \tag{5.6}$$

The fit of eq. 5.6 was performed for all investigated diodes from 5 V forward to 50 V reverse bias voltage as shown in figure 5.10. The model and the data agree within a few percent except at $U \approx 0$ V and under forward bias. The deviation around $U = 0$ is probably because of a voltage offset from the voltage source, which was operated at the minimum voltage step size of $\Delta U = 50$ mV. The deviation under forward bias may be due to the fact that the electric field dependence of the mobility $\mu(E)$ was neglected here.

The parameters extracted from the fit are shown in fig. 5.11. The results of $\rho_{ohm}(\Phi_{eq})$ are very similar for the initially n-type and p-type diodes (fig. 5.11(a)).

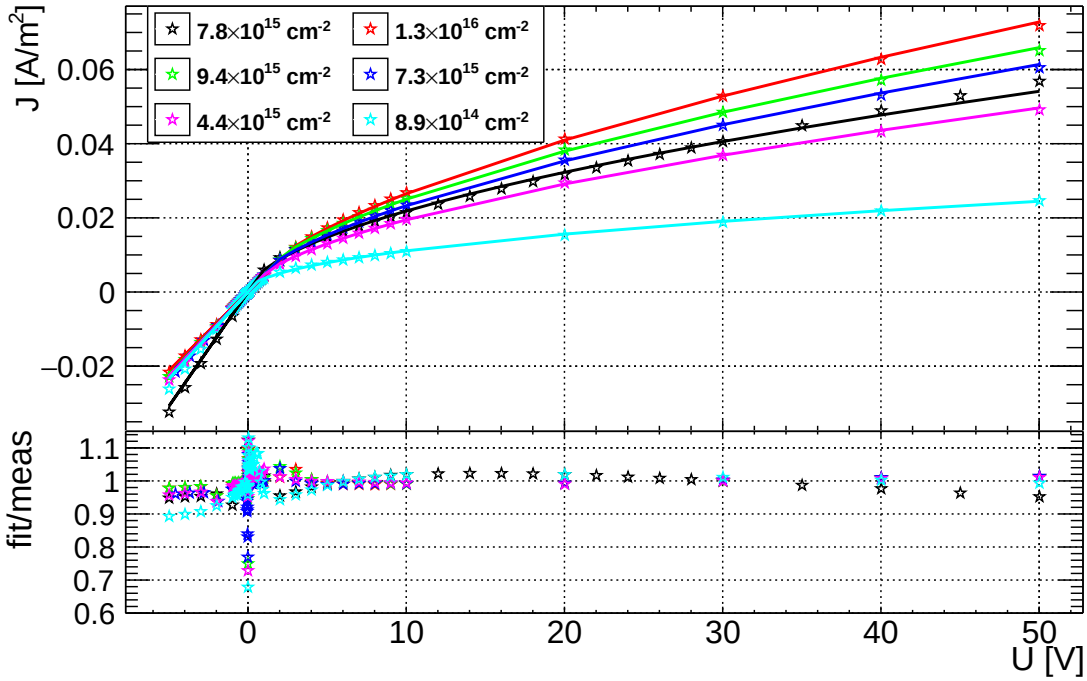

(a) n-type

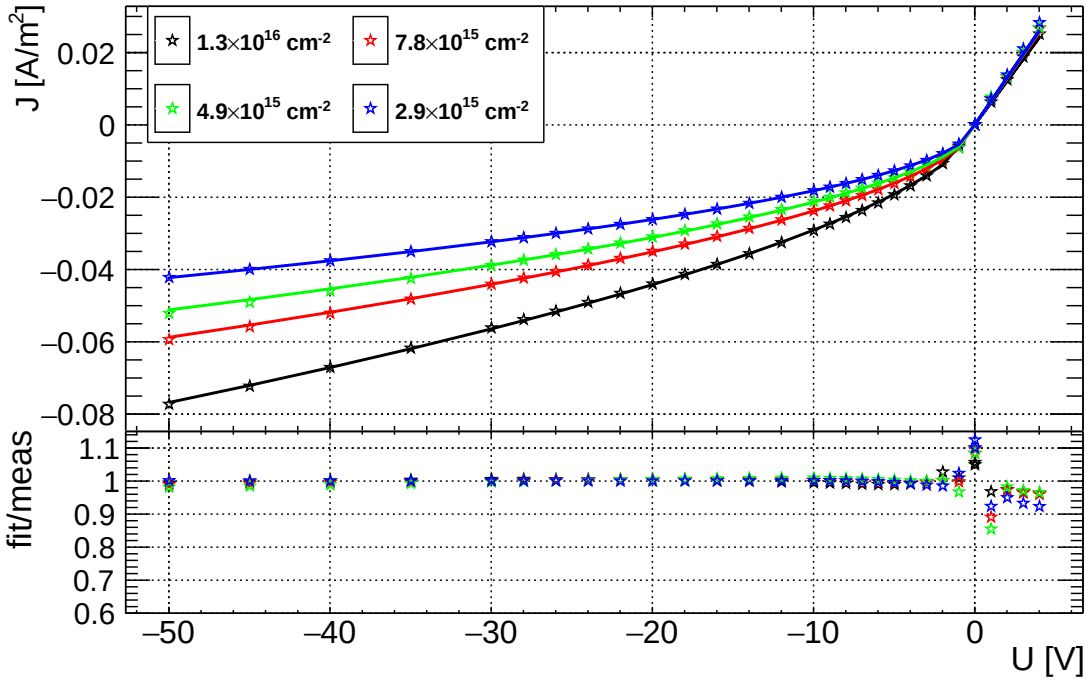

(b) p-type

Figure 5.10.: Current measurements (stars) and the fit of eq. 5.6 (lines) to the data for the diodes irradiated to the fluences given in the figures between ±5 V forward and ±50 V reverse bias at 243 K. The residuals are shown below. (a) Shows the 285 µm n-type diodes and the 200 µm n-type diode (black, $7.8 \cdot 10^{15}\,\mathrm{cm}^{-2}$). (b) Shows the 285 µm p-type diodes.

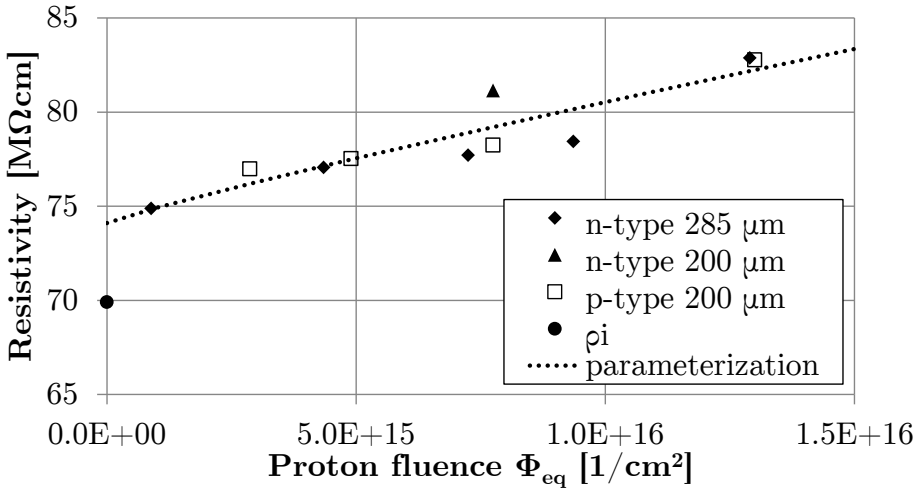

(a)

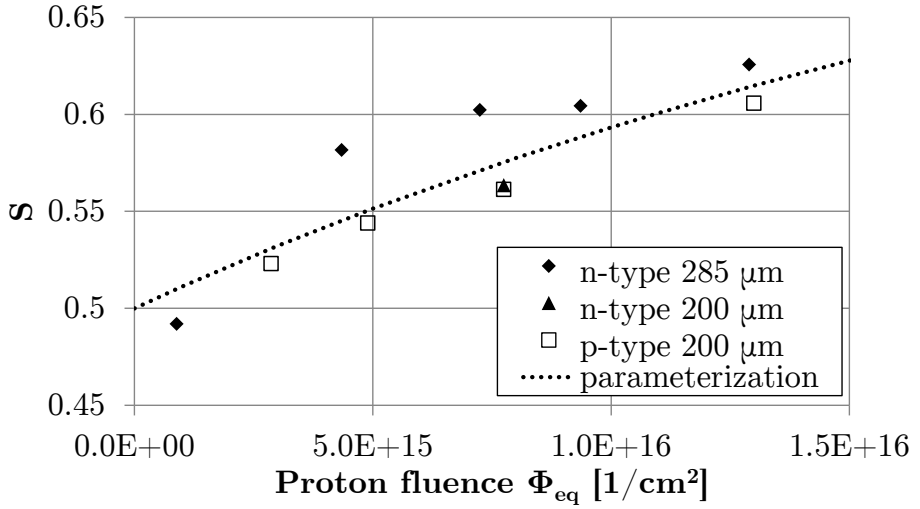

(b)

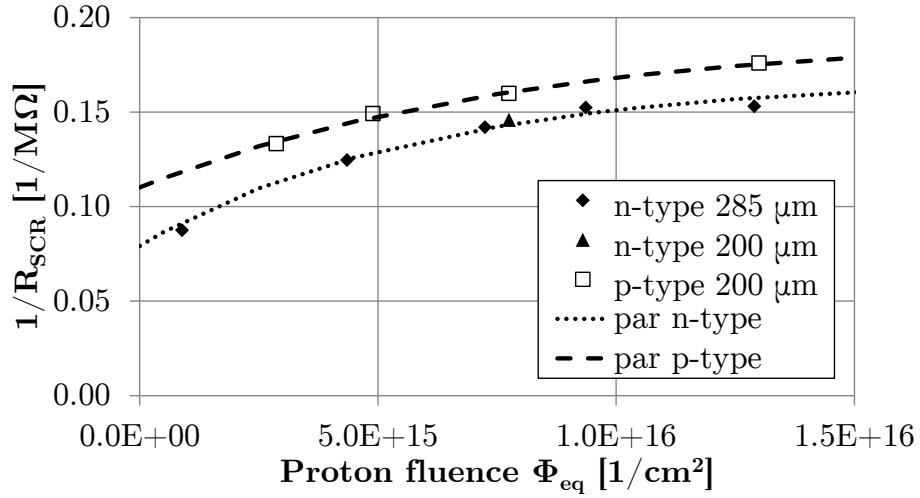

(c)

Figure 5.11.: Parameters obtained from the fit from 5 V forward to 50 V reverse bias using eq. 5.6, 5.8, and eq. 5.11 of diodes of different thickness at 243 K. The parameterizations (lines) are eq. 5.9 in (a), eq. 5.11 in (b), and eq. 5.12 in (c).

However, the p-type diodes seem to have a slightly lower $\widetilde{R}_{SCR}(\Phi_{eq}, A)$ (fig. 5.11(c)) and there is a trend towards lower $S(\Phi_{eq})$ values compared to the initially n-type diodes (fig. 5.11(b)).

Fluence dependence of the low-field mobility A more accurate description of $\rho_{ohm}(\Phi_{eq})$ and $\mu(\Phi_{eq})$ compared to assuming $\rho_{ohm} \propto \Phi_{eq}$ like in sec. 5.3.1 may be to assume the mobility dependence on the fluence is similar to the dependence on ionized-impurity scattering, which is often [122, 123, 124] parameterized as

$$\mu(N) = \mu_{min} + \frac{\mu_{max} - \mu_{min}}{1 + \left(\frac{N}{N_{ref}}\right)^{\varsigma}} \tag{5.7}$$

with the concentration of ionized impurities $N < 10^{20}\,\mathrm{cm}^{-3}$, a reference concentration $N_{ref} \approx 1 \cdot 10^{17}\,\mathrm{cm}^{-3}$ for phosphorus and boron, the lattice scattering mobility $\mu_{max} = \mu_0$ and the limit μ_{min} for high N, and the exponent $\varsigma \approx 0.9$ for electrons and holes between 200 K and 300 K according to ref. [122, 124].

If only the beginning of the mobility decrease is considered for moderate $N \lesssim N_{ref}$ ionized impurity concentrations $\mu_{min,e} + \mu_{min,h} \approx 140\,\mathrm{cm}^2/\mathrm{Vs}$ (ref. [122] at 300 K) can be neglected as the mobility saturates at μ_{min} at ionized impurity concentrations $N > 10^{19}\,\mathrm{cm}^{-3}$.[6] Assuming a constant effective introduction rate g_{eff} of ionized impurities with irradiation $N = g_{eff} \cdot \Phi_{eq}$ and the same fluence dependence for the electron mobility and the hole mobility one can rewrite eq. 5.7 so

$$\mu_0^e(\Phi_{eq}) + \mu_0^h(\Phi_{eq}) \approx \frac{\mu_0^e + \mu_0^h}{1 + \left(\frac{\Phi_{eq}}{\beta_{mob}}\right)^{\varsigma}} \tag{5.8}$$

where the parameter $\beta_{mob} = N_{ref}/g_{eff}$ can be compared to the N_{ref} for ionized-impurity scattering to estimate g_{eff}.

Figure 5.12 shows ρ_{ohm} versus $(\Phi_{eq})^{\varsigma}$ for the determination $(\beta_{mob})^{\varsigma}$ with $\varsigma = 0.9$. The fit yields

$$\rho_{ohm}(\Phi_{eq}) = 74.1\,\mathrm{M\Omega cm} \cdot \left(1 + \left(\frac{\Phi_{eq}}{\beta_{mob}}\right)^{0.9}\right) \tag{5.9}$$

with $\beta_{mob} = 1.52 \cdot 10^{17}\,\mathrm{cm}^{-2}$. This is approximately the same result compared to $\rho_{ohm} \propto \Phi_{eq}$ (which translates to $\varsigma = 1$) as discussed in sec. 5.3.1.

The sum of the mobilities extrapolated up to fluences of $10^{17}\,\mathrm{cm}^{-2}$ is shown in fig. 5.13. These high fluences will become relevant for a possible future hadron collider. However, few measurements at these high fluences are available. Fig-

[6] The authors of ref. [125] report a very similar electron mobility of $100\,\mathrm{cm}^2/\mathrm{Vs}$ after $6.4 \cdot 10^{19}\,\mathrm{cm}^{-3}$ neutron irradiation.

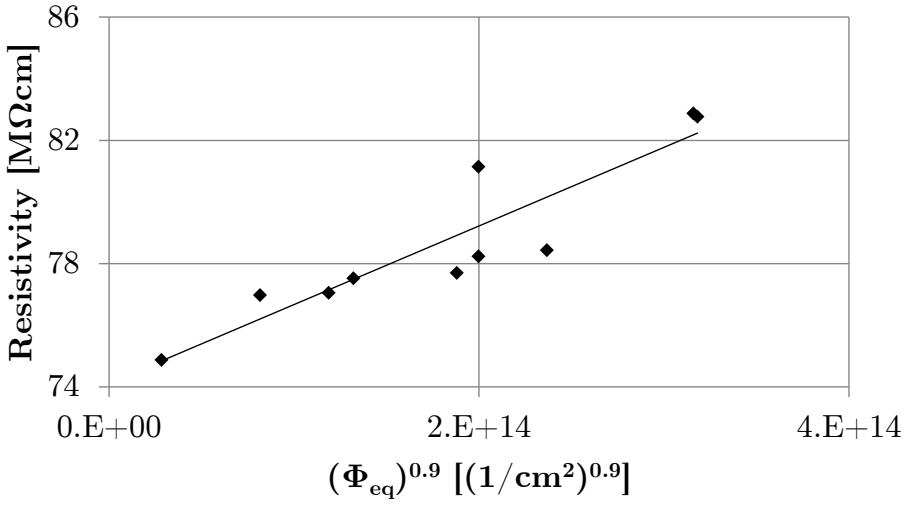

Figure 5.12.: Resistivity at low bias voltage $\rho_{ohm}(\Phi_{eq})$ determined for n- and p-diodes of different thickness as a function of the fluence at 243 K versus $(\Phi_{eq})^{0.9}$. The solid line shows a fit to the data.

ure 5.14 shows the resistivity of diodes irradiated up to $10^{17}\,\mathrm{cm}^{-2}$ at room temperature extracted from ref. [126]. At room temperature the change is only $\rho\left(\Phi_{eq} = 10^{17}\,\mathrm{cm}^{-2}\right)/\rho\left(\Phi_{eq} = 10^{16}\,\mathrm{cm}^{-2}\right) \approx 1.06$ while a change of 1.55 is expected at 243 K from β_{mob}. The mobility is the inverse sum (Matthiessen's rule) of different scattering processes. The relevant ones here are ionized-impurity scattering, which decreases with T, and lattice (phonon) scattering which increases with T. Lattice scattering is assumed not to change with the fluence and seems to dominate the mobility at room temperature for these fluences. The radiation-induced decrease of the carrier mobility is much more pronounced at low temperatures.

The β_{mob} is similar to $N_{ref} \approx (0.5 - 2.4) \cdot 10^{17}\,\mathrm{cm}^{-3}$ for phosphorus and boron doping assuming an effective introduction rate of all ionized defects combined $g_{eff} \approx 1\,\mathrm{cm}^{-1}$. The value is similar to individual introduction rates $\sim 0.01\,\mathrm{cm}^{-1} - 1\,\mathrm{cm}^{-1}$ of various defect levels measured at low fluence given in tab. 2.1. This is an interesting result as the the concentration of ionized defects in the neutral „intrinsic" bulk material can roughly be estimated.

The results qualitatively agree with ref. [127] where no significant change of μ was found up to $\Phi_{eq} = 2.4 \cdot 10^{14}\,\mathrm{cm}^{-2}$. The authors of ref. [128] found a strong decrease $> 10\,\%$ of μ already at low fluences around $5 \cdot 10^{13}\,\mathrm{cm}^{-2}$ which has not been reproduced since. A fast reduction of the mobilities was reported in ref. [129] at 253 K of about 50 % at $\Phi_{eq} = 10^{16}\,\mathrm{cm}^{-2}$ and 85 % at $\Phi_{eq} = 10^{17}\,\mathrm{cm}^{-2}$ with a value of $\beta_{mob} = (6 - 10) \cdot 10^{15}\,\mathrm{cm}^{-2}$ which would correspond to a cumulative introduction rate of ionized defects $g \gtrsim 10\,\mathrm{cm}^{-1}$.

It should be noted that bandgap narrowing has to be taken into account for defect concentrations beyond $10^{17}\,\mathrm{cm}^{-3}$ as shown in ref. [124]. Also, the scattering

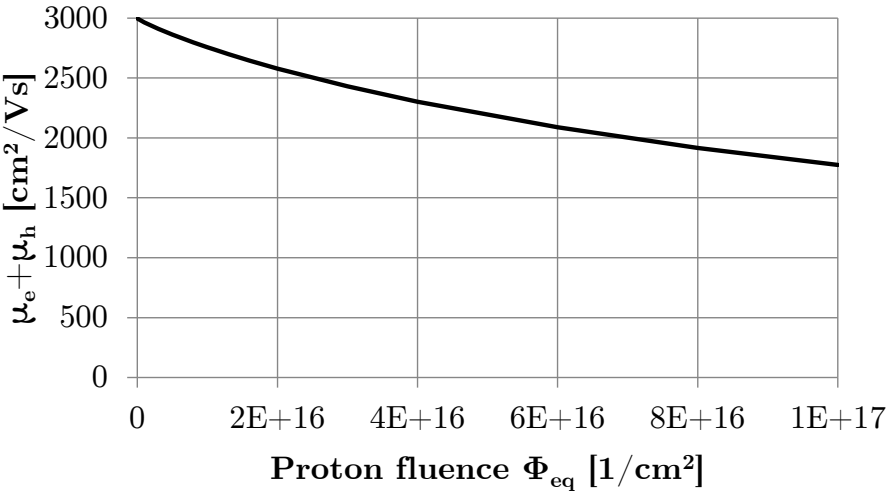

Figure 5.13.: Parameterization of the sum of the low-field mobilities. Obtained from the fit from 5 V forward bias to 50 V reverse bias using eq. 5.8 with $\beta_{mob} = 1.52 \cdot 10^{17}\,\mathrm{cm}^{-2}$ at 243 K.

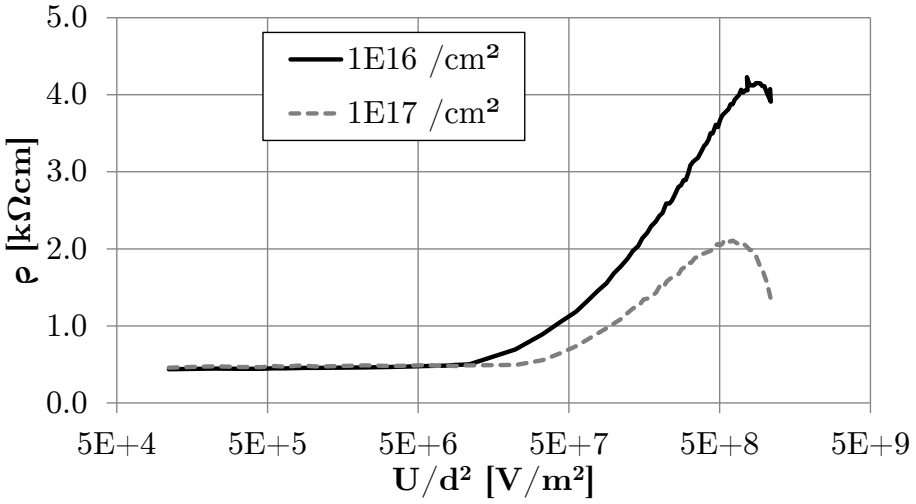

Figure 5.14.: Resistivity of diodes irradiated to $\Phi_{eq} = 10^{16}\,\mathrm{cm}^{-2}$ and $10^{17}\,\mathrm{cm}^{-2}$ for reverse bias at 302 K. The data was extracted from current measurements of Moloi et al. [126].

mechanisms at defect clusters and other defects may be different from ionized-impurity scattering (see ref. [45, 130, 125]).

The threshold voltage The threshold voltage U_{th} calculated from the fit results with eq. 5.5 is shown in fig. 5.15. The dependence of U_{th} on Φ_{eq} is different for the diodes of different thickness as shown in fig. 5.15(a). It was expected that the cross section of the straight line fit with the y-axis at zero fluence coincides approximately with the built-in voltage U_{bi}. The width of the depletion region is assumed $w \propto \sqrt{U_{bi} + U - IR_{ohm}}$. Therefore, the width of the depletion region does not change much for $U \ll U_{bi}$ even if $R_{ohm}(\Phi_{eq})$ is small. However, $\frac{U_{th}}{d^2}$ versus Φ_{eq} has a similar dependence for the n-type diodes of different thickness and it is only slightly different for p- and n-type diodes as shown in figure fig. 5.15(b). The fit results can be described by

$$\frac{U_{th}}{d^2}(\Phi_{eq}) = \frac{U_{th}}{d^2}(0) \cdot \left(1 + \frac{\Phi_{eq}}{\beta_{Uth}}\right) \tag{5.10}$$

with $\frac{U_{th}}{d^2}(0) = 1.1 \cdot 10^7\,\mathrm{V/m^2}$ and $\beta_{Uth} = 5.3 \cdot 10^{15}\,\mathrm{cm^{-2}}$ for the p-type diodes and $\frac{U_{th}}{d^2}(0) = 5.8 \cdot 10^6\,\mathrm{V/m^2}$ and $\beta_{Uth} = 2.5 \cdot 10^{15}\,\mathrm{cm^{-2}}$ for the n-type diodes. This leads to $\frac{U_{th}}{d^2}(0) \cdot d^2 = 0.48\,\mathrm{V}$ for the p-type diodes, $\frac{U_{th}}{d^2}(0) \cdot d^2 = 0.47\,\mathrm{V}$ for the 285 µm n-type diodes, and $\frac{U_{th}}{d^2}(0) \cdot d^2 = 0.23\,\mathrm{V}$ for the 200 µm n-type diode.

The exponent Assuming limiting cases of $S(\Phi_{eq} = 0) = 0.5$ and $S(\Phi_{eq} \to \infty) = 1$ when $\rho_{SCR} = \rho_{ohm}$ the parameterization

$$S(\Phi_{eq}) = 1 - \frac{0.5}{1 + \frac{\Phi_{eq}}{\beta_S}} \tag{5.11}$$

can be used with $\beta_S = 4.36 \cdot 10^{16}\ \mathrm{cm^{-2}}$ at $T = 243\,\mathrm{K}$, excluding the diode irradiated to the lowest fluence where $S < 0.5$. Figure 5.11(b) shows the fit of the parameterization to the data. The values of S are slightly larger for the 285 µm thick diodes and smaller for the 200 µm thick diodes - also for the 200 µm n-type diode. This is an indication that this parameter may reflect the voltage drop in the neutral bulk IR_{ohm} as S appears to depend not only on the fluence but also on the thickness.

Additionally, the parameter S decreases with increasing temperature as shown in fig. 5.16(a). This is most probably because the bulk resistivity decreases with $1/n_i(T)$, and so does the voltage drop in the bulk region. The exponent S comes closer to 0.5 with increasing temperature.

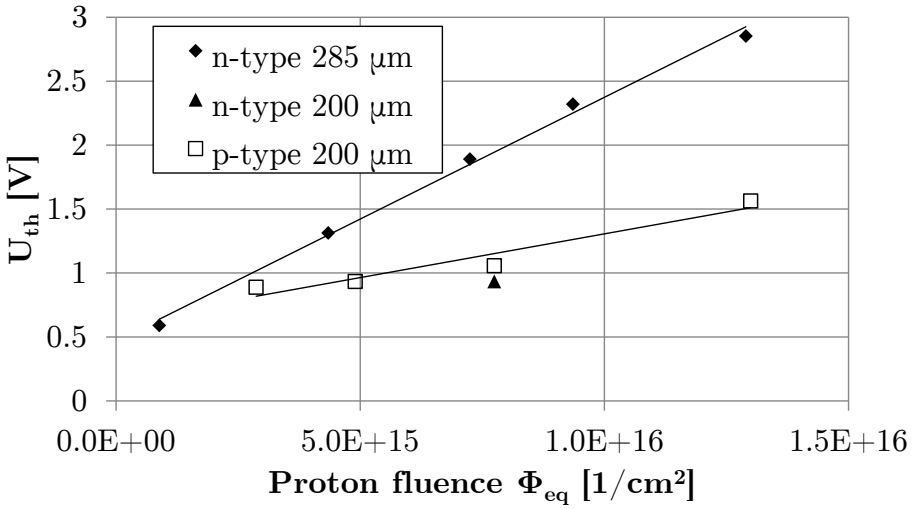

(a)

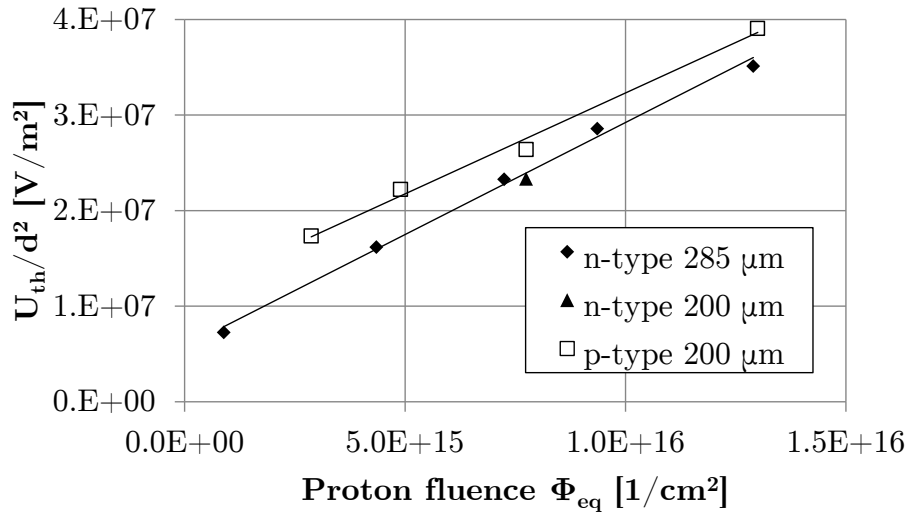

(b)

Figure 5.15.: Threshold voltages U_{th} (a) calculated using eq. 5.5 with the fit results from 5 V forward bias to 50 V reverse bias at 243 K. (b) Shows $\frac{U_{th}}{d^2}$ with linear fits for p- and n-type (lines).

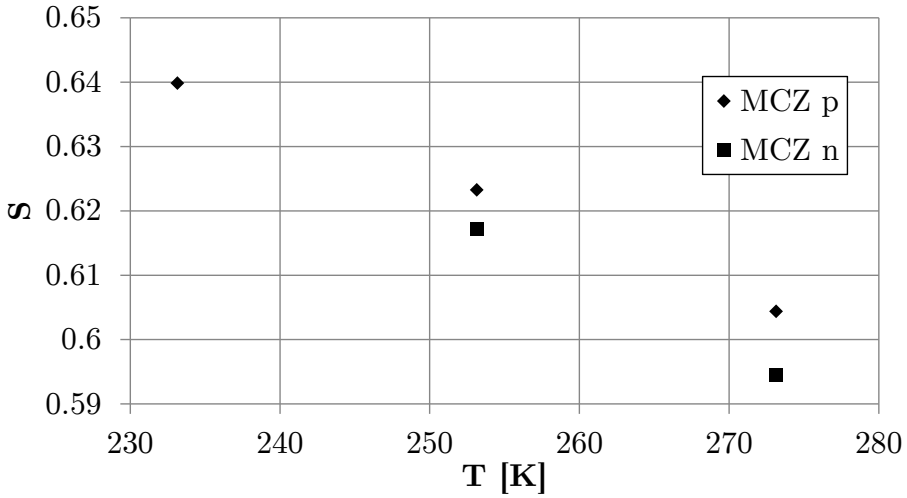

(a)

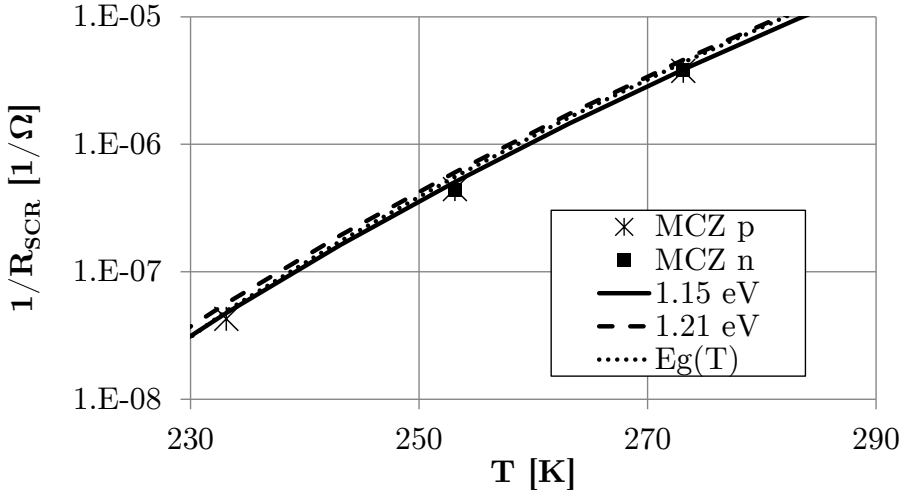

(b)

Figure 5.16.: Temperature dependence of the parameters obtained from the fit from 10 V to 100 V reverse bias using $R(U) = \widetilde{R}_{SCR} \cdot U^{1-S}$ (see eq. 5.6) of 200 µm magnetic Czochralski p- and n-type diodes irradiated to $\Phi_{eq} = 1.3 \cdot 10^{16}\,\mathrm{cm}^{-2}$. (a) Shows the exponent S and (b) the parameter $1/\widetilde{R}_{SCR}$ and its parameterization with eq. 5.14 using $E_{eff} = 1.15\,\mathrm{eV}$ (solid), $E_{eff} = 1.21\,\mathrm{eV}$ (dashed), and $E_g(T)$ of eq. 2.6 (dotted).

The space-charge region The parameter $\widetilde{R}_{SCR}\left(\Phi_{eq}, A\right)^{-1}$ is rather unpractical as a fit parameter. It seems to depend on the effective doping and not only on the generation current, since it is different for n-type and p-type as seen in fig. 5.11(c). Ideally, a parameter should be used which scales linearly with the fluence and is proportional to the volume generation rate $1/\tau$ (and α). The parameter $\frac{U_{th}}{d^2}\left(\Phi_{eq}\right) \propto \Phi_{eq}$ should rather be used as a fit parameter instead of $\widetilde{R}_{SCR}$ (see fig. 5.15(b)). However, $\widetilde{R}_{SCR}\left(\Phi_{eq}\right)$ can be calculated with eq. 5.5 using $\rho_{ohm}\left(\Phi_{eq}\right)$ of eq. 5.9, $\frac{U_{th}}{d^2}\left(\Phi_{eq}\right)$ of eq. 5.10, and $S\left(\Phi_{eq}\right)$ of eq. 5.11 so

$$\widetilde{R}_{SCR}\left(\Phi_{eq}\right)^{-1} = \frac{A\left(d^2 \cdot \frac{U_{th}}{d^2}\left(\Phi_{eq}\right)\right)^{1-S(\Phi_{eq})}}{d \cdot \rho_{ohm}\left(\Phi_{eq}\right)} \tag{5.12}$$

as shown in fig. 5.11(c). Of course, also $\widetilde{\rho}_{SCR}\left(\frac{U}{d^2}\right)$ can be used (see fig. 5.19(b)).

The treatment of the SCR as a resistive region like in ref. [26] is misleading. The current in the depletion region is actually volume generation current. The depletion region should rather be treated as a current source and the whole sensor as a current source with an internal resistance R_{ohm}. The depletion region with the volume $V = A \cdot w(U)$ can supply a maximum volume current of $I/V = \alpha\Phi_{eq}$ (see eq. 2.43). At low voltages the resistance of the bulk and the related voltage drop IR_{ohm} will limit the current. The width of the depletion region will be small until the generation current in the maximum volume of the depletion region is equal to the ohmic current at this voltage $U/R_{ohm} \approx \alpha\Phi_{eq}A \cdot w(U)$ neglecting diffusion current. For higher voltages the depletion region cannot supply enough current to sustain the linear current. In other words, the conductivity in the depletion region becomes smaller than the conductivity in the ohmic region when $n, p < n_i$ in the SCR and the SCR starts to expand. The depletion region approximately has the width[7] $w\left(U_{th}\right) \approx U_{th}/\left(\alpha\Phi_{eq} \cdot \rho_{ohm} d\right)$. It should be noted that $w\left(U_{th}\right)$ should be similar to the width of the depletion region from the built-in voltage. Accordingly, the effective concentration of shallow defects can be roughly estimated $N_{eff} \approx \frac{2\epsilon\epsilon_0 U_{bi}}{ew(U_{th})^2}$. Assuming $U_{bi} \approx \frac{U_{th}}{d^2}\left(\Phi_{eq} = 0\right) \cdot d^2 \approx 0.5\,\mathrm{V}$ the estimated N_{eff} is too low compared with the capacitance and edge-TCT measurements. I.e. for the diode irradiated to $\Phi_{eq} = 9 \cdot 10^{14}\,\mathrm{cm}^{-2}$ the estimated full-depletion voltage is 300 V while the measurements show a value between 400 V and 800 V (see fig. 5.17, 5.28(a)). However, at 300 V the conductance starts do decrease strongly for this diode (see fig. 5.28(b)).

[7] If the width of the ohmic region $d - w$ decreases by the width of the depletion region w the relation is $I_V = I_{ohm} \Leftrightarrow \alpha\Phi_{eq}Aw = \frac{U}{\rho_{ohm}(d-w)/A}$ so $w\left(U_{th}\right) \approx \frac{d}{2} - \sqrt{\frac{d^2}{4} - \frac{U_{th}}{\alpha\Phi_{eq}\rho_{ohm}}}$ which gives very similar results.

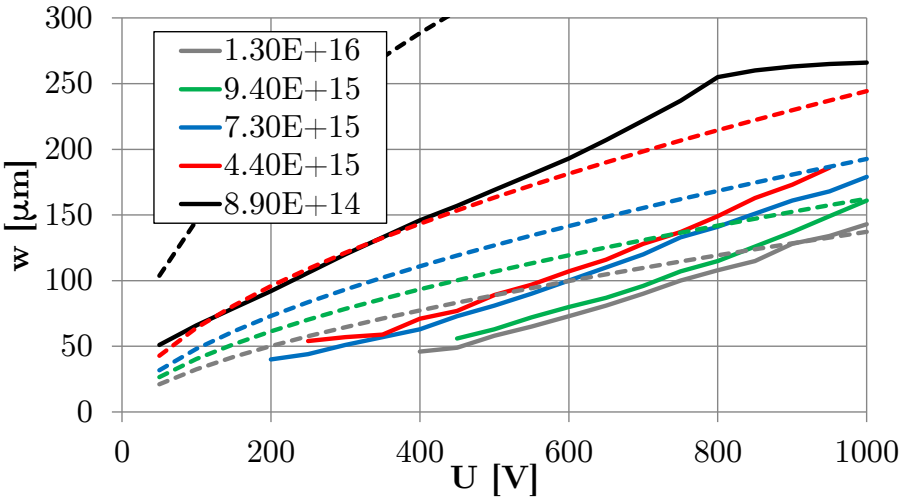

Figure 5.17.: $FWHM$ of the velocity profiles (solid) from sec. 5.2 compared to the estimated $w\,(U)$ using eq. 5.13 (dashed) at the fluences Φ_{eq} [cm^{-2}] given in the figure at 243 K for 285 µm thick sensors.

For higher reverse bias voltages the width of the SCR

$$w(U) \approx \frac{1}{\alpha \Phi_{eq}} \cdot \frac{U^S}{A \cdot \widetilde{R}_{SCR}} \tag{5.13}$$

determines the current where $U/\left(\rho_{ohm} d\right)$ is substituted with $U^S/\left(A \cdot \widetilde{R}_{SCR}\right)$. Figure 5.17 gives the $FWHM$ of the depletion region from the velocity profiles (see sec. 5.2) for the different fluences compared to eq. 5.13 using the values obtained for S and $\widetilde{R}_{SCR}$ between 5 V forward and 50 V reverse bias and using eq. 2.43 for α. The calculated width of the depletion region is always larger than the measured one except at the highest fluences at the highest voltages. This is expected since the voltage drop $I \cdot \rho_{ohm}\left(d - w(U)\right)/A$ in the bulk is not taken into account and is especially significant at low bias voltages where $w\,(U)$ is small.

The parameter

$$\widetilde{R}_{SCR}\left(\Phi_{eq}, A, T\right)^{-1} = \widetilde{R}_{SCR}\left(\Phi_{eq}, A, T_R\right)^{-1} \cdot \left(\frac{T}{T_R}\right)^2 exp\left(\frac{E_{eff}}{2k_B} \cdot \left(\frac{1}{T_R} - \frac{1}{T}\right)\right) \tag{5.14}$$

scales with temperature the same way like $\alpha(T)$ as shown in fig. 5.16(b), with $T_R = 293.15$ K and $\widetilde{R}_{SCR}\left(1.3 \cdot 10^{16}\,\text{cm}^{-2}, 24.4\,\text{cm}^2, T_R\right)^{-1} = (2.26 \pm 0.09) \cdot 10^{-5}\,\Omega^{-1}$ for the Czochralski n- and p-type diodes with $E_{eff} = 1.15$ eV.

At low fluences the volume generation current seems to be governed by an effective defect level close to the mid-gap energy. It was found that using an effective $E_{eff} = 1.21$ eV instead of the band gap energy in the exponent gives the

best description of the volume current at fluences $\Phi_{eq} \leq 10^{15}\,\mathrm{cm}^{-2}$ as shown in ref. [71]. The best fit to the data at $1.3 \cdot 10^{16}\,\mathrm{cm}^{-2}$ yields $E_{eff} = 1.15\,\mathrm{eV}$ which agrees with the result of ref. [71] at $10^{16}\,\mathrm{cm}^{-2}$ of $E_{eff} = 1.16\,\mathrm{eV}$. If the term $\exp\left(\left(E_g\left(T_R\right)/T_R - E_g\left(T\right)/T\right)/\left(2k_B\right)\right)$ is used the description of the data with $\widetilde{R}_{SCR}\left(T_R\right)^{-1} = (2.61 \pm 0.21) \cdot 10^{-5}\,\Omega^{-1}$ is better than for $E_{eff} = 1.21\,\mathrm{eV}$ with $\widetilde{R}_{SCR}\left(T_R\right)^{-1} = (2.69 \pm 0.26) \cdot 10^{-5}\,\Omega^{-1}$; but, it is still worse than using a constant $E_{eff} = 1.15\,\mathrm{eV}$ with the value given above. This suggests the effective generation center $E_{eff}/2 = 0.58\,\mathrm{eV}$ is very close to mid-gap $E_g/2 = 0.57\,\mathrm{eV}$ at 243 K.

5.3.3. Exponential increase of the reverse current

Figure 5.18 shows the differential resistivity $\rho = \frac{A}{d}\frac{\mathrm{d}U}{\mathrm{d}I}$ for the pad and $\frac{1}{d} \cdot R = \frac{1}{d}\frac{\mathrm{d}U}{\mathrm{d}I}$ for the guard ring. At higher reverse voltages $U \gtrsim 100\,\mathrm{V}$ the resistivity ρ of the pad and $\frac{1}{d} \cdot R$ of the guard ring are decreasing. Also, the noise increases significantly which can be seen in the variations of ρ at high voltages in fig. 5.18(a). The guard ring shows a much stronger decrease of $\frac{1}{d} \cdot R$ compared to ρ of the pad. The 200 µm thick n-type diode irradiated to $\Phi_{eq} = 7.8 \cdot 10^{15}\,\mathrm{cm}^{-2}$ shows the strongest decrease of $\frac{1}{d} \cdot R$ - which means the highest current increase - of the guard ring and also the highest noise of the pad ρ (green in fig. 5.18). The p-type diode of the same thickness irradiated to the same fluence (red in fig. 5.18) shows a decrease of $\frac{1}{d} \cdot R$ of the guard ring at higher voltages. Still, the pad resistivity of both diodes is very similar at high voltages. This is an indication for surface and/or edge effects for the guard ring current.

After irradiation, the junction is at the uniformly implanted back side for the initially n-type diode while it is on the side of the pad and guard ring for the p-type diode. Accordingly, the high field is at the back side for n-type (see chapter 5.2) and at the front side for p-type. Again, the pad currents are very similar as most of the surface effects are absorbed by the guard rings.

Part of the noise and resistivity increase at high fields can probably be attributed to micro-discharges as described by others [131]. However, the mechanism creating micro discharges is poorly studied. Micro-discharges are described as randomly quenched avalanche discharges or tunneling of oxide charges in high-field regions near the junction edges and at metal overhangs over the implants. The noise and the onset voltage of the current increase should depend on the concentration of oxide charge if micro-discharges are responsible. This means there should be a dependence on the biasing history (see ref. [132]), the geometry of the sensor (p- or n-type, metal overhang etc.), and on other parameters like the humidity.

Another possible contribution is soft breakdown due to impact ionization [133]

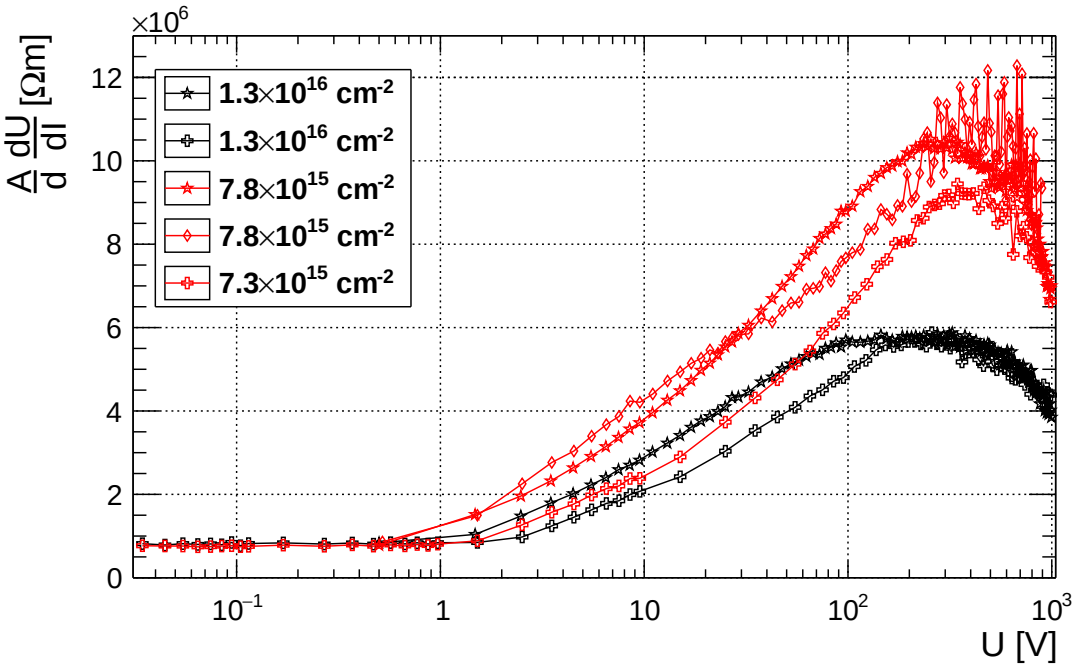

(a) Pad

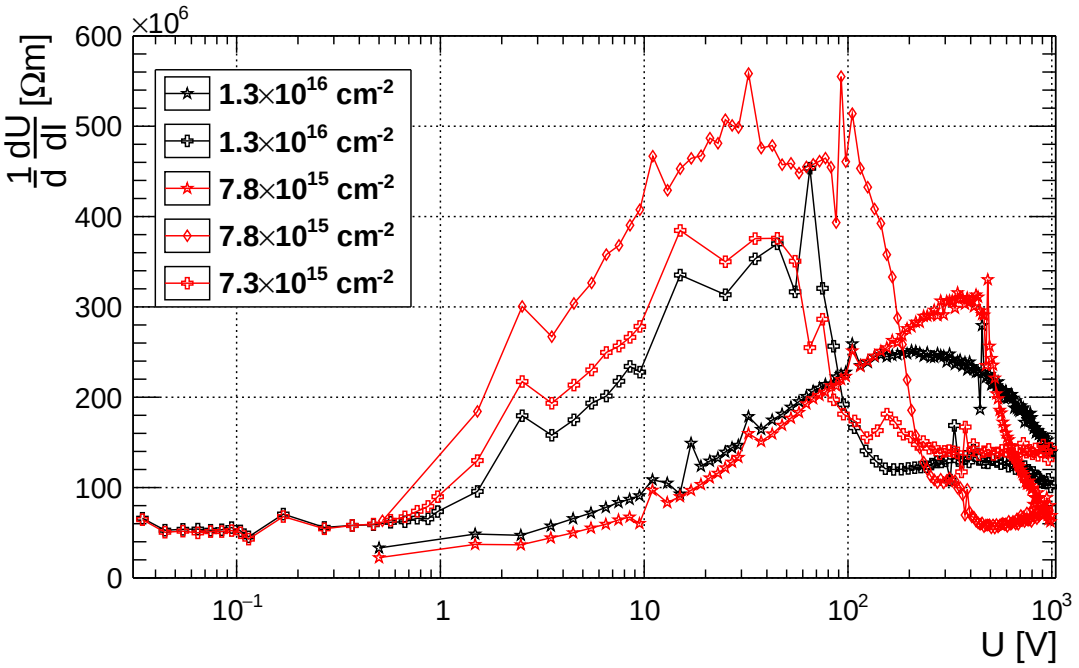

(b) Guard ring

Figure 5.18.: $\frac{A}{d}\frac{\mathrm{d}U}{\mathrm{d}I}$ vs. U for the pad (a) and $\frac{1}{d}\frac{\mathrm{d}U}{\mathrm{d}I}$ vs. U for the guard ring (b) of the $d = 200\,\mu\mathrm{m}$ p-type diodes (stars), the $200\,\mu\mathrm{m}$ n-type diode (diamonds), and the $285\,\mu\mathrm{m}$ n-type diodes irradiated to $\Phi_{eq} = 1.3 \cdot 10^{16}\,\mathrm{cm}^{-2}$ (black) and $\sim 7.6 \cdot 10^{15}\,\mathrm{cm}^{-2}$ (red) at 243 K.

in high field regions near the pad or guard ring implant edges and possibly at the pad junction. Such a contribution should not lead to excessive noise. The pad current should not depend on whether the junction is at the back side or at the pad if there is a junction breakdown. Apart from this, the increase may be explained by trap-assisted tunneling [134].

This regime was not studied thoroughly. But, the different behavior of the guard ring current for n- and p-type while the pad currents are comparable suggest there are different mechanisms responsible for the increase of the pad and the guard ring current. This region of the I/V should be studied more as it is very important to understand the mechanism responsible for the increase of the current and the noise. This range of high reverse bias voltages and mean electric fields is typically used for operation of most radiation detectors exposed to radiation levels comparable to the ones investigated here, e.g. at CMS. Below, the observations concerning the increase of the pad current and an empirical parameterization for the pad current will be discussed.

The pad current The differential resistivity of the pad $\rho\,(U) = R(U) \cdot \frac{A}{d}$ shown in fig. 5.18(a) increases with U until it reaches a maximum value which is very similar for the diodes of different thickness irradiated to similar fluences. The maximum value of $\rho\,(U)$ decreases with the fluence. For thicker diodes, the voltage at which the maximum value of $\rho\,(U)$ is reached is higher. $\rho\,(U)$ decreases for even higher voltages and the voltage dependence of $\rho(U)$ is very similar for the diodes of different thickness.

Figure 5.19(a) shows the volume current versus $\frac{U}{d^2}$ which is very similar for the diodes of different thickness irradiated to a comparable fluence. The departure from the $S \approx 0.6$ dependence of ρ starts at similar $\frac{U}{d^2}$ rather than similar U or E comparing fig. 5.19(a) and fig. 5.9. The resistivity shows a $\rho \propto \frac{U}{d^2}$ dependence until ρ starts to deviated for the different thicknesses at a certain $\frac{U}{d^2}$. This value $\frac{U}{d^2}$ approximately coincides with the maximum value of $\rho\,(U) \propto \frac{U}{d^2}$ as shown in fig. 5.19(b). For even higher voltages the dependence becomes $\rho(U) \propto U$ as discussed above (see fig. 5.18(b)).

The temperature dependence of the current could possibly provide information on the nature of the mechanism of the current increase. Figure 5.20 shows J versus U for diodes measured at different temperatures. The voltage where the current increase starts is similar for the p- and n-type Czochralski diodes at 233 K and 253 K. At 273 K the current increase is more pronounced than at lower temperatures. The current increase at high voltages is less pronounced for the n-type float-zone diode.

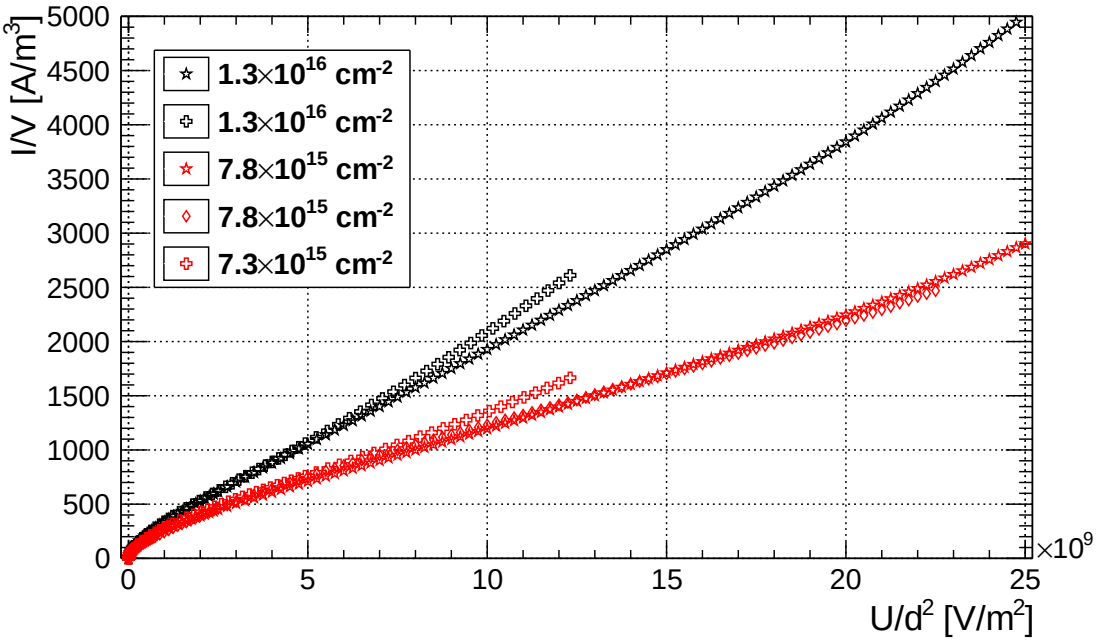

(a) $\frac{I}{A \cdot d}$ vs. $\frac{U}{d^2}$

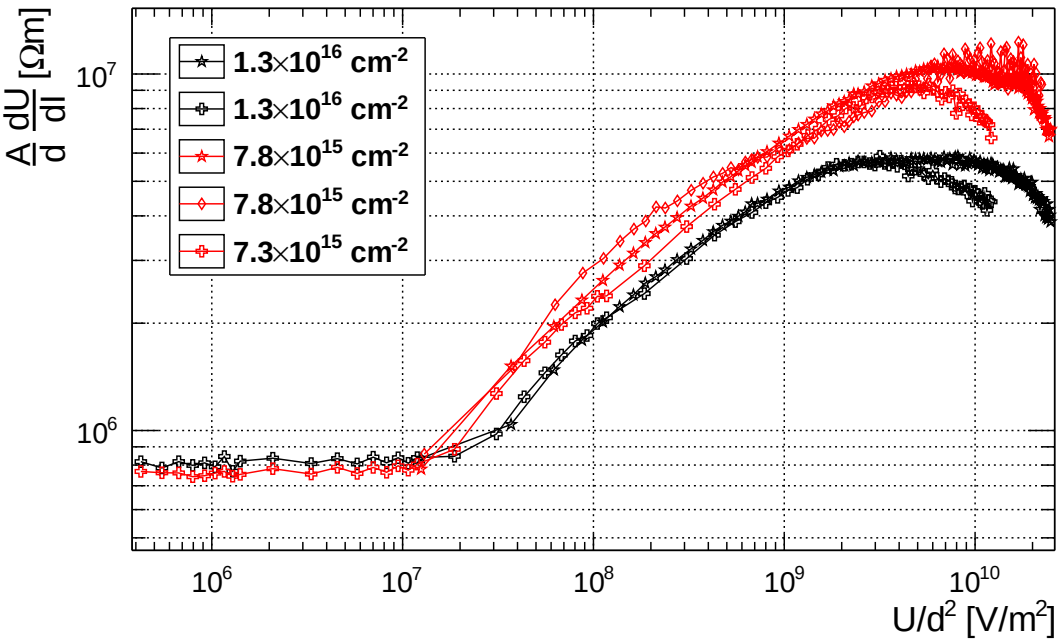

(b) $\rho = \frac{A}{d}\frac{\mathrm{d}U}{\mathrm{d}I}$ vs. $\frac{U}{d^2}$

Figure 5.19.: Pad volume current (a) and resistivity (b) versus $\frac{U}{d^2}$ of the $d = 200\,\mu\mathrm{m}$ p-type diodes (stars), the 200 µm n-type diode (diamonds), and the 285 µm n-type diodes irradiated to $\Phi_{eq} = 1.3 \cdot 10^{16}\,\mathrm{cm}^{-2}$ (black) and $\sim 7.6 \cdot 10^{15}\,\mathrm{cm}^{-2}$ (red) at K. The values are the same for the diodes of different thickness irradiated to the same fluences until the exponential current increase happens around $5 \cdot 10^9\,\mathrm{V/m}^2$.

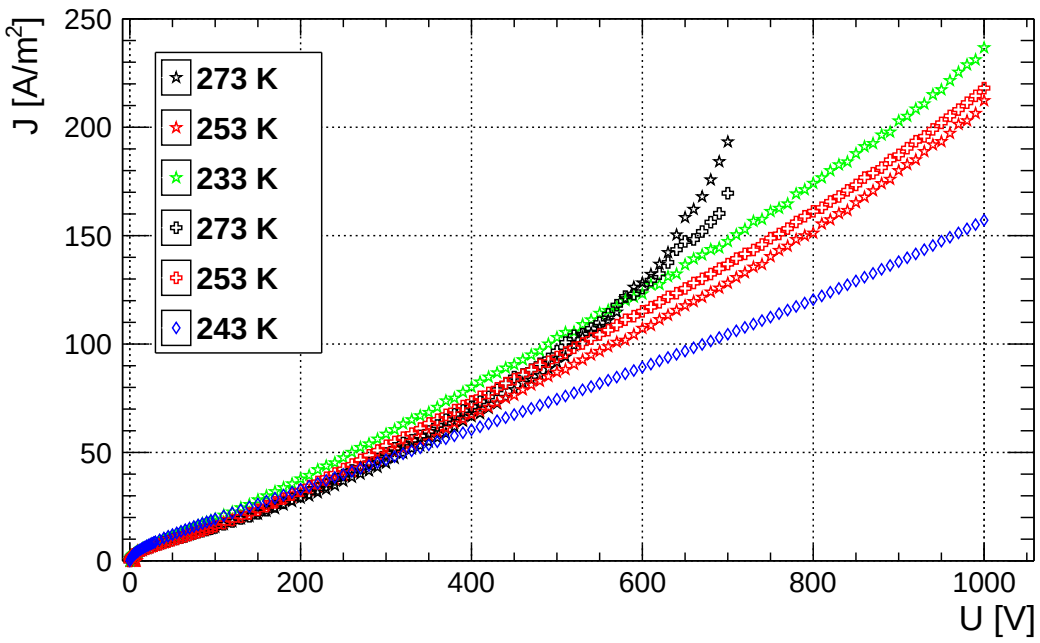

Figure 5.20.: Current density J for high reverse bias at different temperatures scaled to $T = 293.15\,\mathrm{K}$ with $E_{eff} = 1.15\,\mathrm{eV}$ (eq. 5.14) of 200 µm thick diodes irradiated to $\Phi_{eq} = 1.3 \cdot 10^{16}\,\mathrm{cm}^{-2}$. The stars show a Czochralski p-type, the crosses a Czochralski n-type, and the diamonds a float-zone p-type diode.

Parameterization Despite many open questions a simple parameterization is introduced. It is based on the following result: The increase of the pad current approaches an exponential voltage dependence $\frac{\mathrm{d}ln(I)}{\mathrm{d}U} \approx const$ for high U. There are several different mechanism which can contribute to this behavior. Probably, the most relevant ones are trap-assisted tunneling *TAT* [112, 134, 135] and field-enhanced emission from deep defects due to the Poole-Frenkel effect [136]. TAT describes tunneling of carriers not directly band-to-band but via traps which decreases the effective energy barrier. The field dependence is $I \propto E \cdot \exp(E^2)$ according to ref. [22]. The field dependence for Poole-Frenkel emission is $I \propto E \cdot \exp\left(\sqrt{E}\right)$ according to ref. [136]. Both models have been tested and slightly better fits are obtained using the Poole-Frenkel parameterization. However, the data is not very sensitive to any specific model and both describe the data at high fields within a few percent.

Simply adding an empirical term $I_{0,t}\,(exp\,(U/U_{0,t}) - 1)$ to the current gives the best fit results

$$I = \frac{U}{R(U)} + I_{0,t} \cdot \left(\exp\left(\frac{U}{U_{0,t}}\right) - 1\right) \tag{5.15}$$

with $R(U)$ of eq. 5.6 and the parameters $I_{0,t}$ and $U_{0,t}$. A fit of eq. 5.15 to the

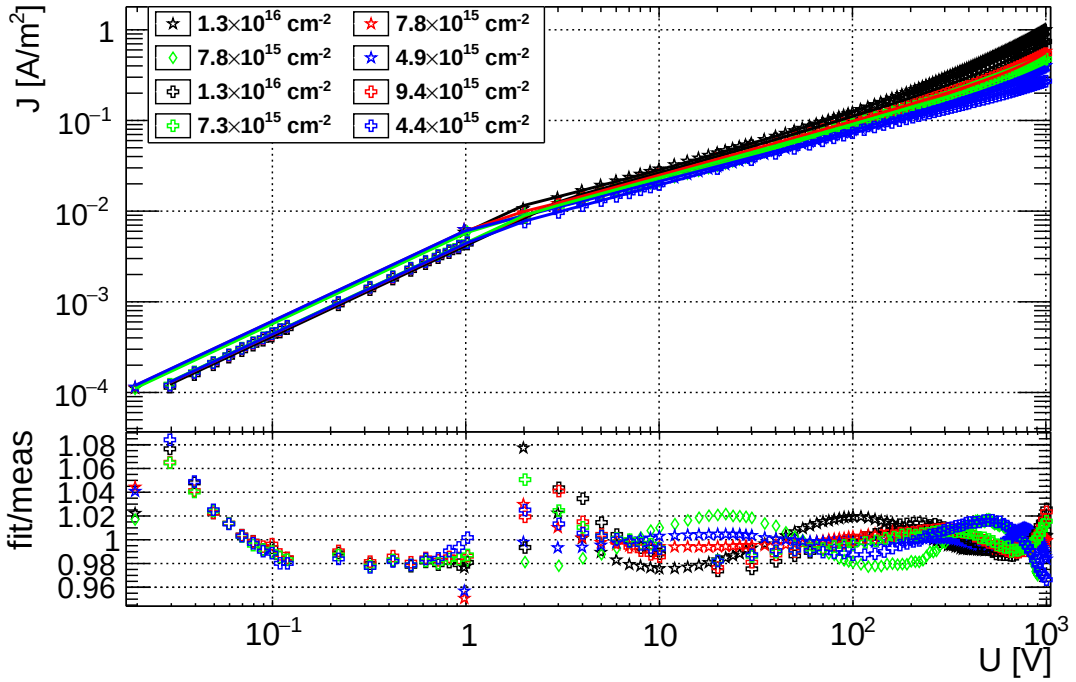

Figure 5.21.: Fit of eq. 5.15 (lines) to measurements at high reverse bias voltages of the 200 µm p-type diodes (stars), the 200 µm n-type diode (diamonds), and the 200 µm n-type diodes (crosses); all at 243 K. The residuals are shown below.

data with ρ_{ohm}, S, and $\widetilde{R}_{SCR}$ as free parameters is shown in fig. 5.21. The data is described within $2\,\% - 4\,\%$ at high bias voltages. This parameterization does not take into account a possible $\frac{U}{d^2}$ dependence. The best fit values of ρ_{ohm}, $\widetilde{R}_{SCR}$, and S do not differ too much from the results presented above when the exponential increase is added. Even if these parameters are fixed at the results for low voltages presented above, a fit of eq. 5.15 gives a good agreement with the data. However, if the parameters of eq. 5.6 are fixed the Poole-Frenkel parameterization gives a better fit due to the less steep increase $I \propto \exp\left(\sqrt{E}\right)$.

The measurements for the diodes irradiated to the lowest fluences are not shown here since diodes fully deplete and eq. 5.15 cannot be used. For these measurements the onset of the exponential current increase is observed after „full depletion".[8] Without the exponential increase the current would be expected to stay constant after full depletion.

5.3.4. Discussion

It is observed that ρ vs. $\frac{U}{d^2}$ is very similar for diodes of different thickness but comparable fluence at low voltages, and up to a certain value of $\frac{U}{d^2}$ (see fig. 5.19(b)). Accordingly, also the volume current $\frac{I}{A \cdot d} = \frac{U}{R(U) \cdot Ad} = \frac{U}{\rho(U) d^2}$ is very similar (see

[8] E.g. the diode irradiated to $\Phi_{eq} = 8.9 \cdot 10^{14}\,\mathrm{cm}^{-2}$ in fig. 5.3(b).

fig. 5.19(a)). At high reverse bias voltages the current is ohmic until a threshold $\frac{U_{th}}{d^2}(\Phi_{eq}) \propto \Phi_{eq}$ is reached. After the threshold the current increases approximately with a square-root dependence until it starts to increase exponentially at high reverse bias voltages. The parameterizations presented here describe the measured reverse current within a few percent and several laws were identified.

The formulas are shortly summarized below for easy application. All parameters have been determined at $T = 243\,\mathrm{K}$. The parameterization for the resistance is

$$R(U) = \begin{cases} \rho_{ohm}(\Phi_{eq}) \cdot \frac{d}{A} & U \leq U_{th} \\ \widetilde{\rho}_{SCR}(\Phi_{eq}) \cdot U^{1-S(\Phi_{eq})} \cdot \frac{d}{A} & U \geq U_{th} \end{cases}. \tag{5.16}$$

The ohmic resistivity is

$$\rho_{ohm}(\Phi_{eq}) = \rho_0 \cdot \left(1 + \left(\frac{\Phi_{eq}}{\beta_{mob}}\right)^{0.9}\right) \tag{5.17}$$

with the parameters $\rho_0 = 74.1\,\mathrm{M\Omega cm}$ and $\beta_{mob} = 1.52 \cdot 10^{17}\,\mathrm{cm}^{-2}$. The exponent is

$$S(\Phi_{eq}) = 1 - \frac{0.5}{1 + \frac{\Phi_{eq}}{\beta_S}} \tag{5.18}$$

with the parameter $\beta_S = 4.36 \cdot 10^{16}\ \mathrm{cm}^{-2}$. The threshold between ohmic currents and SCR generation currents is

$$\frac{U_{th}}{d^2}(\Phi_{eq}) = \frac{U_{th}}{d^2}(0) \cdot \left(1 + \frac{\Phi_{eq}}{\beta_{Uth}}\right) \tag{5.19}$$

with $\frac{U_{th}}{d^2}(0) = 1.1 \cdot 10^7\,\mathrm{V/m^2}$ and $\beta_{Uth} = 5.3 \cdot 10^{15}\,\mathrm{cm}^{-2}$ for the p-type and $\frac{U_{th}}{d^2}(0) = 5.8 \cdot 10^6\,\mathrm{V/m^2}$ and $\beta_{Uth} = 2.5 \cdot 10^{15}\,\mathrm{cm}^{-2}$ for n-type diodes.

The effective resistivity when the SCR is expanding can be calculated from these parameters

$$\widetilde{\rho}_{SCR}(\Phi_{eq})^{-1} = \frac{\left(d^2 \cdot \frac{U_{th}}{d^2}(\Phi_{eq})\right)^{1-S(\Phi_{eq})}}{\rho_{ohm}(\Phi_{eq})}. \tag{5.20}$$

At high voltages the current is described by

$$I = \frac{U}{R(U)} + I_{0,t} \cdot \left(\exp\left(\frac{U}{U_{0,t}}\right) - 1\right) \tag{5.21}$$

with the additional parameters $I_{0,t}$ and $U_{0,t}$. These parameters have not been determined systematically as the mechanism generating the current is not understood and the data is not very sensitive to different models.

5.4. Forward current

5.4.1. Results

The forward I/V is very similar to the reverse I/V at low voltages. Figure 5.22(a) shows the differential resistance for low forward and reverse voltages. The resistances are equal near the intrinsic value at very low bias. For the lowest fluence (green) a clear decrease of the resistance towards higher forward voltages is observed. The forward bias resistance stays more or less constant for the higher fluences. This may be due to the non-uniform field observed at the lowest fluence (see fig. 5.5(b)). For the higher fluences the resistance for low forward bias is almost constant.

At high forward voltages the current of highly irradiated diodes is many orders of magnitude lower than expected from the ideal Shockley diode equation 2.34. The resistance even increases with the applied voltage as shown in figure 5.22(b). This is expected as $\rho_{ohm}(E) \propto (\mu_e(E) + \mu_h(E))^{-1}$ and the carrier mobilities $\mu_{e,h}(E)$ decrease with increasing electric field. Figure 5.9(c) shows that $\rho_{ohm}(E)$ is approximately the same for diodes of different thickness but at similar fluence in this region.

After a certain applied voltage, which increases with the fluence, the resistance suddenly decreases strongly. This happens at different mean electric fields and voltages for the sensors of different thickness irradiated to similar fluences. The current starts to increase exponentially in this regime.

5.4.2. Parameterization

For highly irradiated diodes the forward current will be described with the theory of space-charge-limited currents *SCLC* for an insulator with one injecting contact and high trap concentrations as discussed in sec. 2.1.4. A constant trap concentration per unit energy in the band gap N_t is assumed, owing to the high defect concentrations and possible cluster defects with a broad energy spectrum (see ref. [137] for a discussion).

In the literature only one type of free charge carriers was considered for SCLC. Equation 2.38 has to be modified in order to describe a semiconductor with $n \approx p \approx n_i$. If we consider a semiconductor with thermal free majority carriers (holes) with a constant intrinsic concentration $p \approx n_i$ not influenced by injection, minority carrier (electron) injection with an equilibrium electron concentration $n \approx n_i$, and a constant trap distribution, the current can be parameterized as

$$I(U) = en_i \cdot A\frac{U}{d} \cdot \left(\mu_h(\Phi_{eq}, E) + \mu_e(\Phi_{eq}, E) \cdot \exp\left(\Xi\frac{U}{T \cdot d^2}\right)\right) \tag{5.22}$$

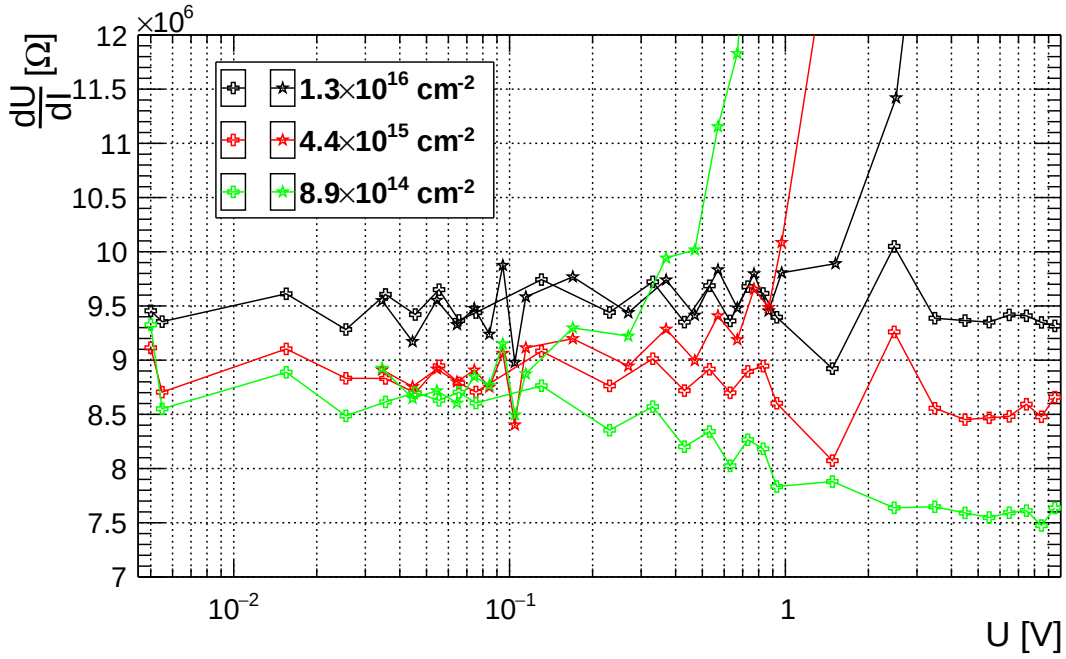

(a)

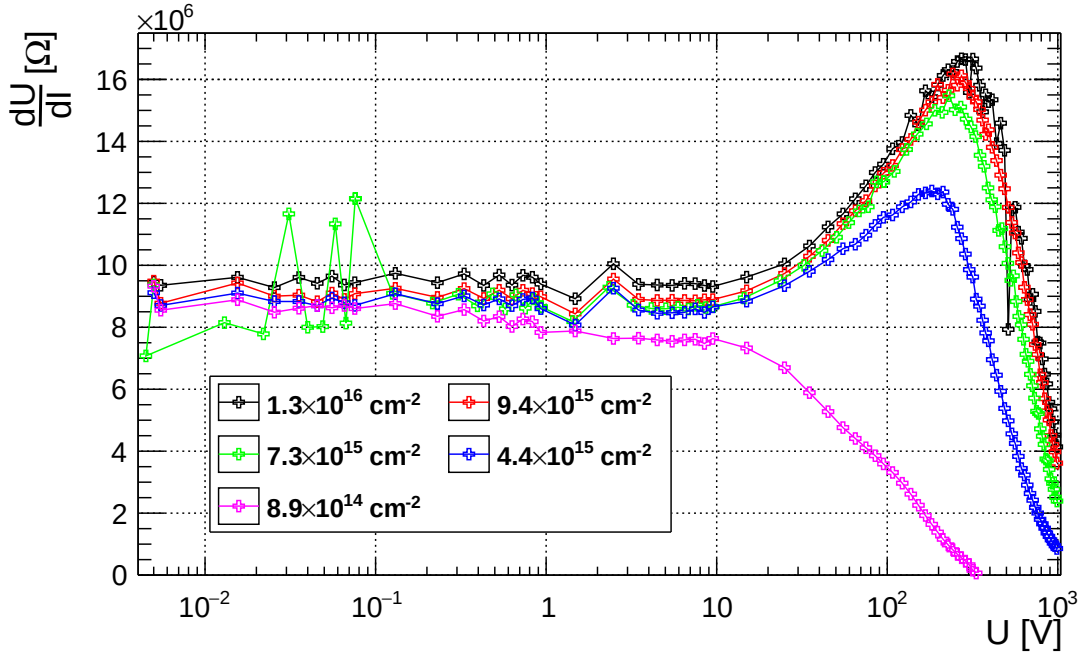

(b)

Figure 5.22.: (a) Comparison of the differential resistance $R = \frac{dI}{dU}$ for forward (crosses) and reverse (stars) bias for different fluences at low voltages. (b) $R = \frac{dI}{dU}$ for forward bias up to 1000 V. Measured at 243 K.

with $\Xi = \frac{\epsilon\epsilon_0}{eN_t k_B}$. The electric field is assumed $E = U/d \approx const.$ The mobilities $\mu_{e,h}(\Phi_{eq}, E)$ given in sec. 7 are used. At low voltages the term $\exp\left(\Xi \frac{U}{T \cdot d^2}\right) \approx 1$ and $I(U) \approx \frac{U \cdot A}{\rho_{ohm}(E) \cdot d}$. At high voltages the hole current becomes negligible as the hole concentration is assumed to be constant $p = n_i$ while the electron concentration increases $n = n_i \cdot \exp\left(\Xi \frac{U}{T \cdot d^2}\right)$.

Figure 5.23 shows a fit of eq. 5.22 to the data with only n_i and Ξ as free parameters. The agreement between the model and the data is very good except at high voltages where the measured current increases faster than the exponential term of the parameterization. The goodness of the fit is remarkable as there are only two free parameters and the voltage as well as the current cross up to seven orders of magnitude.

Fit parameters Figure 5.24(a) shows the fit parameter $1/\Xi$. The results seem to be independent of the different thicknesses and initial doping. The electron trap concentration

$$N_{tot} = E_g \cdot \frac{\epsilon\epsilon_0}{e\Xi k_B} \tag{5.23}$$

extracted from the fit is shown in fig. 5.24(b). However, it is not clear whether these values represent physical concentrations. The extracted introduction rate $g_{eff} = N_{tot}/\Phi_{eq}$ shown in fig. 5.24(c) clearly decreases with the fluence.

A possible reason for the non-linear increase of the extracted N_{tot} could be that the mobility at high voltages decreases stronger with fluence than estimated by the model. However, the resistivity at higher voltages (around $U = 100\,\mathrm{V}$ in fig. 5.22(b)) is similar for the different fluences, indicating that the mobility at high fields does not change much with the fluence.

The values of N_{tot} are much higher than the space charge concentration estimated from the edge-TCT measurements discussed in sec. 5.2. The space charge for the trap-filled limit should lead to a potential drop („full depletion voltage") around 10 kV for $N_{tot} \approx 10^{14}\,\mathrm{cm}^{-3}$ and 285 µm thickness. An introduction rate $g = 0.03\,\mathrm{cm}^{-1}$ has been reported in ref. [138] (see tab. 2.1) for an electron trap at the energy 0.52 eV below the conduction band. This value is similar to g_{eff} extracted at low fluence (see fig. 5.24).

The model assumes an increase of the concentration of free electrons in the bulk and subsequent filling of electron traps. Yet, the sign of the space charge in the regime where the conductivity of the bulk is increased seems to be positive (see sec. 5.2), indicating an increased free and trapped hole concentration in the bulk.

The fit values of n_i shown in fig. 5.25 agree well with the literature value (eq. 2.5). The mean value of the fit results is 2 % below the literature value. This is a strong

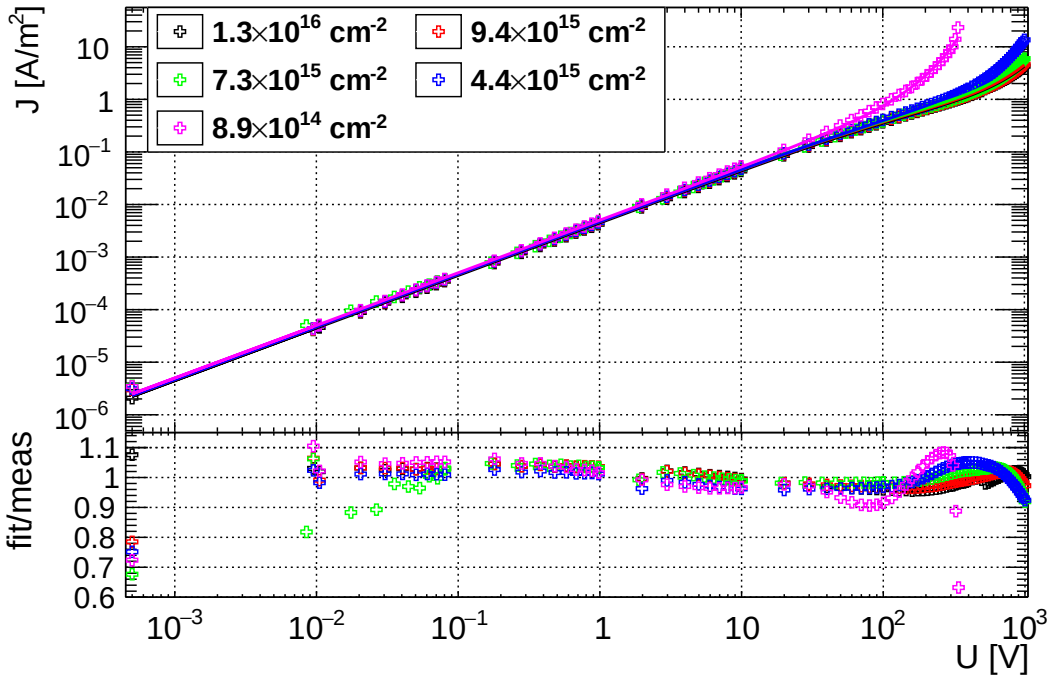

(a) 285 µm n-type

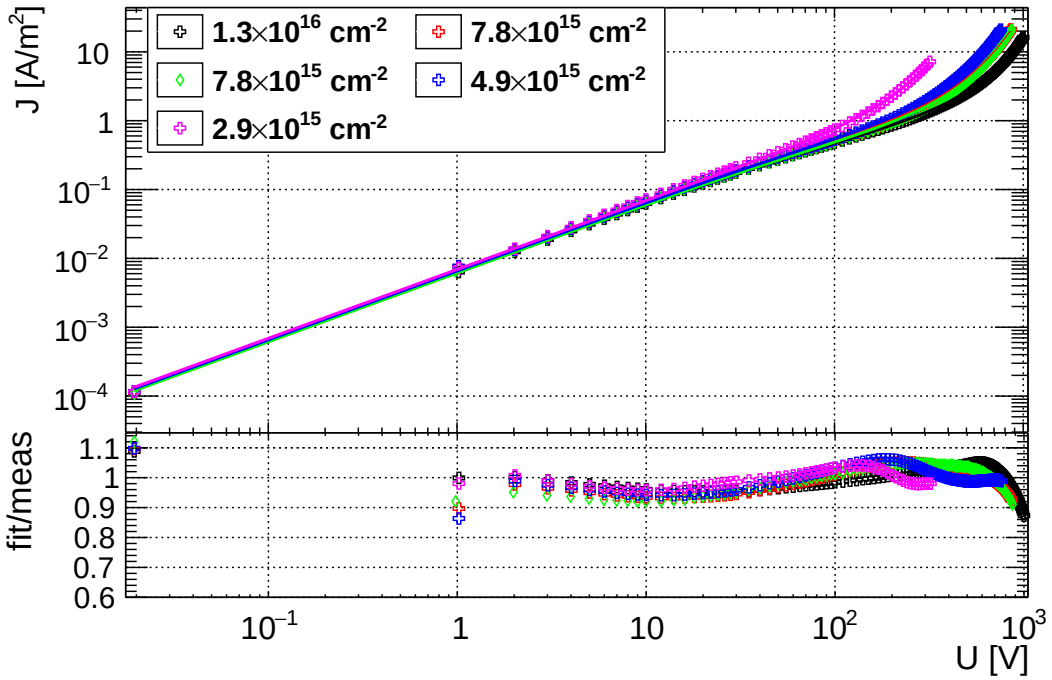

(b) 200 µm p-type and n-type

Figure 5.23.: Fit (lines) of the forward current measurements (crosses, diamonds) with eq. 2.38 and two fit parameters for the 285 µm n-type diodes shown in (a) and the 200 µm p-type diodes (crosses) and the n-type diode (diamonds) shown in (b) at 243 K. The residuals are shown below the current plots.

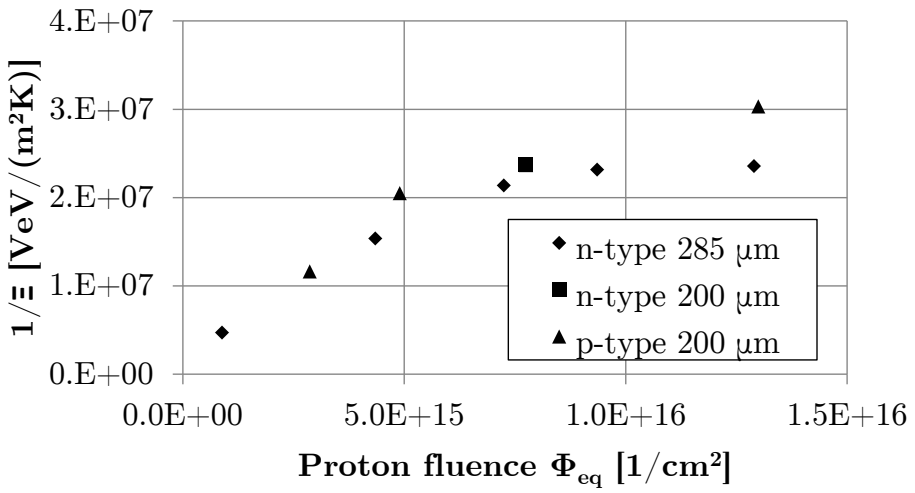

(a)

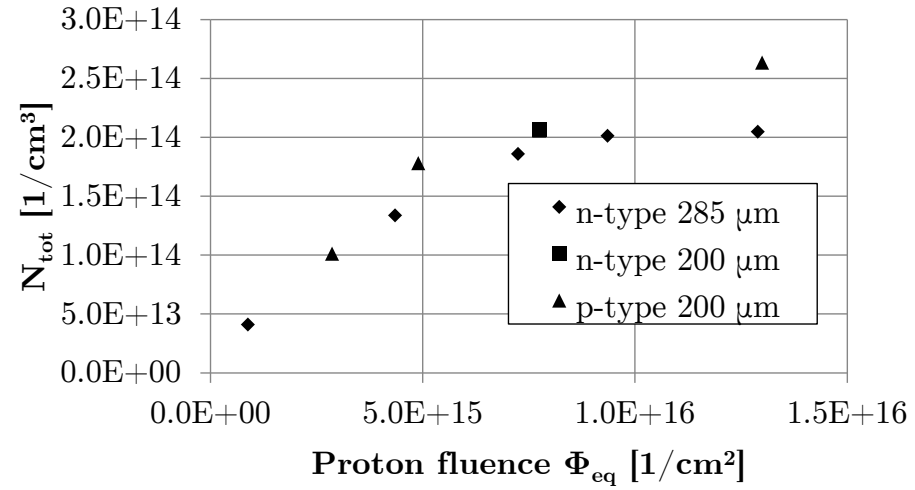

(b)

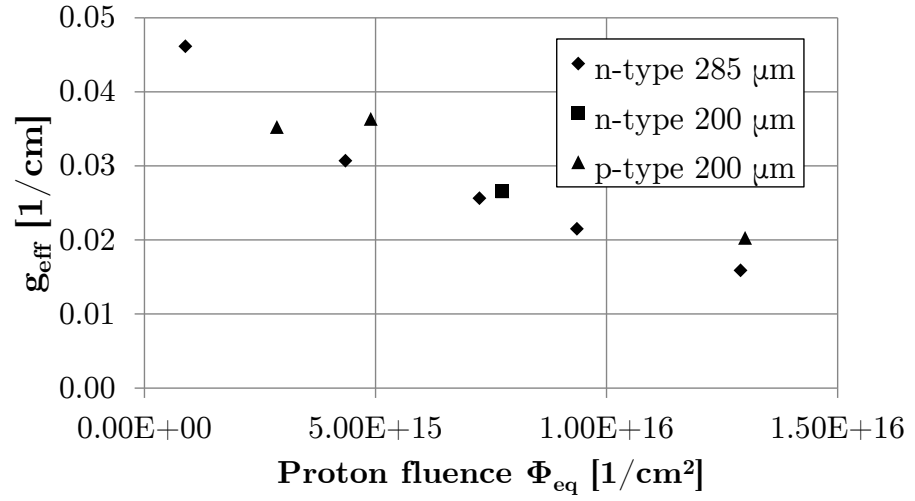

(c)

Figure 5.24.: Fit result of $1/\Xi$ (a) of eq. 2.38 for the forward current at 243 K. (b) Shows a hypothetical the electron trap concentration N_{tot} calculated from Ξ. (c) Shows the effective introduction rates g_{eff} for N_{tot}.

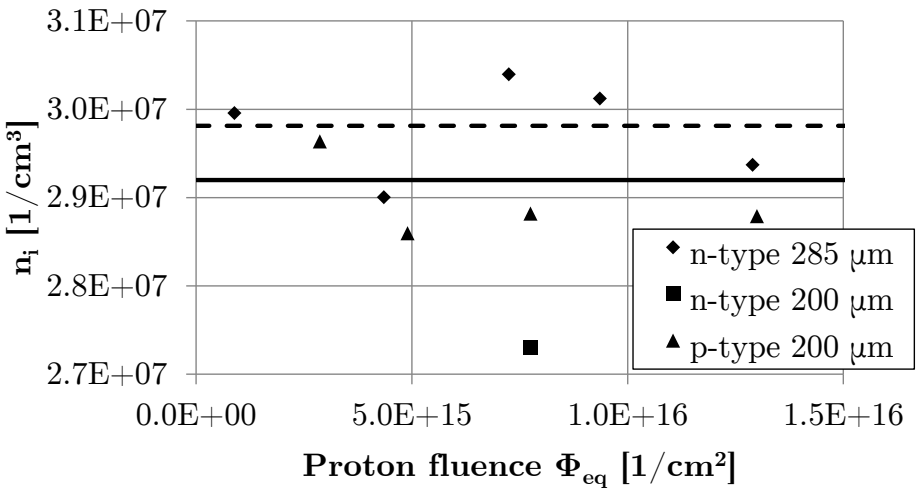

Figure 5.25.: Fit results of the intrinsic carrier concentration n_i of eq. 2.38 for the forward current at 243 K compared to the literature value for non-irradiated silicon (dashed line). The solid line shows the mean value of the fit results.

indication that the model is useful at least at low voltages since only the parameter Ξ has to be fitted to describe the data. Additionally, it is a strong indication that the assumption $n \approx p \approx n_i$ is justified.

5.4.3. Discussion

Equation 2.38 describes the I/V measurements within about 10 % using the results of $\mu_{e,h}(E, \Phi_{eq})$ presented in sec. 7 and a parameter Ξ. However, the electron trap concentration N_{tot} extracted from Ξ does not increase linearly with the fluence and the current at high voltages (trap-filled limit) increases faster than the exponential term of the model. Most importantly, the model does not account for the positive space charge in the bulk which is observed in the edge-TCT measurements for high forward voltages.

Important open question are the description of the electric field for forward bias, its origin in SCLC, and the influence of recombination. The width of the transition region with negative space charge at the injecting junction and the bulk seems to be related to the density of traps, as it decreases with increasing fluence. Also, the near-linear field in the bulk after the transition to SCLC has to be explained (see sec. 5.2).

The SCLC regime will be discussed first. According to Rose [33], the charge distribution in a trap-free insulator with plane parallel electrodes is $N_{t,filled} \propto x^{-1/2}$ and the electric field $E \propto x^{1/2}$ with the distance from the junction x. In the

presence of traps exponentially distributed in the bandgap these relations take the form $N_{t,filled} \propto x^{-1/(n+1)}$ and $E \propto x^{n/(n+1)}$. For the lowest fluence the velocity profile somewhat resembles the $E \propto x^{n/(n+1)}$ relation (see fig. 5.5(b)). For traps distributed in the band gap ($n \gg 1$) the charge distribution $N_{t,filled}$ becomes constant and the electric field linear. This is to some degree what is observed in the edge-TCT measurements when SCLC become significant compared to ohmic currents as e.g. in fig. 5.5(f) at the highest voltages. At higher fluences and at higher voltages, where the SCLC dominate the current, a decrease of the electric field can be observed from the maximum value near the injecting contact towards the opposite contact. However, as mentioned above the extracted trap concentration from the fit of the forward current is much higher than what is expected from the slope of the velocity profiles. Also, the velocity profiles indicate positive space charge in the bulk.

The transition region close to the injecting contact is discussed by Lampert [32]. According to Lampert, it is governed by the injected free carriers and not by traps. As stated by Rose [33], ohmic currents and SCLC compete at all voltages, which can be confirmed looking at the velocity profiles measured for forward bias. Even at low voltages, where the ohmic current clearly dominates, a decrease of the field towards the injecting electrode can be observed (fig. 5.5(b), 5.7(b)). As mentioned before, the width of the transition region does not change within the accuracy of the measurement. Lampert gives a discussion about two-carrier injection including cases with constant positions of the extrema of the electric field. However, there is no clear indication for or against double injection in the measurements discussed here. Double injection may well happen because of the ambivalent nature of irradiated silicon. Since both acceptors and donors are present in the neutral bulk, all compensated by deep traps in equilibrium, there might well be a hole-injecting p^+-n junction for forward bias similar to the double junction for reverse bias. Others [139] have measured velocity profiles of highly irradiated sensors for forward bias which resemble the fields discussed by Lampert for double injection. They investigated annealed sensors where also the double junction under reverse bias is more pronounced. Additionally, for low-gain avalanche diodes *LGADs* measurements have shown how the irradiated bulk material switches the sign of the space charge from n-type to p-type with the bias voltage, in the same LGAD (see ref. [140]).

The initial increase of the field near the injecting contact towards a constant field in the bulk may be explained by the influence of relaxation via recombination of carriers. In the relaxation regime (see sec. 2.1.3) the space charge from injected free and trapped minority carriers in the injection region is increased due to the

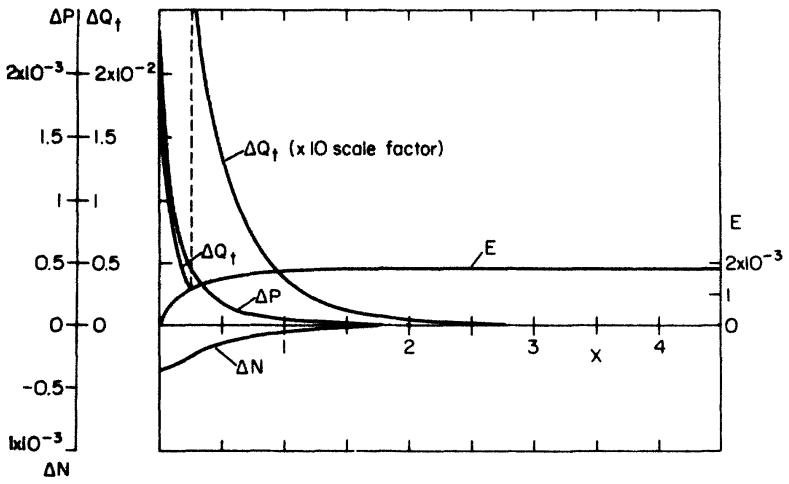

Figure 5.26.: Change of the carrier concentrations ΔN, ΔP for hole injection in the relaxation regime. Recombination centers below mid-gap are assumed. Injected holes are trapped near the injecting contact creating positive space charge ΔQ_t. Additionally, electrons are removed in the injection region due to recombination. The electric field E increases from the injecting contact and until it is constant in the bulk when the injected holes have recombined with electrons. All units are arbitrary. Modified from [27].

removal of majority carriers via recombination. Arguing from the relaxation regime including traps, Manifacier and Henisch [27] obtain an electric field distribution similar to the observations discussed here and even give an analytical model of the electric field shown in fig. 5.26.

Let's assume no increase of the bulk conductivity: Injected carriers cannot traverse the whole sensor. Some of the injected minority carriers[9] will recombine with the majority carriers of the bulk silicon. If the recombination lifetime is short the injected minority carriers will quickly recombine. Additionally, injected minority carriers will be trapped at defects creating additional space charge. Majority carriers will be drawn towards the recombination region to establish charge neutrality. Depending on the dielectric relaxation time and the recombination lifetime, the width of the transition region from the injecting contact (high recombination) until charge neutrality is established in the bulk (zero net recombination) will change. This might explain the decrease of the width of the transition region between the injecting contact and the neutral bulk with increasing fluence. Even if the recombination lifetime is larger than the dielectric relaxation time diffusion and drift current of majority carriers will work against the current of the injected minority carriers and the space charge from trapped injected minority carriers. This might explain the positive space charge observed in the bulk at high bias voltages.

Figure 5.26 illustrates the change of the free carrier concentrations ΔN, ΔP,

[9]The injected carriers are holes in fig. 5.26 and electrons for the sensors investigated here.

and ΔQ_t, the concentration of trapped minority carriers, and the electric field E for hole injection in the presence of recombination centers below the mid-gap in the relaxation regime.

As mentioned before, clear indications for a change of the width of the transition region with applied voltage are not observed. Even if the conductivity of the bulk is increased under forward bias the width of the transition region hardly changes (see e.g. fig. 5.7(b)). Once injected carriers can enter the high field bulk region, the recombination front (described e.g. in ref. [141]) seems to stay at a fixed position.

It should be noted that previous publications have used empirical parameterizations such as

$$I(U) = G_0 U \cdot \left(\exp\left(\frac{U}{U_0}\right) - 1 \right) \tag{5.24}$$

in refs. [142, 143] with a constant conductivity G_0. This is essentially a version of eq. 2.38. Another version is

$$I(U) = I_0 \cdot \left(\exp\left(\frac{U}{U_0}\right) - 1 \right) + G_0 U \tag{5.25}$$

used in ref. [144], where a distinct ohmic part $G_0 U$ was added.

As a closing remark, it should be noted that the dependence of the SCLC on defects makes it possible to perform so-called temperature-dependent space-charge-limited-current *TD-SCLC* spectroscopy to study deep traps (see e.g. ref. [145, 146]). This method could be applied to study radiation damage at lower fluences and compare the results to other methods. For the diode which received the lowest fluence, shown in fig. 5.3(b), a step in the forward current can clearly be observed which may represent the filling of a localized defect level. At lower temperatures TD-SCLC might also reveal new features even at higher fluences which may be used to determine the density of states as a function of the energy.

5.5. Capacitance-voltage characteristics

The capacitance-voltage measurements reflect many of the effects discussed above. Figure 5.27(a) shows the parallel capacitance versus the voltage under forward and reverse bias measured with an AC voltage of ±50 mV at a frequency of 200 Hz. Figure 5.27(b) shows the conductance which is similar to the inverse of the DC resistance (compare fig. 5.9(a)). The frequency dependence of the capacitance for reverse bias is shown in fig. 5.28. In order to investigate highly irradiated diodes for near steady-state conditions low frequencies are used. The lower the frequency the closer the system is to the steady state conditions since (de-)charging of defects is associated with certain time-constants. At very high frequencies the reverse bias C/V characteristics are mostly constant at the geometrical capacitance since the defects cannot react to the fast change of the potential.

Reverse bias At low bias voltages the geometrical capacitance of the diode is measured within 10 % as expected for a parallel-plate capacitor with a highly resistive dielectric (silicon) in-between. As discussed above, the width of the depletion region w is negligible in this region. The ohmic, non-depleted bulk determines the properties of the diodes. At the threshold voltage U_{th} the capacitance suddenly increases. The width of the depletion region starts to increase and the voltage drop in the depletion region becomes significant. A maximum in the capacitance can be observed at a certain voltage which increases with Φ_{eq}. The value of the maximum decreases and shifts to higher voltages with increasing frequency f. Then, the capacitance decreases again as the depletion region increases similar to a non-depleted diode. The capacitance eventually reaches the geometrical capacitance for the lowest fluence in fig. 5.27, indicating full depletion.

Forward bias Under forward bias the capacitance is first constant at the geometrical capacitance until it starts to increase approximately at mean electric fields where the mobility starts to decrease. It increases further when the injection of free carriers becomes significant and the current starts to increase exponentially. For the lowest fluence negative capacitance values are observed at high bias voltages (see fig. 5.27(a)).

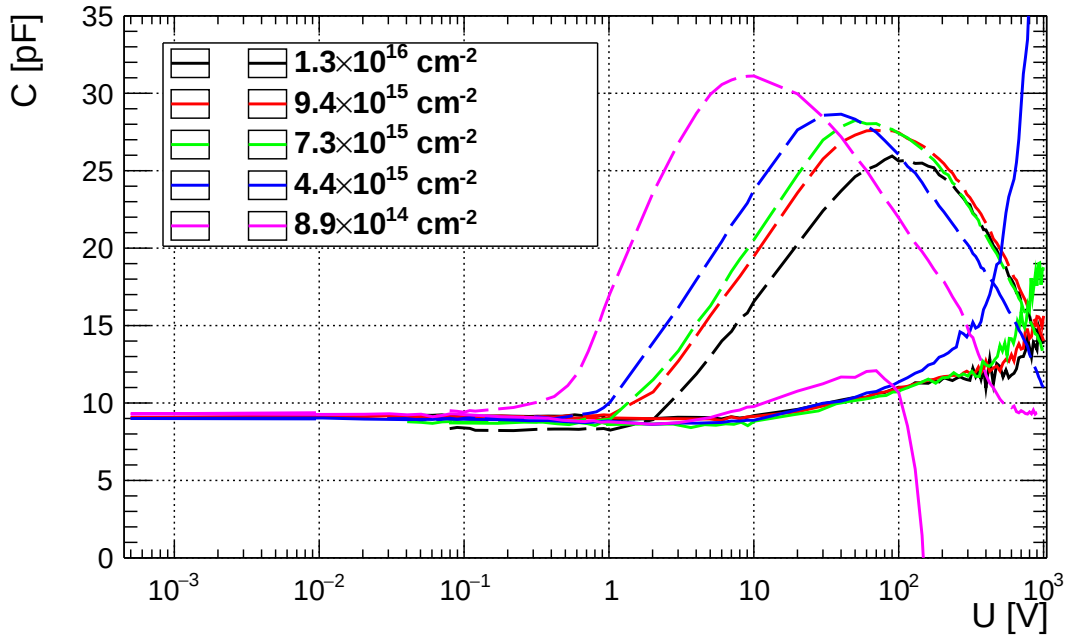

(a)

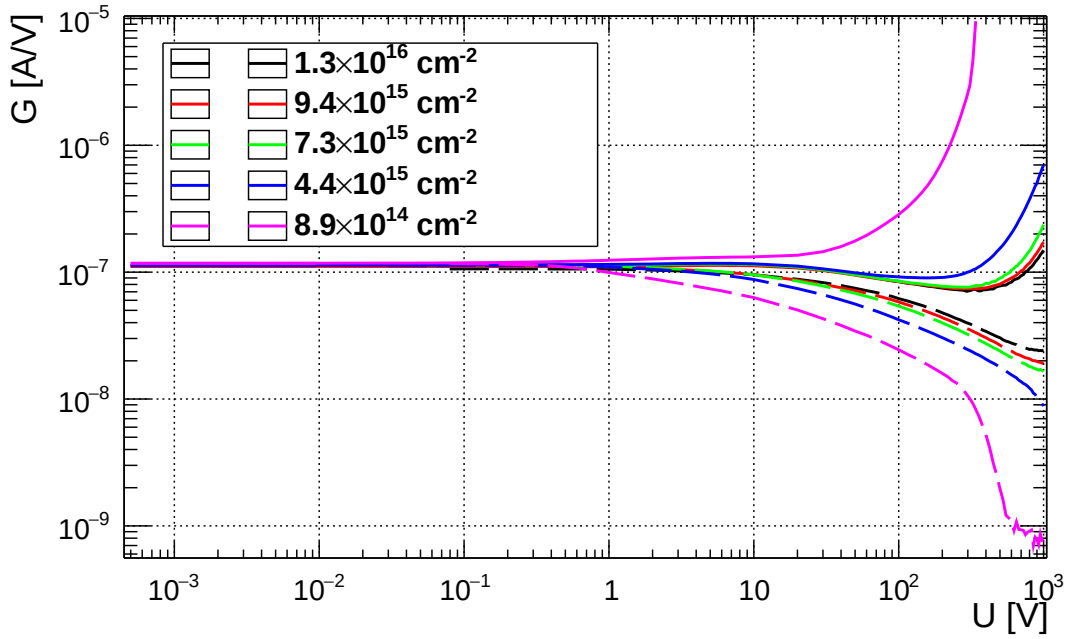

(b)

Figure 5.27.: Pad capacitance (a) and conductance (b) of the irradiated $d = 285$ µm n-type diodes for forward (solid) and reverse (dashed) bias voltages. Measured with 200 Hz AC voltage with a peak amplitude of 50 mV at 243 K.

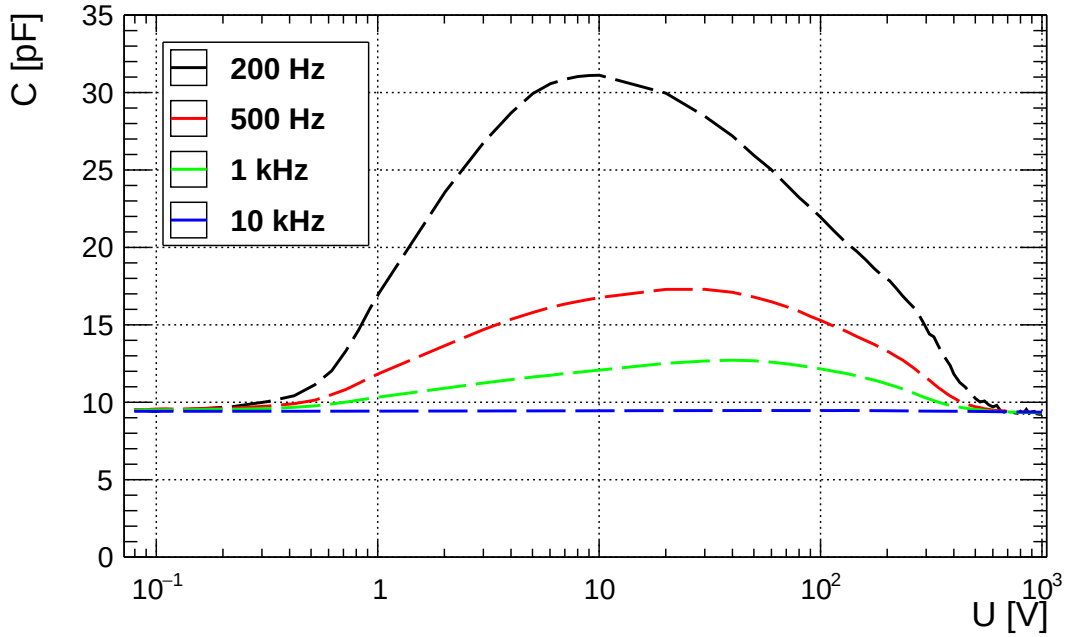

(a)

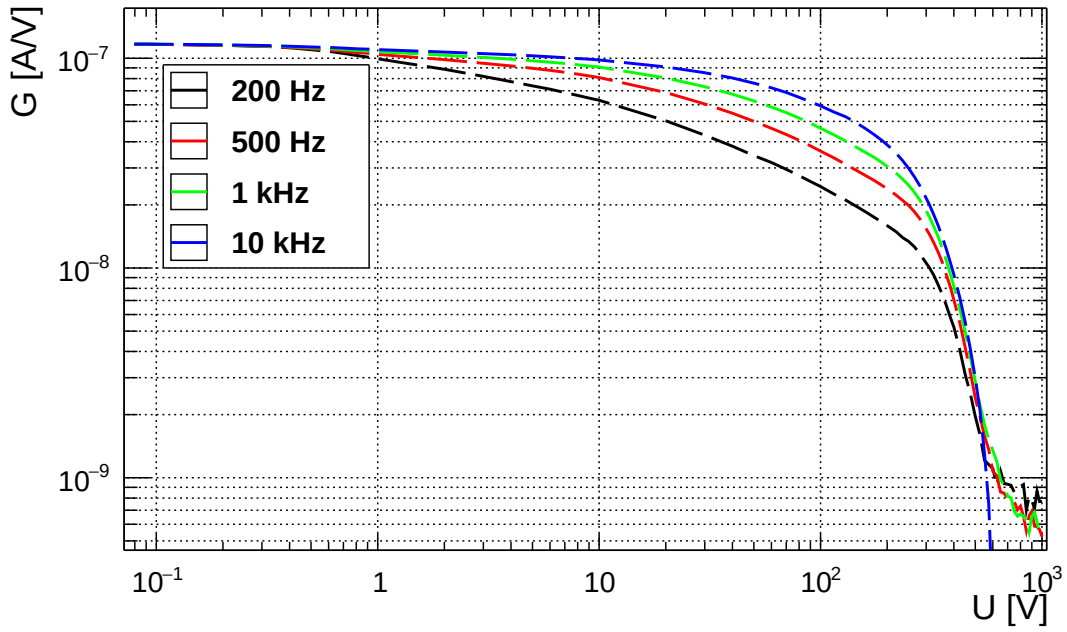

(b)

Figure 5.28.: Pad capacitance (a) and conductance (b) of the diode irradiated to $\Phi_{eq} = 8.9 \cdot 10^{14}\,\mathrm{cm}^{-2}$ for reverse bias. Measured with an AC voltage of different frequencies and a peak amplitude of 50 mV at 243 K.

5.6. Conclusion

By comparing the current of irradiated diodes under forward and reverse bias to the velocity profiles of irradiated strip sensors, different regimes can be distinguished under forward and reverse bias. Capacitance measurements of the diodes support the results. Additionally, by comparing current measurements of silicon diodes of different thickness the dependence of the different current regimes and the transitions between them on the voltage U, the mean electric field $E = U/d$, and $\frac{U}{d^2}$ can be determined.

Reverse bias For low reverse bias highly irradiated sensors behave like silicon resistors with intrinsic carrier concentrations $n \approx p \approx n_i$. The current is ohmic and the capacitance constant $C \approx \frac{\epsilon\epsilon_0 A}{d}$. A high concentration of deep defects pins the Fermi energy near mid-gap [110, 115]. Free majority carriers are trapped at deep defects and there is zero net fixed space charge, independent of the initial doping concentration and sign.

The bulk resistivity increases with the hadron fluence. This is interpreted as a decrease of the carrier mobilities with increasing defect concentration. An effective degradation factor of $\beta_{mob} = 1.52 \cdot 10^{17}\,\mathrm{cm}^{-2}$ for the low-field mobilities is derived from measurements of the low-field resistivity $\rho_{ohm}\,(\Phi_{eq})$ (compare eq. 5.8, 5.9).

If the reverse voltage is increased the resistivity suddenly increases at a certain value $\frac{U_{th}}{d^2}\,(\Phi_{eq})$ (eq. 5.10), which increases proportional to the fluence. The current now has a dependence on the voltage $I \propto U^S$ with $S \approx 0.6$ (eq. 5.11) The interpretation of the author is that the transition happens, when the ohmic current of the neutral bulk is approximately equal to the volume generation current of the maximum volume of the depletion region at this voltage; or, in other words, when the generation current of the SCR cannot sustain the ohmic current of the bulk anymore. The depletion region starts to expand and dominates the current.

The capacitance C supports the interpretation of an expanding depletion region. C is first constant until it suddenly starts to increase up to a maximum value which strongly depends on the frequency. Then C starts to decrease again until the geometrical capacitance is reached for the diodes which reach full depletion - similar as for non-irradiated diodes.

The edge-TCT measurements also support this interpretation. A high field „depletion region" forms at the p-n junction and there is a sizable, for high fluences almost constant, electric field in the bulk.

A parameterization for the reverse current at medium voltages $\frac{U}{d^2} \leq 100\,\mathrm{kV/cm}^2$ was introduced and its parameters were discussed and parameterized (compare

eq. 5.6, 5.11, 5.10, 5.12).

The parameter $\widetilde{R}_{SCR}\left(\Phi_{eq}, A, T\right)^{-1}$ scales the same way with the temperature as the damage parameter α. This means it is probably related to the generation lifetime $\tau_0 = \frac{en_i}{\alpha\Phi_{eq}}$. The best fit of the temperature dependence is given by $\widetilde{R}_{SCR}\left(\Phi_{eq}, A, T\right)^{-1} \propto \exp\left(\frac{E_{eff}(T)}{2k_BT}\right)$ with $E_{eff} = 1.15\,\mathrm{eV}$ rather than an $E_{eff} = 1.21\,\mathrm{eV}$ found at lower fluences [71].

An important result is that the reverse bias resistance $\rho(U)$ depends on $\frac{U}{d^2}$ rather than U or E (compare fig. 5.19(b)). As mentioned before, the transition between ohmic current and volume generation current from the SCR happens at a certain threshold voltage U_{th}. It is observed that $\frac{U_{th}}{d^2} \propto \Phi_{eq}$ and $\frac{U_{th}}{d^2}$ is equal for diodes of different thickness. But, the values slightly differ for n- and p-type. However, it is not yet clear how to interpret $\frac{U_{th}}{d^2}$.

At very high reverse voltages the current suddenly starts increase more rapidly. At a certain $\frac{U}{d^2}$ the resistivity is no longer proportional to $\frac{U}{d^2}$ but approximately $\rho\left(U\right) \propto U$. The current starts to increase approximately exponentially and the noise increases drastically. Additionally, the guard ring current suddenly increases very strongly. Several possible explanations for this behavior at high voltages are discussed. It is found that simply adding an exponential term to the current equation 5.6 leads to a good agreement with the data.

Forward bias The forward current is ohmic at low voltages with the same resistivity as for low reverse bias. If the voltage is increased the resistance increases and depends on the mean electric field $\rho \propto E$. This is interpreted as the reduction of the carrier mobilities at high fields. It can be well described by using the field-dependent mobilities $\mu\left(E\right)$ for $\rho\left(E\right)$. Since the fluence dependence of the mobility at high fields is not known, the fluence dependent low-field mobility $\mu_0\left(\Phi_{eq}\right)$ is used for $\mu\left(E, \Phi_{eq}\right)$ (see chapter 7).

At high voltages the current suddenly starts to increase exponentially which is described with the theory of space-charge limited currents (see eq. 5.22). A semiconductor with thermally generated carriers $n \approx p \approx n_i$ and electron injection from the junction is assumed. The exponential increase of the current depends on $\exp\left(\frac{U}{d^2}\right)$. A trap concentration was extracted from the fit results.

The edge-TCT measurements show a low electric field at the junction which increases towards the opposite contact for the lowest fluences. For higher fluences the field increases from the injecting contact and quickly reaches a constant value. Once the current increases exponentially the electric field seems to have a maxi-

mum near the injecting contact and then decreases approximately linearly towards the contact opposite to the injecting contact. The space charge seems to be almost constant and positive in the bulk in this regime. Positive space charge is contrary to the expectation of injected electrons traversing the bulk. It seems like holes are drawn towards the electron-injecting contact. Accordingly, the increase of the conductivity at high forward bias voltages might be due to an increase of the hole concentration in the bulk rather than an increase of the electron concentration.

6. The charge collection length for forward bias

The edge-TCT measurements of highly irradiated strip sensors indicate an almost constant electric field $E(x)$ for forward bias as demonstrated in sec. 5.2. Assuming a constant electric field makes the equations for charge collection much simpler as the drift velocity can also be assumed constant. The equations for charge collection become purely geometrical if the drift velocity is independent of $x\,(t)$.

A model was developed to analyze TCT measurements of the charge collection efficiency CCE of pad diodes discussed in sec. 6.1. Additionally, the model was extended to analyze normalized charge profiles, „charge collection efficiency profiles", obtained from edge-TCT measurements with strip sensors as discussed in sec. 6.2. The results are compared and concluded in sec. 6.3.

6.1. Measurements of pad diodes

6.1.1. Analysis

Determination of the charge collection length If the electric field $E(x)$, the trapping times $\tau(x)$, and the drift velocities $v(x)$ for electrons and holes are assumed to be independent of the depth in the sensors x, a simple quantity can be introduced to describe the charge collection efficiency: The charge collection length $\lambda_{ccl}\,(E) = \tau\,(E) \cdot v\,(E)$. It should be possible to determine $\lambda_{ccl}^{e,h}$ of electrons and holes from TCT measurements of silicon diodes under forward bias using red light. Because the absorption length λ_{abs} of red light is very short, the charge collection efficiency CCE measured by illumination of the front side or the back side with red light is dominated by the drift of either electrons or holes. Accordingly, it should be possible to obtain $\lambda_{ccl}^{e,h}$ from these measurements.

For an arbitrary λ_{abs} the integral of the current transient induced by a light

pulse is the sum of the electron and the hole contributions

$$\underset{\rightarrow}{Q} = q_0 \cdot \frac{\int_0^d \left(\int_{x_0}^d e^{-\frac{x_0}{\lambda_{abs}}} \cdot e^{-\frac{x-x_0}{\lambda_{ccl}^e}} dx \right) \mathrm{d}x_0 + \int_0^d \left(\int_0^{x_0} e^{-\frac{x_0}{\lambda_{abs}}} \cdot e^{-\frac{x_0-x}{\lambda_{ccl}^h}} dx \right) \mathrm{d}x_0}{d\lambda_{abs} \left(1 - e^{-\frac{d}{\lambda_{abs}}}\right)} \tag{6.1}$$

if the electrons are collected opposite to the illuminated electrode, denoted by the arrow $\underset{\rightarrow}{Q}$. The charge collection efficiency is $CCE = \underset{\rightarrow}{Q}/Q_0$ with the deposited charge $Q_0 = q_0$. On the other hand, if the holes are collected at the electrode opposite to the illuminated electrode, all λ_{ccl}^e have to be replaced with λ_{ccl}^h and vice versa, denoted by $\underset{\leftarrow}{Q}$. Executing the integrals yields

$$\underset{\rightarrow}{Q} = q_0 \cdot \frac{\frac{\lambda_{ccl}^e \left(\lambda_{ccl}^e \left(1 - e^{-\frac{d}{\lambda_{ccl}^e}} \right) + \lambda_{abs} \left(e^{-\frac{d}{\lambda_{abs}}} - 1 \right) \right)}{\lambda_{ccl}^e - \lambda_{abs}} + \lambda_{ccl}^h \left(1 - e^{-\frac{d}{\lambda_{abs}}} + \frac{e^{-d\left(\frac{1}{\lambda_{abs}} + \frac{1}{\lambda_{ccl}^h}\right)} - 1}{1 + \frac{\lambda_{abs}}{\lambda_{ccl}^h}} \right)}{d \left(1 - e^{-\frac{d}{\lambda_{abs}}}\right)}. \tag{6.2}$$

If $\lambda_{abs} \ll d$ is assumed (red light) the fraction of the deposited charge drifting towards the illuminated electrode is approximately $\frac{\lambda_{abs}}{d}$. If $\lambda_{abs} \ll \lambda_{ccl}^h$ trapping can be neglected for the charge drifting towards the illuminated electrode.[1] However, the fraction of charge drifting towards the opposite electrode is approximately $1 - \frac{\lambda_{abs}}{d}$ and the charge carriers have to drift through the whole sensor. Taking trapping of the carriers drifting to the opposite electrode into account, the total collected charge can be approximated by

$$\underset{\rightarrow}{Q} \approx q_0 \cdot \left(\frac{\lambda_{ccl}^e}{d} \cdot \left(1 - \frac{\lambda_{abs}}{d}\right) \left(1 - e^{-\frac{d}{\lambda_{ccl}^e}}\right) + \frac{\lambda_{abs}}{d} \right) \tag{6.3}$$

if the electrons are collected opposite of the illuminated electrode. $\lambda_{ccl}^{e,h}$ can now be approximated individually for electrons and holes by illumination of the electrode at the front side or the back side.

A further approximation $\lambda_{ccl}^{e,h} \approx d \cdot \left(CCE - \frac{\lambda_{abs}}{d}\right) / \left(1 - \frac{\lambda_{abs}}{d}\right)$ is used to calculate starting values for a zero finding algorithm of ROOT for the approximation for

[1] For red light $\lambda_{abs}\,(670\,\mathrm{nm}) = (7.6 \cdot T + 720)^{-1}\,\mathrm{cm}$ of ref. [147] was used as an approximation for 675 nm.

red laser light illumination

$$0 \approx \frac{\lambda_{ccl}^{e}}{d} \cdot \left(1 - \frac{\lambda_{abs}}{d}\right)\left(1 - e^{-\frac{d}{\lambda_{ccl}^{e}}}\right) + \frac{\lambda_{abs}}{d} - CCE \tag{6.4}$$

derived from eq. 6.3.

Charge collection for infrared light For illumination with infrared light also reflection of the light at the air-silicon-interface ($\hat{T}_a$, $\hat{R}_a$) and the rear silicon-aluminum-interface ($\hat{R}_b$) has to be taken into account (see sec. 3.3.1).[2] The same model illustrated in figure 4.4 is used. Since now $\hat{R}_a \neq \hat{R}_b$ the intensities I_l have to be split into odd parts

$$I_l^{odd} = I_0 \hat{T}_a \left(e^{-\frac{d}{\lambda_{abs}}}\right)^{l-1} \left(\hat{R}_a \hat{R}_b\right)^{\frac{l-1}{2}}, \; l \geq 1 \tag{6.5}$$

and even parts

$$I_l^{even} = I_0 \hat{T}_a \left(e^{-\frac{d}{\lambda_{abs}}}\right)^{l-1} \hat{R}_a^{\frac{l-2}{2}} \hat{R}_b^{\frac{l}{2}}, \; l \geq 2. \tag{6.6}$$

The absorbed intensity is now

$$A_i^{even,odd} = I_{i+1}^{even,odd} \left(1 - e^{-\frac{d}{\lambda_{abs}}}\right), \; i \geq 0 \tag{6.7}$$

and the total absorbed intensity is the sum over all parts

$$\begin{aligned} A_{tot} &= \sum A_i^{even} + \sum A_i^{odd} = \left(1 - e^{-\frac{d}{\lambda_{abs}}}\right) \cdot \left[\sum_{i=0}^{\infty} I_{2i+2}^{even} + \sum_{i=0}^{\infty} I_{2i+1}^{odd}\right] \\ &= I_0 \hat{T}_a \left(1 - e^{-\frac{d}{\lambda_{abs}}}\right) \cdot \left[\left(1 + \hat{R}_b e^{-\frac{d}{\lambda_{abs}}}\right) \sum_{i=0}^{\infty} \left(\hat{R}_a \hat{R}_b e^{-\frac{2d}{\lambda_{abs}}}\right)^i\right] \\ &= I_0 \cdot \hat{T}_a \frac{\left(1 - e^{-\frac{d}{\lambda_{abs}}}\right) \cdot \left(1 + \hat{R}_b e^{-\frac{d}{\lambda_{abs}}}\right)}{1 - \hat{R}_a \hat{R}_b e^{-\frac{2d}{\lambda_{abs}}}}. \end{aligned} \tag{6.8}$$

Since the photon density in the TCT measurements is below $10^{12}\,\mathrm{cm}^{-2}$ two-photon absorption and free carrier (intraband) absorption (see ref. [99]) is assumed to be negligible. Therefore, only single-photon interband absorption contributes and the intensity loss and A_{tot} is proportional to the number of generated electron-hole pairs q_0.

In order to take trapping into account the collected charge Q_i, $i \geq 0$ has to be calculated for each order of reflection with eq. 6.2. Now, q_0 is replaced by e and the deposited charge is accounted for by $A_i^{even,odd}$. Each reflection is treated

[2] Oxide layers and possible passivation layers are neglected here.

as alternating top and bottom illumination with decreasing light intensity. The odd parts are $Q_i^{odd} = A_i^{odd} \underset{\rightarrow}{Q}$ while the even parts are $Q_i^{even} = A_i^{even} \underset{\leftarrow}{Q}$. Following eq. 6.8, the total collected charge becomes

$$Q = I_0 \cdot \hat{T}_a \frac{\left(1 - e^{-\frac{d}{\lambda_{abs}}}\right) \cdot \left(\underset{\rightarrow}{Q} + \underset{\leftarrow}{Q} \hat{R}_b e^{-\frac{d}{\lambda_{abs}}}\right)}{1 - \hat{R}_a \hat{R}_b e^{-\frac{2d}{\lambda_{abs}}}} \tag{6.9}$$

for electrons being collected at the electrode opposite of the illuminated electrode, taking reflections into account. If there is no trapping $\underset{\rightarrow}{Q} = \underset{\leftarrow}{Q} = q_0 = e$ and the total collected charge is the deposited charge $Q = eA_{tot} \equiv Q_0$. The charge collection efficiency is $CCE = Q/Q_0$. It should be noted that $Q_0\left(\lambda_{abs}\left(\Phi_{eq}\right)\right)$ also depends on the fluence with $\lambda_{abs}\left(\Phi_{eq}\right)$ of chapter 4.

For the final analysis eq. 6.2 is used to fit $\lambda_{ccl}^{e,h}$ simultaneously to the values of $CCE_{red}^{front} = \underset{\rightarrow}{Q}/Q_0$ and $CCE_{red}^{back} = \underset{\leftarrow}{Q}/Q_0$ for front side and back side illumination of p-bulk diodes with red laser light. For initially n-type bulk diodes $CCE_{red}^{front} = \underset{\leftarrow}{Q}/Q_0$ and $CCE_{red}^{back} = \underset{\rightarrow}{Q}/Q_0$ for back illumination. For the starting values of $\lambda_{ccl}^{e,h}$ the results of the zero finding algorithm described earlier are used. The fitted values of $\lambda_{ccl}^{e,h}$ are then used to calculate the CCE for illumination with infrared laser light using eq. 6.2, 6.9 with $\lambda_{abs}\left(\Phi_{eq}\right)$ for the infrared light of eq. 4.14 and compared to the measurements. If the assumptions of constant electric field and constant trapping are fulfilled, the measured CCE_{IR} for infrared light should be reproduced using the values $\lambda_{ccl}^{e,h}$ extracted from $CCE_{red}^{front,back}$ - as long as $\lambda_{abs}\left(\Phi_{eq}\right) = const$ for red light.

Fit of the drift velocities and trapping times It should be possible to extract the drift velocities $v_{e,h}$ and the trapping times $\tau_{e,h}$ fitting a transient current simulation (see appendix B) to measurements using the values of $\lambda_{ccl}^{e,h} = \tau_{e,h} \cdot v_{e,h}$ determined as described above. Assuming $E = const$, the transient current is

$$I\left(t\right) = Q_0\left(\Phi_{eq}\right) \cdot \left(v_e \exp\left(-t \cdot \frac{v_e}{\lambda_{ccl}^e}\right) + v_h \exp\left(-t \cdot \frac{v_h}{\lambda_{ccl}^h}\right)\right). \tag{6.10}$$

Accordingly, the drift velocities $v_{e,h}\left(\Phi_{eq}\right)$ can be fitted and $\tau_{e,h} = \lambda_{ccl}^{e,h}/v_{e,h}$ can be calculated with the fitted drift velocities.

Unfortunately, this procedure is difficult for very fast current pulses since the information in the transient current pulse is very limited. The measured pulse is dominated by the electronics transfer function. Still, the integral of the current transient and the shape of the oscillations after the signal should be sufficient for a fit as long as the response of the setup is linear. However, it was found

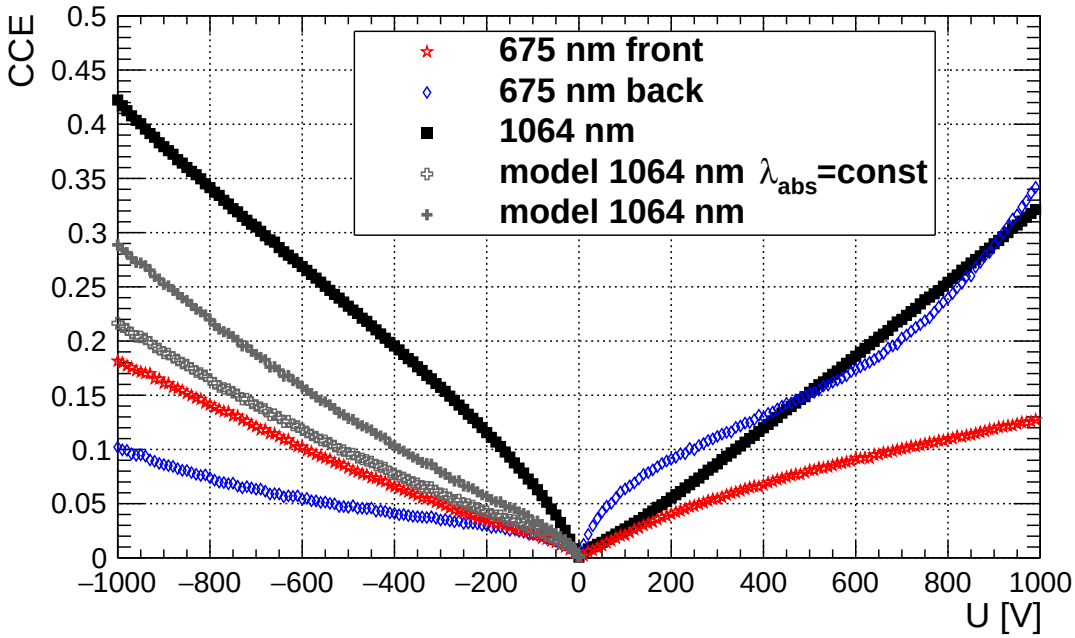

Figure 6.1.: Measured and calculated CCE for red and infrared light illumination of a $d = 200\,\mu\text{m}$ p-bulk pad diode irradiated to $1.3{\cdot}10^{16}\,\text{cm}^{-2}$ at 243 K. For forward bias (negative) red light illumination of the front side corresponds to electron drift (stars) and hole drift for illumination of the back side (diamonds). For reverse bias (positive) the drift direction are reversed, stars show hole drift and diamonds electron drift. For forward bias the CCE for illumination with infrared light was calculated with eq. 6.9 from the $\lambda_{ccl}^{e,h}$ obtained from the red light CCE using a constant absorption length (open crosses) and the fluence dependent absorption length (crosses).

that the response is not linear for the diode TCT setup. For very small signal amplitudes ($CCE \lesssim 10\,\%$), the measured undershoot after the signal has a higher frequency than the electronics response function obtained for a non-irradiated diode. The non-linear response of the read-out electronics to extremely small signal amplitudes of irradiated sensors makes fitting with a linear model impossible. Still, this method should be applicable for linear setups.

6.1.2. Results

For the infrared light measurements the laser is scanned over the window in the pad electrode to find the position with the highest collected charge. This is needed in order to make sure the laser spot is fully contained in the pad window. The back side of the sensors features a highly reflective aluminum grid as a contact and the internal reflection is larger if the back side aluminum is illuminated instead of the windows of the grid. Eq. 6.9 does take this into account and it is assumed that

the laser beam is fully contained in the 1 mm width of the back side aluminum grid. The reflectivity is $\hat{R}_b = 0.87$ at the silicon-aluminum interface.[3]

Figure 6.1 shows the measured CCE for illumination with red light and infrared light for forward and reverse bias voltages. The CCE for illumination with infrared light is higher under forward bias than reverse bias.

The CCE for infrared light is calculated with the model described above using the fluence-dependent absorption length of eq. 4.13 for infrared light. $\lambda_{ccl}^{e,h}$ is obtained from the measurements with red light assuming $\lambda_{abs}\left(675\,\mathrm{nm}, \Phi_{eq}\right) = const.$ The measured CCE for illumination with infrared light is not reproduced; even if the measured fluence-dependent absorption coefficient is used. The results are similar for all fluences and different diodes: The calculated CCE for infrared light is always smaller than the measured value.

There are several possible explanations why this method does not work as expected. First of all, the electric field is not constant. At the electron-injecting junction the electric field decreases (SCLC, see sec. 5.4). This means, that λ_{ccl}^{e} is underestimated for this method. Measurements have been performed with DC illumination of the non-injecting contact and simultaneous hole injection by red laser light. It was found that the CCE for hole drift is greatly reduced by the additional SCLC from the DC illumination.

Additionally, the normalization Q_0 might be wrong for red light. It is possible, that the absorption of red light in the oxide, the passivation, and the silicon also increases similar to the increase of the absorption of infrared light in silicon with the fluence. This would mean that less red light reaches the bulk silicon due to additional absorption in the oxide and the implants and less charge Q_0 is created for irradiated diodes.

Another issue is given by a peculiar behavior of the non-irradiated HPK p-type bulk diodes (see tab. 3.2). It was found that the hole lifetime in the highly doped n^+-implant is unusually long (see ref. [148]). It is so long that free holes generated in the zero-field n^+-implant can diffuse into the high-field SCR and contribute to the current. The delayed diffusion current of the injected holes lasts up to 3 ns. The contribution of the diffusing holes from the implant to the total charge is estimated to be 20 % for illumination with red light. For highly irradiated diodes the lifetimes are decreasing so most of the free holes generated in the implant will recombine before they can diffuse into the SCR. Accordingly, the CCE is reduced for red light illumination of the n^+-implant of the p-type bulk diodes. However, the method does not work for n-type bulk diodes as well, where this effect is not

[3] Using the complex Fresnel equation with $n = 1.22$ and the imaginary extinction coefficient $k = 10.5$ for aluminum and 1064 nm light.

observed.

Concluding, the method cannot be applied due to several difficulties. The assumption of a constant electric field is not justified at injecting contact, where the field is close to zero (see sec. 5.2). Additionally, the normalization of the charge collection efficiency for illumination with red light is not precisely known since the number of the generated carriers reaching the SCR changes. Carriers diffusing from the highly doped implants are lost with irradiation and the absorption length of red light in the silicon and/or the SiO_2 might change with irradiation. Using light with a slightly longer absorption length in silicon can reduce these effects since the field is more homogeneous further from the injecting contact and proportionally less charge is deposited in the implants compared to the bulk.

6.2. Measurements with strip sensors

Here, the charge collection lengths are obtained from edge-TCT measurement of the strip sensors introduced in sec. 3.1.3 with initial n-type bulk. For forward bias electrons drift towards the strips while holes drift towards the back side.

6.2.1. Analysis

The charge profile is obtained by summing up the transient current pulses at each depth x in the strip sensor as described in sec. 3.3.2.

For forward bias the charge profile can be described similar to the model above. Again, the electric field is assumed to be constant for highly irradiated sensors. Now, the initial charge distribution for illumination of a certain position x in the sensor with a Gaussian light beam is

$$Q_0(x) = \frac{Q_0}{\sigma\sqrt{2\pi}} \cdot e^{-\frac{(x_0-x)^2}{2\sigma^2}} \tag{6.11}$$

with the standard deviation $\sigma = \omega/2$ (compare eq. 3.1), the position of the laser beam x_0, and the position in the sensor x.

Similar to eq. 6.1 the charge profile is

$$Q(x) = \frac{\int_0^d \left(\int_{x_0}^d Q_0(x) \cdot e^{-\frac{x-x_0}{\lambda_{ccl}^e}} dx \right) dx_0 + \int_0^d \left(\int_0^{x_0} Q_0(x) \cdot e^{-\frac{x_0-x}{\lambda_{ccl}^h}} dx \right) dx_0}{\sigma d \cdot \sqrt{2\pi}} \tag{6.12}$$

with the charge collection lengths of electrons and holes $\lambda_{ccl}^{e,h}$ and the thickness of the sensor d. Figure 6.2 shows the charge profile calculated with this model for

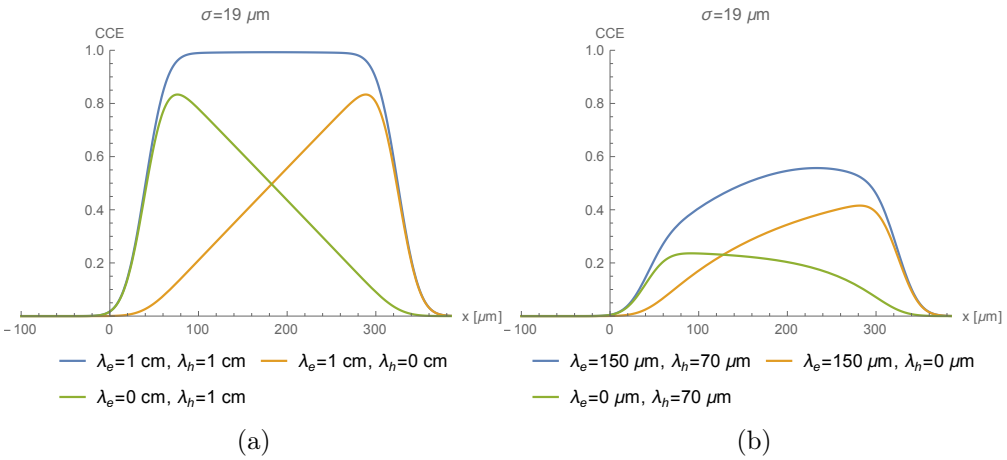

(a) (b)

Figure 6.2.: Charge profiles calculated with eq. 6.12 for a sensor with $d = 285\,\mu\text{m}$. (a) Shows a non-irradiated sensor (blue) and the contributions of electrons (yellow) and holes (green). (b) Shows the model for $\lambda^e_{ccl} = 150\,\mu\text{m}$ and $\lambda^h_{ccl} = 70\,\mu\text{m}$.

$\sigma = 19\ \mu\text{m}$ and different charge collection lengths. A parameter $x_s = 40\,\mu\text{m}$ is introduced to describe the shift of the sensor surface relative to $x = 0$. The limits of the integrals become $0 \to x_s$ and $d \to d + x_s$.

In order to fit the model to measurements of charge profiles under forward bias an offset

$$Q_{off}(x) = Q_{off,0} \cdot \left(\frac{1}{2}\left(\text{erf}\left(\frac{x_s - x}{\sigma\sqrt{2}}\right) - \text{erf}\left(\frac{x_s + d - x}{\sigma\sqrt{2}}\right)\right) + 1\right) \tag{6.13}$$

is added to eq. 6.12 to account for stray light entering the sensor if the beam exits the sensor bulk.[4] This is probably a fair approximation since zero charge is observed if the beam is in the non-depleted region of an partially depleted, non-irradiated sensor. At the same time, if the beam exits the sensor bulk almost constant charge $Q_{off,0}$ is measured which is similar outside the front side and the back side of the sensor (see fig. 4.11(a) of [85]).

Additionally, refraction of the laser beam at the corners of the edge of the sensor has to be accounted for since the corners are rounded from the polishing. Additionally, there is probably internal reflection of the beam as the strips are more than 1 mm from the edge. If the beam is moved towards the corners of the sensor edge the transient current pulse becomes similar to infrared illumination of a diode or edge illumination of a strip sensor with a defocused beam (see sec. 3.4, 4.1.3 of [85]). In other words, the initial charge distribution becomes close to uniform

[4] The sensor bulk is between $x = x_s$ and $x = x_s + d$ in fig. 6.2.

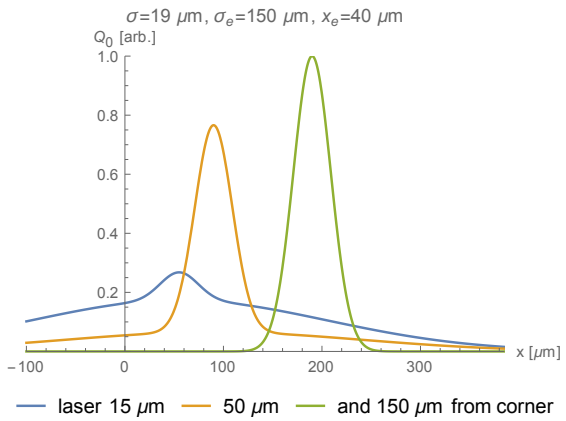

Figure 6.3.: Initial charge distribution calculated with eq. 6.14 for different distances from the sensor corner. The beam has $\sigma = 19\,\mu\text{m}$ and the refracted part at the corners is a Gaussian with $\sigma = 150\,\mu\text{m}$ with an area equal to the integral of the initial beam within $x_e = 40\,\mu\text{m}$ from the sensor edges at $x_s = 40\,\mu\text{m}$ and $d + x_s = 325\,\mu\text{m}$.

in the sensor. Therefore, an edge parameter x_e is introduced. It is assumed equal for both the front and the back corners. If the integral of the initial charge distribution $Q_0(x)$ (eq. 6.11) within x_e from the sensor edges is > 0 a second Gaussian distribution with σ_e is added so the initial charge distribution is the sum of two Gaussian distributions. The initial charge distribution becomes

$$Q_0(x) = Q_0 \cdot \left(N_1\left(x_0\right) \cdot e^{-\frac{(x_0-x)^2}{2\sigma^2}} + N_2(x_0) \cdot e^{-\frac{(x_0-x)^2}{2\sigma_e^2}}\right) \tag{6.14}$$

with the normalizations

$$N_1(x_0) = \frac{1}{2}\left(\operatorname{erf}\left(\frac{x_0 - x_e - x_s}{\sigma\sqrt{2}}\right) - \operatorname{erf}\left(\frac{-d + x_0 + x_e - x_s}{\sigma\sqrt{2}}\right)\right) \tag{6.15}$$

and

$$N_2(x_0) = \frac{\sigma \cdot \left(\operatorname{erf}\left(\frac{-d+x_0+x_e-x_s}{\sigma\sqrt{2}}\right) + \operatorname{erf}\left(\frac{d-x_0+x_s}{\sigma\sqrt{2}}\right) - \operatorname{erf}\left(\frac{x_0-x_e-x_s}{\sigma\sqrt{2}}\right) + \operatorname{erf}\left(\frac{x_0-x_s}{\sigma\sqrt{2}}\right)\right)}{\sigma_e\left(\operatorname{erf}\left(\frac{d-x_0+x_s}{\sigma_e\sqrt{2}}\right) + \operatorname{erf}\left(\frac{x_0-x_s}{\sigma_e\sqrt{2}}\right)\right)}. \tag{6.16}$$

Figure 6.3 shows examples of initial charge distributions for different beam positions x_0. Instead of a second Gaussian contribution also a constant contribution was tested, with very similar results.

The charge profile $Q\left(x\right)$ is now obtained by plugging eq. 6.14 into eq. 6.12 and executing the integrals. The formula is not shown here since it is very lengthy.

Figure 6.4 shows the comparison of $Q\left(x\right)$ using the $Q_0(x)$ of eq. 6.11 and eq. 6.14 for the charge profiles calculated with eq. 6.12 for a sensor with trapping. More

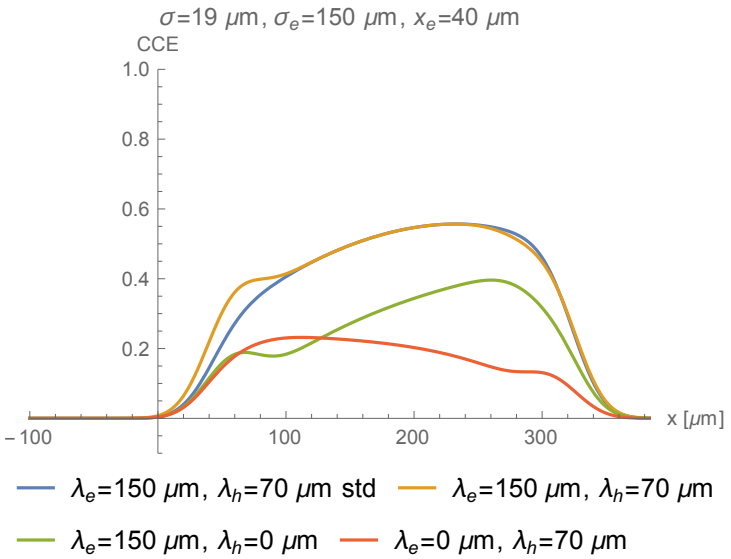

Figure 6.4.: Charge profiles calculated with eq. 6.12 for a sensor with $d = 285\,\mu\text{m}$ with $\lambda^e_{ccl} = 150\,\mu\text{m}$ and $\lambda^h_{ccl} = 70\,\mu\text{m}$. The blue line was calculated with an initial charge distribution according to eq. 6.11. The yellow line was calculated with eq. 6.14 to model refractions of the laser beam near the corners of the sensor edge. The individual contributions of electrons and holes are shown in green and red, respectively.

charge is observed near the front side and less charge near the back side of the sensor if the refraction model (eq. 6.14) is used. This is because $\lambda^e_{ccl} > \lambda^h_{ccl}$. As the initial charge distribution gets broader near the corners electrons contribute more to the measured charge if the laser beam is near the front side of the sensor - the local $Q(x)$ increases - or holes contribute more to the measured charge if the beam is near the back side of the sensor - the local $Q(x)$ decreases. The $FWHM$ of $Q(x)$ is larger if the model for refraction is used which is reproduced in measurements, as discussed below.

In total there are 9 fit parameters, most of which were fixed for the final determination of $\lambda^{e,h}_{ccl}$. The thickness was always fixed to the thickness of the bulk $d = 285\,\mu\text{m}$. The initially generated charge Q_0 was always fixed to the value measured for a reverse biased, non-irradiated sensor above full depletion. Q_0 was corrected with eq. 4.13, 4.15 for the change of the absorption coefficient $\alpha\,(\Phi_{eq}, T)$ and with eq. 4.1 for the distance of the strip from the edge in order to use the total CCE as constraint.[5] The standard deviation of the Gauss beam σ, the width of the second Gauss at the edge σ_e, the corner parameter x_e, and the shift of the corner x_s were free for the first iterations and subsequently fixed at the fit results

[5]It should be noted that an earlier value $\Phi_{abs}\,(1064\,\text{nm}) = 4.3{\cdot}10^{16}\,\text{cm}^{-2}$ was used instead of the value given in chapter 4. The values of $\lambda^{e,h}_{ccl}$ are underestimated by up to 3 % at the highest fluence due to this. However, given the total uncertainty of the method this is neglected here.

to allow the fit to converge more reliably.[6] If a significant part of the measurement was with the beam outside of the sensor volume the charge offset $Q_{off,0}$ of eq. 6.13 was left free for the final fit. Otherwise, it was set to zero. The only parameters which were always free in the final fit are the charge collection lengths $\lambda_{ccl}^{e,h}$.

This model does not take into account that the width of the beam $\omega(z)$ (see eq. 3.1) changes from the edge to the strips, which are $\Delta z = 1350\,\mu\text{m}$ and $\Delta z = 1750\,\mu\text{m}$ from the edge. For example when the focus is between the strips the equations above assume the charge distribution under strips is very wide while it is actually much narrower; the beam is wide only at the edge and then decreases until the minimum is reached between the strips. If this is taken into account the shape of the charge profile changes slightly. However, the formulas get very complicated and the change is more pronounced if the focus is at the edge; but, most measurements have been performed with the focus between the strips where the effect is marginal. This level of accuracy is probably not needed here given the not completely fulfilled assumption of a constant electric field and the uncertainty of the temperature, to name two factors.

6.2.2. Results

Figure 6.5 shows the measured charge profiles for an irradiated sensor and the fits of eq. 6.12 with eq. 6.13 and eq. 6.14. Fig. 6.5(a) shows the measurements with the focus between the read-out strips yielding $\sigma = 22.5\,\mu\text{m}$, $x_e = 37\,\mu\text{m}$, and $\sigma_e = 110\,\mu\text{m}$. The focus of the beam was at the edge for fig. 6.5(b), yielding $\sigma = 4.5\,\mu\text{m}$, $x_e = 20\,\mu\text{m}$, and $\sigma_e = 120\,\mu\text{m}$. The results for $\lambda_{ccl}^{e,h}$ are very similar for both focus positions. However, the measurements seem to be a bit more sensitive to λ_{ccl} if the focus is placed at the edge. Still, most measurements were performed with the focus between the read-out strips.

It is apparent from fig. 6.5(b) that the charge profile decreases at the injecting contact (at $x \approx 300\,\mu\text{m}$), especially at low bias voltages. The reason is the decrease of the electric field due to SCLC, as discussed in sec. 5.4. Accordingly, the assumption of a constant electric field is not fulfilled in this region and λ_{ccl}^{h} is overestimated while λ_{ccl}^{e} is underestimated. The effect is relevant for low bias voltages, where the field increases slower from the injecting contact, and low fluences, where the transition region with non-constant field is larger.

[6] For some measurements x_s was free in the fit since the supply lines sometimes forced a drag on the moving stages. This can lead to a gradual (negative) x shift of the stage position by up to 10 µm for a complete scan ($\sim 2\,\text{nm}$ per step Δx), also observed for non-irradiated sensors.

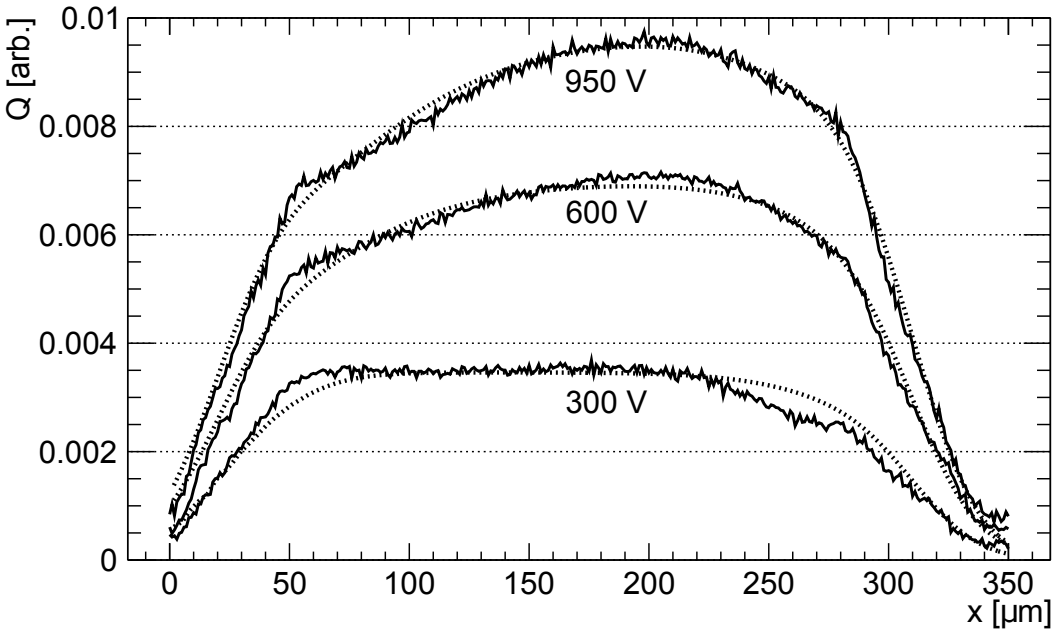

(a)

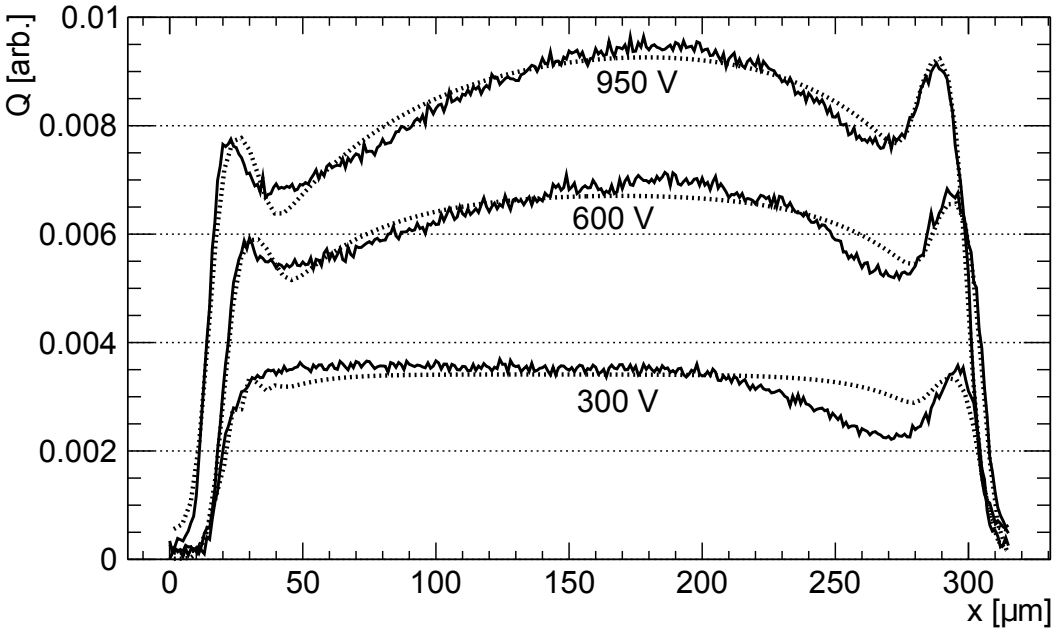

(b)

Figure 6.5.: Charge profiles of the second read-out strip $Q_2(x)$ of the strip sensor irradiated to $\Phi_{eq} = 7.25{\cdot}10^{15}\,\mathrm{cm}^{-2}$ for forward bias at 243 K. The focus was between the r/o strips in (a) and at the edge in (b). The positive electrode is at $x_s \approx 20\,\mu\mathrm{m}$. The line is the measurement and the dashed line is the fit of eq. 6.12 using $Q_0\,(x)$ of eq. 6.14. The extracted values are $\lambda^e_{ccl} \approx 62\,\mu\mathrm{m}$ and $\lambda^h_{ccl} \approx 41\,\mu\mathrm{m}$ at 950 V, $\lambda^e_{ccl} \approx 40\,\mu\mathrm{m}$ and $\lambda^h_{ccl} \approx 31\,\mu\mathrm{m}$ at 600 V, and $\lambda^e_{ccl} \approx 14\,\mu\mathrm{m}$ and $\lambda^h_{ccl} \approx 21\,\mu\mathrm{m}$ at 300 V.

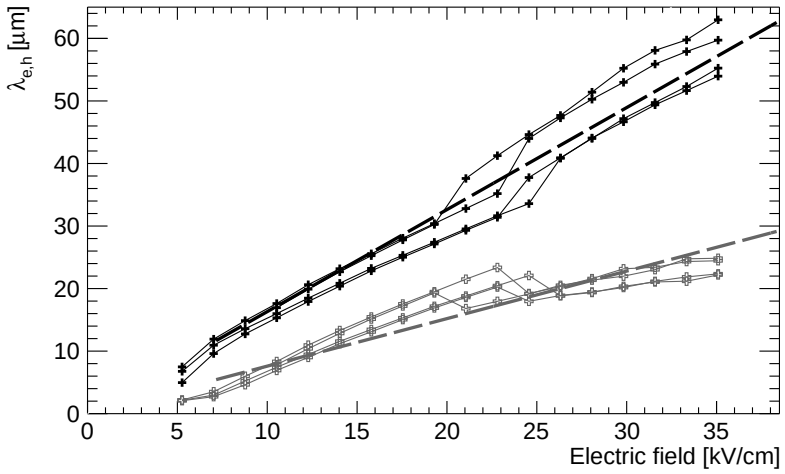

Figure 6.6.: Charge collection lengths of electrons (black) and holes (gray) from the charge profiles of the strip sensor irradiated to $1.3 \cdot 10^{16}\,\mathrm{cm}^{-2}$ at 243 K.

Figure 6.6 shows $\lambda_{ccl}^{e,h}(E)$ determined from repeated measurements of an irradiated sensor. $\lambda_{ccl}^{e,h}(E)$ increases to first approximation linearly with the mean electric field $E = U/d$. Therefore, the fit results can be expressed as $\mu_{e,h}(E)\,\tau_{e,h}(E) = \lambda_{ccl}^{e,h}(E)/E \approx const$. Figure 6.7 shows $\mu_{e,h}(E)\,\tau_{e,h}(E)$ for all measurements combined and the extracted mean values.

The measurements were repeated to increase statistics and to make sure the normalization $Q(x,\Phi_{eq})/Q(x,0)$ is correct. The charge profiles for the first read-out strip were not analyzed if there were large losses compared to the second strip due to wrong positioning of the beam (see sec. 3.3.2, fig. 3.8(b)). It is apparent that the error on the results of $\mu\tau$ is very large, especially for small E. In some cases the fitted charge collection length of holes is suddenly higher than for electrons. The reason is the transition region at the electron injecting contact, which leads to overestimation of λ_{ccl}^{h} at low voltages since the parameters $\lambda_{ccl}^{e}(E)$ and $\lambda_{ccl}^{h}(E)$ can be exchanged leading to the same $Q(x)$ if $\lambda_{ccl}^{e,h}(E) \lesssim \sigma$.

It is surprising to find $\mu_{e,h}(E)\,\tau_{e,h}(E) \approx const$ as $\mu_{e,h}(E)$ decreases with increasing E. Accordingly, $\tau_{e,h}(E) \neq const$ for forward bias. The trapping times of electrons and holes $\tau_{e,h}(E)$ seem to increase with increasing mean electric field. An interpretation is that the fraction of filled traps increases with E due to the increasing current density, leading to decreasing $\tau_{e,h}(E)$. It was expected that mostly the fraction of filled electron traps increases for forward bias since electrons are injected into the sensor (see sec. 5.4). However, it seems like hole traps are filled as well since also $\tau_h(E)$ increases. A reason could be compensation of the space charge of trapped electrons similar to the neutral bulk discussed in sec. 5.3.1.

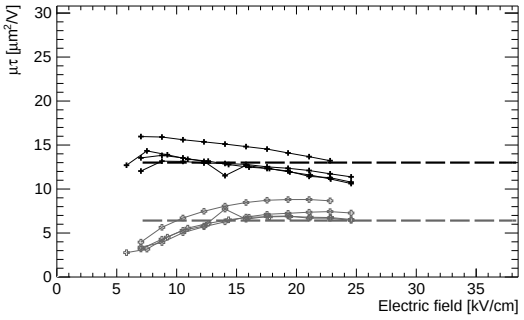

(a) $1.3 \cdot 10^{16}\,\mathrm{cm}^{-2}$ at 253 K

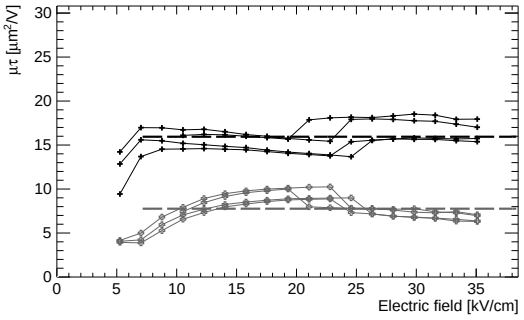

(b) $1.3 \cdot 10^{16}\,\mathrm{cm}^{-2}$ at 243 K

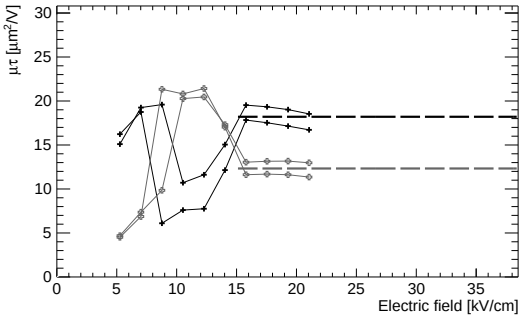

(c) $9.4 \cdot 10^{15}\,\mathrm{cm}^{-2}$ at 253 K

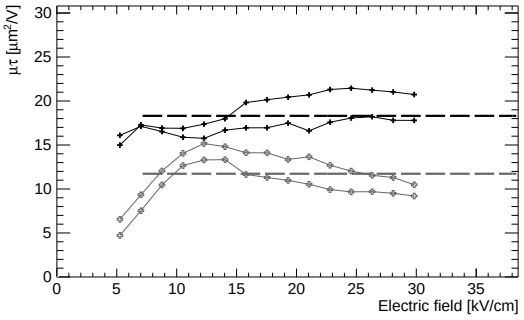

(d) $9.4 \cdot 10^{15}\,\mathrm{cm}^{-2}$ at 243 K

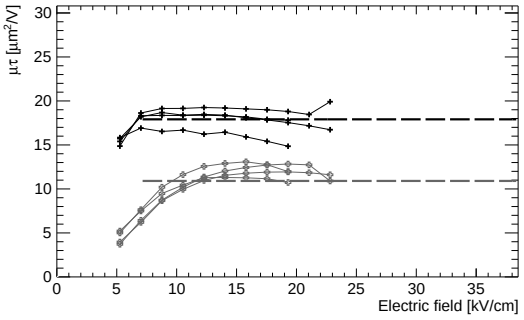

(e) $7.3 \cdot 10^{15}\,\mathrm{cm}^{-2}$ at 253 K

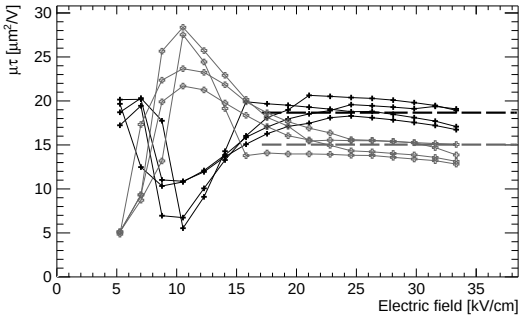

(f) $7.3 \cdot 10^{15}\,\mathrm{cm}^{-2}$ at 243 K

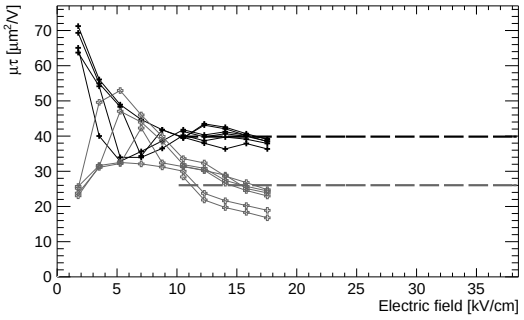

(g) $4.4 \cdot 10^{15}\,\mathrm{cm}^{-2}$ at 253 K

Figure 6.7.: $\mu_{e,h}(E)\,\tau_{e,h}(E) = \frac{\lambda^{e,h}_{ccl}(E)}{E}$ for the measured charge profiles of all sensors. The dashed lines are the mean values for electrons (black) and holes (gray) in the plotted region of E. Note the different scale of the y-axis for (g).

The velocity profiles have shown a small positive and constant space charge density for high injection levels (see sec. 5.2), meaning hole traps are probably being filled. Unfortunately, the mechanism is not yet understood.

For some measurements a slight decrease of $\mu_{e,h}(E)\,\tau_{e,h}(E)$ at the highest E is observed[7] which may be caused by heating of the sensors. However, this effect is rather small.

Figure 6.8 shows the mean $1/(\mu_{e,h}\tau_{e,h}) = E/\lambda_{ccl}^{e,h}$ for all measurements obtained for the values of E where the mean value is plotted in fig. 6.7 (dashed lines). It seems that $\lambda_{ccl}^{e,h}$ hardly depends on the temperature as expected. The fluctuation of the data points is rather large. A linear model is chosen to describe the fluence dependence

$$\frac{1}{\mu_{e,h}\tau_{e,h}}(\Phi_{eq}) - \frac{1}{\mu_{e,h}\tau_{e,h}}(\Phi_{eq}=0) = \Delta_{\mu\tau}^{e,h}\cdot\Phi_{eq}. \tag{6.17}$$

The value $\frac{1}{\mu_{e,h}\tau_{e,h}}(\Phi_{eq}=0) \approx 0$ before irradiation is assumed to be negligible since $\tau_{e,h}$ is very long before irradiation.[8] The fit of eq. 6.17 to the measured parameters yields $\Delta_{\mu\tau}^{e} = (6.19 \pm 0.96)\cdot 10^{-10}\,\mathrm{V}$ for electrons and $\Delta_{\mu\tau}^{h} = (1.00 \pm 0.12)\cdot 10^{-9}\,\mathrm{V}$ for holes.

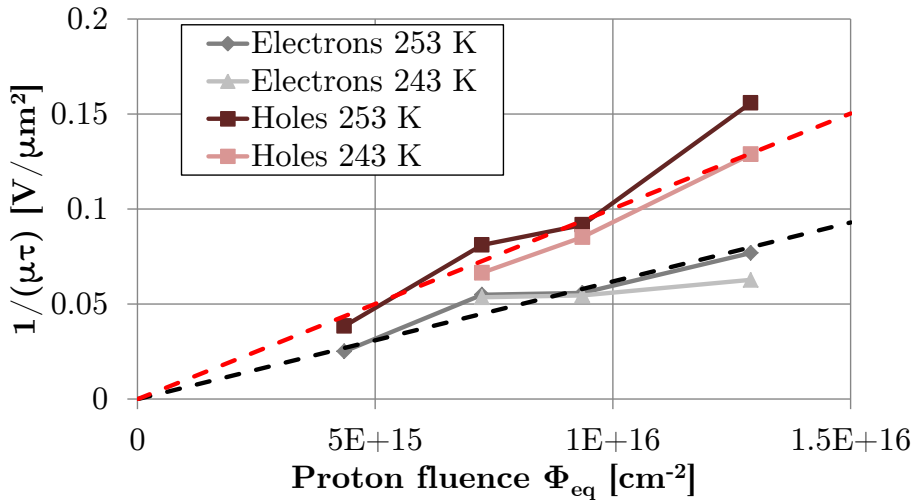

Figure 6.8.: $\frac{1}{\mu_{e,h}\tau_{e,h}}(\Phi_{eq})$ from the all measurements shown in fig. 6.8.

6.3. Comparison of diode and strip sensor results

The values $\frac{1}{\mu_{e,h}\tau_{e,h}}(\Phi_{eq})$ (eq. 6.17) determined from edge-TCT measurements of strip sensors should predict the CCE of pad diodes for illumination with infrared

[7] E.g. for electrons and holes in fig. 6.8(f).
[8] E.g. $\frac{1}{\mu_e\tau_e}(\Phi_{eq}=0) \approx 5\cdot 10^{-8}\,\mathrm{V/\mu m^2}$ assuming $\mu_e = 2200\,\mathrm{cm^2/Vs}$ and $\tau_e = 100\,\mu\mathrm{s}$.

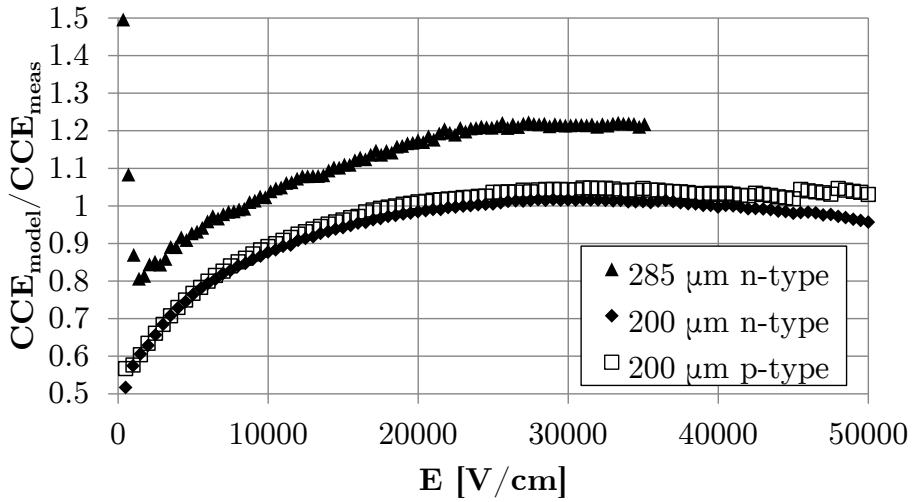

Figure 6.9.: Mean ratios of the calculated CCE with eq. 6.9 using $\mu_{e,h}\tau_{e,h}$ of eq. 6.17 from edge-TCT measurements and the measured CCE for 17 different pad diodes measured at 243 K and 253 K. The fluences are $\Phi_{eq} = (9 \cdot 10^{14} - 1.3 \cdot 10^{16})$ cm^{-2}. The ratios for all pad diodes are given in appendix D.

light. Therefore, $CCE\,(E)$ as a function of the mean electric field E was determined with eq. 6.9 and compared to measurements of the pad diodes discussed in tab. 3.2, 3.3. The change of the absorption length of infrared light has been taken into account as well as internal reflections of the signal.

In total, the predicted CCE is compared to the measured CCE for 17 different diodes of different thickness, initially n-type and p-type bulk, and float-zone and Czochralski silicon, all at $T = 243\,\mathrm{K}$ and $253\,\mathrm{K}$.[9] Measurements were performed with voltage steps of $\Delta U = 10\,\mathrm{V}$. The maximum current was $< 0.5\,\mathrm{mA}$. The diodes are irradiated to fluences between $\Phi_{eq} = 9 \cdot 10^{14}\,\mathrm{cm}^{-2}$ to $1.3 \cdot 10^{16}\,\mathrm{cm}^{-2}$. Most of the measurements discussed here are the average of repeated measurements. The relative error of the measured CCE is estimated to be $5\,\% - 10\,\%$. The results for all diodes are shown in appendix D.

Figure 6.9 shows the mean ratios of the calculated and the measured CCE. For the 200 µm thick initially n-type and p-type diodes the deviation between the calculated and the measured CCE is below 5 % for mean fields $E > 15\,\mathrm{kV/cm}$, which corresponds to bias voltages $U \geq 300\,\mathrm{V}$. At smaller mean fields the model underestimates the measured CCE. However, the deviation between the model and the measurements is up to 20 % for the 285 µm thick n-type diodes. The ratio has an almost constant offset compared to the 200 µm thick diodes. The CCE is overestimated by the model for the 285 µm diodes. This is surprising since the

[9] As mentioned earlier, the CCE hardly depends on the temperature and annealing (ref. [91, 92]).

thicker diodes are from the same wafers as the strip sensors which were used to determine $\frac{1}{\mu_{e,h}\tau_{e,h}}(\Phi_{eq})$.

A distinct shape can be observed in the ratios. Accordingly, it is not a very good approximation to use $\mu_{e,h}(E)\,\tau_{e,h}(E) = const$ at small mean electric fields $E < 15\,\mathrm{kV/cm}$. However, at higher bias voltages it seems to be a good approximation.

Most measurements agree very well with the prediction of the model. There are only a few measurements which show large deviations. An almost constant offset of $15\,\% - 20\,\%$ is observed for the 285 µm thick n-type diodes irradiated to $9.4 \cdot 10^{15}\,\mathrm{cm}^{-2}$ and $1.3 \cdot 10^{16}\,\mathrm{cm}^{-2}$. Additionally, approximately the same offset is observed only for the 200 µm thick p-type diode irradiated with the highest fluence $1.3 \cdot 10^{16}\,\mathrm{cm}^{-2}$. Additionally, two measurements of Czochralski diodes show an approximately constant offset of about 10 % with the opposite sign, the model underestimates the measured CCE. However, in this case only for the measurements performed at 253 K. It is not understood why some measurements show an almost constant offset of the ratios compared to the majority ($> 80\,\%$) of the measurements. This is a very unfortunate result since the model can not be confirmed but it can also not be discarded.

Figure 6.10 shows the comparison of the measured CCE and the model for selected measurements, including one with the large difference between model and measurement.

6.4. Conclusion

More than a hundred CCE measurements of highly irradiated pad diodes have been investigated with the goal of determining the charge collection lengths $\lambda_{ccl}^{e,h}$ of electrons and holes for forward bias. An analysis model has been developed to determine $\lambda_{ccl}^{e,h}$ from TCT measurements of the pad diodes using red light. However, it has been found that $\lambda_{ccl}^{e,h}$ determined in this way does not reproduce the CCE measured with TCT using infrared light.

In a new approach a model has been developed to determine $\lambda_{ccl}^{e,h}$ by fitting the parameters of the model to the charge profiles of strip sensors measured with edge-TCT. The extracted $\lambda_{ccl}^{e,h}(E)$ increase approximately linear with the mean electric field in the investigated range $10\,\mathrm{kV/cm} - 35\,\mathrm{kV/cm}$. Accordingly, $\frac{1}{\mu_{e,h}\tau_{e,h}}(\Phi_{eq}) = E/\lambda_{ccl}^{e,h}(E, \Phi_{eq})$ has been determined and parameterized as a function of the fluence. The results have been used to calculate the expected CCE for the pad diodes measured with the diode TCT setup with infrared light. The measured CCE of the pad diodes is very well reproduced for most diodes for electric fields $15\,\mathrm{kV/cm} -$

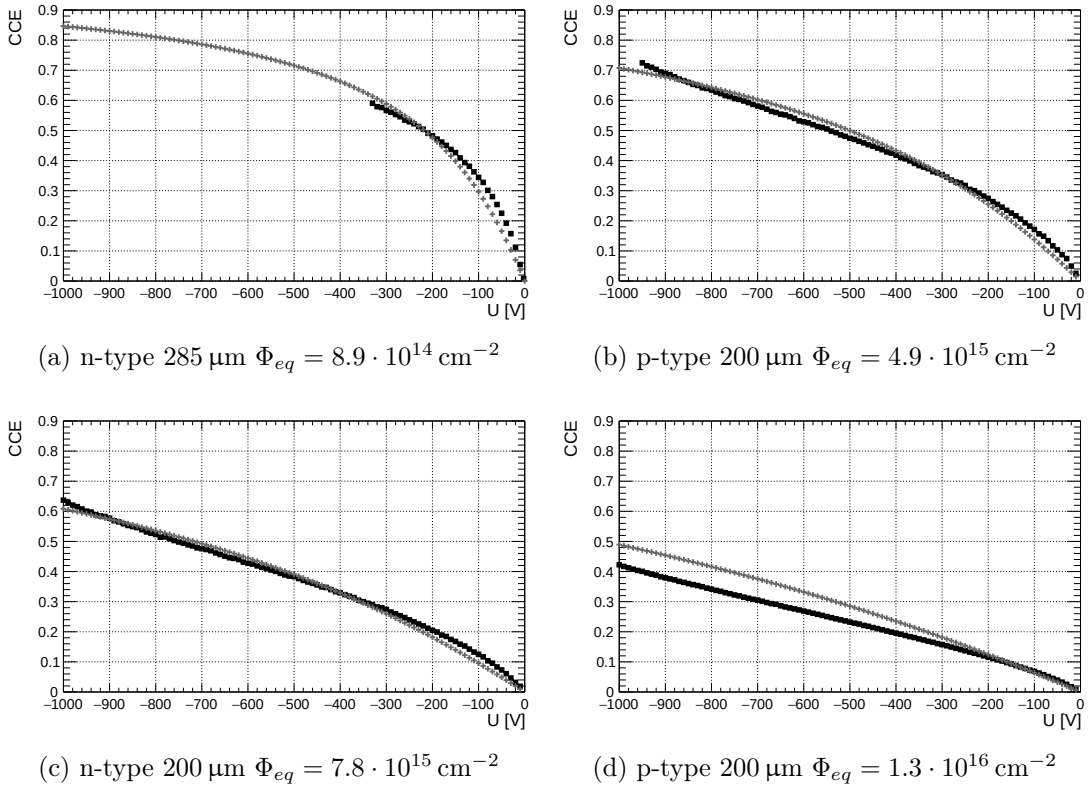

(a) n-type 285 µm $\Phi_{eq} = 8.9 \cdot 10^{14}\,\mathrm{cm}^{-2}$

(b) p-type 200 µm $\Phi_{eq} = 4.9 \cdot 10^{15}\,\mathrm{cm}^{-2}$

(c) n-type 200 µm $\Phi_{eq} = 7.8 \cdot 10^{15}\,\mathrm{cm}^{-2}$

(d) p-type 200 µm $\Phi_{eq} = 1.3 \cdot 10^{16}\,\mathrm{cm}^{-2}$

Figure 6.10.: Comparison of the measured CCE of diodes (black) and the calculated CCE (gray) using eq. 6.9, 6.17 as a function of the bias voltage for selected diodes at 243 K. The fluence, initial bulk doping, and the thickness is given in the captions. (d) Shows a case where the calculated CCE is about 20 % higher than the measured one.

50 kV/cm and fluences $\Phi_{eq} = 9 \cdot 10^{14}\,\mathrm{cm}^{-2} - 1.3 \cdot 10^{16}\,\mathrm{cm}^{-2}$. However, the CCE of the three diodes with the highest fluences is overestimated by the model by about 20 %.

The ratio of the calculated and the measured CCE has a very distinct shape for all measurements. In order to extend the model to smaller E a parameterization should be used which accounts for $\mu_{e,h}(E)\,\tau_{e,h}(E) \neq const$ in the range $E < 15\,\mathrm{kV/cm}$.

7. Measurement of the mobilities

7.1. Non-irradiated silicon

The mobilities of electrons and holes $\mu_{e,h}(E,T)$ in high-ohmic $\langle 100 \rangle$ silicon have been measured as part of a previous thesis and parameterized as a function of the electric field and the temperature. The results were already published in ref. [81, 148, 149]. The results have been obtained by the rather simple time-of-flight *TOF* method and the fit of a simulation to TCT measurements of non-irradiated pad diodes. The different analysis methods are compared to literature values in ref. [148]. Large differences of up to 20 % compared to the commonly used literature values were observed, especially for the hole drift velocity.

A new parameterization of the drift velocities of electrons and holes was introduced which should be used for electric fields $E \lesssim 50\,\mathrm{kV/cm}$ and temperatures $233\,\mathrm{K} \lesssim T \lesssim 333\,\mathrm{K}$. A good description of the data for electron drift was found by the parameterization

$$1/\mu_e(E) = 1/\mu_0^e + E/v_s^e \tag{7.1}$$

with the low-field mobility μ_0 and the saturation velocity v_s. The data for the hole drift is described by

$$1/\mu_h(E) = \begin{cases} 1/\mu_0^h & E < E_0 \\ 1/\mu_0^h + b \cdot (E - E_0) + c \cdot (E - E_0)^2 & E \geq E_0 \end{cases} \tag{7.2}$$

with the parameters b, c, E_0. The temperature dependence of the parameters is given by

$$par_i(T) \;=\; par_i\,(T = 300\,\mathrm{K}) \cdot \left(\frac{T\,[\mathrm{K}]}{300\,\mathrm{K}} \right)^{\alpha_i} \tag{7.3}$$

with the parameter at room temperature $par_i\,(T = 300\,\mathrm{K})$ and the exponent α_i. The values of all parameters of eq. 7.1, 7.2, 7.3 for $\langle 100 \rangle$ silicon are given in tab. 7.1.

In the scope of this thesis the TOF method was modified for a linear field and a linear or constant inverse mobility as discussed in ref. [148]. The drift velocity

		$2.5\,\mathrm{kV/cm} \leq E \lesssim 50\,\mathrm{kV/cm}$		$E \leq 2.5\,\mathrm{kV/cm}$	
		$par_i(T = 300\,\mathrm{K})$	α_i	$par_i(T = 300\,\mathrm{K})$	α_i
Electrons	μ_0^e	$1430\,\mathrm{cm^2/Vs}$	-1.99	$1530\,\mathrm{cm^2/Vs}$	-2.42
	v_{sat}^e	$1.05 \cdot 10^7\,\mathrm{cm/s}$	-0.302	$1.03 \cdot 10^7\,\mathrm{cm/s}$	-0.226
Holes	μ_0^h	$457\,\mathrm{cm^2/Vs}$	-2.80	$464\,\mathrm{cm^2/Vs}$	-2.20
	b	$9.57 \cdot 10^{-8}\,\mathrm{s/cm}$	-0.155	$9.57 \cdot 10^{-8}\,\mathrm{s/cm}$	-0.101
	c	$-3.24 \cdot 10^{-13}\,\mathrm{s/V}$	$-$	$-3.31 \cdot 10^{-13}\,\mathrm{s/V}$	-
	E_0	$2970\,\mathrm{V/cm}$	5.63	$2640\,\mathrm{V/cm}$	0.526

Table 7.1.: The mobility parameters for $\langle 100 \rangle$ silicon of eq. 7.1 for electrons, eq. 7.2 for holes, and eq. 7.3 for the temperature dependence for $233\,\mathrm{K} \lesssim T \lesssim 333\,\mathrm{K}$. The parameters on the right side were obtained fixing the low-field mobility $\mu_0^{e,h}(T)$ and its α_i of Jacoboni et al. [118] and should be used for $E \leq 2.5\,\mathrm{kV/cm}$. The left side should be used for $E \gtrsim 2.5$ kV/cm. The estimated uncertainty is 2.5 % for electrons and 5 % for holes.

determined by the TOF method is $v(E_{tof}) = d/t_{tof}$ with the time-of-flight t_{tof} at the scaled electric field

$$E_{tof} = \left\langle \frac{1}{E(x)} \right\rangle^{-1} = \frac{E_{max} - E_{min}}{\ln(E_{max}/E_{min})} \tag{7.4}$$

for a linear field with the maximum and minimum values $E_{max,min}$. Figure 7.1 shows the comparison of the TOF results using E_{tof} and the mean electric field $\langle E(x) \rangle$ for the determination of $1/\mu_{e,h}(E)$ for two diodes[1] with different U_d. It can be seen how using E_{tof} yields consistent results for both diodes even if the bias voltage is similar to the full-depletion voltage U_d (the smallest E shown for each diode). The the results hardly change if $U \gg U_d$.

It should be noted that the parameterization for the hole mobility eq. 7.2 with constant $\mu_h(E < E_0) = \mu_0^h$ was chosen after analyzing the TOF results published by Canali et al. [150] (see fig. 1 of ref. [148]). Their data suggests that the mobility becomes constant at small mean electric fields. However, they did not take E_{tof} into account; instead, they used $\langle E(x) \rangle$ leading to wrong results if the bias voltage is near the full-depletion voltage, mimicking constant mobilities as shown in fig. 7.1(a). Unfortunately, the resistivity and thickness of the sample used is not given so their data cannot be re-evaluated. However, using $\mu_h(E < E_0) = \mu_0^h$ still seems to be a justified approximation as shown below.

Additional measurements have been performed in the low-field region $\langle E \rangle < 5\,\mathrm{kV/cm}$ with a very high-ohmic $\langle 111 \rangle$ n-bulk diode (RD48 in tab. 3.2) in order to study the low-field mobility behavior. Because of the low bulk doping concentra-

[1] The properties of the diodes RD48 and CIS111 are listed in tab. 3.2.

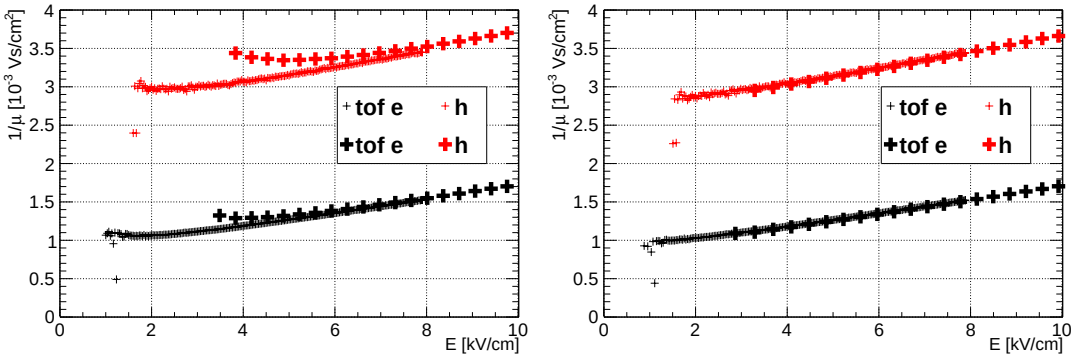

(a) (b)

Figure 7.1.: Comparison of the TOF mobility of electrons (black) and holes (red) for the RD48 (crosses) and the CIS111 (thick crosses) diodes with different full-depletion voltages U_d. (a) Shows $1/\mu_{e,h}(E)$ determined using the mean field U/d and (b) using E_{tof} of eq. 7.4.

tion ($U_d \approx 19.5\,\mathrm{V}$, $d = 300\,\mu\mathrm{m}$) the slope $\frac{\mathrm{d}E}{\mathrm{d}x}$ is small. This allows for measurement of the carrier drift velocities at fields close to zero. The low-field mobility of charge carriers is determined by lattice scattering due to thermal movement of the carriers. In the limit $E \to 0$ the scattering rate should be independent of the direction of the electric field and determined only by the thermal movement, as the drift velocity is small compared to the thermal velocity. Therefore, the mobilities are expected to be independent of the crystal direction at small fields.

Figure 7.2 shows a comparison of the ⟨111⟩ TOF results for electrons using the diodes RD48 and CIS111, the ⟨100⟩ parameterization for $2.5\,\mathrm{kV/cm} \leq E \leq 50\,\mathrm{kV/cm}$ of this work, and the Jacoboni ⟨111⟩ mobility parameterization (see ref. [118]). The TOF results of both diodes agree well. Furthermore, the TOF results agree well with the Jacoboni parameterization at low fields and the inverse mobility is almost linear at all investigated temperatures and fields. Still, some differences can be observed: At 333 K the measured $1/\mu_e(E)$ is about 5 % higher and at 233 K and large fields about 15 % higher than the Jacoboni results. At high fields, the TOF results agree better with the ⟨100⟩ results of this work than with Jacoboni. Concluding, the Jacoboni parameterization should provide sufficient precision to be used for the ⟨111⟩ electron mobility at lower fields. However, at higher fields the ⟨100⟩ parameterization gives a beeter description for the measured ⟨111⟩ mobility compared to the Jacoboni parameterization. The parameters in the right part of tab. 7.1 should be used for the ⟨100⟩ electron mobility at fields $E \leq 2.5\,\mathrm{kV/cm}$.

Figure 7.3 shows the same comparison as above, now for holes. Again, the TOF results of both diodes agree well. However, the TOF results exhibit a distinctly

different shape compared to the Jacoboni parametrization - a very similar observation like for the ⟨100⟩ hole mobility. The TOF results suggest a parameterization like eq. 7.2 should be used at high fields also for the ⟨111⟩ direction. At low fields the TOF results seem to merge with the ⟨100⟩ parameterization of this work for $2.5\,\mathrm{kV/cm} \leq E \leq 50\,\mathrm{kV/cm}$ rather than the Jacoboni ⟨111⟩ parameterization (except at 333 K in fig. 7.3(b)). A constant mobility is not observed at very low fields. Still, the parameterization of this work seems to give a very good approximation of the hole mobility at very low fields. Concluding, the Jacoboni parameterization should also provide sufficient precision for the ⟨111⟩ hole mobility at fields $E \gtrsim 2\,\mathrm{kV/cm}$. However, at low fields the agreement of the ⟨111⟩ TOF results and the ⟨100⟩ parameterization of this work for $2.5\,\mathrm{kV/cm} \leq E \leq 50\,\mathrm{kV/cm}$ is better than for the Jacoboni values. Accordingly, for the ⟨100⟩ hole mobility the $2.5\,\mathrm{kV/cm} \leq E \leq 50\,\mathrm{kV/cm}$ parameters of the left part of tab. 7.1 should be used also for fields $E \leq 2.5\,\mathrm{kV/cm}$.

7.2. Irradiated silicon

Apart from lattice scattering the mobility is influenced by ionized-impurity scattering. The contribution by ionized-impurity scattering decreases with increasing temperature. For high-ohmic silicon the concentration of ionized impurities does not influence the mobility around room temperature. However, radiation damage introduces defects into the silicon crystal which can be ionized. Accordingly, the mobility decreases for high fluences. Up to now the fluence dependence of the mobility is not well studied. Because of the short carrier lifetimes and the associated fast decay of current transients the TOF method or a fit of current transients is not possible or very difficult for high fluences (see sec. 6.1.1).

In the course of this thesis, the low field mobilities were obtained as a function of the fluence (see fig. 5.13) as discussed in detail in sec. 5.3.2. The high field behavior of the drift velocity is assumed not change with irradiation as an approximation since the velocity saturation is driven by phonon emission which should not depend on the fluence. Additionally, ionized-impurity scattering decreases with increasing velocity. The fluence dependence of the low field mobility is approximately

$$\mu_0^{e,h}\left(\Phi_{eq}\right) = \frac{\mu_0^{e,h}}{1 + \left(\frac{\Phi_{eq}}{\beta_{mob}}\right)^{0.9}} \tag{7.5}$$

with the parameter $\beta_{mob} = 1.52 \cdot 10^{17}\,\mathrm{cm}^{-2}$ (see eq. 5.8) at $T = 243\,\mathrm{K}$. For the field and fluence-dependent mobility eq. 7.5 is simply inserted into eq. 7.1 for electrons and eq. 7.2 for holes. Again, sec. 5.3.2 gives a more detailed discussion.

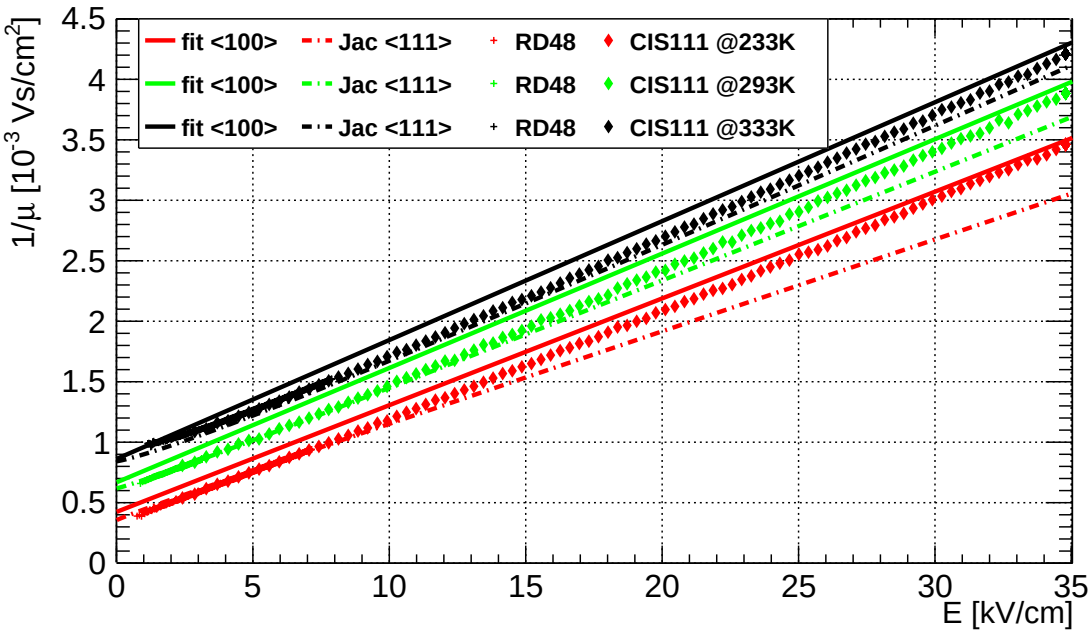

(a)

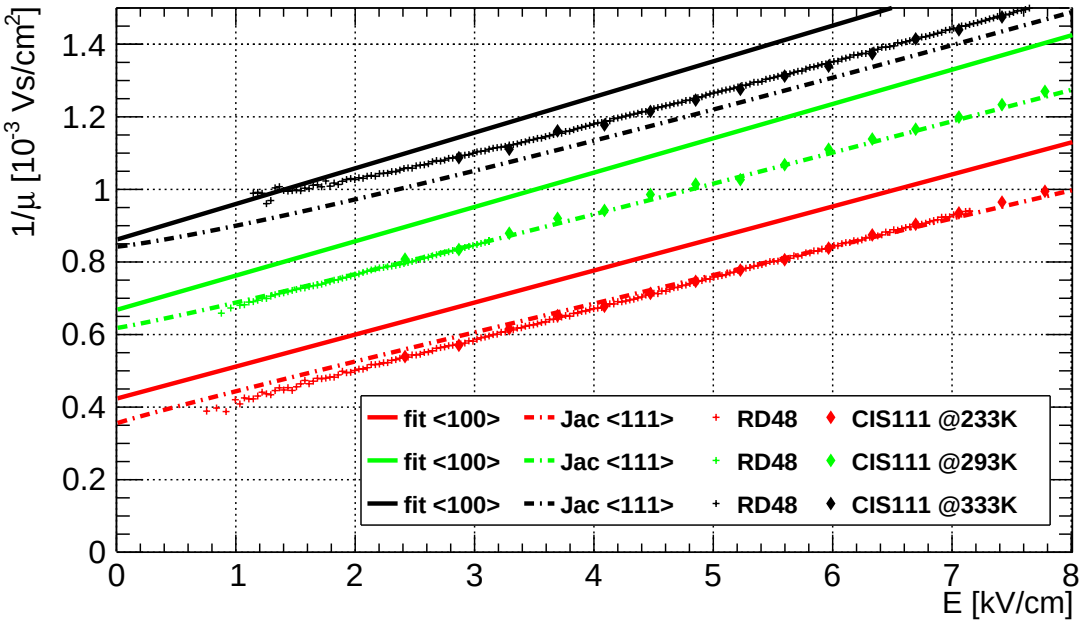

(b)

Figure 7.2.: (a) Comparison of the measured $\langle 111 \rangle$ inverse electron mobility $1/\mu_e\,(E)$ with the diode RD48 (crosses) and the diode CIS111 (diamonds), the $\langle 100 \rangle$ parameterization of this work (lines), and the Jacoboni $\langle 111 \rangle$ parameterization (dashed dotted) for $T = 233\,\mathrm{K} - 333\,\mathrm{K}$. (b) Shows the low-field region.

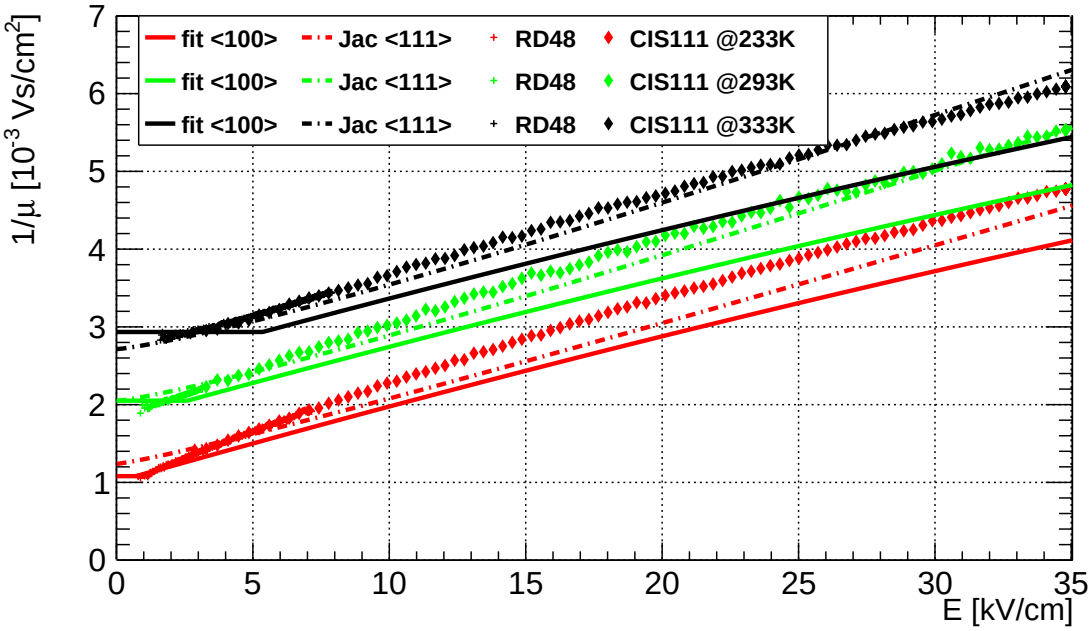

(a)

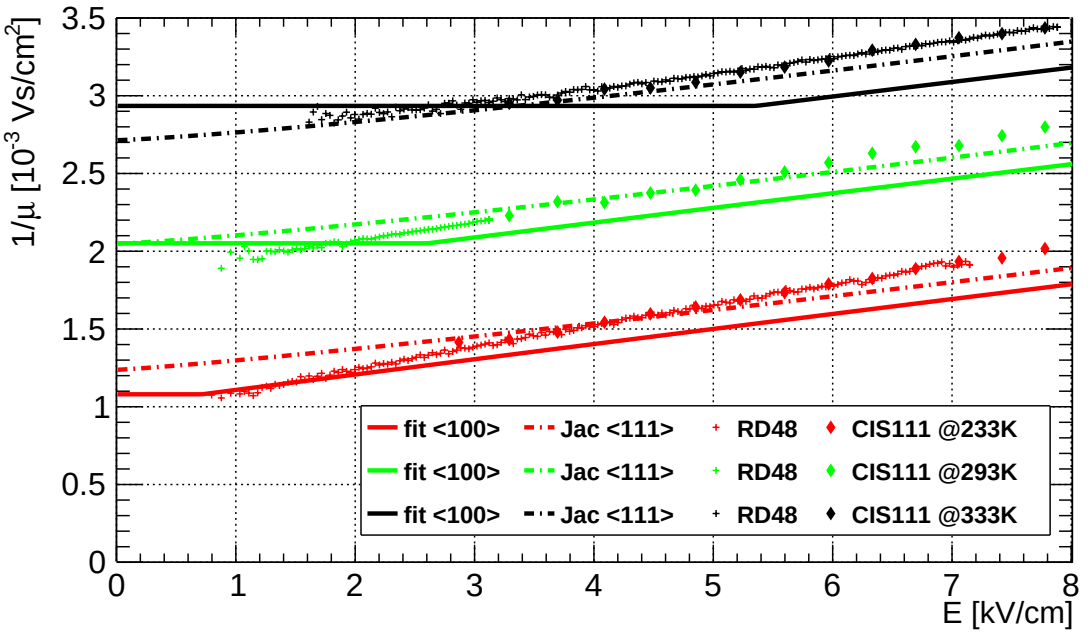

(b)

Figure 7.3.: (a) Comparison of the measured ⟨111⟩ inverse hole mobility $1/\mu_h\,(E)$ with the diode RD48 (crosses) and the diode CIS111 (diamonds), the ⟨100⟩ parameterization of this work (lines), and the Jacoboni ⟨111⟩ parameterization (dashed dotted) for $T = 233\,\mathrm{K} - 333\,\mathrm{K}$. (b) Shows the low-field region.

8. Conclusion

This thesis addresses many topics relevant for the investigation, description, understanding, and the design of silicon detectors operated in harsh radiation environments with hadron fluences beyond neutron-equivalent fluences $\Phi_{eq} = 10^{15}\,\mathrm{cm}^{-2}$. These high fluences will be reached in large volumes of the inner detector systems at the Large Hadron Collider LHC experiments after an integrated luminosity of $3000\,\mathrm{fb}^{-1}$. The inner detector systems, most notably the tracking detectors, are often instrumented with silicon sensors.

The absorption length of near-infrared light in silicon has been determined as a function of the fluence. A detailed discussion of the current of irradiated sensors is given and the current of pad diodes has been parameterized, revealing certain laws. An edge-Transient Current Technique *edge-TCT* setup has been developed and commissioned, and a new method to determine the charge collection lengths of charge carriers from edge-TCT charge profiles has been developed. The results were parameterized to reproduce diode measurements. Different geometries of novel radiation-hard, fine-pitch pixel sensors and many test structures have been designed and were produced as R&D for the future Compact Muon Solenoid *CMS* tracking detector. Finally, a method for the partial deconvolution of measured current transients was developed which can significantly reduce oscillations and reflections of fast signals. The individual results are shortly summarized below.

An increase of the absorption of infrared light in silicon has been observed for high fluences. The change of the absorption coefficient of near-infrared light in silicon has been measured and parameterized as a function of the fluence independent of the temperature for wavelengths relevant for TCT: $\lambda = 1000\,\mathrm{nm} - 1150\,\mathrm{nm}$. Additionally, it has been shown that the change of the absorption length directly translates into a change of the number of the generated free charge carriers. This information is very valuable for TCT charge collection measurements employing near-infrared light. For example, the initially generated charge by a $\lambda = 1064\,\mathrm{nm}$ light pulse increases by up to 30 % for pad sensors irradiated to $\Phi_{eq} = 1.3{\cdot}10^{16}\,\mathrm{cm}^{-2}$ compared to a non-irradiated sensor. The results are discussed in chapter 4. Charge collection measurements with minimum ionizing particles *MIPs* and near-

infrared light should be compared for the same irradiated sensors in order to directly compare the change of the initially generated charge.

Chapter 5 gives a detailed discussion of current and capacitance measurements of irradiated pad diodes and velocity profiles of irradiated strip sensors from edge-TCT. Rather complex behavior of highly irradiated silicon diodes has been observed. The results can be used to predict the current density of pad diodes as a function of the bias voltage, the thickness of the bulk, the pad area, and the fluence. Additionally, the carrier mobilities have been determined as a function of the fluence.

At low bias voltages, the neutral bulk of highly irradiated diodes has approximately zero net fixed space charge and the free carrier concentrations are approximately equal to intrinsic silicon, which is known as carrier removal. Fixed space-charge of shallow defects is compensated by filling of deep defects rather than by free carriers like in non-irradiated silicon. Consequently, the resistivity of the neutral bulk is very high. Since the generation lifetime is very short, the conductivity of the space-charge region *SCR* has been found to be high for low bias voltages. Accordingly, the current and capacitance characteristics at low bias voltages are determined by the bulk rather than the SCR.

It has been observed that the constant bulk resistivity $\rho = \left(en_i \left(\mu_0^e + \mu_0^h\right)\right)^{-1}$ measured at low bias voltages increases with the fluence. This is interpreted as a decrease of the carrier mobilities $\mu_0^{e,h}$ due to the scattering of carriers at ionized defects. The dependence of $\mu_0^{e,h}(\Phi_{eq})$ on the fluence has been estimated from the measurements of the bulk resistivity assuming ionized impurity scattering.

The reverse current changes abruptly from the ohmic behavior $\rho(U) = const$ once the generation current of the SCR cannot sustain the linear ohmic current of the bulk anymore. It has been discovered that the transition between bulk-dominated behavior and SCR-dominated behavior occurs at a characteristic threshold $\frac{U_{th}}{d^2}(\Phi_{eq}) \propto \Phi_{eq}$, with the thickness of the diode d and the threshold voltage U_{th}. This quantity is assumed to contain valuable information about relevant parameters of highly damaged sensors.

After the threshold is passed, the high resistivity of the bulk still causes a significant voltage drop and leads to a sizable electric field in the bulk. Accordingly, it hinders the increase of the SCR for reverse bias as the effective voltage drop over the SCR is reduced. Still, it has been observed that the resistivity of the irradiated diodes is approximately $\rho(\Phi_{eq}) \propto \frac{U}{d^2}$. Additionally, a small difference of the threshold $\frac{U_{th}}{d^2}(\Phi_{eq})$ has been observed for initially n-type and p-type bulk.

An empirical model has been developed to describe the current of pad diodes as function of the fluence and the applied voltage for small to medium reverse bias

voltages. The measurements are described within a few percent by the model.

At high reverse bias voltages a faster increase of the current is observed. It seems to originate in the high-field region of the SCR due to the high concentration of radiation-induced acceptor-like defects, which dominate the space-charge in the SCR. The mechanism generating additional current in the high field is probably related to the Frenkel effect, trap-assisted tunneling, and/or impact ionization. Fluctuations of the current at short timescales are observed in this regime, hinting at impact ionization and associated „micro-discharges". In order to describe the current increase at high voltages an exponential term is added to the model developed for smaller bias voltages. Again, the measurements are described within a few percent.

For forward bias the diode current at all bias voltages can be reasonably described within about 10 % assuming space-charge-limited currents for a semiconductor containing traps uniformly distributed in the band gap. The assumption of bulk carrier densities approximately equal to the intrinsic values is confirmed by the good description of the measurements with this model. A hypothetical electron trap concentration has been extracted from the fits of the model to measurements. The results for forward bias are discussed in sec. 5.4.

Further current measurements should be performed systematically for different temperatures in order to determine the low-field mobilities as a function of the temperature and the electric field. Also, the effects of annealing should be studied. The parameters of the model have to be understood in detail and a model should be established to describe the electric fields. For high reverse bias voltages further studies are needed to identify the voltage dependence and the mechanisms generating the current. For forward bias the model should be revised with a focus on the relaxation via recombination.

An existing multi-channel TCT setup has been modified in order to perform edge-TCT measurements with two read-out channels. The setup and the measurement procedure is described in sec. 3.3.

A new method to analyze edge-TCT charge profiles has been developed as discussed in chapter 6. The model can be used to estimate the charge collection lengths $\lambda_{ccl}^{e,h} = \tau_{e,h} v_{e,h}$ of the carriers as a function of the fluence and the mean electric field E from charge profiles of forward biased strip sensors, with the trapping times $\tau_{e,h}$ and the drift velocity $v_{e,h}(E) = \mu_{e,h}(E) \cdot E$. The charge profiles are well-described and light refraction at the corners has been modeled successfully. The product $\mu_{e,h}(E)\,\tau_{e,h}(E) = {}^{\lambda_{ccl}^{e,h}(E)}/_{E}$ has been found to be approximately constant for $E > 15$ kV/cm. The extracted parameters have been used to calculate the charge collection efficiency obtained from infrared light illumination

of irradiated pad diodes. The model is compared to charge collection efficiency measurements of many diodes of different material and geometries. A reasonable agreement within about 5 % has been found between the model and the measurements. However, the results are ambiguous as 3 of 17 diodes show a charge collection efficiency 20 % smaller than the expectation from the model. Nevertheless, as most measurements are remarkably well-described the method seems to be sound. All diode measurements confirm the edge-TCT result $\mu_{e,h}(E)\,\tau_{e,h}(E) \approx const$ for $15\,\mathrm{kV/cm} \leq E \leq 50\,\mathrm{kV/cm}$, even the measurements which show the 20 % offset. It seems like the carrier trapping times $\tau_{e,h}(E)$ increase with E due to filling of defects from the space-charge-limited currents.

The models developed for this part should be extended for reverse bias, where $\mu(E,x)\,\tau(E,x) \neq const$. Information about the charge collection lengths as a function of the position, the bias voltage, and the fluence would be very helpful for simulations of detectors.

The mobilities of electrons and holes have been determined for non-irradiated silicon with $\langle 111 \rangle$ and $\langle 100 \rangle$ crystal orientation and for irradiated $\langle 100 \rangle$ silicon as discussed in chapter 7. For non-irradiated silicon, the results have been parameterized as a function of the electric field and large differences compared to literature values are observed. Mean electric fields between $1\,\mathrm{kV/cm}$ and $50\,\mathrm{kV/cm}$ have been investigated. Additionally, the low-field mobilities of electrons and holes have been determined as a function of the fluence from resistivity measurements of irradiated sensors as discussed above. The results should be implemented into simulation programs like TCAD [151].

A complete set of photolithography masks for the production of prototype wafers has been developed as discussed in appendix A. The designs include novel, fine-pitch planar pixel sensors for different read-out chips as well as many different test-structures. The pixel sensors are prototypes for the inner barrel tracker of the Compact Muon Solenoid *CMS* experiment. The inner barrel tracker will experience some of the highest radiation damage demanding for especially radiation-hard sensors. The smallest pixel dimensions are $50 \times 50\,\mu\mathrm{m}^2$ and $100 \times 25\,\mu\mathrm{m}^2$ which is six times smaller compared to the current pixel sensors of the inner CMS tracker. All structures have been programmed for easy adjustment of parameters like the pixel dimension, the metal overhang, and many others. Different biasing schemes for the pixel sensors have been implemented to compare the efficiency. Thousands of sensors have been produced and are subject to beam tests as of the publication of this thesis.

A method for the deconvolution of current transients obtained with TCT has been developed as described in appendix B. The transfer function of the read-out circuit usually leads to oscillations and reflections for fast signals obscuring the original signal. The presented deconvolution method can be used to correct for oscillations and reflections in the analysis. This can be very helpful in order to understand the pulse shape of fast current transients, e.g. of irradiated sensors.

Appendix

A. Design of pixel sensors and test structures

For the high-luminosity upgrade of the LHC many parts of the detectors have to be replaced. Notably, the silicon pixel detector will be replaced in order to cope with increasing track densities (pile-up) and radiation damage. For the Phase II upgrade of the barrel pixel detector the pixel size will be reduced from currently $150\times100\,\mu m^2$ to $100\times25\,\mu m^2$ or $50\times50\,\mu m^2$ (see ref. [11, 152]). In the course of this thesis the photolithography masks of fine-pitch pixel sensors and test structures have been produced within the CMS collaboration for a R&D submission for the future CMS barrel pixel detector. The masks have been coded in the RUBY programming language using KLayout [153] for conversion to the .gds file format. Full 6″ wafer layouts have been assembled as shown in fig. A.1. The designs have been produced by Hamamatsu Photonics K.K. [82] and are being tested as of the submission of this thesis.

The innermost pixel layers of the future CMS tracker will be subject to extremely high fluences as shown in fig. 1.2. The equivalent fluence will reach up to $\Phi_{eq} = 2.3 \cdot 10^{16}\,cm^{-2}$ and the total ionizing dose will be up to 1.2 Grad for $3000\,fb^{-1}$ of integrated luminosity. Accordingly, the sensors and the read-out chips *ROC*s have to be especially radiation-hard. In order to achieve a high radiation tolerance (see sec. 2.3.3) the bulk thickness of the sensors for the CMS submission was chosen to be 150 µm opposed to 285 µm of the current CMS pixel sensors. The segmented side has n^+ implants and the bulk is p-type. In total, 35 wafers have been produced with a bulk resistivity of $1\,k\Omega cm - 5\,k\Omega cm$ and a high oxygen concentration of $1.5 \cdot 10^{16}\,cm^{-3} - 6.5 \cdot 10^{17}\,cm^{-3}$. Some wafers are physically thinned to 150 µm and some of the thinned wafers were bonded to additional 50 µm thick low-ohmic handle wafers for increased mechanical stability. Additionally, some wafers are physically 200 µm thick with 50 µm thick deep-diffused back side implants. The back side of the wafers features a 50 µm wide aluminum grid with $200 \times 200\,\mu m^2$ windows to allow for measurements illuminating the back side with light (see sec. 3.3).

For reverse biased n^+-p sensors the electrons drift towards the segmented n^+ side. Positive fixed oxide charge can lead to inversion layers of electrons at the

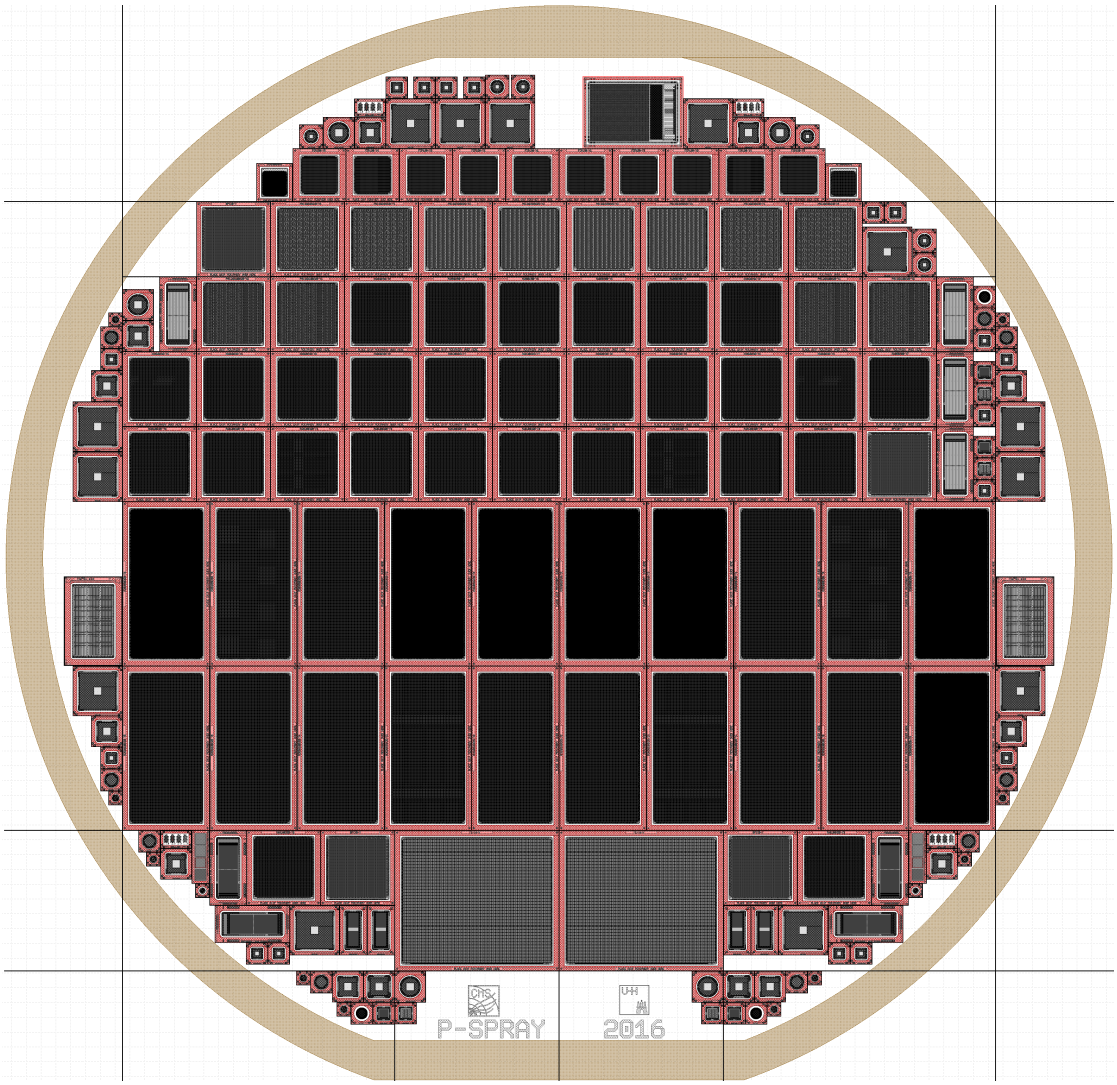

Figure A.1.: Picture of a full 6″ wafer for the CMS planar pixel submission. The upper half contains the pixel sensors for the ROC4SENS and the FCP130 ROCs. The larger dies are in the middle are for the RD53A. The very large dies on the bottom are for the FE-I4 and the smaller dies for the PSI46digi. The small dies around the central region are mostly test structures or pixel sensors for other ROCs.

Si-SiO_2 interface which can short the individual pixels reducing the efficiency. Therefore, the individual pixels have to be isolated by additional thin p^+-implants in-between the pixels with peak doping concentrations around $10^{15}\,cm^3 - 10^{17}\,cm^3$. Two different methods for isolation were implemented: For p-spray isolation the whole segmented side of the wafer is uniformly implanted and for p-stop a dedicated photolithography mask has been programmed to place the isolating p^+-implants where needed.

New ROCs are being developed for the smaller pixel size and to increase the radiation tolerance of the ROC for application at the high-luminosity LHC. At the time of the design of the sensors it was not clear which ROCs would be available by the time of receiving the sensors. Therefore, sensor designs for the read-out pattern (bump pattern) of several ROCs have been implemented in the submission. In order to test the small pixels with the ROC of the current CMS detector complex structures with routing lines have been programmed during this thesis in order to connect the small pixels with the read-out channels of the ROC. Since few ROCs can survive the harsh radiation environment expected for Phase II operation alternative „cold" methods of connection of the sensors to ROCs (bump-bonding, see e.g. ref. [154]) were foreseen to connect irradiated sensors to non-irradiated ROCs causing minimum annealing to the irradiated sensors due to the bump-bonding process.

The production needed eleven photolithography layers in total. There are aluminum layers for the back side grid and for the front contacts. Implant layers for the n^+ implants, the p-stop implants, and p^+ implants in the periphery. Then a layer for windows in the SiO_2 layer, called „vias", connecting the aluminum contacts to implants and a layer for openings in the SiO_2 passivation on top of the metal for contacting the metal with needles or by bump-bonding. A layer for polysilicon resistors was also implemented for pixel and strip sensors as well a layer for the polysilicon vias. A layer for under-bump metalization is needed to ensure mechanical stability and high yield of the bump-bonding process which was performed at Fraunhofer IZM [155]. Finally, a layer for benzocyclobutene *BCB* coating in the peripheral region is needed for spark protection of pixel sensors after bump-bonding to ROCs since the edges of the sensors are at high voltage during operation while the ROCs are at ground potential. The BCB coating was also performed at Fraunhofer IZM.

The goal of the submission is to test the efficiency, position resolution, breakdown behavior, and the radiation-hardness of different designs. The parameters which are being investigated are different biasing schemes, different pixel implant and pixel aluminum contact sizes, p-spray and p-stop, and the minimum design

rules due to the greatly reduced pixel size of structures such as the punch-through structure (explained below) and p-stop implants. Many different pixel designs with p-stop and p-pray implants have been implemented. In total, several thousand sensors and test structures have been produced and are now being tested by several member institutes of CMS. Below, some example sensor designs for different ROCs are discussed and some test structures are explained. The final designs are not shown here due to corporate policy of the producer.

A.1. Pixel sensors

Here, the design of pixel sensors is discussed and some examples of designs for a few ROCs are shown. Additional designs not discussed here were implemented for the FE-I4 [156], CHIPIX65 [157], FCP130 [158], and the MaPSA [159] ROCs.

A.1.1. Biasing schemes

Biasing schemes are often added to pixel sensors to test the sensors before bump-bonding to ROCs. Electrical testing of the sensors before bump-bonding increases the yield and lowers the cost, since bump-bonding is an expensive process and defective sensor can be discarded before bonding. A biasing scheme interconnects all pixels via a resistive network which is connected to the bias ring. In this way the bias ring, and with it all interconnected pixels, can be easily probed with needles. The inter-pixel resistance has to be sufficiently high to ensure isolation of the pixels after bump-bonding ($\tau = RC$). A biasing scheme is also helpful to extract the large amount of charge created in case of a partial beam loss, ideally without damaging the ROC. Unfortunately, a biasing scheme is usually associated with a decrease of the detection efficiency. Carriers can induce a signal to resistive network of the biasing scheme since it is coupled to the same potential as the pixels. The part of the signal induced in the bias network will largely be lost since it will be shared between many pixels and the bias ring. Therefore, the charge loss due to the biasing scheme is mitigated by minimizing the surface area of the sensor where the bulk and surface potentials are influenced by the biasing scheme while trying to retain the functionality of the biasing scheme.

Different biasing schemes have been implemented to qualify the ones which offer maximum efficiency: No biasing scheme, polysilicon resistors on top of the SiO_2, open p-spray barriers, and the so-called punch-through design. The polysilicon designs are not discussed here. It should be noted that another approach not implemented here is to use a temporary aluminum layer for testing which is removed

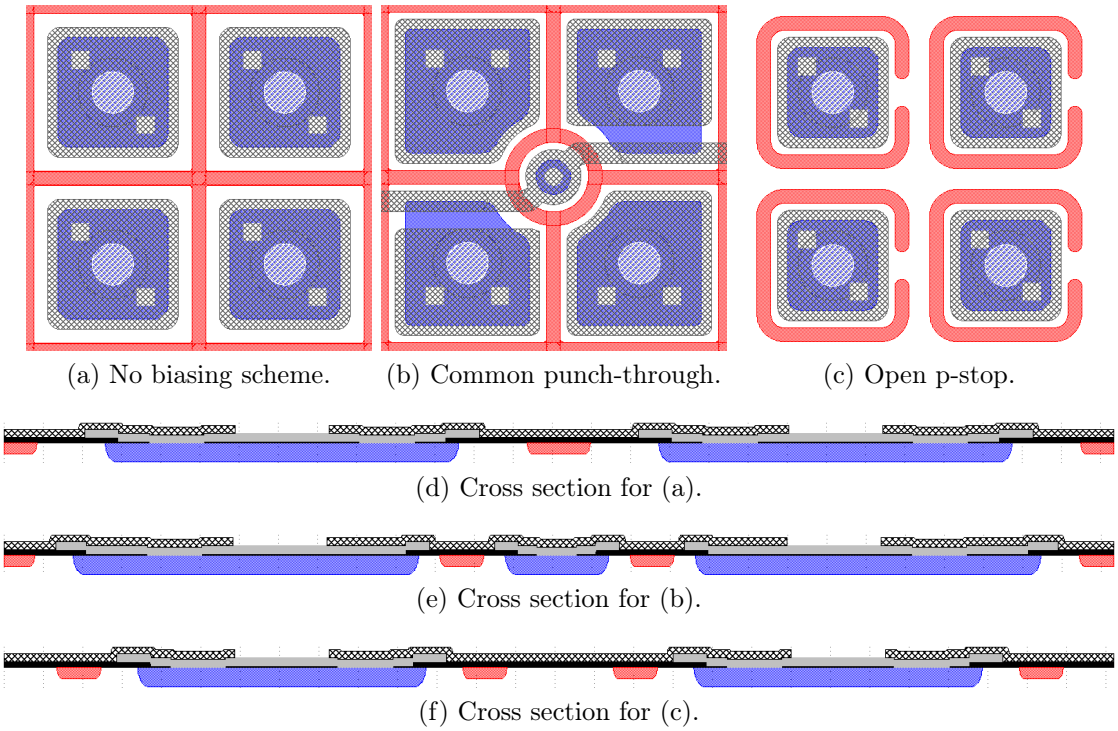

(a) No biasing scheme. (b) Common punch-through. (c) Open p-stop.

(d) Cross section for (a).

(e) Cross section for (b).

(f) Cross section for (c).

Figure A.2.: Implementation of different biasing schemes with p-stop isolation (red) for $50 \times 50\,\mu m^2$ pixels and the RD53A ROC bump pattern. (a) Shows a design with no bias scheme with a common p-stop. (b) Shows a common punch-through design where four pixels share a bias dot with a wiggle bias line (middle) partly on top of the pixel implants. (c) Shows an open p-stop design. Below, the cross sections of the surface are shown for a diagonal line from the top left corner to the bottom right corner of (a)-(c). The p-stop implant is shown in red, the n^+ pixel implant in blue, the aluminum layer in gray, the thermal oxide in black, and the chemical vapor deposited oxide passivation in black (rhombic pattern).

before the bump-bonding process.

Figure A.2(a) shows a p-stop design for the RD53A ROC with no biasing scheme. The common p-stop implant between the pixels prevents interconnection of the individual pixels by blocking electron inversion layers. The inter-pixel resistance is very high. In order to test the sensors before bump-bonding, each pixel would have to be tested individually which is not viable. However, the size of the pixel implant can be maximized which increases the efficiency.

Figure A.2(b) shows a punch-through design with a wiggle bias line. The bias dot in the middle acts as a diode (like the pixels). It it connected to the bias ring via the aluminum bias line on top of the oxide layer. For a certain applied voltage the depletion region will extend to the pixels (the „punch-through" voltage) and the whole sensor can be tested simply by connection of the bias ring. However,

it is apparent that the bias dot will collect a part of the signal if it is generated near the bias dot, decreasing the detection efficiency. Additionally, the bias line may change the potential near the interface or collect part of the signal due to AC coupling which decreases the efficiency further. Therefore, designs as shown here were implemented where the bias line is partly on top of the pixel implants („wiggle" bias line) to minimize distortion of the potential. Designs with a straight bias line (see fig. A.5(b)) were also implemented as well as different bias dot geometries.

Figure A.2(c) shows an open p-stop biasing scheme. The insular p-stop implants encompassing the pixel implants have small openings to allow for moderate resistive coupling of the pixels through electron inversion layers. It is apparent that this biasing scheme limits the possible pixel implant size due to the minimum distances and widths of the p-stop implant according to the design rules.

A.1.2. PSI46digi

The PSI46digi [160] ROC is readily available and is supposed to be a backup option and for control measurements. It was developed for the CMS Phase I tracker with a pitch of $100 \times 150\,\mu m^2$, 80×52 pixels, and a radiation tolerance > 500 Mrad produced with a 250 nm process. The bump pattern is a design with two-columns of bump pads with 100 µm spacing every 200 µm. Several sensor designs with aluminum routing lines to the bump pads have been implemented to test the reduced pixel size with the $100 \times 150\,\mu m^2$ bump pattern of the PSI46digi. Examples are shown in fig. A.3. In order to compare the new 150 µm thick sensors to the 285 µm thick CMS Phase I sensors also the original designs were reproduced (see fig. A.3(c)).

A.1.3. ROC4SENS

The ROC4SENS [161, 162] is a ROC with a pitch of $50 \times 50\,\mu m^2$ and 155×160 pixels produced with a 250 nm process. The radiation-hardness is > 500 Mrad. It features a staggered bump pattern which is optimized for $100 \times 25\,\mu m^2$ pixel size. Some examples of sensor designs are shown in fig. A.4.

A.1.4. RD53A

The RD53A ROC is developed within the RD53 collaboration [163, 164] and a candidate for the CMS Phase II upgrade. It has a pitch of $50 \times 50\,\mu m^2$ in a non-staggered bump pattern of 400×192 pixels produced with a 65 nm process. The radiation-hardness is up to 1 Grad. Figure A.5 shows two examples for sensor designs implemented for this ROC.

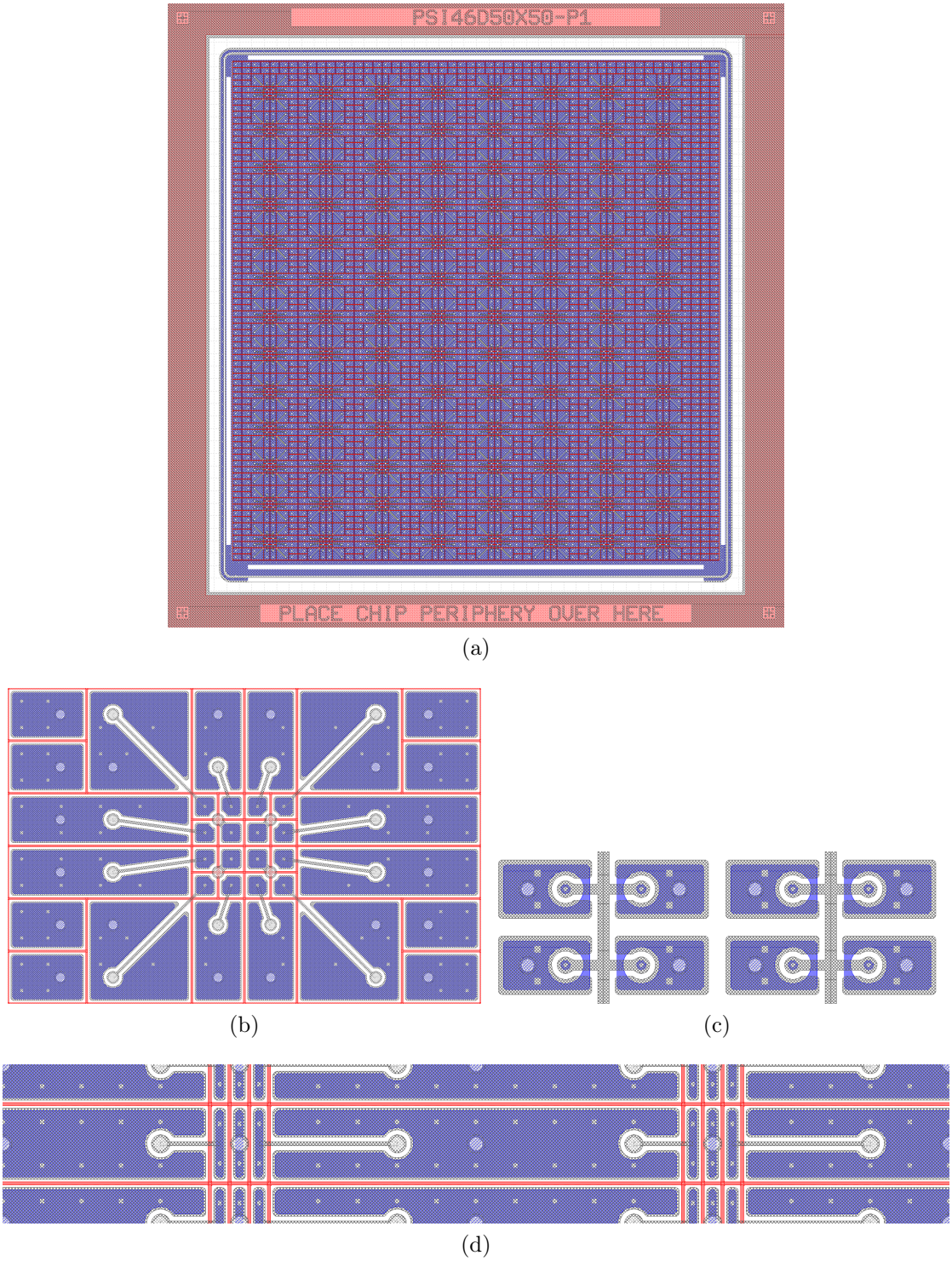

(a)

(b)

(c)

(d)

Figure A.3.: Sensor designs for the PSI46digi ROC (not to scale). (a) Shows a full sensor with periphery, the „die", and (b) a super-cell with routing lines to connect the central 4×4 grid of $50 \times 50\,\mu m^2$ pixels to the $150 \times 100\,\mu m^2$ bump pattern of the ROC. (c) Shows a reproduced Phase I p-spray design with a pitch of $150 \times 100\,\mu m^2$ and individual punch-through for each pixel and (d) a p-stop design with routing lines to test $100 \times 25\,\mu m^2$ pixels.

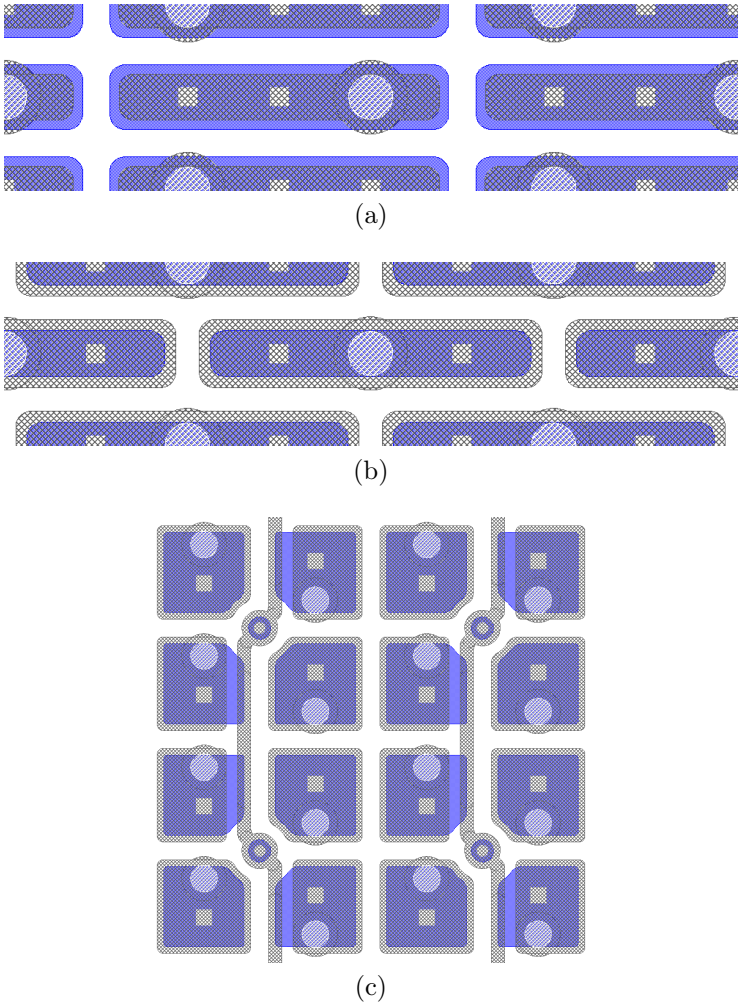

Figure A.4.: P-spray sensor designs for the ROC4SENS (not to scale). (a) Shows a non-staggered $100 \times 25\,\mu m^2$ design where the aluminum is smaller than the pixel implant, maximizing the size of the implant. The distance between the pixel implants is only 7.5 µm. (b) Shows a staggered $100 \times 25\,\mu m^2$ design with 2 µm aluminum overhang and 12.5 µm distance between the implants. (c) Shows a $50 \times 50\,\mu m^2$ common punch-through design with a wiggle bias line. The distance between the bias dot and the pixel implant is 11 µm.

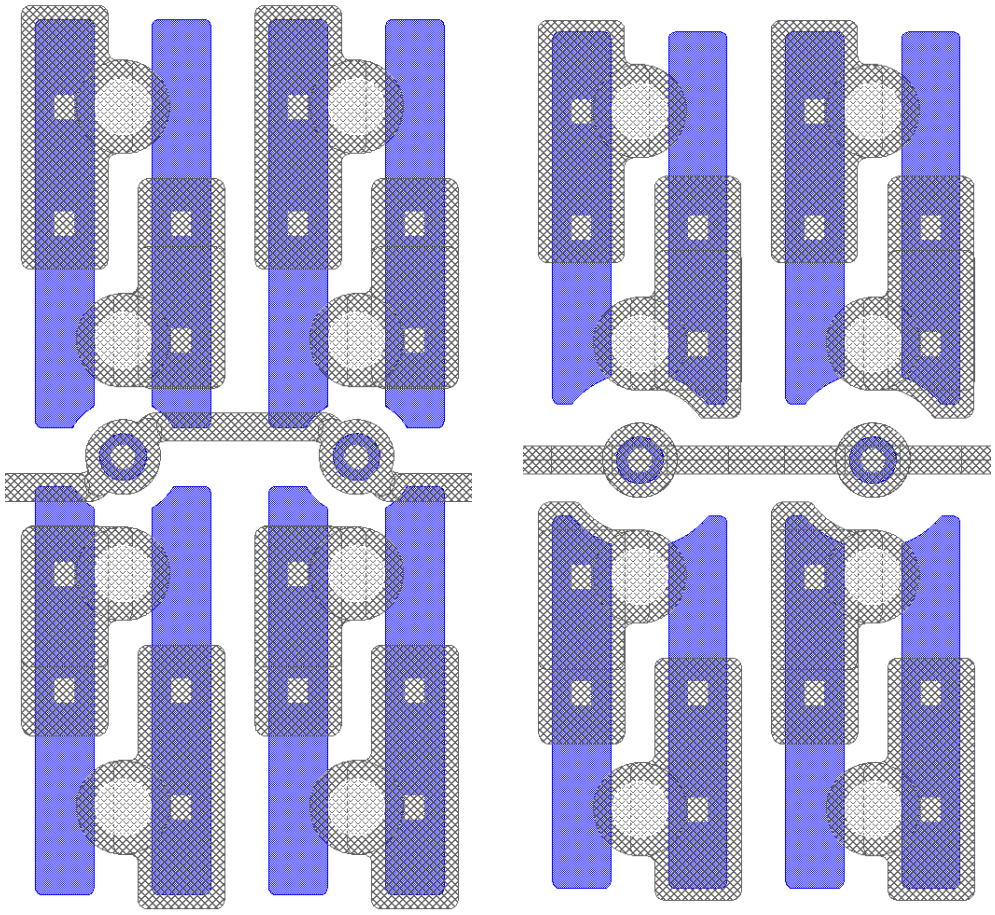

(a) (b)

Figure A.5.: Common punch-through p-spray designs with $100 \times 25\,\mu m^2$ pixels for the RD53A ROC with a wiggle bias line (a) and a straight bias line (b).

A.2. Test structures

The test fields in the outer regions of the wafers, often called half moon, hold many different test structures used to qualify the processes and the bulk material as well as to perform dedicated studies such as the ones presented in this thesis.

A.2.1. Pad diodes

Pad diodes are very basic structures consisting of a single large area diode (see sec. 3.1.2). They can be used e.g. to determine the effective doping concentration of the bulk material and to study the current and charge collection under well-defined conditions. Figure A.6 shows different diodes as implemented in the submission. The electrode is surrounded by a guard ring in order to define the area of the pad and to exclude edge effects. Square and round diodes of different pad areas have been implemented. The diodes are created automatically and the number of guard

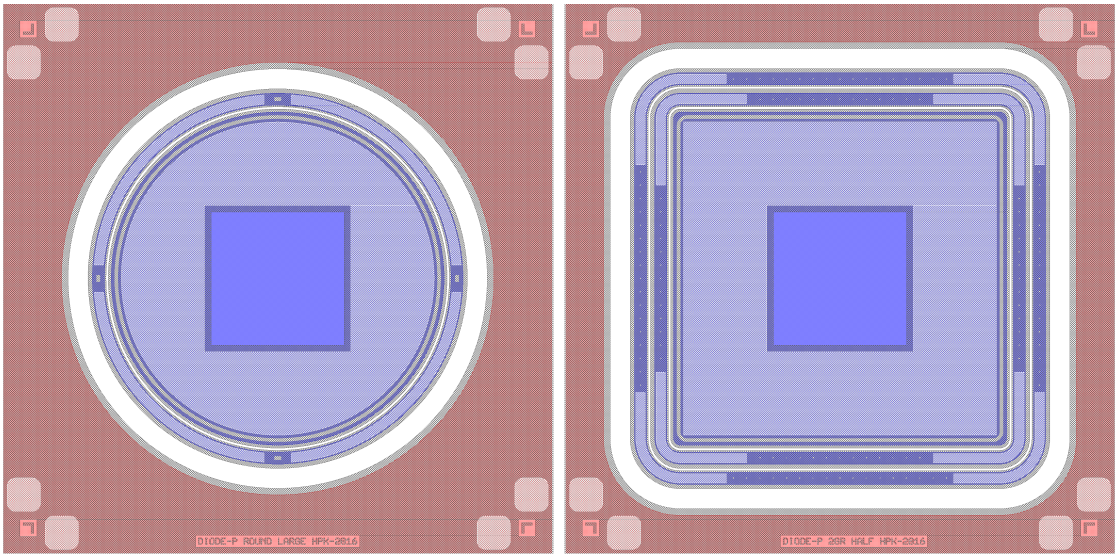

Figure A.6.: Implemented round and square diodes with a diameter of 2.5 mm. The pad aluminum contact has a window in the middle to allow for TCT measurements.

rings, the diameter of the pad and of the corners, as well as other parameters like the aluminum overhang can be specified in the code.

The doping of the material can be determined from capacitance measurements of two diodes of different pad areas for reverse bias with and without connecting the guard ring to correct for edge effects (see ref. [23]).

Due to the usually large pad area the capacitance of a diode is rather large and limits the rise time for fast current transients. Therefore, diodes with a small pad area have been implemented in order to measure the drift velocity of holes at very high electric fields, where the current transients are very short. The available edge lengths of the pad implants are 5 mm, 2.5 mm, and 1.25 mm for the square diodes and the available radii for the round diodes are 2.5 mm and 1.5 mm.

A.2.2. Strip sensors

Strip sensors can be used to study the charge collection as a function of the depth in the bulk of the sensor with edge-TCT (see sec. 3.3.2). The relatively small area of the strips results in a low capacitance and fast rise time as well as low noise.

The strip sensors implemented here have 33 strips with a pitch of 80 µm, a strip length of 7620 µm, and implant widths of 20 µm and 40 µm. The die size is $10 \times 5\,\mathrm{mm}^2$. Figure A.7 shows a strip sensor with an implant width of 40 µm. Both ends of the strips feature DC and AC pads. The strips are connected to a surrounding bias ring by polysilicon resistors (see fig. A.7(b)). An additional

guard ring is encompassing the bias ring. In the middle of the strips the the strip metal narrows to 10 µm width on the upper/lower edge of the implant as shown in fig. A.7(c). This was implemented in order to allow for front side illumination with light also in the region of the strip for TCT studies.

A.2.3. Spaghetti diodes

Spaghetti diodes [165] are similar to strip sensors; but, all strips are shorted. This results in a weighting field similar to pad diodes, as all strips are read out simultaneously, while the electric field is approximately the same as in strip sensors. They can be used to disentangle the effects of the weighting field and the electric field on the measured signal in a simple TCT setup. Figure A.8 shows a spaghetti diode as implemented here.

A.2.4. Miscellaneous

Other test structures implemented are metal-oxide semiconductor *MOS* capacitors, MOS field-effect transistors *MOSFET*s (see fig. A.9), gate-controlled diodes, a test-field for sheet resistance measurements, and a secondary-ion mass spectroscopy *SIMS* structure. The MOS structures can be used to investigate the surface of the material (see e.g. ref. [38, 166]). For example the doping profile of the p-spray implant can be measured and the space charge of the oxide and the number of interface traps can be determined before and after irradiation.

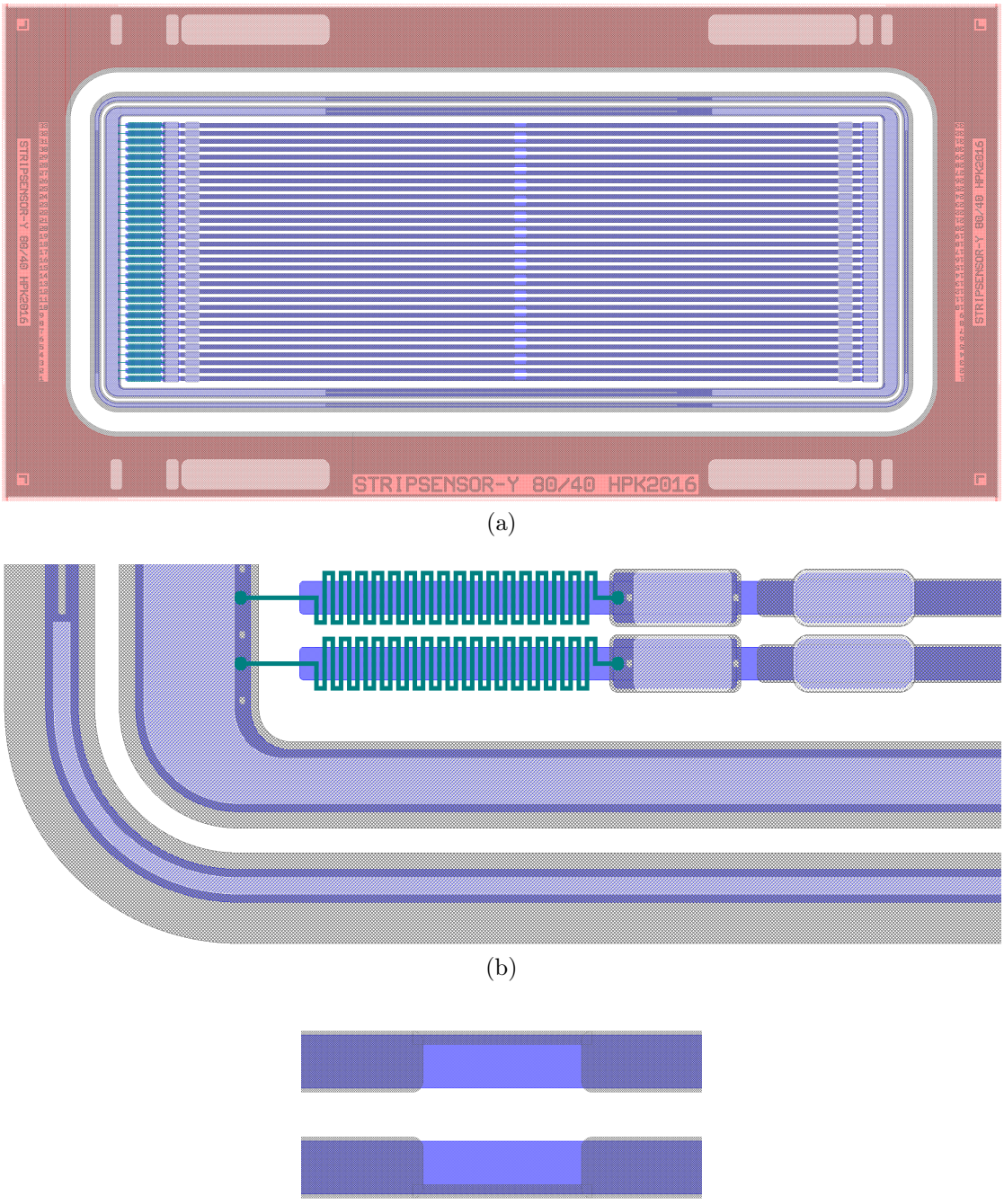

(a)

(b)

(c)

Figure A.7.: P-spray strip sensor design with 40 µm implant width and a pitch of 80 µm. (a) Shows the whole die and (b) a close-up of the guard and bias rings and the polysilicon resistors (green) connecting the strips to the bias ring. The left pad in (b) is the DC pad and the right one the AC pad. (c) Shows the central region of the strips with thin metalization for TCT studies.

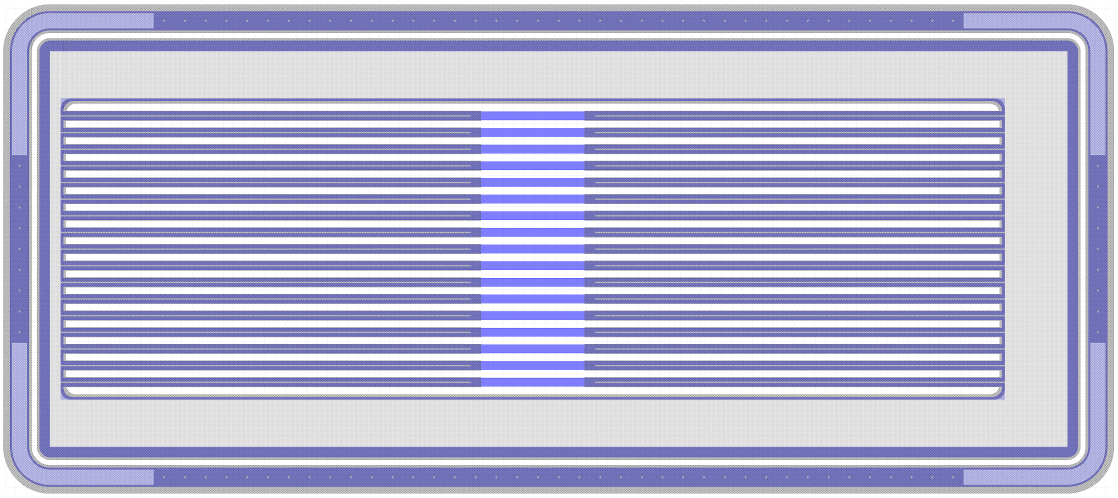

Figure A.8.: Design of a spaghetti diode with 40 µm spaghetti implant width and a spaghetti pitch of 80 µm, the same as for the strip sensors. All spaghetti are connected to form a pad („spaghetti monster"). The central region of the spaghetti is not metalized to allow for TCT measurements with light.

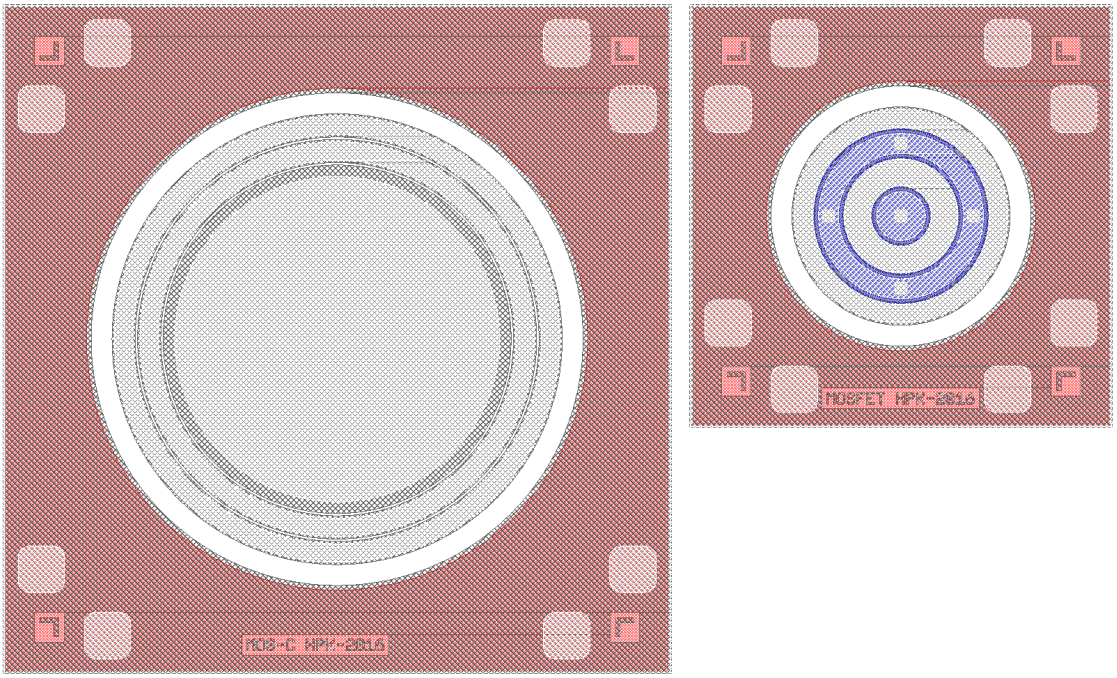

Figure A.9.: Examples of a circular MOS capacitor (left) and a circular MOSFET (right).

B. Deconvolution of current transients

A method has been developed to determine the transfer function of the read-out electronics for TCT measurements. It is published in ref. [167, 81] and used e.g. in ref. [168]. In the course of this thesis the method has been extended to the partial deconvolution of measured current transients. This can be very helpful to analyse the charge collection. The read-out circuit results in oscillations and reflections obscuring the signal which can be reduced significantly by deconvolution.

In order to determine the transfer function of the read-out electronics[1] for a TCT setup the transient current measurement of a well-understood (non-irradiated) sensor is needed plus a precise simulation of the transient current. The simulation used here is described in ref. [87, 81]. The convolution theorem

$$\mathcal{F}\{f \star g\} \;=\; \mathcal{F}\{f\} \cdot \mathcal{F}\{g\} \tag{B.1}$$

is used to determine the transfer function $conv \equiv g$ from the measured transient current $meas \equiv f \star g$ and the simulated transient current $sim \equiv f$:

$$conv \;=\; \mathcal{F}^{-1}\left(\frac{\mathcal{F}\{meas\}}{\mathcal{F}\{sim\}}\right). \tag{B.2}$$

Here $\mathcal{F}$ is the Fourier transform and $\mathcal{F}^{-1}$ the inverse Fourier transform.

The C++ code developed here for performing the circuit convolution has been incorporated in an open-source TCT analysis framework [169] by G. Kramberger. The transfer function obtained with this method can be used to convolute simulated current transients in order to compare them to measurements. Figure B.1 shows the comparison of a simulation and a measurement. The simulation is folded with the transfer function obtained for a different measurement with a completely different pulse shape. The measurement is very well described by the simulation, even reflections are well-described which demonstrates the power of the method.

[1] Including the capacitance of the measured electrode.

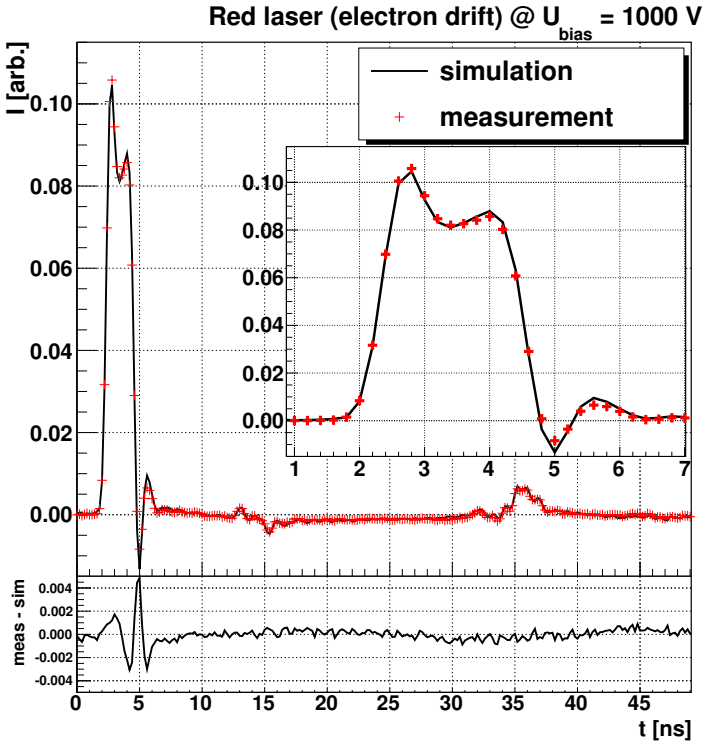

Figure B.1.: Example for the performance of the convolution method. Shown is the measured TCT spectrum (crosses) for electron drift from illumination with red light and the simulation (red line) with the response function obtained from the measurement for illumination with infrared light. Note the description of the reflection of the current pulse on the right. The insert shows the pulse with an expanded time-scale. Previously published in ref. [167].

However, if the pulse shape cannot be reliably simulated, like for irradiated sensors, it may be convenient to use the transfer function to perform a deconvolution $\mathcal{F}^{-1}\left(\frac{\mathcal{F}\{meas\}}{\mathcal{F}\{conv\}}\right)$ of the measured current transient.

Deconvolution of a measurement is an intrinsically ill-defined problem. A complete deconvolution is very difficult due to noise and the limited sampling rate of read-out electronics. Therefore, only a partial deconvolution up to a limiting frequency is possible without excessive fluctuations of the signal. It was found that a partial deconvolution to a Gauss function with a standard deviation similar to the rise-time of the signal lead to stable results. The partial deconvolution of the measured current transient is

$$deconv = \mathcal{F}^{-1}\left(\mathcal{F}\{meas\}\,\frac{\mathcal{F}\{Gauss\}}{\mathcal{F}\{conv\}}\right). \tag{B.3}$$

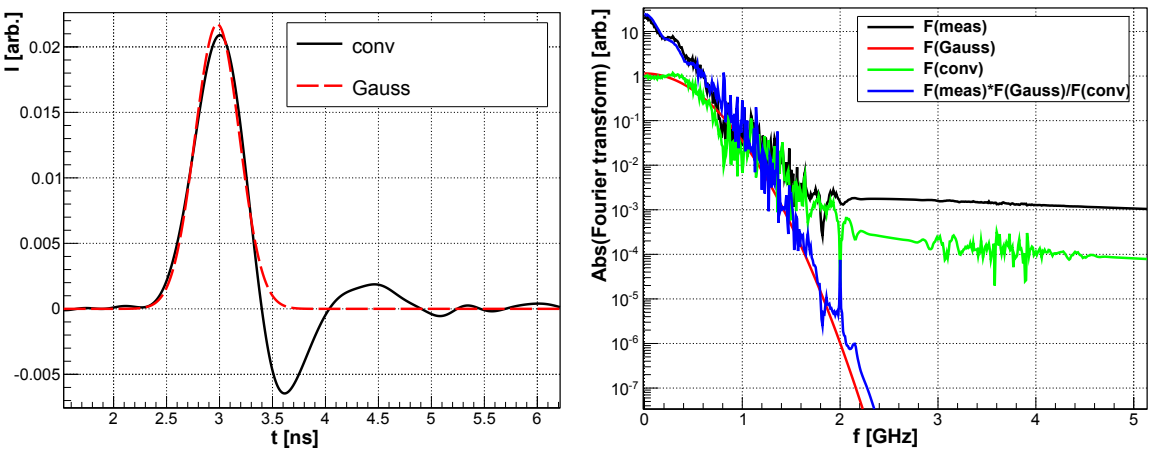

(a) (b)

Figure B.2.: (a) The transfer function for a well-known diode and a Gauss distribution with the same rise time as the measurement. (b) Absolute values of the Fourier transforms of the measurement, the Gauss distribution, the transfer function, and $\mathcal{F}\{meas\}\frac{\mathcal{F}\{Gauss\}}{\mathcal{F}\{conv\}}$.

In this way only the asymmetrical part of the electronics response is removed from the signal and the noise contribution in the transfer function is convoluted with the Gauss function. Figure B.2 shows the transfer function and the Gauss as well as the absolute values of the Fourier transforms for a measurement of a well-known non-irradiated diode measured with the diode TCT setup. It is apparent how $\mathcal{F}\{meas\}\frac{\mathcal{F}\{Gauss\}}{\mathcal{F}\{conv\}}$ removes higher frequencies observed in $\mathcal{F}\{meas\}$.

Figure B.3 shows the measured current transients of a non-irradiated diode as well as the simulation and the partial deconvolution. The asymmetrical parts of the transfer function are largely removed by the partial deconvolution, like the oscillations after fast changes and the reflections. Figure B.4 shows the measured current transients of an irradiated diode and the deconvolution of the current transients using the transfer function and the Gauss distribution shown in fig. B.2. The deconvoluted current transients provide a much better idea of the actual pulse shape and can be used e.g. to tune the parameters of the simulation.

The method presented here is especially helpful to remove asymmetrical contributions like LC oscillations (undershoot, overshoot) and reflections of the signal from the measurement. The method is not intended for final analysis, where a simulation can directly be convoluted with the transfer function; but, for a better understanding of measurements e.g. to find useful parameters for a fit.

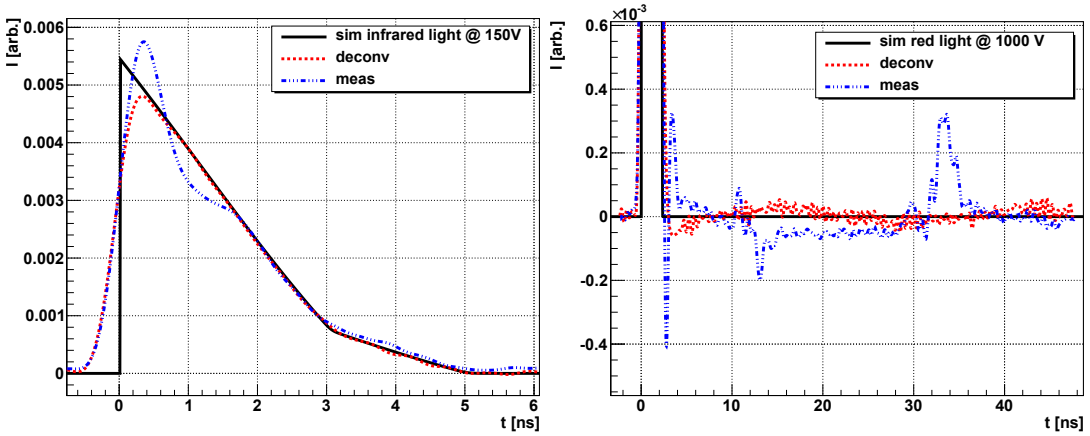

(a) (b)

Figure B.3.: Measured current transients (blue), the deconvolution of the measurements (red), and simulations (black) for a non-irradiated diode for illumination with infrared light (a) and a zoom (b) to visualize the reflections for illumination with red light (electron drift). The bulk thickness of the diode is $d = 200\,\mu\text{m}$.

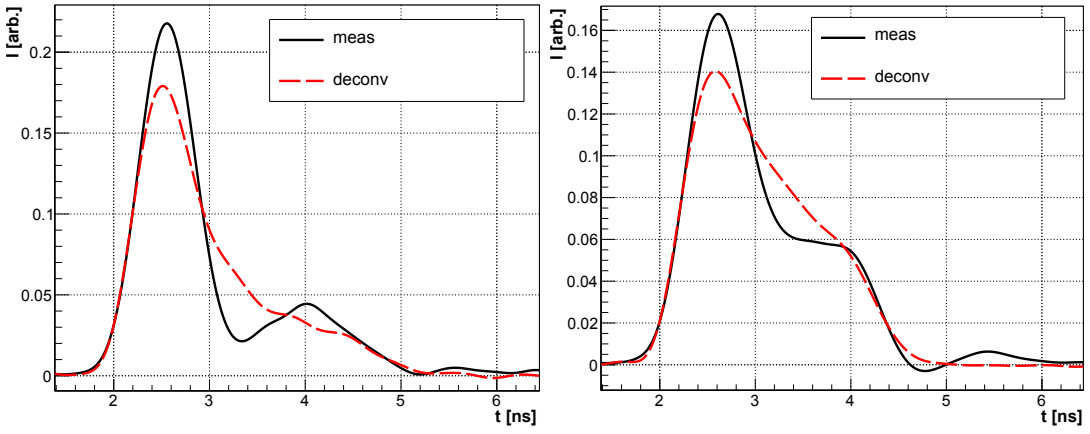

(a) (b)

Figure B.4.: Measured current transients (black) and the deconvolution of the measurements (red) for an irradiated diode for mixed irradiation with $\Phi_{eq} = 3 \cdot 10^{15}\,\text{cm}^{-2}$ protons and $\Phi_{eq} = 7 \cdot 10^{14}\,\text{cm}^{-2}$ neutrons for illumination with red light (electron drift). (a) Shows a reverse bias voltage of 500 V and (b) shows 1000 V. No simulation is shown as the electric field and the trapping are not known. The bulk thickness of the diode is $d = 200\,\mu\text{m}$.

C. Table of the NIR absorption coefficient with fluence

Here, the absorption coefficient as a function of the fluence is given for wavelengths between $\lambda = 1000\,\mathrm{nm}$ and $\lambda = 1150\,\mathrm{nm}$ with[1] $\Delta\lambda = 5\,\mathrm{nm}$. The data has been obtained by spectrophotometer transmittance measurements of silicon crystals as described in chapter 4. All measurements have been performed at $T = 293 \pm 1\,\mathrm{K}$. The data of $\Phi_{abs}(\lambda)$ of eq. 4.13 presented in tab. C.1 below should be independent of the temperature.

[1] In the measurement it is $\Delta\lambda = 1\,\mathrm{nm}$. Here, every fifth data point is given without averaging.

$\lambda\,[nm]$	$\alpha\,(0)$	$\alpha\,(2.4)$	$\alpha\,(4.9)$	$\alpha\,(6.4)$	$\alpha\,(8.6)$	Φ_{abs}	$\sigma_{\Phi_{abs}}$
1150	7.64E-5	1.35E-4	1.77E-4	2.35E-4	2.95E-4	3.21E-1	2.88E-2
1145	9.18E-5	1.51E-4	1.93E-4	2.51E-4	3.14E-4	3.81E-1	3.43E-2
1140	1.09E-4	1.69E-4	2.12E-4	2.70E-4	3.34E-4	4.48E-1	4.02E-2
1135	1.28E-4	1.89E-4	2.32E-4	2.91E-4	3.56E-4	5.22E-1	4.64E-2
1130	1.52E-4	2.13E-4	2.57E-4	3.15E-4	3.84E-4	6.08E-1	5.58E-2
1125	1.77E-4	2.39E-4	2.83E-4	3.42E-4	4.11E-4	7.03E-1	6.38E-2
1120	2.05E-4	2.67E-4	3.12E-4	3.71E-4	4.42E-4	8.07E-1	7.27E-2
1115	2.36E-4	3.00E-4	3.45E-4	4.04E-4	4.77E-4	9.21E-1	8.30E-2
1110	2.73E-4	3.36E-4	3.82E-4	4.41E-4	5.17E-4	1.05E+0	9.58E-2
1105	3.13E-4	3.77E-4	4.24E-4	4.82E-4	5.61E-4	1.20E+0	1.09E-1
1100	3.57E-4	4.22E-4	4.70E-4	5.28E-4	6.09E-4	1.35E+0	1.23E-1
1095	4.10E-4	4.75E-4	5.23E-4	5.82E-4	6.65E-4	1.53E+0	1.41E-1
1090	4.69E-4	5.35E-4	5.84E-4	6.42E-4	7.28E-4	1.73E+0	1.60E-1
1085	5.36E-4	6.03E-4	6.52E-4	7.10E-4	7.99E-4	1.96E+0	1.81E-1
1080	6.14E-4	6.80E-4	7.31E-4	7.88E-4	8.81E-4	2.23E+0	2.09E-1
1075	7.02E-4	7.69E-4	8.20E-4	8.77E-4	9.73E-4	2.54E+0	2.41E-1
1070	8.05E-4	8.71E-4	9.23E-4	9.79E-4	1.08E-3	2.89E+0	2.79E-1
1065	9.21E-4	9.89E-4	1.04E-3	1.10E-3	1.20E-3	3.28E+0	3.21E-1
1060	1.09E-3	1.16E-3	1.21E-3	1.26E-3	1.37E-3	3.85E+0	3.84E-1
1055	1.32E-3	1.39E-3	1.44E-3	1.49E-3	1.61E-3	4.70E+0	4.94E-1
1050	1.57E-3	1.64E-3	1.69E-3	1.74E-3	1.86E-3	5.53E+0	5.88E-1
1045	1.86E-3	1.92E-3	1.98E-3	2.02E-3	2.15E-3	6.67E+0	7.63E-1
1040	2.18E-3	2.24E-3	2.30E-3	2.35E-3	2.48E-3	7.87E+0	9.54E-1
1035	2.55E-3	2.61E-3	2.67E-3	2.71E-3	2.85E-3	9.24E+0	1.19E+0
1030	2.96E-3	3.02E-3	3.08E-3	3.12E-3	3.26E-3	1.08E+1	1.53E+0
1025	3.41E-3	3.47E-3	3.53E-3	3.56E-3	3.72E-3	1.26E+1	1.97E+0
1020	3.90E-3	3.95E-3	4.02E-3	4.05E-3	4.21E-3	1.44E+1	2.43E+0
1015	4.42E-3	4.48E-3	4.54E-3	4.56E-3	4.74E-3	1.68E+1	3.16E+0
1010	4.99E-3	5.04E-3	5.11E-3	5.12E-3	5.31E-3	1.92E+1	4.03E+0
1005	5.59E-3	5.64E-3	5.71E-3	5.72E-3	5.91E-3	2.20E+1	5.22E+0
1000	6.23E-3	6.28E-3	6.35E-3	6.35E-3	6.56E-3	2.48E+1	6.81E+0

Table C.1.: Absorption coefficient $\alpha\,(\Phi_{eq}\ [10^{15}\,\mathrm{cm}^{-2}])\ [cm^{-1}]$ and the damage parameter $\Phi_{abs}\,(\lambda)\ [10^{16}\,\mathrm{cm}^{-2}]$ with error $\sigma_{\Phi_{abs}}\ [10^{16}\,\mathrm{cm}^{-2}]$ for $\lambda = 1150\,\mathrm{nm}$ to $\lambda = 1000\,\mathrm{nm}$.

D. Measured and calculated charge collection efficiency of diodes

Here, the measured CCE of irradiated pad diodes is compared to the calculated CCE with eq. 6.9 using the parameterization $\frac{1}{\mu_{e,h}\tau_{e,h}}(\Phi_{eq})$ of eq. 6.17. The mean values for the diodes are given in fig. 6.9. Please note that $\mu_{e,h}(E)\,\tau_{e,h}(E) = const.$ The parameterization was obtained from edge-TCT measurements of irradiated strip sensors as discussed in sec. 6.2.1. The CCE of the pad diodes (see tab. 3.2, 3.3) was measured for forward bias with the diode TCT setup and $\lambda = 1064\,\text{nm}$ light. The fluence-dependent absorption length of eq. 4.14 was used for the diode TCT and eq. 4.15 for the edge-TCT setup.

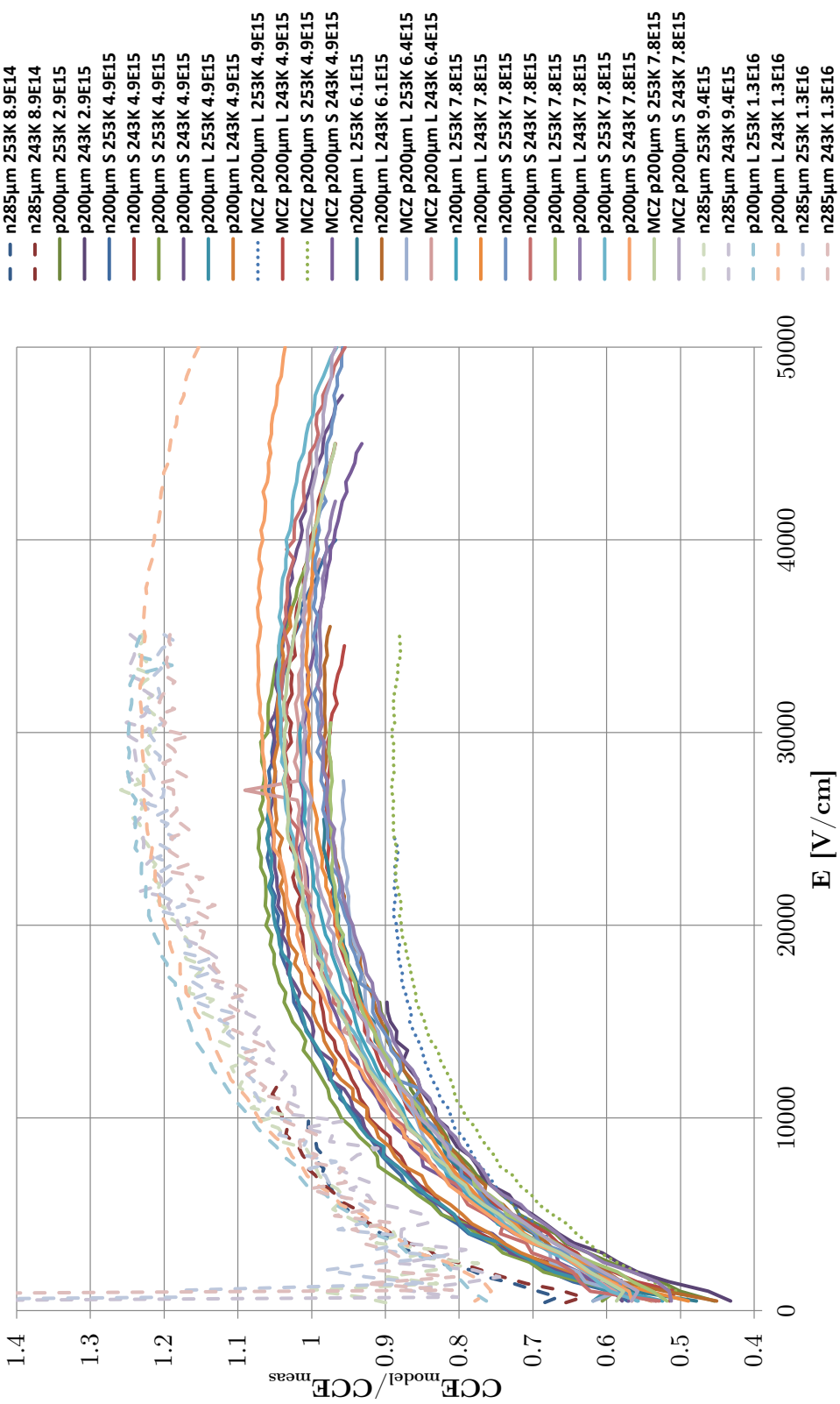

Figure D.1.: Ratios of the calculated CCE with eq. 6.9 using $\frac{1}{\mu_{e,h}\tau_{e,h}}(\Phi_{eq})$ of eq. 6.17 from edge-TCT results and the measured CCE for pad diodes. The measurements were performed with forward bias. The nomenclature p/n200µm gives the initial bulk doping type and the thickness in µm. L/S indicates the pad area, 253K/243K the temperature, and the trailing number gives the equivalent fluence Φ_{eq} in cm^{-2}. Czochralski material is indicated with the prefix „MCZ".

List of Figures

1.1. Drawing of the CMS experiment. 3
1.2. Equivalent fluence in the future CMS tracker after an integrated luminosity of 3000 fb^{-1} at LHC. 4

2.1. Fermi-Dirac distribution and the Fermi energy. 7
2.2. Shockley-Read-Hall generation. 9
2.3. An asymmetric p-n junction in thermal equilibrium. 12
2.4. Ideal diode current. 15
2.5. Reaction of a relaxation and a lifetime semiconductor to a local disturbance. 16
2.6. Simulated initial distribution of vacancies produced by different particles. 19
2.7. Non-ionizing energy loss of various particles as a function of the energy. 20
2.8. Cluster defect representation used to derive the Coulomb interaction. 23
2.9. Current increase and calculated hardness parameters for irradiations with different particles. 23
2.10. Schematic of a silicon radiation detector. 26
2.11. Schematic cross section of a strip sensor showing the weighting potential. 27
2.12. Comparison of the charge collection efficiency of irradiated silicon pad sensors of different thickness. 29

3.1. Schematic cross-section of a pad diode. 32
3.2. Microscope picture of a strip sensor showing the read-out strips. . . 34
3.3. Determination of the voltage offset for the I/V and C/V measurements. 35
3.4. Initial charge distribution and drift for the pad diode TCT. 36
3.5. Simulation of the transient current for TCT. 37
3.6. Schematic principle of edge-TCT. 38
3.7. Picture of the multi-channel edge-TCT setup. 39
3.8. Picture of the PCB and a wire-bonded strip sensor for edge-TCT. . 41
3.9. Drawing of the second-generation PCB. 42

3.10. The edge of a strip sensor before and after polishing. 43
3.11. Intensity of the edge-TCT laser light beam for different positions of the focus. 44
3.12. Determination of the position of the focus for edge-TCT. 45
3.13. Charge profiles obtained with edge-TCT. 46
3.14. Velocity profiles obtained with edge-TCT. 47
3.15. Current transients under a forward bias and the sum of the charge and velocity profiles. 49
3.16. Schematic of the spectrophotometer used for light absorption measurements. 51

4.1. Schematic of attenuation measurements with the edge-TCT setup. . 54
4.2. Charge profiles of the two read-out strips and the ratio of the charge profiles of an irradiated strip sensor. 55
4.3. Measured absorption length of an irradiated sensor versus the bias voltage. 56
4.4. Transmission and absorption of incident light in a plate of bare silicon. 57
4.5. Transmittance measured with silicon plates irradiated to different fluences. 59
4.6. Reproducibilty of the measured transmittance. 60
4.7. Comparison of the literature absorption length and measurements of non-irradiated silicon. 61
4.8. Relative change of the attenuation coefficient at 1052 nm with irradiation at different temperatures. 62
4.9. Damage parameter $\Phi_{abs}(\lambda)$ for different λ. 63
4.10. Increase of the relative absorbed light intensity with fluence in silicon sensors of different thickness. 65

5.1. Energy band diagram of a highly irradiated silicon diode with applied voltage. 67
5.2. Hall resistivity vs. fluence of silicon samples with different initial doping concentrations. 69
5.3. Current density and $\frac{dln(|J|)}{dln(|U|)}$ vs. $|U|$ of diodes irradiated to different fluences for reverse and forward bias. 70
5.4. Velocity profiles of the sensor irradiated to $8.9 \cdot 10^{14}\,\mathrm{cm}^{-2}$. 72
5.5. Velocity profiles for reverse and forward bias of the strip sensors irradiated to $(8.9 - 94) \cdot 10^{14}\,\mathrm{cm}^{-2}$. 73
5.6. Velocity profiles for reverse and forward bias of the sensor irradiated to $1.3 \cdot 10^{16}\,\mathrm{cm}^{-2}$. 74

5.7. Velocity profiles for reverse and forward bias of the sensor irradiated to $7.3 \cdot 10^{15}\,\mathrm{cm}^{-2}$ with the focus at the edge. 74
5.8. Resistivity at low bias voltages $\rho_{ohm}(\Phi_{eq})$ as a function of the fluence. 77
5.9. Differential values of the current measurements for forward and reverse bias. 79
5.10. Current measurements and a fit to the data for n-type and p-type diodes between 5 V forward and 50 V reverse bias. 81
5.11. Parameters obtained from the fit from 5 V forward to 50 V reverse bias. 82
5.12. Ohmic resistivity as a function of $(\Phi_{eq})^{0.9}$. 84
5.13. Sum of the low field mobilities as a function of the fluence. 85
5.14. Resistivity of diodes irradiated to $10^{16}\,\mathrm{cm}^{-2}$ and $10^{17}\,\mathrm{cm}^{-2}$ for reverse bias at 302 K. 85
5.15. Threshold voltages as a function of the fluence. 87
5.16. Temperature dependence of S and $\widetilde{R}_{SCR}$. 88
5.17. $FWHM$ of the velocity profiles compared to the estimated $w\,(U)$ from the current parameterization. 90
5.18. $\frac{A}{d}\frac{\mathrm{d}U}{\mathrm{d}I}$ vs. U of diodes of different thickness for the pad and $\frac{1}{d}\frac{\mathrm{d}U}{\mathrm{d}I}$ for the guard ring at high reverse bias voltage. 92
5.19. Pad volume current and resistivity versus $\frac{U}{d^2}$ for diodes of different thickness. 94
5.20. Current density for high reverse bias at different temperatures scaled to 293.15 K for diodes irradiated to $1.3 \cdot 10^{16}\,\mathrm{cm}^{-2}$. 95
5.21. Fit of the reverse current at high reverse bias voltages. 96
5.22. Comparison of the differential resistance for forward and reverse bias and for different fluences. 99
5.23. Fit of the parameterization for forward current to measurements. . 101
5.24. Fit results of the parameters for the forward current. 102
5.25. Fit results of n_i for the forward current. 103
5.26. Change of the carrier concentrations, the trapped charge, and the electric field for hole injection in the relaxation regime. 105
5.27. Pad capacitance and conductance of irradiated diodes for forward and reverse bias voltages. 108
5.28. Pad capacitance and conductance of the diode irradiated to $\Phi_{eq} = 8.9 \cdot 10^{14}\,\mathrm{cm}^{-2}$ for different AC frequencies. 109

6.1. Measured CCE for red and infrared light illumination of a pad diode irradiated to $1.3 \cdot 10^{16}\,\mathrm{cm}^{-2}$. 117
6.2. Calculated charge profiles for a strip sensor with and without trapping. 120

6.3. Initial charge distribution calculated with eq. 6.11 for different distances from the sensor corner. . . . 121
6.4. Calculated charge profiles for a strip sensor with and without trapping with corrections for light refraction. . . . 122
6.5. Fit of the charge profiles of the strip sensor irradiated to $\Phi_{eq} = 7.25 \cdot 10^{15}\,\mathrm{cm}^{-2}$. . . . 124
6.6. Charge collection lengths for the strip sensor irradiated to $1.3 \cdot 10^{16}\,\mathrm{cm}^{-2}$. . . . 125
6.7. $\mu_{e,h}(E)\,\tau_{e,h}(E) = \frac{\lambda_{ccl}^{e,h}(E)}{E}$ for the measured charge profiles of all sensors. . . . 126
6.8. $1/\mu_{e,h}\tau_{e,h}(\phi_{eq})$ from the fits of the charge profiles. . . . 127
6.9. Mean ratios of the calculated CCE from the charge collection lengths determined with edge-TCT and the measured CCE for pad diodes. 128
6.10. Comparison of the measured CCE of diodes and the calculated CCE as a function of the bias voltage for selected diodes. . . . 130

7.1. Example of the performance of the time-of-flight method. . . . 133
7.2. Comparison of the measured electron mobility and literature parameterizations. . . . 135
7.3. Comparison of the measured hole mobility and literature parameterizations. . . . 136

A.1. Picture of a full wafer for the CMS planar pixel submission. . . . 145
A.2. Implementation of different biasing schemes. . . . 148
A.3. Pixel sensor designs for the PSI46digi ROC. . . . 150
A.4. Pixel sensor designs for the ROC4SENS. . . . 151
A.5. Pixel sensor designs for the RD53A ROC. . . . 152
A.6. Different diode designs. . . . 153
A.7. Design of a strip sensor. . . . 155
A.8. Design of a spaghetti diode. . . . 156
A.9. Designs of a MOS capacitor and a MOSFET. . . . 156

B.1. Example for the performance of the convolution method. . . . 158
B.2. Transfer function and the absolute values of the Fourier transforms used for the deconvolution. . . . 159
B.3. Measured current transients and deconvolution of the measurements for a non-irradiated diode. . . . 160
B.4. Measured current transients and deconvolution of the measurements for an irradiated diode. . . . 160

D.1. Ratio of the calculated CCE from the charge collection lengths determined with edge-TCT and the measured CCE for all pad diodes for forward bias. 164

List of Tables

2.1. Energy levels and estimated introduction rates of various known radiation-induced defects. 21

3.1. Thickness and fluence of the silicon samples used for transmission measurements. 31
3.2. Physical properties of the investigated diodes. 32
3.3. Available fluences for the diodes. 33

7.1. The mobility parameters for $\langle 100 \rangle$ silicon. 132

C.1. Absorption coefficient $\alpha(\lambda)$ at 293 K as a function of the fluence and $\Phi_{abs}(\lambda)$ for $\lambda = 1150\,\text{nm}$ to 1000 nm. 162

Bibliography

[1] Large Hadron Collider (LHC). http://home.web.cern.ch/about/accelerators/large-hadron-collider.

[2] S. Chatrchyan, V. Khachatryan, A.M. Sirunyan, A. Tumasyan, W. Adam, E. Aguilo, T. Bergauer, M. Dragicevic, J. Erö, C. Fabjan, et al. Observation of a new boson at a mass of 125 GeV with the CMS experiment at the LHC. *Physics Letters B*, 716(1):30–61, 2012.

[3] G. Aad, T. Abajyan, B. Abbott, J. Abdallah, S.A. Khalek, A.A. Abdelalim, O. Abdinov, R. Aben, B. Abi, M. Abolins, et al. Observation of a new particle in the search for the Standard Model Higgs boson with the ATLAS detector at the LHC. *Physics Letters B*, 716(1):1–29, 2012.

[4] A Toroidal LHC ApparatuS (ATLAS). http://atlas.cern/.

[5] Compact Muon Solenoid (CMS). http://cms.cern/.

[6] P.W. Higgs. Broken symmetries and the masses of gauge bosons. *Physical Review Letters*, 13(16):508, 1964.

[7] O. Brüning M. Lamont L. Rossi G. Apollinari, I. Bejar Alonso. Prelimary Design Report: High-Luminosity Large Hadron Collider. Technical report, CERN-2015-005, Geneva, 2015.

[8] G. Apollinari, O. Brüning, T. Nakamoto, and L. Rossi. High Luminosity Large Hadron Collider HL-LHC. *arXiv preprint arXiv:1705.08830*, 2017.

[9] V. Sola, R. Arcidiacono, A. Bellora, N. Cartiglia, F. Cenna, R. Cirio, S. Durando, M. Ferrero, Z. Galloway, B. Gruey, et al. Ultra-fast silicon detectors for 4D tracking. *Journal of Instrumentation*, 12(02):C02072, 2017.

[10] D. Contardo, M. Klute, J. Mans, L. Silvestris, and J. Butler. Technical Proposal for the Phase-II Upgrade of the CMS Detector. Technical Report CERN-LHCC-2015-010. LHCC-P-008. CMS-TDR-15-02, Geneva, Jun 2015.

[11] K. Klein. The Phase-2 Upgrade of the CMS Tracker. Technical report, 2017.

[12] E. Currás, M. Fernández, C. Gallrapp, L. Gray, M. Mannelli, P. Meridiani, M. Moll, S. Nourbakhsh, C. Scharf, P. Silva, et al. Radiation hardness and precision timing study of silicon detectors for the CMS High Granularity Calorimeter (HGC). *Nuclear Instruments and Methods in Physics Research Section A: Accelerators, Spectrometers, Detectors and Associated Equipment*, 845:60–63, 2017.

[13] N. Akchurin, V. Ciriolo, E. Currás, J. Damgov, M. Fernández, C. Gallrapp, L. Gray, A. Junkes, M. Mannelli, K.H. Martin Kwok, et al. On the timing performance of thin planar silicon sensors. *Nuclear Instruments and Methods in Physics Research Section A: Accelerators, Spectrometers, Detectors and Associated Equipment*, 859:31–36, 2017.

[14] T. Quast. Construction and beam-tests of silicon-tungsten prototype modules for the CMS High Granularity Calorimeter for HL-LHC. *arXiv preprint arXiv:1712.05638*, 2017.

[15] J. Butler, M. Klute, L. Silvestris, J. Mans, D. Contardo, et al. CMS Phase II upgrade scope document. Technical report, 2015.

[16] M. Moll. *Radiation Damage in Silicon Particle Detectors Microscopic Defects and Macroscopic Properties.* PhD Thesis, University of Hamburg, 1999. DESY-THESIS-1999-040.

[17] A.S. Grove. *Physics and Technology of Semiconductor Devices.* Wiley, New York, 1967.

[18] R. Couderc, M. Amara, and M. Lemiti. Reassessment of the intrinsic carrier density temperature dependence in crystalline silicon. *Journal of Applied Physics*, 115(9):093705, 2014.

[19] R. Pässler. Dispersion-related description of temperature dependencies of band gaps in semiconductors. *Physical Review B*, 66(8):085201, 2002.

[20] W.M. Bullis. Properties of gold in silicon. *Solid-State Electronics*, 9(2):143–168, 1966.

[21] R.F. Bass. Influence of impurities on carrier removal and annealing in neutron-irradiated silicon. *IEEE Transactions on Nuclear Science*, 14(6):78–81, 1967.

[22] S.M. Sze and K.K. Ng. *Physics of semiconductor devices.* John Wiley & Sons, 2006.

[23] E. Fretwurst, E. Garutti, M. Hufschmidt, R. Klanner, I. Kopsalis, and J. Schwandt. The influence of edge effects on the determination of the doping profile of silicon pad diodes. *Nuclear Instruments and Methods in Physics Research Section A: Accelerators, Spectrometers, Detectors and Associated Equipment*, 867:231–236, 2017.

[24] W. Shockley. The Theory of p-n Junctions in Semiconductors and p-n Junction Transistors. *Bell Labs Technical Journal*, 28(3):435–489, 1949.

[25] G.H. Döhler and H. Heyszenau. Conduction in the relaxation regime. *Physical Review B*, 12(2):641, 1975.

[26] H.J. Queisser, H.C. Casey Jr, and W. Van Roosbroeck. Carrier transport and potential distributions for a semiconductor p-n junction in the relaxation regime. *Physical Review Letters*, 26(10):551, 1971.

[27] J.C. Manifacier and H.K. Henisch. Minority-carrier injection into semiconductors containing traps. *Physical Review B*, 17(6):2648, 1978.

[28] C.D. Child. Discharge from hot CaO. *Physical Review (Series I)*, 32(5):492, 1911.

[29] N.F. Mott and R.W. Gurney. Electronic processes in ionic crystals. 1940.

[30] M.A. Lampert. Volume-controlled current injection in insulators. *Reports on Progress in Physics*, 27(1):329, 1964.

[31] M.A. Lampert. Simplified theory of space-charge-limited currents in an insulator with traps. *Physical Review*, 103(6):1648, 1956.

[32] M.A. Lampert and R.B. Schilling. Current injection in solids: The regional approximation method. *Semiconductors and Semimetals*, 6:1–96, 1970.

[33] A. Rose. Space-charge-limited currents in solids. *Physical Review*, 97(6):1538, 1955.

[34] J.R. Srour, C.J. Marshall, and P.W. Marshall. Review of displacement damage effects in silicon devices. *IEEE Transactions on Nuclear Science*, 50(3):653–670, 2003.

[35] D.M. Fleetwood. Total ionizing dose effects in MOS and low-dose-rate-sensitive linear-bipolar devices. *IEEE Transactions on Nuclear Science*, 60(3):1706–1730, 2013.

[36] T. Poehlsen, E. Fretwurst, R. Klanner, S. Schuwalow, J. Schwandt, and J. Zhang. Charge losses in segmented silicon sensors at the Si-SiO2 interface. *Nuclear Instruments and Methods in Physics Research Section A: Accelerators, Spectrometers, Detectors and Associated Equipment*, 700:22–39, 2013.

[37] Tracker Group of the CMS Collaboration and others. Impact of low-dose electron irradiation on n+ p silicon strip sensors. *Nuclear Instruments and Methods in Physics Research Section A: Accelerators, Spectrometers, Detectors and Associated Equipment*, 803:100–112, 2015.

[38] J. Schwandt, E. Fretwurst, E. Garutti, R. Klanner, and I. Kopsalis. Surface effects in segmented silicon sensors. *Nuclear Instruments and Methods in Physics Research Section A: Accelerators, Spectrometers, Detectors and Associated Equipment*, 845:159–163, 2017.

[39] M. Huhtinen. Simulation of non-ionising energy loss and defect formation in silicon. *Nuclear Instruments and Methods in Physics Research Section A: Accelerators, Spectrometers, Detectors and Associated Equipment*, 491(1):194–215, 2002.

[40] G.H. Kinchin and R.S. Pease. The displacement of atoms in solids by radiation. *Reports on progress in physics*, 18(1):1, 1955.

[41] V.A.J. Van Lint, T.M. Flanagan, R.E. Leadon, J.A. Naber, and V.C. Rogers. Mechanisms of radiation effects in electronic materials. volume 1. *NASA STI/Recon Technical Report A*, 81, 1980.

[42] J.J. Loferski and P. Rappaport. Radiation damage in Ge and Si detected by carrier lifetime changes: damage thresholds. *Physical Review*, 111(2):432, 1958.

[43] G. Lindström. Radiation damage in silicon detectors. *Nuclear Instruments and Methods in Physics Research Section A: Accelerators, Spectrometers, Detectors and Associated Equipment*, 512(1):30–43, 2003.

[44] A. Scheinemann and A. Schenk. TCAD-based DLTS simulation for analysis of extended defects. *physica status solidi (a)*, 211(1):136–142, 2014.

[45] B.R. Gossick. Disordered regions in semiconductors bombarded by fast neutrons. *Journal of Applied Physics*, 30(8):1214–1218, 1959.

[46] A. Junkes. *Influence of Radiation Induced Defect Clusters on Silicon Particle Detectors*. PhD Thesis, University of Hamburg, 2011. DESY-THESIS-2011-031.

[47] E.M. Donegani. *Energy-Dependent Proton Damage in Silicon*. PhD Thesis, University of Hamburg, 2017. DESY-THESIS-2017-042.

[48] Victor A.J. van Lint, G. Gigas, and J. Barengoltz. Correlation of displacement effects produced by electrons protons and neutrons in silicon. *IEEE Transactions on Nuclear Science*, 22(6):2663–2668, 1975.

[49] A. Van Ginneken. Nonionizing energy deposition in silicon for radiation damage studies. Technical report, 1989.

[50] A. Van Ginneken. Nonionizing energy deposition in silicon for radiation damage studies. 1989.

[51] R. Radu, I. Pintilie, L.C. Nistor, E. Fretwurst, G. Lindström, and L.F. Makarenko. Investigation of point and extended defects in electron irradiated silicon - dependence on the particle energy. *Journal of Applied Physics*, 117(16):164503, 2015.

[52] C. Neubüser. *Impact of Irradiations by Protons with different Energies on Silicon Sensors*. Master's Thesis, University of Hamburg, 2013. DESY-THESIS-2013-021.

[53] D.V. Lang. Deep-level transient spectroscopy: A new method to characterize traps in semiconductors. *Journal of applied physics*, 45(7):3023–3032, 1974.

[54] V. Eremin, E. Verbitskaya, and Z. Li. The origin of double peak electric field distribution in heavily irradiated silicon detectors. *Nuclear Instruments and Methods in Physics Research Section A: Accelerators, Spectrometers, Detectors and Associated Equipment*, 476(3):556–564, 2002.

[55] R. Wunstorf, W.M. Bugg, J. Walter, F.W. Garber, and D. Larson. Investigations of donor and acceptor removal and long term annealing in silicon with different boron/phosphorus ratios. *Nuclear Instruments and Methods in Physics Research Section A: Accelerators, Spectrometers, Detectors and Associated Equipment*, 377(2-3):228–233, 1996.

[56] W.E. Johnson and K. Lark-Horovitz. Neutron irradiated semiconductors. *Physical Review*, 76(3):442, 1949.

[57] D. Pitzl, N. Cartiglia, B. Hubbard, D. Hutchinson, J. Leslie, K. O'Shaughnessy, W. Rowe, H.F.W. Sadrozinski, A. Seiden, E. Spencer, et al. Type inversion in silicon detectors. *Nuclear Instruments and Methods in Physics Research Section A: Accelerators, Spectrometers, Detectors and Associated Equipment*, 311(1-2):98–104, 1992.

[58] M. Moll, E. Fretwurst, G. Lindström, et al. Investigation on the improved radiation hardness of silicon detectors with high oxygen concentration. *Nuclear Instruments and Methods in Physics Research Section A: Accelerators, Spectrometers, Detectors and Associated Equipment*, 439(2):282–292, 2000.

[59] A. Khan, M. Yamaguchi, Y. Ohshita, N. Dharmaraso, K. Araki, V.T. Khanh, H. Itoh, T. Ohshima, M. Imaizumi, and S. Matsuda. Strategies for improving radiation tolerance of Si space solar cells. *Solar energy materials and solar cells*, 75(1):271–276, 2003.

[60] S. Terzo, RD50 Collaboration, et al. Radiation hard silicon particle detectors for HL-LHC-RD50 status report. *Nuclear Instruments and Methods in Physics Research Section A: Accelerators, Spectrometers, Detectors and Associated Equipment*, 845:177–180, 2017.

[61] J.H. Crawford Jr. Radiation effects in diamond lattice semiconductors. *IEEE (Inst. Elec. Electron. Engrs.), Trans. Nucl. Sci.*, 10(5), 1963.

[62] O.L. Curtis. Effects of oxygen and dopant on lifetime in neutron-irradiated silicon. *IEEE Transactions on Nuclear Science*, 13(6):33–40, 1966.

[63] E.M. Donegani, E. Fretwurst, E. Garutti, R. Klanner, G. Lindstroem, I. Pintilie, R. Radu, and J. Schwandt. Study of point- and cluster-defects in radiation-damaged silicon. *arXiv preprint arXiv:1803.06950*, 2018.

[64] A. Vasilescu. The NIEL scaling hypothesis applied to neutron spectra of irradiation facilities and in the ATLAS and CMS SCT. *ROSE= TN*, pages 97–2, 1997.

[65] G.P. Summers, E.A. Burke, C.J. Dale, E.A. Wolicki, P.W. Marshall, and M.A. Gehlhausen. Correlation of particle-induced displacement damage in silicon. *IEEE Transactions on Nuclear Science*, 34(6):1133–1139, 1987.

[66] J.R. Srour, S.C. Chen, S. Othmer, and R.A. Hartmann. Radiation damage coefficients for silicon depletion regions. *IEEE Transactions on Nuclear Science*, 26(6):4783–4791, 1979.

[67] F. Pozzi, R. Garcia Alia, M. Brugger, P. Carbonez, S. Danzeca, B. Gkotse, M. Richard Jaekel, F. Ravotti, M. Silari, and M. Tali. CERN irradiation facilities, 2017.

[68] H. Feick. *Radiation tolerance of silicon particle detectors for high-energy physics experiments*. PhD Thesis, University of Hamburg, 1997. DESY-F35D-97-08.

[69] M. Moll, E. Fretwurst, G. Lindström, et al. Leakage current of hadron irradiated silicon detectors-material dependence. *Nuclear Instruments and Methods in Physics Research Section A: Accelerators, Spectrometers, Detectors and Associated Equipment*, 426(1):87–93, 1999.

[70] M. Moll, E. Fretwurst, M. Kuhnke, and G. Lindström. Relation between microscopic defects and macroscopic changes in silicon detector properties after hadron irradiation. *Nuclear Instruments and Methods in Physics Research Section B: Beam Interactions with Materials and Atoms*, 186(1):100–110, 2002.

[71] A. Chilingarov. Temperature dependence of the current generated in Si bulk. *Journal of instrumentation*, 8(10):P10003, 2013.

[72] G. Lindström, M. Ahmed, S. Albergo, P. Allport, D. Anderson, L. Andricek, M.M. Angarano, V. Augelli, N. Bacchetta, P. Bartalini, et al. Radiation hard silicon detectors-developments by the RD48 (ROSE) collaboration. *Nuclear Instruments and Methods in Physics Research Section A: Accelerators, Spectrometers, Detectors and Associated Equipment*, 466(2):308–326, 2001.

[73] V. Eremin, Z. Li, and I. Iljashenko. Trapping induced Neff and electrical field transformation at different temperatures in neutron irradiated high resistivity silicon detectors. *Nuclear Instruments and Methods in Physics Research Section A: Accelerators, Spectrometers, Detectors and Associated Equipment*, 360(1-2):458–462, 1995.

[74] H.F.W. Sadrozinski, S. Ely, V. Fadeyev, Z. Galloway, J. Ngo, C. Parker, B. Petersen, A. Seiden, A. Zatserklyaniy, N. Cartiglia, et al. Ultra-fast silicon detectors. *Nuclear Instruments and Methods in Physics Research Section A: Accelerators, Spectrometers, Detectors and Associated Equipment*, 730:226–231, 2013.

[75] V. Radeka. Low-noise techniques in detectors. *Annual Review of Nuclear and Particle Science*, 38(1):217–277, 1988.

[76] S. Ramo. Currents Induced by Electron Motion. *Proceedings of the IRE*, 27(9):584–585, 1939.

[77] Esteban Currás Rivera. *Advanced silicon sensors for future collider experiments*. PhD Thesis, Universidad de Cantabria, 2017. CERN-THESIS-2017-212.

[78] C. Da Via, E. Bolle, K. Einsweiler, M. Garcia-Sciveres, J. Hasi, C. Kenney, V. Linhart, S. Parker, S. Pospisil, O. Rohne, et al. 3D active edge silicon sensors with different electrode configurations: Radiation hardness and noise performance. *Nuclear Instruments and Methods in Physics Research Section A: Accelerators, Spectrometers, Detectors and Associated Equipment*, 604(3):505–511, 2009.

[79] C. Da Via, M. Boscardin, G.F. Dalla Betta, G. Darbo, C. Fleta, C. Gemme, P. Grenier, S. Grinstein, T.E. Hansen, J. Hasi, et al. 3D silicon sensors: Design, large area production and quality assurance for the ATLAS IBL pixel detector upgrade. *Nuclear Instruments and Methods in Physics Research Section A: Accelerators, Spectrometers, Detectors and Associated Equipment*, 694:321–330, 2012.

[80] J. Lange, M.C. Areste, E. Cavallaro, F. Förster, S. Grinstein, I.L. Paz, M. Manna, G. Pellegrini, D. Quirion, S. Terzo, et al. 3D silicon pixel detectors for the High-Luminosity LHC. *Journal of Instrumentation*, 11(11):C11024, 2016.

[81] C. Scharf. *Measurement of the Drift Velocities of Electrons and Holes in High-Ohmic <100> Silicon*. MSc Thesis, University of Hamburg, 2014. DESY-THESIS-2014-015.

[82] Hamamatsu Photonics K.K. http://www.hamamatsu.com/.

[83] CiS Forschungsinstitut für Mikrosensorik und Photovoltaik GmbH. http://www.cismst.org/.

[84] STMicroelectronics. http://www.st.com/.

[85] F. Feindt. *Edge-TCT for the Investigation of Radiation Damaged Silicon Strip Sensors*. MSc Thesis, University of Hamburg, 2017. DESY-THESIS-2017-006.

[86] Tektronix, Inc. http://www.tek.com/.

[87] J. Becker. *Signal development in silicon sensors used for radiation detection*. PhD Thesis, University of Hamburg, 2010. DESY-THESIS-2010-33.

[88] Deutsches Elektronen-Synchrotron (DESY). http://www.desy.de/.

[89] W. Seibt, K.-E. Sundström, and P.A. Tove. Charge collection in silicon detectors for strongly ionizing particles. *Nuclear Instruments and Methods*, 113(3):317–324, 1973.

[90] J. Becker, D. Eckstein, R. Klanner, and G. Steinbrück. Impact of plasma effects on the performance of silicon sensors at an X-ray FEL. *Nuclear Instruments and Methods in Physics Research Section A: Accelerators, Spectrometers, Detectors and Associated Equipment*, 615(2):230–236, 2010.

[91] I. Mandić, V. Cindro, G. Kramberger, and M. Mikuž. Annealing effects in n+-p strip detectors irradiated with high neutron fluences. *Nuclear Instruments and Methods in Physics Research Section A: Accelerators, Spectrometers, Detectors and Associated Equipment*, 629(1):101–105, 2011.

[92] M. Milovanović, V. Cindro, G. Kramberger, I. Mandić, M. Mikuž, and M. Zavrtanik. Effects of accelerated long term annealing in highly irradiated n+-p strip detector examined by edge-TCT. *Journal of Instrumentation*, 7(06):P06007, 2012.

[93] G. Kramberger, V. Cindro, I. Mandic, M. Mikuz, M. Milovanovic, M. Zavrtanik, and K. Zagar. Investigation of irradiated silicon detectors by edge-TCT. *IEEE transactions on nuclear science*, 57(4):2294–2302, 2010.

[94] Agilent Technologies. http://www.agilent.com/.

[95] G. Davies, S. Hayama, L. Murin, R. Krause-Rehberg, V. Bondarenko, A. Sengupta, C. Davia, and A. Karpenko. Radiation damage in silicon exposed to high-energy protons. *Physical Review B*, 73(16):165202, 2006.

[96] H.Y. Fan and A.K. Ramdas. Infrared absorption and photoconductivity in irradiated silicon. *Journal of Applied Physics*, 30(8):1127–1134, 1959.

[97] M.A. Green and M.J. Keevers. Optical properties of intrinsic silicon at 300 K. *Progress in Photovoltaics: Research and Applications*, 3(3):189–192, 1995.

[98] M.F. García, J.G. Sánchez, R.J. Echeverría, M. Moll, R.M. Santos, D. Moya, R.P. Pinto, and I. Vila. High-resolution three-dimensional imaging of a depleted CMOS sensor using an edge Transient Current Technique based on the two photon absorption process (TPA-eTCT). *Nuclear Instruments and*

Methods in Physics Research Section A: Accelerators, Spectrometers, Detectors and Associated Equipment, 845:69–71, 2017.

[99] K.G. Svantesson and N.G. Nilsson. Determination of the temperature dependence of the free carrier and interband absorption in silicon at 1.06 μm. *Journal of Physics C: Solid State Physics*, 12(18):3837, 1979.

[100] R. Soref and B. Bennett. Electrooptical effects in silicon. *IEEE journal of quantum electronics*, 23(1):123–129, 1987.

[101] J. Lange, R. Klanner, G. Kramberger, I. Mandic, E. Fretwurst, G. Lindstrom, and J. Becker. Charge multiplication properties in highly irradiated epitaxial silicon detectors. *PoS*, page 025, 2010.

[102] W. Van Roosbroeck and H.C. Casey Jr. Transport in relaxation semiconductors. *Physical Review B*, 5(6):2154, 1972.

[103] J. Santana, B.K. Jones, T. Sloan, and K. Zdansky. GaAs radiation detectors in the relaxation regime. In *Proc. GaAs and Related Compounds*, pages 61–66, 1995.

[104] J. Dacuña and A. Salleo. Modeling space-charge-limited currents in organic semiconductors: Extracting trap density and mobility. *Physical Review B*, 84(19):195209, 2011.

[105] J.M. Swartz and M.O. Thurston. Analysis of the Effect of Fast-Neutron Bombardment on the Current-Voltage Characteristic of a Conductivity-Modulated p-i-n Diode. *Journal of Applied Physics*, 37(2):745–755, 1966.

[106] M. McPherson, B.K. Jones, and T. Sloan. Effects of radiation damage in silicon p-i-n photodiodes. *Semiconductor science and technology*, 12(10):1187, 1997.

[107] A. Saadoune, L. Dehimi, N. Sengouga, M. McPherson, and B.K. Jones. Modelling of semiconductor diodes made of high defect concentration, irradiated, high resistivity and semi-insulating material: The capacitance–voltage characteristics. *Solid-state electronics*, 50(7-8):1178–1182, 2006.

[108] V. Eremin, J. Härkönen, Z. Li, and E. Verbitskaya. Current injected detectors at super-LHC program. *Nuclear Instruments and Methods in Physics Research Section A: Accelerators, Spectrometers, Detectors and Associated Equipment*, 583(1):91–98, 2007.

[109] V. Eremin, N. Fadeeva, and E. Verbitskaya. The impact of active base on the bulk current in silicon heavily irradiated detectors. *Journal of Instrumentation*, 12(09):P09005, 2017.

[110] Z. Li. Modeling and simulation of neutron induced changes and temperature annealing of n_{eff} and changes in resistivity in high resistivity silicon detectors. *Nuclear Instruments and Methods in Physics Research Section A: Accelerators, Spectrometers, Detectors and Associated Equipment*, 342(1):105–118, 1994.

[111] V.N. Brudnyi, S.N. Grinyaev, and V.E. Stepanov. Local neutrality conception: Fermi level pinning in defective semiconductors. *Physica B: Condensed Matter*, 212(4):429–435, 1995.

[112] R. Coates and E.W.J. Mitchell. Tunnel assisted hopping in neutron irradiated gallium arsenide. *Journal of Physics C: Solid State Physics*, 5(10):L113, 1972.

[113] E. Borchi, M. Bruzzi, B. Dezillie, S. Lazanu, Z. Li, and S. Pirollo. Hall effect analysis in irradiated silicon samples with different resistivities. *IEEE Transactions on Nuclear Science*, 46(4):834–838, 1999.

[114] N. Croitoru, R. Dahan, P.G. Rancoita, M. Rattaggi, G. Rossi, and A. Seidman. Study of resistivity and majority carrier concentration of silicon damaged by neutron irradiation. *Nuclear Physics B-Proceedings Supplements*, 61(3):456–463, 1998.

[115] G. Lutz. Effects of deep level defects in semiconductor detectors. *Nuclear Instruments and Methods in Physics Research Section A: Accelerators, Spectrometers, Detectors and Associated Equipment*, 377(2-3):234–243, 1996.

[116] I. Mandić, RD50 Collaboration, et al. Silicon sensors for HL-LHC tracking detectors. *Nuclear Instruments and Methods in Physics Research Section A: Accelerators, Spectrometers, Detectors and Associated Equipment*, 732:126–129, 2013.

[117] L.W. Aukerman, P.W. Davis, R.D. Graft, and T.S. Shilliday. Radiation effects in GaAs. *Journal of Applied Physics*, 34(12):3590–3599, 1963.

[118] C. Jacoboni, C. Canali, G. Ottaviani, and A. Alberigi Quaranta. A review of some charge transport properties of silicon. *Solid-State Electronics*, 20(2):77–89, 1977.

[119] C. Da Via and S.J. Watts. Can silicon operate beyond 10^{15} neutrons cm^{-2}? *Nuclear Instruments and Methods in Physics Research Section A: Accelerators, Spectrometers, Detectors and Associated Equipment*, 501(1):138–145, 2003.

[120] A. Saadoune, S.J. Moloi, K. Bekhouche, L. Dehimi, M. McPherson, N. Sengouga, and B.K. Jones. Modeling of Semiconductor Detectors Made of Defect-Engineered Silicon: The Effective Space Charge Density. *IEEE Transactions on Device and Materials Reliability*, 13(1):1–8, 2013.

[121] C.T. Sah, R.N. Noyce, and W. Shockley. Carrier generation and recombination in pn junctions and pn junction characteristics. *Proceedings of the IRE*, 45(9):1228–1243, 1957.

[122] N.D. Arora, J.R. Hauser, and D.J. Roulston. Electron and hole mobilities in silicon as a function of concentration and temperature. *IEEE Transactions on Electron Devices*, 29(2):292–295, 1982.

[123] G. Masetti, M. Severi, and S. Solmi. Modeling of carrier mobility against carrier concentration in arsenic-, phosphorus-, and boron-doped silicon. *IEEE Transactions on electron devices*, 30(7):764–769, 1983.

[124] D.B.M. Klaassen, J.W. Slotboom, and H.C. De Graaff. Unified apparent bandgap narrowing in n- and p-type silicon. *Solid-State Electronics*, 35(2):125–129, 1992.

[125] T. Maekawa, S. Inoue, M. Aiura, and A. Usami. The effect of radiation damage on carrier mobility in neutron-transmutation-doped silicon. *Semiconductor science and technology*, 3(2):77, 1988.

[126] S.J. Moloi and M. McPherson. Radiation-hardness of silicon p-i-n photodiodes operated under illumination by light of different wavelengths. *Nuclear Instruments and Methods in Physics Research Section A: Accelerators, Spectrometers, Detectors and Associated Equipment*, 632(1):59–68, 2011.

[127] T.J. Brodbeck, A. Chilingarov, T. Sloan, E. Fretwurst, M. Kuhnke, and G. Lindstroem. Carrier mobilities in irradiated silicon. *Nuclear Instruments and Methods in Physics Research Section A: Accelerators, Spectrometers, Detectors and Associated Equipment*, 477(1):287–292, 2002.

[128] C. Leroy, P. Roy, G. Casse, M. Glaser, E. Grigoriev, and F. Lemeilleur. Study of charge transport in non-irradiated and irradiated silicon detectors.

Nuclear Instruments and Methods in Physics Research Section A: Accelerators, Spectrometers, Detectors and Associated Equipment, 426(1):99–108, 1999.

[129] M.F. García. Two Photon Absorption-TCT of irradiated LGADs. Las Caldas, Spain, 2017. Presented at the 26th International Workshop on Vertex Detectors.

[130] L.R. Weisberg. Anomalous mobility effects in some semiconductors and insulators. *Journal of Applied Physics*, 33(5):1817–1821, 1962.

[131] T. Ohsugi, Y. Iwata, H. Ohyama, T. Ohmoto, M. Yoshikawa, T. Handa, K. Kurino, K. Fujita, N. Tamura, T. Hatakenaka, et al. Micro-discharge at strip edge of silicon microstrip sensors. *Nuclear Instruments and Methods in Physics Research Section A: Accelerators, Spectrometers, Detectors and Associated Equipment*, 383(1):116–122, 1996.

[132] T. Ohsugi, Y. Iwata, H. Ohyama, T. Ohmoto, M. Yoshikawa, T. Handa, K. Kurino, K. Fujita, H. Kitabayashi, N. Tamura, et al. Micro-discharge noise and radiation damage of silicon microstrip sensors. *Nuclear Instruments and Methods in Physics Research Section A: Accelerators, Spectrometers, Detectors and Associated Equipment*, 383(1):166–173, 1996.

[133] W. Maes, K. De Meyer, and R. Van Overstraeten. Impact ionization in silicon: A review and update. *Solid-State Electronics*, 33(6):705 – 718, 1990.

[134] G.A.M. Hurkx, D.B.M. Klaassen, and M.P.G. Knuvers. A new recombination model for device simulation including tunneling. *IEEE Transactions on electron devices*, 39(2):331–338, 1992.

[135] A. Poyai, E. Simoen, and C. Claeys. Impact of a high electric field on the extraction of the generation lifetime from the reverse generation current component of shallow n^+-p-well diodes. *IEEE Transactions on Electron Devices*, 48(10):2445–2446, 2001.

[136] J.G. Simmons. Poole-frenkel effect and schottky effect in metal-insulator-metal systems. *Physical Review*, 155(3):657, 1967.

[137] I. Solomon, R. Benferhat, and H. Tran Quoc. Space-charge-limited conduction for the determination of the midgap density of states in amorphous silicon: Theory and experiment. *Phys. Rev. B*, 30:3422–3429, Sep 1984.

[138] E. Fretwurst, V. Eremin, H. Feick, J. Gerhardt, Z. Li, and G. Lindström. Investigation of damage-induced defects in silicon by TCT. *Nuclear Instruments and Methods in Physics Research Section A: Accelerators, Spectrometers, Detectors and Associated Equipment*, 388(3):356–360, 1997.

[139] M. Mikuž. Personal communication.

[140] M.F. García. Two Photon Absorption-TCT of irradiated LGADs. Geneva, Switzerland, 2017. Presented at the 31st RD50 Workshop.

[141] Y. Moreau, J.C. Manifacier, and H.K. Henisch. Minority-carrier injection into relaxation semiconductors. *Journal of applied physics*, 60(8):2904–2909, 1986.

[142] B.K. Jones and M. McPherson. Radiation damaged silicon as a semi-insulating relaxation semiconductor: static electrical properties. *Semiconductor science and technology*, 14(8):667, 1999.

[143] J. Mekki, M. Moll, M. Fahrer, M. Glaser, and L. Dusseau. Prediction of the response of the commercial BPW34FS silicon pin diode used as radiation monitoring sensors up to very high fluences. *IEEE Transactions on Nuclear Science*, 57(4):2066–2073, 2010.

[144] L.J. Beattie, A. Chilingarov, T. Sloan, et al. Forward-bias operation of Si detectors:: a way to work in high-radiation environment. *Nuclear Instruments and Methods in Physics Research Section A: Accelerators, Spectrometers, Detectors and Associated Equipment*, 439(2):293–302, 2000.

[145] G.G. Roberts and F.W. Schmidlin. Study of localized levels in semi-insulators by combined measurements of thermally activated ohmic and space-charge-limited conduction. *Physical Review*, 180(3):785, 1969.

[146] F. Schauer, R. Novotny, and S. Nešpůrek. Space-charge-limited-current spectroscopy: Possibilities and limitations. *Journal of applied physics*, 81(3):1244–1249, 1997.

[147] W.C. Dash and R. Newman. Intrinsic optical absorption in single-crystal germanium and silicon at 77 K and 300 K. *Physical Review*, 99(4):1151, 1955.

[148] C. Scharf and R. Klanner. Measurement of the drift velocities of electrons and holes in high-ohmic <100> silicon. *Nuclear Instruments and Methods in Physics Research Section A: Accelerators, Spectrometers, Detectors and Associated Equipment*, 799:81–89, 2015.

[149] C. Scharf and R. Klanner. Precision measurement of the carrier drift velocities in <100> silicon. *Journal of Instrumentation*, 10(11):C11008, 2015.

[150] C. Canali, G. Ottaviani, and A. Alberigi Quaranta. Drift velocity of electrons and holes and associated anisotropic effects in silicon. *Journal of Physics and Chemistry of Solids*, 32(8):1707–1720, 1971.

[151] Synopsis TCAD. http://www.synopsys.com/Tools/TCAD/.

[152] G. Steinbrück. Small pitch pixel sensors for the CMS phase ii upgrade. In *Nuclear Science Symposium and Medical Imaging Conference (NSS/MIC), 2015 IEEE*, pages 1–6. IEEE, 2015.

[153] KLayout. http://www.klayout.de/.

[154] M. Caselle, T. Blank, F. Colombo, A. Dierlamm, U. Husemann, S. Kudella, and M. Weber. Low-cost bump-bonding processes for high energy physics pixel detectors. *Journal of Instrumentation*, 11(01):C01050, 2016.

[155] Fraunhofer-Institut für Zuverlässigkeit und Mikrointegration IZM. https://www.izm.fraunhofer.de/en.html.

[156] M. Garcia-Sciveres, D. Arutinov, M. Barbero, R. Beccherle, S. Dube, D. Elledge, J. Fleury, D. Fougeron, F. Gensolen, D. Gnani, et al. The FE-I4 pixel readout integrated circuit. *Nuclear Instruments and Methods in Physics Research Section A: Accelerators, Spectrometers, Detectors and Associated Equipment*, 636(1):S155–S159, 2011.

[157] N. Demaria, G. Dellacasa, G. Mazza, A. Rivetti, M.D. Da Rocha Rolo, E. Monteil, L. Pacher, F. Ciciriello, F. Corsi, C. Marzocca, et al. CHIPIX65: Developments on a new generation pixel readout ASIC in CMOS 65 nm for HEP experiments. In *Advances in Sensors and Interfaces (IWASI), 2015 6th IEEE International Workshop on*, pages 49–54. IEEE, 2015.

[158] F. Fahim. Fermi CMS Pixel (FCP130) test ASIC. Technical report, Fermi National Accelerator Laboratory (FNAL), Batavia, IL (United States), 2014.

[159] T. Bergauer, On behalf for the CMS Collaboration, et al. Silicon sensor prototypes for the Phase II upgrade of the CMS tracker. *Nuclear Instruments and Methods in Physics Research Section A: Accelerators, Spectrometers, Detectors and Associated Equipment*, 831:161–166, 2016.

[160] B. Meier. CMS pixel detector with new digital readout architecture. *Journal of Instrumentation*, 6(01):C01011, 2011.

[161] J. Christiansen and M. Garcia-Sciveres. RD Collaboration Proposal: Development of pixel readout integrated circuits for extreme rate and radiation. Technical report, 2013.

[162] L. Gaioni, A. Rozanov, M. Bagatin, G. Marchiori, S. Godiot, T. Kishishita, Z. Janoska, G. Calderini, M. Marcisovsky, J. Hoff, et al. Design of analog front-ends for the RD53 demonstrator chip. *PoS*, page 036, 2017.

[163] M. Garcia-Sciveres. RD53A Integrated Circuit Specifications. Technical report, 2015.

[164] M. Garcia-Sciveres. The RD53A Integrated Circuit. Technical Report CERN-RD53-PUB-17-001, 2017.

[165] G. Kramberger. Advanced transient current technique systems. *PoS*, page 032, 2015.

[166] I. Kopsalis. *Surface Effects in Segmented Silicon Sensors*. PhD Thesis, University of Hamburg, 2017. 10.3204/PUBDB-2017-02889.

[167] C. Scharf and R. Klanner. Determination of the electronics transfer function for current transient measurements. *Nuclear Instruments and Methods in Physics Research Section A: Accelerators, Spectrometers, Detectors and Associated Equipment*, 779:1–5, 2015.

[168] W. Adam, T. Bergauer, M. Dragicevic, M. Friedl, R. Fruehwirth, M. Hoch, J. Hrubec, M. Krammer, W. Treberspurg, W. Waltenberger, et al. Trapping in proton irradiated p^+-n-n^+ silicon sensors at fluences anticipated at the HL-LHC outer tracker. *Journal of Instrumentation*, 11(04):P04023, 2016.

[169] TCTAnalyse. http://www.particulars.si/TCTAnalyse/index.html.

Acknowledgements

First of all I'd like to thank my mentor Robert Klanner for many important impulses. I'd also like to thank Erika Garutti, Alexandra Junkes, Jörn Schwandt, Eckhard Fretwurst, and Georg Steinbrück for very useful discussions and comments which made this work possible. Very special thanks also to Michael Matysek and Peter Buhmann for their cheerful attitude and for very helpful discussions building the edge-TCT setup. Furthermore, I'd like to thank Finn Feindt and Hendrik Jansen for the enthusiasm during the development of the edge-TCT setup at Hamburg University and DESY and the organization of meetings and workshops and Jörg Wellhausen and Jens Schaarschmidt for technical drawings and electronics support.

Then, I'd like to thank Michael Moll, Hannes Neugebauer, and Christian Gallrapp of CERN for discussions and especially for performing TCT measurements with their setup; Gregor Kramberger and Marko Mikuž of Jožef Stefan Institute for stimulating discussions and for providing edge-TCT measurements and the high-ohmic <111> silicon diode for the drift velocity measurements; Philip Metz and Alexander Heuer of the Institute of Laser Physics at Hamburg University for help with the Cary spectrophotometer; Andreas Wieck and Sergej Markmann of Ruhr Universität Bochum for the help and for letting me use the FTIR spectrometer - even though the measurements were not successful; Sven Wonsak of University of Liverpool and the RD50 collaboration for kindly providing thin p-type strip sensors to be used for edge-TCT studies; Alexander Dierlamm and Daniel Schell of Karlsruhe Institute of Technology for developing and discussing the sensor design code in a joint effort and Marko Dragicevic of HEPHY for providing his code, which served as the basis of our development; Julian Becker for providing the code and a crash course of his simulation program developed at Hamburg University.

Many thanks also to all the people of the Hamburg University detector group who provided help and knowledge along the way and of course for the countless table soccer matches. Finally, I'd like to thank my family and friends for the continuous support!

Eidesstattliche Versicherung / Declaration on oath

Hiermit versichere ich an Eides statt, die vorliegende Dissertationsschrift selbst verfasst und keine anderen als die angegebenen Hilfsmittel und Quellen benutzt zu haben. Die eingereichte schriftliche Fassung entspricht der auf dem elektronischen Speichermedium. Die Dissertation wurde in der vorgelegten oder einer ähnlichen Form nicht schon einmal in einem früheren Promotionsverfahren angenommen oder als ungenügend beurteilt.

Hamburg den 15.04.2018

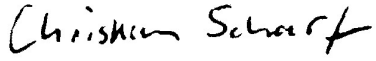

Unterschrift des Doktoranden